Assistive Motor Reeducation via Brain Computer Interface for Neurological Deficiencies

Juan Carlos Arceo Luzanilla

Thèse de doctorat

Pour obtenir le grade de Docteur de

l'UNIVERSITÉ POLYTECHNIQUE HAUTS-DE-FRANCE
et de l'INSA HAUTS-DE-FRANCE

spécialité

Automatique

Présentée et à soutenir par Juan Carlos ARCEO LUZANILLA.

Le 23/04/2021, à Valenciennes

Ecole doctorale : Sciences Pour l'Ingénieur (ED SPI 072)

Laboratoire : Laboratoire d'Automatique, de Mécanique et d'Informatique Industrielles et Humaines (LAMIH - UMR 8201)

Rééducation Motrice Assistée par Interface cerveau machine pour les Déficiences neurologiques

JURY

Président du jury

- Kevin Guelton, PU, Université de Reims Champagne.

Rapporteurs

- Dalil Ichalal, PU, IBISC, Université d'Evry Val d'Essonne.
- Samer Mohammed, PU, LISSI, University of Paris-Est Créteil.

Directrice de thèse :

- Simoneau-Buessinger, Emilie. Pr. UPHF, LAMIH UMR CNRS 8201.

Directeur de thèse :

- Lauber, Jimmy. Pr. UPHF, INSA, HdF, LAMIH UMR CNRS 8201.

Co-encadrant de thèse :

- Sylvain Crémoux, MCF, CerCo, Université de Toulouse.

PhD Thesis

Submitted for the degree of Doctor of Philosophy from

UNIVERSITÉ POLYTECHNIQUE HAUTS-DE-FRANCE
and INSA HAUTS-DE-FRANCE

Subject :

Automatic Control

Presented and defended by Juan Carlos ARCEO LUZANILLA.

Le 23/04/2021, à Valenciennes

Doctoral school : Sciences for Engineers (ED SPI 072)

Laboratory : Laboratory of Industrial and Human Automation control Mechanical engineering and Computer science (LAMIH – UMR 8201)

Assistive Motor Reeducation via Brain Computer Interface for Neurological Deficiencies

JURY

President of the jury

- Kevin Guelton, PU, Université de Reims Champagne.

Reviewers

- Dalil Ichalal, PU, IBISC, Université d'Evry Val d'Essonne.
- Samer Mohammed, PU, LISSI, University of Paris-Est Créteil.

Thesis co-director :

- Simoneau-Buessinger, Emilie. Pr. UPHF, LAMIH UMR CNRS 8201.

Thesis co-director :

- Lauber, Jimmy. Pr. UPHF, INSA, HdF, LAMIH UMR CNRS 8201.

Co-supervisor :

- Sylvain Crémoux, MCF, CerCo, Université de Toulouse.

Résumé

L'AVC est l'une des principales causes d'invalidité à long terme et de décès dans le monde, il existe plusieurs facteurs ou indicateurs qui pourraient influencer la souffrance de l'AVC tels que le vieillissement, le tabagisme, la consommation d'alcool, le cholestérol, le stress psychologique auto-perçu, l'alimentation, l'exercice, le récent virus COVID-19, entre autres causes. Les soins post-AVC représentent l'un des plus gros fardeaux pour les systèmes de santé, le coût total de l'AVC dans l'Union européenne était estimé à plus de 38 milliards d'euros par an en 2006.

Cette thèse porte sur le développement d'une interface cerveau-ordinateur hybride capable de coupler des données électrophysiologiques (signaux d'électroencéphalographie et d'électromyographie) et des informations biomécaniques du sujet (force et moment) pour produire une rééducation personnalisée de la cheville via un ergomètre motorisé, développé au LAMIH, nommé comme le motoBOTTE. Le travail présenté dans ce manuscrit a été divisé en deux thèmes principaux: 1) la modélisation et le contrôle du dispositif de rééducation pour suivre des trajectoires prédéfinies et 2) la prise en compte de l'interaction humaine avec le système, ceci en employant des modèles de suivi de la cheville humaine et de création dynamique trajectoires à suivre par le robot d'assistance.

La première partie consiste à obtenir différents modèles mathématiques du dispositif de rééducation (chapitre 2), qui est un robot parallèle; puis, à l'aide de ces modèles, différents contrôleurs sont conçus et implémentés en temps réel pour suivre des trajectoires prédéfinies (chapitres 3 et 4). Dans ce contexte, deux modèles ont été développés, un premier est obtenu via une approche boîte noire et le second utilisant une variante de l'approche Euler-Lagrange pour les robots parallèles.

La deuxième partie traite du problème de la prise en compte d'un humain en interaction avec des systèmes d'assistance robotique. Une première proposition est d'introduire un modèle mathématique (chapitre 5) afin d'estimer l'estimation de la force de la cheville via des signaux EMG en temps réel. La deuxième proposition concerne les signaux EEG pour déclencher le mouvement du robot via l'imaginaire moteur, qui a été appliqué à la conception d'un exosquelette de poignet imprimé en 3D à faible coût (chapitre 6).

Mots-clés: Rééducation motrice, robot parallèle, interface cerveau machine, équations différentielles-algébriques, modélisation et contrôle de systèmes singuliers non linéaires, estimation de la force par électromyographie, induction de plasticité neuronale.

Abstract

Stroke is one of the leading causes of long-term disability and death worldwide. There are several factors or indicators that might influence the probability of suffering of stroke such as aging, smoking, alcohol intake, cholesterol, self-perceived psychological stress, diet, physical inactivity, the recent COVID-19 virus, among other causes. Post-stroke care represents one of the biggest burdens to health care systems, the total cost of stroke in the European Union was estimated to be over € 38 billion per year in 2006.

There are many strategies that can be used to improve motor function recovery in post-stroke rehabilitation such as functional electrical stimulation, transcranial magnetic stimulation, standing balance, strength training, constrained induced movement, mental practice with motor imaginary and robot assisted therapy. This thesis focuses on the development of an hybrid brain computer interface capable of coupling electrophysiological data (electroencephalography and electromyography signals) and biomechanical information of the subject (force and moment produced by the ankle muscles) to produce a personalized ankle rehabilitation via a motorized ergometer known as the motoBOTTE.

This work has been divided in two main topics : 1) modeling and control of the rehabilitation device for tracking predefined trajectories and 2) consider the human interaction with the system, this by employing models for monitoring the human ankle and create dynamical trajectories to be followed by the robot. The first part consists in obtaining different mathematical models of the rehabilitation device (chapter 2), which is a parallel robot; then, using these models different controllers are designed and implemented in real-time for tracking predefined trajectories (chapters 3 and 4). In this context, two models have been developed, a first one is obtained via a black-box approach and the second using a variant of the Euler-Lagrange approach for parallel robots. The second part deals with the problem of considering a human interacting with robotic assistive systems. A first proposal is to introduce a mathematical model (chapter 5) in order to estimate ankle force estimation via EMG signals in real-time. The second proposal is to EEG signals for triggering the robot movement via motor imaginary, which has been applied to the design of a low-cost 3D printed exoskeleton (chapter 6). Finally, some perspectives of this work are provided by the end of this manuscript (Chapter 7).

Keywords : Motor reeducation, parallel robot, brain computer interface, differential-algebraic equations, modeling and control of nonlinear singular systems, force estimation via electromyography, neural plasticity induction.

Declaration of Authorship

I, Juan Carlos Arceo Luzanilla, declare that this thesis titled, "Assistive Motor Reeducation via Brain Computer Interface for Neurological Deficiencies" and the work presented in it are my own. I confirm that:

- The thesis comprises only my original work towards the DOCTEUR D'UNIVERSITÉ degree, except where indicated in the preface;
- due acknowledgement has been made in the text to all other material used; and
- the thesis is fewer than the maximum word limit in length, exclusive of tables, maps, bibliographies and appendices as approved by the Research Higher Degrees Committee.

Signed: _____

Date: _____

Preface

Some of the results presented within this manuscript were obtained in collaboration with the following universities :

- Sonora Institute of Technology, 5 de Febrero 818 Sur, Ciudad Obregon, Sonora, Mexico.
- Department of Health Science and Technology, Aalborg University, 9220 Aalborg, Denmark
- Health and Rehabilitation Research Institute, Auckland University of Technology, Auckland 0627, New Zealand.

The content of the sections and chapters within this document has been submitted, published or accepted for publication as follows :

International Journals (3)

- The results on optimal afferent feedback for rehabilitation using brain computer interface in section 6.1 have been published as Jochumsen, M., Cremoux, S., Robinault, L., Lauber, J., **Arceo, J. C.**, Navid, M.S., Niazi, I. K. (2018). Investigation of optimal afferent feedback modality for inducing neural plasticity with a self-paced brain-computer interface. Sensors, 18(11), 3761. (IF= 3.275).
- The grey box model of the robot, the parameter estimation and its validation process presented in subsection 2.2.3 as well as the controllers based on an extension of the computed-torque control for parallel robots and the active disturbance rejection control shown in subsection 3.1.2 and section 3.2 have been accepted for a publication as **Arceo, J. C.**, Alvarez, J., Armenta, C., Lauber, J., Cremoux, S., Simoneau-Buessinger, E., Bernal, M. (2021). Novel Solutions on Model-Based and Model-Free Robotic-Assisted Ankle Rehabilitation. Accepted In Archives of Control Sciences (IF= 1.697).

- The results from the application of a low-cost solution for a open hardware brain computer interface (OpenBCI) and a 3D printed wrist exoskeleton in section 6.2 have been published as Jochumsen, M., Janjua, T. A. M., **Arceo, J.C.**, Lauber, J., Simoneau-Buessinger, E., Kæseler., R.L. (2021). Induction of Neural Plasticity Using a Low-Cost Open Source Brain-Computer Interface and a 3D-Printed Wrist Exoskeleton. Sensors. (IF= 3.332).

International Conferences (5)

- The black box model of the robot from subsection 2.2.1 and the convex proportional-integral (PI) controller based on convex structures shown in subsection 4.1.4 have been published as **Arceo, J. C.**, Lauber, J., Simoneau, E., Cremoux, S. (2018, October). Nonlinear Convex Control for Robotic Assistive Therapy via LMIs. Workshop on Assistance and Service Robotics in a Human Environment: From Personal Mobility Aids to Rehabilitation Oriented Robotics in the International Conference on Intelligent Robots 2018 (IROS 2018).

- The black box model of the robot from subsection 2.2.1 and the convex proportional-integral-derivative (PID) controller based on convex structures presented in subsection 4.1.5 have been published as **Arceo, J. C.**, Lauber, J., Robinault, L., Paganelli, S., Jochumsen, M., Niazi, I.K., Cremoux, S. (2018, October). Modeling and Control of Rehabilitation Robotic Device: motoBOTTE. In International Conference on NeuroRehabilitation (pp. 546-550).Springer.

- The white box model of the robot presented in subsection 2.2.2 and the computed torque control for parallel robots in a state-space representation in subsection 3.1.1 have been published as Álvarez, J., **Arceo, J. C.**, Armenta, C., Lauber, J., Bernal, M. (2019). An Extension of Computed-Torque Control for Parallel Robots in Ankle Reeducation. IFAC-Papers OnLine, 52(11), 1-6.

- The application of the nonlinear sector methodology to obtain an exact convex representation for singular systems and parallel distributed compensation design for nonlinear singular systems in subsection 4.2 have been published as **Arceo, J. C.**, Lauber, J. (2020, May). Nonlinear Convex Control Design for Differential Algebraic Equation Systems via LMIs. In 2020 IEEE International Conference on Automation, Quality and Testing, Robotics (AQTR) (pp. 1-6). IEEE.

- The conditions for nonlinear controller and observer design based on condition for copositive matrices presented in subsection 4.1.3 have been published as **Arceo, J. C.**, Lauber, J. (2020, Jul). Copositive Conditions for LMI-Based Controller and Observer Design. In 21st IFAC World Congress, IFAC-Papers OnLine.

adaptations in the notation and figures of those publications have been made to keep this manuscript as homogeneous as possible.

Acknowledge to the following sources of funding :

- For financing the doctoral contract to the Hauts-de-France Region and the Polytechnic University Hauts-de-France.
- This work has been supported by the ECOS Nord SEP-CONACYT-ANUIES Project (Mexico 291309 / France M17M08).
- This research is sponsored by ELSAT 2020 of the Hauts-de-France Region, the European Community, the Regional Delegation for Research and Technology, the French Ministry of Higher Education and Research, and the French National Center for Scientific Research.
- Erasmus + Agency in France for the mobility contract to Denmark.
- Campus France funding.

Acknowledgements

This is probably one of the most important documents that I write, and this work has taken almost three and a half years of our lives; therefore, there is a list of the people that I would like to acknowledge and extend my gratitude to :

- To my supervisors Jimmy, Emilie and Sylvain, thank you for selecting me as your student and giving me this opportunity. Specially to Jimmy, thank you for all the support, for caring about the project and for being patient with me, even when I committed so many mistakes.
- To the members of the Jury for reviewing the manuscript, Samer Mohammed and Dalil Ichalal, for accepting to be reporters and writing the report, to Kevin Guelton for reviewing the manuscript and accepting to be examinator.
- To my wife Grecia, thank you for always supporting me and believe in me, even when I didn't, I really appreciate it.
- To my mother Maria, my father Juan Carlos, my brother Martin, my sister Andrea and my nephews Santiago and Emilio, thank you for sharing your love with me and motivate me every day.
- To Miguel, for the teachings and for recommending me to this position.
- To Mads, for receiving me and working with me during my stay in Aalborg.
- To my friends from the lab Marcelino, Anh-Tu, Shijie, ~~Braulio~~ Negrita, Guoxi, Marie, Masoud and Carlos, thank you for sharing your time with me.
- To everyone that I've colaborated with during this project, Paganelli, Lucien, ~~Jorge~~ Koke, Rasmus and Taha.
- To all my friends from la tuna ITSON in Mexico, I miss you all.

Contents

List of Figures

List of Tables

Abbreviations

3D	**Tridimensional**
ADRC	**A**ctive **D**isturbance **R**ejection **C**ontrol
BCI	**B**rain **C**omputer **I**nterface
B.O.T.T.E.	**B**ooted, **O**pen-unit, **T**hree dimension, **T**ransportable, **E**rgometer
DAE	**D**ifferential-**A**lgebraic-**E**quation
EMG	**E**lectro**m**yo**g**raphy
EEG	**E**lectro**e**ncephalo**g**raphy
ES	**E**lectrical **S**timulation
FPm	**F**alse **P**ositive detections per **m**inute
LMI	**L**inear **M**atrix **I**nequality
MVC	**M**aximun **V**oluntary **C**ontraction
MEP	**M**otor **E**voked **P**otential
OR	**O**dds **R**atio
PDC	**P**arallel **D**istributed **C**ompensation
PM	**P**assive **M**ovements
SOL	**Sol**eus
SRE	**S**moothed and **R**ectified **E**lectromyography
T-S	**T**akagi-**S**ugeno
TA	**T**ibialis **A**nterior
TMS	**T**ranscranial **M**agnetic **S**timulation
TPR	**T**rue **P**ositive **R**ate
V	**V**olts
WHO	**W**orld **H**ealth **O**rganization
WSO	**W**orld **S**troke **O**rganization

Constants

$$\text{Gravity} \quad g \quad = \quad 9.806 \quad m/s^2$$

Symbols

ϕ	Ankle angle	rads
$\dot{\phi}$	Ankle angular velocity	rads/s
u	Control signal	Volts
d	Piston distance	m
$\dot{d}$	Piston velocity	m/s
Θ_1	Angle of the robot	rads
$\dot{\Theta}_1$	Angular velocity of the robot	rads/s
Θ_2	Angle of the robot	rads
$\dot{\Theta}_2$	Angular velocity of the robot	rads/s
γ_1	Angle of the robot	rads
γ_2	Angle of the robot	rads
l_1	Length of the link 1	rads
l_2	Length of the link 2	rads
l_3	Length of the link 3	rads
l_4	Length of the link 4	rads
l_5	Length of the link 5	rads
m_1	Mass 1	kg
m_2	Mass 2	kg
m_3	Mass 3	kg

Chapter 1

General introduction

This chapter provides background information about stroke and post-stroke rehabilitation, and the state-of-the-art of the role of robots in assisted rehabilitation; the motivation, scope and list of publications of this work are presented after that.

1.1 Background and Motivation

Stroke is a disease in which there is a failure in supplying enough oxygen to brain cells (interruption or leakage of blood supply) [1, 2]. The common symptoms are 1) numbness or weakness of face, arm or leg, 2) loss of coordination during walking, 3) severe headache with no apparent reason, 4) sudden confusion and 5) sudden trouble of sight [3].

The total economic cost of stroke in the European Union was estimated to be over €38 billion in 2006 [1, 4], this includes health care, loss of productivity and informal care. In France, stroke is the third cause of death and leading cause of disability, the estimate for 1-year cost of stroke health-care in 2000 was € 17 800 per patient [5].

Some of the consequences of stroke are permanent or long-term disabilities in approximately 39 % of the cases [3, 6], as example of these long-term impairments are hemiplegia and paraplegia [7], which consists on paralysis of one side of the body or the lower limbs, respectively. Since each case is different (it might be produced by different causes and have different consequences), the nature of stroke recovery itself is heterogeneous [8]; this means that each case should be analyzed and treated with an ad-hoc strategy.

Despite the many efforts, stroke is one of the major causes of death and disability worldwide [8]. According to the World Health Organization (WHO) [9–11] and the World Stroke Organization (WSO) [12] there are 13 million new cases every year, the incidence rates of stroke have decreased due to a better prevention and control in risk factors; but the number of people who had a stroke, died or were disabled due to stroke has increased by almost two-fold from 1990 to 2016 [12]. There are several factors that influence the risk of suffering from this cardiovascular disease such as :

- Aging, an augmentation on life expectancy of the global population has led to an increasing in the group of people at risk of stroke [13]. The incidence of stroke has been reported to increase from $2.28/1,000$ for patients in the range of $55-64$ years of age to $24.23/1,000$ in patients over 80 years of age [6].
- Heavy consumption of alcohol (60 g of alcohol per day, more than 5 drinks) increases the relative risk of stroke; while light or moderate alcohol intake ($12-24$ g/d) may protect against suffering ischemic stroke compared to abstainers (<12 g/d) [14].
- Smoking status, environmental tobacco smokers (passive smokers) compared to non-smokers and long-term ex-smokers have an increased risk of stroke (odds ratio, OR=1.82); compared with people who reported never smoked cigarettes, active smokers have a fourfold risk of stroke (OR=4.14) [15].
- Drug abuse, 4.8% of the world's population consume illegal drugs each year, drug abusers have an increased risk (OR=6.5) of presenting hemorrhagic and ischemic stroke, the drugs commonly associated with stroke are stimulants such as cocaine (OR=2.03-2.33) and amphetamine (OR=4.95) [16].
- Diabetes, the risk of stroke is increased in patients with diabetes mellitus (OR=1.5-3) and risk of recurrence is doubled; patients with diabetes may develop silent lacunar strokes and the levels of glycaemia (measured via HbA1c) have been reported to be a risk factor for stroke fatality [2, 17].
- Psychological stress, a frequent activation of the sympathetic nervous system may lead to hypertension and metabolic disturbances. Subjects that have reported being under self-perceived permanent stress during the last year or more, had a higher risk of stroke (OR=3.49), [18, 19].

- Exercise, vigorous exercise once a week (enough for sweating) decreases the risk by 21% (OR=0.79), no further risk reductions were reported at greater exercise frequency [20].
- COVID-19, the infection itself has been described to be a risk factor [21]; additionally, stroke patients seem to be more susceptible to develop severe complications and death when suffering the infection. Moreover, the pandemic has led to implications on how therapists and patients must interact to deliver stroke care [22, 23].

Other risk factors that had been identified are unhealthy diet, ethnicity, cholesterol, blood pressure, genetics, obesity, history of cardiovascular diseases, contraceptives with high doses of estrogen, and so on [2, 24], some of these factors are shared with other non-cardiovascular diseases [9]; different prediction models have been elaborated using these indicators [11] to identify people at risk of suffering stroke [25, 26].

As consequence of stroke, patients might suffer from spasticity, which is an hyperexcitability motor disorder characterised by a velocity-dependant increase in tendon jerks, it magnifies muscle weakness and produces difficulty during gait, contractures and permanent joint deformities; it has been also defined as a permanent or intermittent involuntary contraction of muscles that produces motor abnormalities.

1.2 Stroke Motor Rehabilitation Strategies

It is up to an occupational therapist to decide based on the patient's abilities and role demands which will be the therapeutic goal, he can decide to focus on promoting learning or training phenomena on the patient. Where learning is defined as finding ones solution for a certain task and training is considered as memorizing a given solution for a challenge [2]. Some of the strategies employed for stroke rehabilitation are standing balance, strength training, constrained induced movement, electrical stimulation, transcranial magnetic stimulation, mental practice with motor imaginary, and robotic assisted therapy, among other approaches [3, 4, 27, 28]. Most of these approaches aim or share a common goal, which is reducing the disability or handicap produced by stroke [8]; it is possible to estimate or evaluate the efficiency of applying a determined strategy via tools for measuring functional independence in activities of daily living such as

the Katz Index or the Barthel Index [29]. Here is a brief description of the mentioned strategies as well as some concepts that will be used later :

- ***Standing balance*** [3]. It consists on maintaining a relative position and motion of the body center of mass with respect to the foot in contact with the ground; this therapy has been recently combined with virtual reality systems, in order to induce to the patient the sensation of disturbances such as riding subway ride, while keeping him within a safe environment. Ground force plates combined with 3D vision systems have been employed for analyzing the patterns exhibited by the subject during this therapy, using these tools it is possible to measure the position of its center of mass, center of pressure, as well as the movements performed. Which is an interesting therapy since stroke patients often suffer from balance and gait impairments.

- ***Strength training*** [30, 31]. After suffering a stroke, muscle weakness is one of the biggest sources of impairment experienced. The motor function can be affected in several ways and the reduction of strength (in terms of maximum voluntary contraction) is one of the most notorious. Muscle force production can easily be related to activities of daily living such as bringing food to the mouth, standing from a chair or walking; the point in which this strength begins to affect the performance of a certain activity or the one in which additional strength has no impact varies from a subject to another, and it is worth noticing that not all the stroke patients experience muscle weakness. When the exercises in this therapy are performed on specific machines such as dynamometers these can be classified as isometric, isotonic and isokinetic strengthening.

- ***Constrained induced movement*** [31, 32]. According to a systematic review, this strategy has been found to be the most effective for improving motor performance in the upper limp. This strategy has a long history, the first documentations found are from 1909 of some experiments with primates; later in 1917 experiments with monkeys showed that when these were forced (using straps) to use their recovered limb faster after injury.

- ***Electrical Stimulation*** [33]. Electromyography are electrical signals that can be recorded from a muscle, this electrical signal is a chemical reaction that induces a voluntary contraction in the muscle, and neuromuscular electrical stimulation

(NMES) consists in applying an electrical stimulation on the muscle to induce an involuntary contraction, this strategy might influence the subject motor performance and its cortical organization, it has been studied in healthy subjects as well as for subjects with brain injuries, such as stroke. One of the main interests of this approach is that stroke patients are not able to contract their muscles voluntarily, and with NMES, it is possible to activate their muscles in order to limit muscular atrophy (decrease of muscle mass).

- ***Transcranial magnetic stimulation*** [34, 35]. It is a type of therapy as well as a non-invasive tool that can be used for studying the human brain by inducing a magnetic field near to the brain cortex that depolarizes cortical nerve membranes and discharges a group of neurons, it produces a relative synchronous muscle response known as motor evoked potentials (MEP).

- ***Motor imaginary (Mental practice)*** [2]. It consists on creating an internal representation of the movement to execute, it is mentally simulated without performing the physical activity and can be administered via audio therapy.

- ***Robot assisted therapy*** [31, 36]. Using robotic devices in therapy allows to perform a repetitive, highly intensive, task-specific treatment of the impaired limb while monitoring the patient actual state and progress via integrated sensors. These robots can provide a passive movement feedback to the subject and measure residual voluntary activity from the impaired limb during its manipulation.

Some reports agree that most of the patient's recovery occurs during the first three to six months [37, 38]. The strategies previously described rely on neuroplasticity (or plasticity) [39], which is the ability of the neural system to reorganize its structure, functions and connections as a response to intrinsic or external stimulus. It might be produced as a consequence or response to a disease, induced by therapy, as support of learning, among other reasons. Not all plasticity has positive impacts, i.e., epilepsy may appear as complication of cerebral trauma, it might appear even years after the trauma event, and this suggests that during this time there have been progressive changes in the brain. Within this general context, this document focuses mainly on ankle rehabilitation via assisted robotics, this joint plays an important role in gait and balance, although some applications to wrist rehabilitation are reported by the end of this manuscript. More details about robotic assisted rehabilitation will be provided in the next section.

1.3 The Role of Robots in Assisted Therapies

As mentioned before, the strategy of assisted rehabilitation focuses on recovering the motor function of the impaired limb by following therapist's specified routines with the assistance of a robot, while monitoring not only progress, but also the actual state of the subject during therapy. This section presents some of the emerging trends, advantages of using robots for assisted rehabilitation and a list of the commercially available products in the market with a brief description of them.

Popular and emerging trends in rehabilitation robotic devices

The emerging trends in rehabilitation robotics can be summarized by classifying them in different categories as :

- According to the structure of the robot as end-effector robots [31, 40–42] and exoskeletons [7, 40, 41, 43–54]. End-effector robots do not necessary have anthropomorphic shape. To use this kind of devices the impaired limb is generally attached to the end-effector of the robot or it can be grabbed as in the case of upper limb rehabilitation systems; while exoskeletons intend to mimic the shape of the affected limb and they are generally located around that limb.

- Based on the sensors included in their designs, such as surface electromyography sensors (EMG) [38, 42, 48, 53, 55, 56] for measuring the electrical activity within the muscles. They can be coupled to a brain computer interface (BCI) [38, 47] with biopotential amplifiers capable of measuring, amplifying and converting the electrical activity in the brain (named electroencephalography, EEG) into a digital signal (OpenBCI [57]), or with force and torque sensors integrated [7, 42, 45, 46, 51, 54, 55].

- Depending on the task or exercise to be performed by the assistive device : strength training [31], gait training [7, 44–47, 47, 49–52, 54, 58], afferent feedback [40, 55, 56] and standing balance [47, 51].

- In relation to the feedback provided to the user of the robot [38] such as visual feedback [59]. It includes techniques that combine robots with virtual reality or LEDs to perform experiments with brain computer interfaces, audition, haptic

interfaces, functional electric stimulation and transcranial magnetic stimulation (denoted FES and TMS, respectively).

Among the many advantages that can be obtained from applying robots to therapy are : they can be used to perform repetitive tasks or exercises with high intensity [36], a robot will never be exhausted and it can be designed to handle forces with higher magnitude than humans. The integrated sensors allow to measure the progress and behavior of the patient with high accuracy [36], these sensors might even be used in the future to improve a patient diagnosis. A single device can provide different types of feedback to the patient and even combine them in order to maximize the outcome from therapy. The robots allow to assist the patient's movements as needed with high precision or to perform different tasks with a device. Trajectory planning techniques can be employed to avoid painful positions for the subject's impaired limb.

Scientific research and commercially available products for rehabilitation

There is a brief list of the many different available scientific research and commercially available products for rehabilitation that can be found in the literature or the market :

- **MIT-MANUS** [36, 40, 41, 53, 55, 58] is a two degrees-of-freedom robot designed for neurological applications (i.e., shoulder and elbow rehabilitation), it belongs to the category of end-effector robots and its sensors allow measuring different variables involved in the motion of the patient's upper limbs such as position, velocity, interaction forces and surface EMG signals. Also, there is a screen in the system that provides visual feedback to the patient during therapy, it can be used to display the value of the different variables measured or information about the task being performed (target and end-effector positions).
- **Neuro-Rehabilitation-Robot (NeReBot)** [36, 58, 60] is a 3 degrees-of-freedom end-effector robot designed to recover from post-stroke upper limb impairment (shoulder and elbow) by performing repetitive experiments. The system provides visual and auditory feedbacks to the user, the auditory feedback is employed to indicate the beginning and ending of the exercise and the visual feedback is a 3D image representing the upper limb position and the forces applied.
- **Lokomat** [38, 41, 43, 45, 49, 51, 54, 56, 58, 58, 60, 61] is an exoskeleton designed for lower-limb rehabilitation after spinal cord injury or stroke by performing gait

training exercises over a treadmill, it is able to provide body weight to the subject, the device can drive or assist the leg trajectory of the subject in order to perform a gait movement over a treadmill. It has position, force and EMG sensors integrated and can provide to the patient visual and haptic feedbacks as well as functional electrical stimulation (FES).

- **ATLAS** [51, 60]. It is an exoskeleton designed for gait assistance to support people with paralysis caused by spinal cord injury, it can support up to a maximum of 25 kilograms, it has 6 degrees-of-freedom, 3 for each leg (composed by hip, knee and ankle angles variables). The sensors integrated to this system are goniometers for measuring the angular position of the joints and force sensors located at the feet that allows measuring the trajectory of the center of pressure.

- **Vanderbilt lower limb exoskeleton** [7, 38, 46, 50, 50–52] has been designed to provide leg mobility to patients suffering from paraplegia or hemiplegia produced by stroke, the device can control the angular position of the subject hips, knees and ankles. It has sensors for measuring the angle position at each joint as well as an inertial measurement unit (IMU), which is a combination of gyroscopes and accelerometers that can be employed for measuring orientation, velocities and gravitational forces.

- **MINDWALKER** [52] is a powered lower limb exoskeleton with 5 degrees-of-freedom to support people with paraplegia or hemiplegia during gait training, it has encoders for measuring the joint angular positions, joint torque produced by the actuators, as well as IMUs.

Among other solutions found [38, 41, 43, 47, 56, 60].

1.4 Scope of this Work

Given the previous context, the LAMIH (UMR CNRS 8201) developed and obtained a patent for an ergometer with limited size and reasonable production cost [62], the device employed in this thesis is a motorized version of that ergometer, such device can be located in the bed of the patient and would allow early therapy. As mentioned before an early intervention in stroke rehabilitation improves the efficiency of the treatment.

The main goal of this work is to develop a hybrid brain computer interface (hybrid BCI) capable of integrate electrophysiological data from the subject, i.e., electromyography (EMG) and electroencephalography (EEG) signals. The motivation for the development of this system is using it for post-stroke robotic assisted rehabilitation, a system like this would be capable to provide a personalized assisted therapy adapted for each subject, while monitoring its variables with precision.

This work is divided in two stages : 1) modeling and control of the rehabilitation device and 2) integrating the human in the control loop. The first part consists in modeling the rehabilitation device, design and implement control laws for tracking predefined trajectories, the first model is obtained via a black-box approach and the second via a variant of the Euler-Lagrange approach for parallel robots. The second part deals with the problem of considering a human interacting with the system. The first approach presents a model for using EMG signals to estimate the force produced by the ankle in real-time and the second is using EEG signals for triggering the robot movement via motor imaginary.

Remark 1.1. Please notice that there is a limitation in the number of subjects employed and number of experiments that can be performed during the development of this research project.

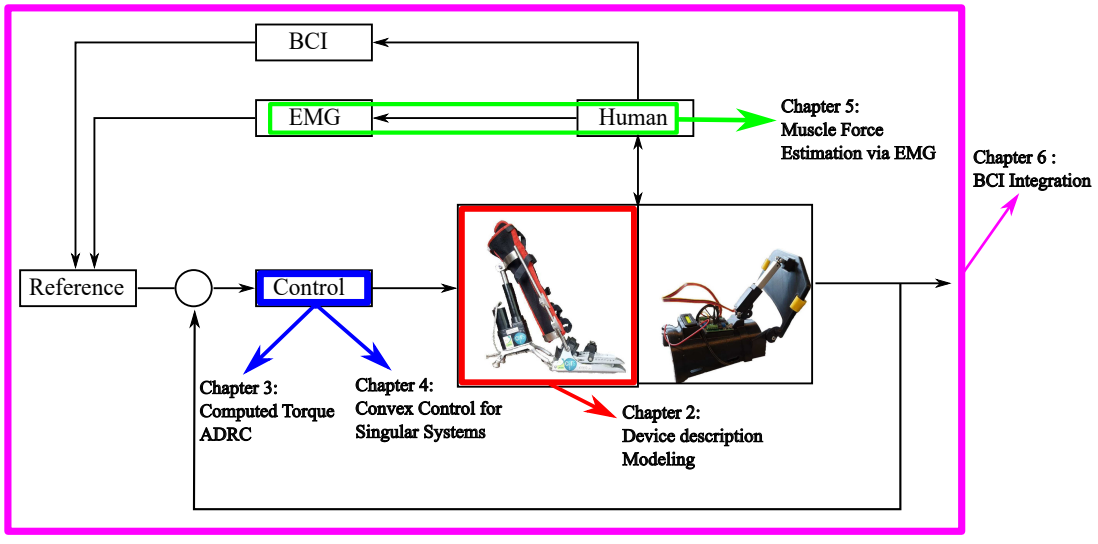

FIGURE 1.1: Organization of this document.

1.5 Structure of this Document

As it is briefly illustrated in Fig. 1.1, this document is organized as follows :

Chapter 2 introduces the main rehabilitation devices involved in the hybrid brain computer interface, a parallel robot named motoBOTTE and the devices that interact with it; then, three different mathematical models for describing its dynamics are presented, the first is obtained via a black-box approach and the second (white box) and third (grey box) models are two sets of differential-algebraic-equations that take into account the algebraic constraints of the system, parameters are estimated and validated using data from real-time experiments.

Chapter 3 presents the design and implementation of different control laws for tracking trajectories, these designs are validated in simulation and implemented in real-time. The model-based technique employed in this chapter is computed-torque control and the model-free approach is active disturbance rejection control, both have been adapted to be used in parallel robots that are described by a set of differential-algebraic-equations.

Chapter 4 deals with problems related to control design for singular and nonsingular systems written as an exact convex representation such as conservative solutions and a new relaxation for double-sums is proposed for it. This chapter focuses on the convex modeling of nonlinear singular systems, where the importance of taking into account the algebraic constraints for this process is highlighted. After that, different designs based on parallel distributed compensation are carried out, similar to the previous chapter, the designs are used for tracking predefined trajectories.

Chapter 5 focuses on considering a human interacting with the robot. In this case, models for estimating the human ankle force via electromyography signals in real-time with the hybrid brain computer interface are adapted from the literature. Each step of the estimation process is described, parameters of the models are estimated and validated using data from real-time experiments (gait analysis), then, a new model used to generate dynamic ankle trajectories is presented and evaluated in simulation.

Chapter 6 exhibits the results obtained when the motoBOTTE and a wrist exoskeleton were coupled (separately) to a brain computer interface, then, the movement of the robots were triggered by detecting motor imaginary and the efficiency of employing

these devices for assisted rehabilitation is evaluated via statistical analysis of the motor evoked potentials measured during three events pre-, post- and post-30. The design of the wrist exoskeleton should be considered as part of the result obtained of this thesis.

Chapter 7 gives a conclusion based on the results presented in previous chapters, and establishes some remarks that could be considered in the future of this work.

1.6 List of Publications

The following publications have been obtained during this thesis :

International Journals

- Jochumsen, M., Cremoux, S., Robinault, L., Lauber, J., **Arceo, J. C.**, Navid, M. S., ... & Niazi, I. K. (2018). Investigation of optimal afferent feedback modality for inducing neural plasticity with a self-paced brain-computer interface. *Sensors*, 18(11), 3761.
- **Arceo, J. C.**, Álvarez, J., Armenta, C., Lauber, J., Cremoux, S., Simoneau-Buessinger, E., & Bernal, M. (2021). Novel Solutions onModel-Based andModel-Free Robotic-Assisted Ankle Rehabilitation*. In *Archives of Control Sciences*.
- Jochumsen, M., Janjua, T. A. M., **Arceo, J.C.**, Lauber, J., Simoneau-Buessinger, É., & Kæseler., R.L. (2021). Induction of Neural Plasticity Using a Low-Cost Open Source Brain-Computer Interface and a 3D-Printed Wrist Exoskeleton. *Sensors*.

International conferences

- **Arceo, J. C.**, Lauber, J., Simoneau, E., & Cremoux, S. (2018, October). Non-linear Convex Control for Robotic Assistive Therapy via LMIs. *Workshop on Assistance and Service Robotics in a Human Environment: From Personal Mobility Aids to Rehabilitation-Oriented Robotics in the International Conference on Intelligent Robots 2018 (IROS 2018).*
- **Arceo, J. C.**, Lauber, J., Robinault, L., Paganelli, S., Jochumsen, M., Niazi, I. K., ... & Cremoux, S. (2018, October). Modeling and Control of Rehabilitation

Robotic Device: motoBOTTE. In *International Conference on NeuroRehabilitation* (pp. 546-550). Springer, Cham.

- Alvarez, J., **Arceo, J. C.**, Armenta, C., Lauber, J., & Bernal, M. (2019). An Extension of Computed-Torque Control for Parallel Robots in Ankle Reeducation. *IFAC-PapersOnLine*, 52(11), 1-6.

- **Arceo, J. C.**, & Lauber, J. (2020, May). Nonlinear Convex Control Design for Differential Algebraic Equation Systems via LMIs. In *2020 IEEE International Conference on Automation, Quality and Testing, Robotics* (pp. 1-6). IEEE.

- **Arceo, J. C.**, & Lauber, J. (2020, Jul). Copositive Conditions for LMI-Based Controller and Observer Design. In *21st IFAC World Congress, IFAC-PapersOnLine*.

Chapter 2

Modelling of Parallel Robots

This chapter introduces a specific parallel robot designed for assisted rehabilitation, the motoBOTTE which is the main device employed in this work. The objective of this chapter is to provide tractable dynamical models of this system for control design. The chapter is organized as follows: Section 2.1 describes the characteristics of the rehabilitation robot as well as all the different devices involved in the signal acquisition and processing (sensors, actuator, power supplies and embedded device employed); Section 2.2 is about system identification and provides basic information from the state-of-the-art of the techniques that will be considered later for obtaining different mathematical models of the robot. Three subsections are contained in this part: 2.2.1 deals with a first approach to identify the model of this robot using a black box approach, i.e., considering input and output signals from real-time experiments and prior knowledge of the system, the model obtained is in terms of the ankle angle ϕ and the control input u; Subsection 2.2.2 proposes a white box modelling approach which is illustrated for parallel robots, the result obtained is a set of differential-algebraic-equations (DAEs) that incorporates the algebraic relations inherit to parallel robots, i.e., constraints in position, velocity and acceleration; Subsection 2.2.3 presents the grey box modelling approach, in which a slightly different set of DAEs is obtained, the parameters of the system are estimated and validated in simulation using data from real-time experiments with the robot.

FIGURE 2.1: The motoBOTTE.

2.1 The motoBOTTE : System Description

The Laboratory of Industrial and Human Automation Control, Mechanical Engineering and Computer Science (LAMIH) developed a transportable robot to perform ankle rehabilitation routines as for example on stroke-hit patients [8]. The motoBOTTE (see Fig. 2.1) is a one-degree-of-freedom parallel robot to be used along constant monitoring of the patient performance, where the ankle angle is denoted by ϕ; the sensor and control signals are computer-processed in a embedded device. As shown in [63], such device can significantly reduce the therapy costs while providing a greater flexibility and adaptation of the required routines to the corresponding case.

A parallel robot, such as the motoBOTTE, is a structurally closed kinematic chain mechanism [64] that is capable of moving large loads with high precision [65]. The geometrical structure of such parallel robots imposes constraints on their position, speed, acceleration, and degrees-of-freedom [66]; their trajectories are restricted to a manifold that satisfies all these constraints at once [67].

The robot is actuated by a linear piston shown in Fig. 2.2, the ankle angle ϕ can be measured via a potentiometer voltage in the piston [63, 68], the relation between ankle angle and voltage of the potentiometer is shown in Table 2.1 and fitting the data with

(a) Piston CAHB-21. (b) Label.

FIGURE 2.2: Linear piston and its label.

a polynomial function the following relation voltage-position is obtained

$$\phi(V) = -0.0113V^2 - 0.0630V + 2.7788,$$

the relation between potentiometer voltage, position and the polynomial approximation $\phi(V)$ is illustrate in Fig. 2.3. The specifications such as maximum load, speed, weight and stroke length of this device can be found in the datasheet [68].

TABLE 2.1: Ankle angle ϕ and potentiometer voltage measurement.

ϕ **(radians)**	**Volts**	ϕ **(radians)**	**Volts**	ϕ **(radians)**	**Volts**
2.5212	2.7507	2.4920	2.9659	2.4613	3.1997
2.4291	3.4060	2.4038	3.6139	2.3688	3.8238
2.3416	4.0500	2.3038	4.2438	2.2745	4.4458
2.2340	4.6630	2.2026	4.8633	2.1704	5.0891
2.1260	5.2959	2.0917	5.4878	2.0565	5.6910
2.0205	5.8959	1.9710	6.0912	1.9329	6.2995
1.8939	6.5229	1.8406	6.7403	1.7856	6.9597
1.7292	7.1970	1.6711	7.4124	1.6415	7.6202
1.5964	7.8451	1.5348	8.0741	1.4717	8.2957
1.4234	8.5050	1.3575	8.7174	1.3071	8.9383
1.2730	9.1120				

The rotation speed of the DC motor inside the linear piston is controlled by an ESCON

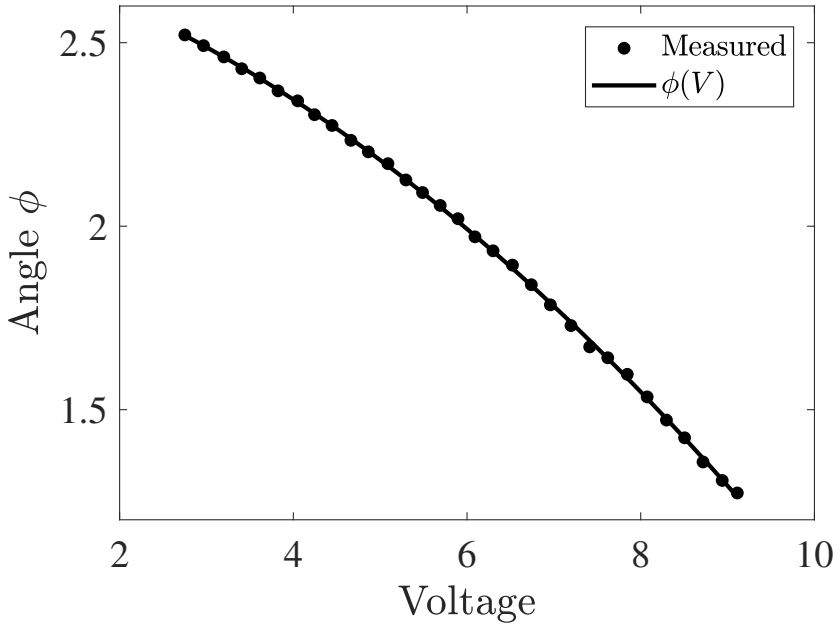

FIGURE 2.3: Ankle position and the polynomial approximation.

50/5 DC motor driver [69] that is shown in Fig. 2.4(a), this is a PWM servo controller which has three different operating modes: speed control (open-loop), speed control (closed-loop) and current control. This card has been configured to operate in the speed control (closed-loop) mode for all the experiments described within this document, due

(a) ESCON 50/5 motor driver.

(b) NI myRIO-1900.

FIGURE 2.4: ESCON 50/5 motor driver and myRIO devices.

to this configuration there is an input saturator such that $u \in [-10\text{ V}, 10\text{ V}]$, where u denotes the control signal send to the ESCON driver card, it is important to know that for a control signal equals zero the piston remains in a steady position (i.e., $u = 0$ produces $\dot{d} = 0$), where d and $\dot{d}$ denote the piston distance and its time derivative, respectively. At the beginning, the servo controller was located below the foot platform of the motoBOTTE (see Fig. 2.1); but later, it was removed from that position, because when this device is operating it produces noise that is transmitted to the EMG sensors when the foot is in contact with the same foot platform. Both, the motor driver card and the linear piston are powered by a lithium-ion battery of 24V-12A. It is possible to measure the motor's current consumed, from which we can obtain a current - piston force relation, as indicated in the piston's manufacturer manual [68]. The functioning of this device can be configured via a USB using a graphical user interface provided by the manufacturer.

The motor driver card is connected to the Mini System Port (MSP) Connector C of a myRIO-1900 embedded device from National Instruments [70], this embedded system has a dual-core processor model Z-7010 from Xilinx, it is running on NI Linux Real-Time at 667 MHz and it can be programmed either with LABVIEW or C/C++ code (in Eclipse). In our case all the controllers designed in further sections that were implemented in real-time are developed via C code programming with the Eclipse IDE. The signals connected to the myRIO card are distributed as follows: the potentiometer differential voltage is in the Analog Input 0 (Pin 7 [+] and Pin 8 [-]), the measure of the motor current is in the Analog Input 1 (Pin 9 [+] and Pin 10 [-]) and the control signal u is taken out from the Analog Output 0 (Pin 3 [GND] and Pin 4 [AO0]). All the input and output signals operate with the same sampling time of 10 milliseconds.

The robot has integrated a 3 dimensional force-torque sensor (shown in Fig. 2.5) from the SENSIX company, according to their website [71], this sensor has been used in sports, rehabilitation and biomechanics. This device allows to directly measure torque-force components produced by the ankle at the center of pressure of the sensor, the forces are denoted as F_x, F_y and F_z, while the torque components are denoted as M_x, M_y and M_z. The force sensor outputs are six voltages that can be gathered in a vector

FIGURE 2.5: Force-torque cylindrical sensor.

as $U = \begin{bmatrix} v_1 & v_2 & v_3 & v_4 & v_5 & v_6 \end{bmatrix}^T$, and the torsor vector T is computed as

$$T = \begin{bmatrix} F_x \\ F_y \\ F_z \\ M_x \\ M_y \\ M_z \end{bmatrix} = \begin{bmatrix} 202.38 & 9.09 & -215.52 & 240.40 & 1.94 & -240.11 \\ -154.06 & 304.03 & -123.49 & -131.98 & 272.04 & -140.37 \\ -232.14 & -219.17 & -236.18 & -229.45 & -229.14 & -229.56 \\ -11.14 & 4.26 & 6.79 & 7.42 & 3.67 & -11.98 \\ 3.16 & 10.04 & 8.71 & -7.48 & -10.17 & -0.88 \\ -10.09 & 11.90 & -10.09 & 9.44 & -8.30 & 8.82 \end{bmatrix} \begin{bmatrix} v_1 \\ v_2 \\ v_3 \\ v_4 \\ v_5 \\ v_6 \end{bmatrix},$$

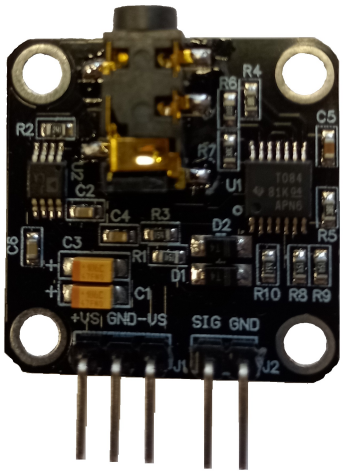

FIGURE 2.6: Surface electromyography sensor employed.

There are two sensors employed to measure surface EMG (see Fig. 2.6), these are connected to the NI embedded device, each sensor has integrated an amplifier, a rectifier and a low-pass filter, these sensors are powered by a ±15 V-2 A symmetric DC power

supply as recommended by the manufacturer, the output of this sensors are connected to the myRIO card in the Analog Inputs A0 and A1, for Tibialis Anterior (TA) and Soleus (SOL) muscles, respectively.

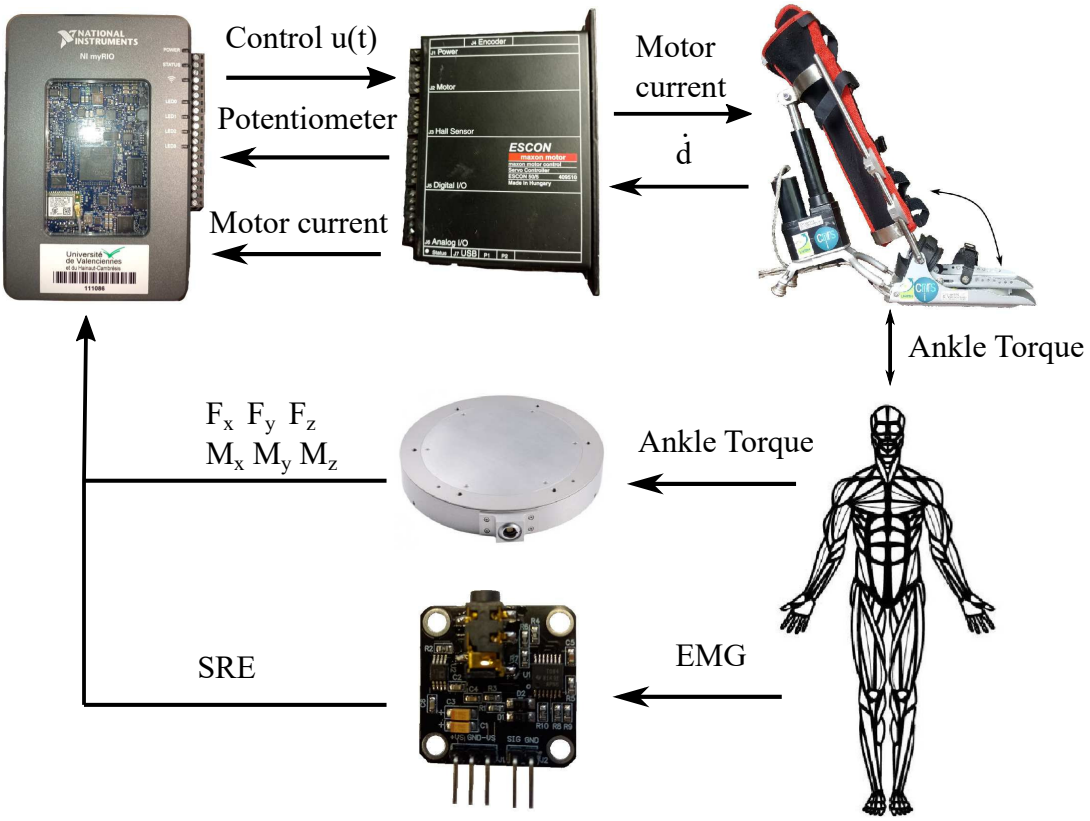

FIGURE 2.7: Diagram with the connections of the robot.

A diagram of the robot and its connection with the different devices is shown in Fig. 2.7, where SRE stands for smooth rectified EMG. After this full description of the components of the device, the next section is dedicated to the construction of control oriented models using system identification method.

Remark 2.1. It is important to take into account these facts about the motoBOTTE :

- It is a motorised version of an existing ergometer designed at the LAMIH [72].
- It is not designed for walking, it is too heavy ($\approx$ 11 Kg.) to be employed for that porpoise.
- Due to the configuration of the motor driver card, the system is not affected by external forces, these forces include gravity and the human itself.

2.2 System Identification

A key point in model-based control techniques is related to the quality of the model employed; the more accurate it is, the better performance that can be obtained from the controllers designed. Thus, the process for obtaining a dynamical mathematical model that describes the behavior of the system from observed data is known as system identification [73–75], where the main objective is to determine the differential or difference equations (as well as its coefficients or parameters values involved in such expressions) for describing the behavior of a system in terms of the input and output signals or according to a predefined criterion [73, 74, 76, 77]. Some authors begin the estimation process by using the prior knowledge of the system to propose a structure for it [74, 75]. According to [73] there are basic ingredients to consider when identifying a system :

1. Measured data, input and output signals as well as any possible disturbance.
2. The set of candidate models, the prior knowledge of the system can be used to propose some candidate models for describing the system.
3. A criterion of fit, this is usually determined using a cost function, in our case the function that we are using during all the manuscript is a sum-of-squared errors between the output of the system measured in real-time and the prediction obtained with our model.
4. Validation, part of the observed data must be separated to evaluate the performance of the identified system and verify if this mathematical model produces a solution within some acceptable margin of error.

In the literature, the identification process can be classified in three different color categories according to the level of knowledge or confidence that we have in the parameters or structure of the system, these categories are [73] :

- Black box models, these structures intend to provide a good approximation for *any* type of nonlinear dynamical system [73], some of the most used modelling techniques in this category are : autoregressive with exogenous input models (ARX), neural networks, fuzzy models, wavelets, among others [74]. Formal proof of convergence for these techniques had been previously established, a common assumption that these techniques share is that the functions or signals involved in the

behavior of the system are continuously differentiable [78], as in the case of recurrent neural networks [79] or polynomial fuzzy systems [80].

- White box models, for this case the model structure and the parameters involved in it are perfectly known, i.e., there are no uncertainties in the system.
- Grey box models, this category is for systems where a structure of the system can be deduced from physical laws or prior knowledge of the system but some of the parameters or coefficients within are unknown, usually this approach are combined with parameter estimation techniques, these parameter estimation procedures can also be divided in offline and online techniques, in our case we focused on offline parameter estimation techniques.

There is not unique solution for the identification problem, it means that there could be different mathematical representations for a single system, within the next subsections the three color categories will be illustrated by obtaining different models for the motoBOTTE.

2.2.1 Black box modelling

In this section we are interested in obtaining a model in terms of the ankle angle ϕ, its location is illustrated in Fig. 2.1. A basic relationship between input and output signals employed to approximate linear systems as a black box [74] is the following difference equation

$$y(t) + a_1 y(t-1) + \cdots + a_n y(t-n) = b_1 u(t-1) + \cdots + b_m u(t-m), \qquad (2.1)$$

this model is known as autoregressive with external input (ARX), where $a_1, \cdots, a_n$ and $b_1, \cdots, b_m$ are parameters to be estimated, $y(t) \in \mathbb{R}$ and $u(t) \in \mathbb{R}$ are the output and input signals, respectively, and $n \in \mathbb{R}$ and $m \in \mathbb{R}$ are the number of samples employed for each signal.

One basic rule for system identification is 'Do not estimate what you already know!' [75]. Therefore, this is the prior knowledge of the system and assumptions that will be considered for proposing a candidate mathematical model that describes the behavior of our system :

1. The sampling time in the embedded device has been set to 10 milliseconds.
2. When the control input u equals zero the system remains in the same position.
3. We assume that the function that describes the system is continuously differentiable.

Based on the latter, we will consider a nonlinear discrete-time model of the form

$$\phi(k+1) = \phi(k) + (b_0 + b_1\phi(k))u(k) \tag{2.2}$$

where b_0 and b_1 are parameters to be estimated, and k denotes the sampling time employed ($k = 0.01$). First, notice that for this candidate structure $u(k) = 0$ yields to $\phi(k+1) = \phi(k)$. It means that if the control input equals zero, then, the next sample of the piston distance will remain on the actual position, which coincides with the point 2) in prior knowledge of the system.

The estimation process for parameters b_0 and b_1 can be done using the Parameter Estimation Toolbox in MATLAB and it consists on following these steps :

1. First, acquire data from real-time experiments, in our case we captured data from 16 experiments, these experiments consist on following different trajectories with the robot moving it from a position to another during 10 seconds, during these experiments the robot was controlled by a proportional integral error feedback controller that was initially calibrated by trial and error, the input and output signals from these 16 experiments were saved and will be used to estimate the values of b_0 and b_1.
2. After that, we filtered the input and output data with a 12-order low pass IIR filter with a cut-off frequency of 0.2 π rad/sample [81], this is important to reduce the magnitude of the high-frequency components in the signals (noise), and it should be done before the estimation; otherwise, we would be modelling this noise.
3. Then, the toolbox runs a simulation and compares every output sample simulated with the real-filtered, they will be denoted as y_{lk} and $\hat{y}_{lk}$, respectively and the samples are indicated with l, $l \in \{1, 2, \cdots, 1000\}$ and then computes a sum squared error cost function to be optimized as $sse_{cf} = \sum_{l=1}^{1000}\sum_{k=1}^{16}(y_{lk} - \hat{y}_{lk})^2$.

4. Finally, using a nonlinear least squares method with the Levenberg-Marquardt algorithm [82] optimizes the cost function.

The results of this estimation are shown in Fig. 2.8(a), the values estimated are $b_0 = -0.00203$, $b_1 = 0.00054$ and the cost function is $sse_{cf} = 1.0475$. The final step in identification consists on validation, this model is considered valid if it matches with the real values within a range of accuracy [83]; we have to use a different signal which must not be included in the first set of signals used for estimation, the results for this are shown in Fig. 2.8(b).

2.2.2 White box modelling

The motoBOTTE in Fig. 2.9 is a 5-bar closed-loop mechanism with a piston as actuator; it is aimed to be employed for ankle reeducation of post-stroke patients by varying ϕ [63]. Clearly, it is a constrained mechanical system which can be characterised by a set of DAEs; its constraints, inherited from geometrical properties [66], and their time derivatives cause a loss of degrees-of-freedom (DOF) [84].

In this subsection, a white-box model in the form of DAEs for a motoBOTTE is obtained [85]; it represents more accurately the system dynamics and properties than the black-box model formerly obtained 2.2. The first step consists in applying the Euler-Lagrange methodology to the serial-arm configuration (open-loop kinematics), then incorporating the parallel characteristics (closed-loop kinematics) by means of algebraic restrictions and their derivatives.

As in some other works dealing with parallel robots [86, 87], analysis is split in open- and closed-loop kinematics; the former is performed hereby via ordinary Euler-Lagrange techniques with punctual masses at the end of each link. Consider an n-serial arm configuration which implies the existence of n generalised joints, each of which has a prismatic or revolute characteristic. The generalised coordinates are grouped in a vector $q \in \mathbb{R}^n$, leading to the following well-known equations once the Lagrangian $L = K - P$ is employed, with K being the total kinetic energy and P the total potential energy of the system [88]:

$$\frac{d}{dt}\left(\frac{\partial L}{\partial \dot{q}}\right) - \frac{\partial L}{\partial q} = \tau, \tag{2.3}$$

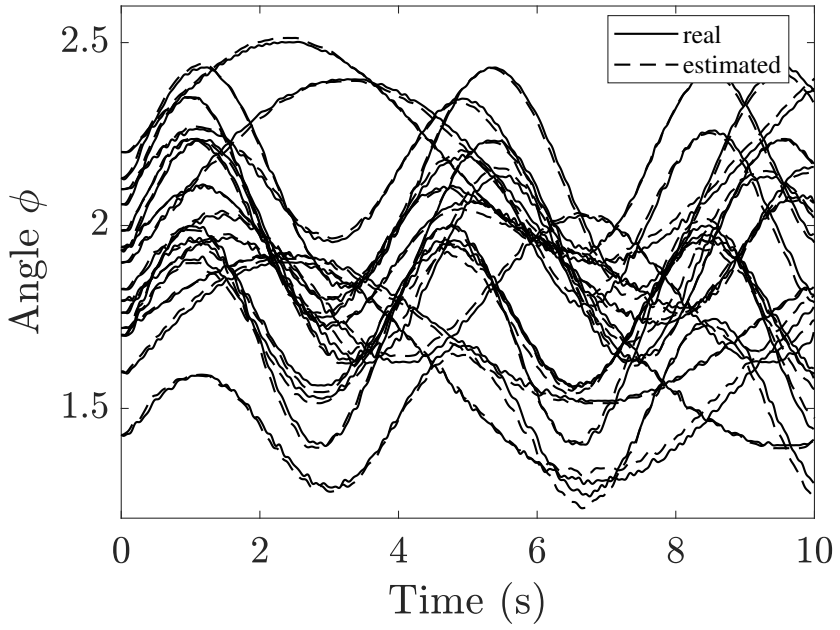

(a) Estimation process.

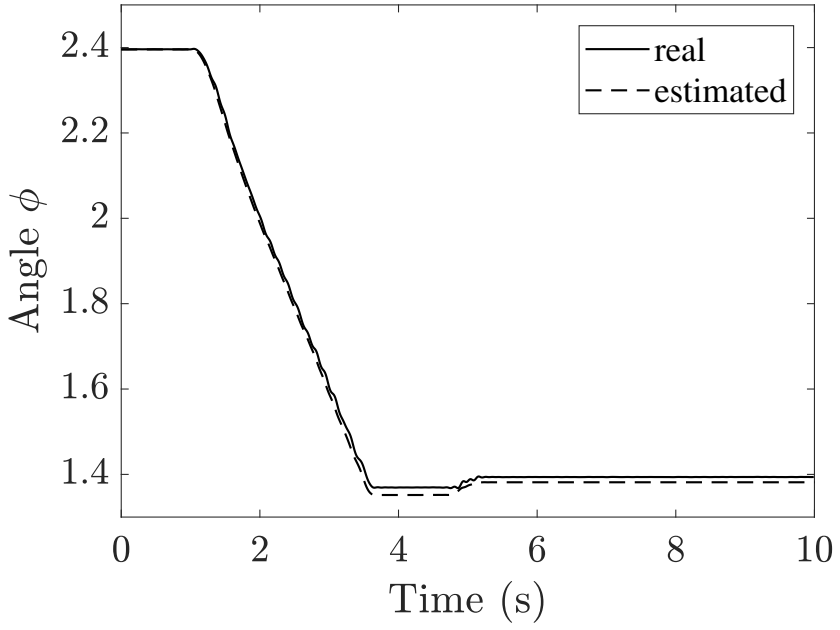

(b) Validation process.

FIGURE 2.8: Estimation and validation processes for the black box approach.

which in turn can be written in terms of the inertia $M(q)$, Coriolis $C(q, \dot{q})$, and gravity $G(q)$ matrices:

$$M(q)\ddot{q} + C(q, \dot{q}) + G(q) = \tau, \tag{2.4}$$

FIGURE 2.9: The motoBOTTE.

with $\tau \in \mathbb{R}^n$ being the generalised torque vector. A state-space representation can be found if $x = [q^T \quad \dot{q}^T]^T$:

$$\dot{x} = \begin{bmatrix} \dot{q} \\ \ddot{q} \end{bmatrix} = \begin{bmatrix} 0 & I \\ 0 & 0 \end{bmatrix} \begin{bmatrix} q \\ \dot{q} \end{bmatrix} + \begin{bmatrix} 0 \\ I \end{bmatrix} u, \tag{2.5}$$

with $u = -M^{-1}(q)\left(C(q,\dot{q}) + G(q) - \tau\right)$.

Importantly, very often a parallel robot is fully actuated irrespectively of the characteristics of its open-loop counterpart. In the open-loop modelling we will assume that every actuator is operating; the corresponding simplifications and further considerations will be left to the second part of the analysis, i.e., for the closed-loop kinematics. As it will be seen later, the motoBOTTE is fully actuated once the algebraic restrictions are taken into account.

Once an open-loop kinematic model in the form (2.4) is obtained, the closure due to the parallel characteristics has to be imposed via algebraic restrictions and its derivatives. In [87] this task is performed using the generalised coordinates q as well as its time derivative. In the state-space framework, we will formalise this closure by grouping m algebraic restrictions in a (possibly nonlinear) function $h(\cdot) : \mathbb{R}^{2n} \to \mathbb{R}^m$

$$h(q,\dot{q}) = 0 \iff h(x) = 0. \tag{2.6}$$

Usually, algebraic restrictions come from geometric considerations and therefore, $h(q) = 0$ does not include any reference to the time derivative $\dot{q}$; nevertheless, since the Euler-Lagrange equation (2.4) has order 2, the time derivative $(\partial h/\partial q)\,\dot{q} = 0$ is also included [87]. Naturally, our proposal in (2.6) includes the latter approach as a particular case. Note also, that (2.6) allows including direct relationships involving $\dot{q}$, for instance, due to actuator limitations.

The dynamic equation (2.5) along with the set of algebraic restrictions in (2.6) constitute a set of DAEs. Should a simulation of such system be performed, consistent initialisation via the Pantelides algorithm must be employed to guarantee the dynamics lie in the algebraic manifold, which physically means that the parallel robot is not "broken". Control tasks in these systems can benefit from the fact that they are redundantly actuated [87] because any action on one of the joints will produce unique effects in the remaining ones. Thus, if a robotic manipulator consists of n serial arms with n actuators (i.e., an actuated system), it will be redundant when closed; conversely, if a parallel robot of n joints has only 1 actuator it will be fully actuated despite the fact that the open-loop is underactuated.

modelling of the motoBOTTE as a Set of DAEs

In order to illustrate the previous discussion, consider the motoBOTTE system in Fig. 2.1. If the arm loop is broken at the end effector from the base as in Fig. 2.10(a), Euler-Lagrange analysis can be performed. There are several ways of accomplishing this task: the most naive approach is to blindly consider every joint as an actuated one; another one consists in imposing some or all of the structural restrictions while preserving the broken-loop characteristic. Never mind the approach, all of them will result in the same equations once the loop is closed.

Note that, by construction, $\gamma_1 = 132^\circ$ while the angle between the links measuring l_2 and l_3 is fixed at 90°; the latter can actually be considered as a single link. Similarly, l_4 and l_6 are also a single link as $\gamma_2 = 103^\circ$ is fixed (l_6 is only a sort of pedal on which the patient's foot lies). These structural considerations should be kept in mind in the sequel. The kinetic energy of the system is the sum of the kinetic energies of links $l_1 - d$, $l_2 - l_3$, $l_4 - l_6$ and l_5, which are $K_1 = (m_1/2)\dot{d}^2$, $K_2 = (m_2/2)\dot{d}^2 + (m_2/2)(l_2^2 + l_3^2)\dot{\Theta}_1^2 + m_2 \dot{d}\dot{\Theta}_1(l_2 \cos\Theta_1 + l_3 \sin\Theta_1)$, $K_3 = (m_3/2)(v_{x3}^2 + v_{y3}^2)$, and $K_4 = (m_4/2)(v_{x3}^2 + v_{y3}^2)$, respectively, with

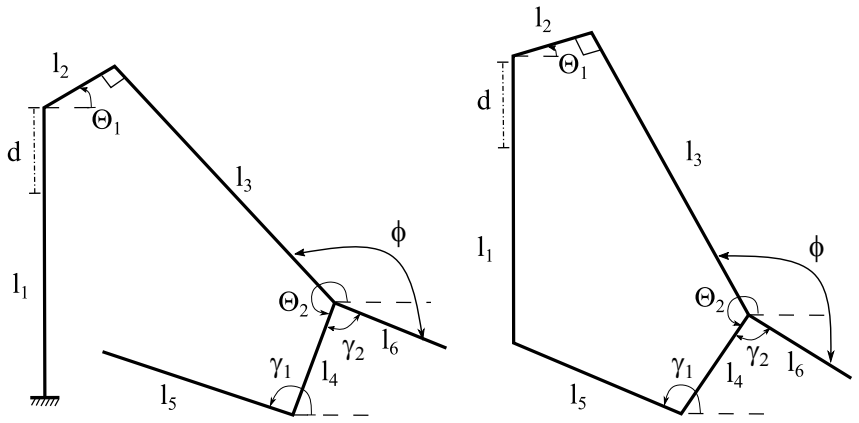

(a) Open-loop kinematics diagram. (b) Diagram of the robot.

FIGURE 2.10: Open and closed diagrams of the robot.

$v_{x3} = l_4 \sin\Theta_2 \dot{\Theta}_2 + (l_2 \sin\Theta_1 - l_3 \cos\Theta_1)\dot{\Theta}_1$, $v_{y3} = \dot{d} + l_4 \cos\Theta_2 \dot{\Theta}_2 + (l_2 \cos\Theta_1 + l_3 \sin\Theta_1)\dot{\Theta}_1$. Similarly, the potential energy of the system is the sum of $P_1 = gm_1(l_1 + d)$, $P_2 = dm_2 g + l_1 m_2 g + l_2 \sin\Theta_1 m_2 g - l_3 \cos\Theta_1 m_2 g$, $P_3 = gm_3(d + l_1 + l_2 \sin\Theta_1 - l_3 \cos\Theta_1 + l_4 \sin\Theta_2)$, and $P_4 = gm_4 l_5 \sin\gamma_1 + gm_4(d + l_1 + l_2 \sin\Theta_1 - l_3 \cos\Theta_1 + l_4 \sin\Theta_2)$, which are the individual potential energies of the four links under consideration.

Based on these energies and $q = \begin{bmatrix} d & \Theta_1 & \Theta_2 \end{bmatrix}^T$ as the joint vector, the matrix Euler-Lagrange form (2.4) is obtained, where:

$$M(q) = \begin{bmatrix} m_1 + m_2 + m_3 + m_4 & M_{12} & (m_3 + m_4)\, l_4 \cos\Theta_2 \\ M_{12} & (m_2 + m_3 + m_4)\left(l_2^2 + l_3^2\right) & M_{23} \\ (m_3 + m_4)\, l_4 \cos\Theta_2 & M_{23} & (m_3 + m_4) l_4^2 \end{bmatrix},$$

$$G(q) = \begin{bmatrix} (m_1 + m_2 + m_3 + m_4)\, g \\ (l_2 \cos\Theta_1 + l_3 \sin\Theta_1)\,(m_2 + m_3 + m_4) g \\ l_4 \cos\Theta_2 (m_3 + m_4) g \end{bmatrix}, \; C(q, \dot{q}) = \begin{bmatrix} C_1 \\ C_2 \\ C_3 \end{bmatrix},$$

with $M_{12} = (m_2 + m_3 + m_4)\,(l_2 \cos\Theta_1 + l_3 \sin\Theta_1)$, $M_{23} = l_4(m_3 + m_4)(l_2 \sin\Theta_1 - l_3 \cos\Theta_1)(\sin\Theta_2 + \cos\Theta_2)$, $C_1 = -(m_3 + m_4) l_4 \sin\Theta_2 \dot{\Theta}_2^2 + (m_2 + m_3 + m4)(l_3 \cos\Theta_1 - l_2 \sin\Theta_1)\dot{\Theta}_1^2$, $C_2 = -l_4(m_3 + m_4)(l_3 \cos(\Theta_1 - \Theta_2) - l_2 \sin(\Theta_1 - \Theta_2))\dot{\Theta}_2^2$, $C_3 = l_4(m_3 + m_4)(l_3 \cos(\Theta_1 - \Theta_2) - l_2 \sin(\Theta_1 - \Theta_2))\dot{\Theta}_1^2$.

Finally, we turn our attention to the algebraic constraints which close the robotic manipulator just modelled, converting it into a parallel setup as in Fig. 2.10(b); they come from the fact that horizontal and vertical displacements along the links should sum up

to 0 [66]:

$$\begin{aligned} l_2\cos\Theta_1 + l_3\sin\Theta_1 + l_4\cos\Theta_2 + l_5\cos\gamma_1 = 0, \\ l_1 + d + l_2\sin\Theta_1 - l_3\cos\Theta_1 + l_4\sin\Theta_2 + l_5\sin\gamma_1 = 0. \end{aligned} \tag{2.7}$$

So far, only Euler-Lagrange representations have been written. For a state-space representation of the DAEs, the state vector $x = \begin{bmatrix} d & \Theta_1 & \Theta_2 & \dot{d} & \dot{\Theta}_1 & \dot{\Theta}_2 \end{bmatrix}^T$ will be considered:

$$\begin{bmatrix} \dot{x}_1 \\ \dot{x}_2 \\ \dot{x}_3 \\ \dot{x}_4 \\ \dot{x}_5 \\ \dot{x}_6 \end{bmatrix} = \begin{bmatrix} 0 & 0 & 0 & 1 & 0 & 0 \\ 0 & 0 & 0 & 0 & 1 & 0 \\ 0 & 0 & 0 & 0 & 0 & 1 \\ 0 & 0 & 0 & 0 & 0 & 0 \\ 0 & 0 & 0 & 0 & 0 & 0 \\ 0 & 0 & 0 & 0 & 0 & 0 \end{bmatrix} \begin{bmatrix} x_1 \\ x_2 \\ x_3 \\ x_4 \\ x_5 \\ x_6 \end{bmatrix} + \begin{bmatrix} 0 & 0 & 0 \\ 0 & 0 & 0 \\ 0 & 0 & 0 \\ 1 & 0 & 0 \\ 0 & 1 & 0 \\ 0 & 0 & 1 \end{bmatrix} u, \tag{2.8}$$

with $u = -M^{-1}(q)\left(C(q,\dot{q}) + G(q) - \tau\right)$, along with the following algebraic constraints

$$\begin{bmatrix} l_2\cos x_2 + l_3\sin x_2 + l_4\cos x_3 + l_5\cos\gamma_1 \\ l_1 + x_1 + l_2\sin x_2 - l_3\cos x_2 + l_4\sin x_3 + l_5\sin\gamma_1 \\ x_4 + x_5 l_2\cos x_2 + x_5 l_3\sin x_2 + x_6 l_4\cos x_3 \\ -x_5 l_2\sin x_2 + x_5 l_3\cos x_2 - x_6 l_4\sin x_3 \end{bmatrix} = \begin{bmatrix} 0 \\ 0 \\ 0 \\ 0 \end{bmatrix}, \tag{2.9}$$

where the last 2 equations are obtained by derivation of the first 2, i.e., those involving d, Θ_1, and Θ_2.

Note that the dynamic equations (2.8) along with the algebraic restrictions (2.9) constitute the set of DAEs representing the behaviour of the motoBOTTE; they are the specific instances of (2.5) and (2.6), respectively. In the next section simulation issues will be considered.

Differential Algebraic Equations

A variety of numerical methods are available for integration of solutions of ordinary differential equations (ODEs); in contrast, a set of DAEs represents a numerical challenge as the algebraic restrictions must hold for any system trajectory, i.e., they are restricted to a manifold induced by the constraints [89]. Formally speaking, to solve the dynamics $\dot{x}(t) = f(x) + g(x)u(t)$, with $f(\cdot)$ and $g(\cdot)$ sufficiently smooth vector fields, subject to

the algebraic constraints $h(x) = 0$ requires (i) proper initialisation as $x(t_0) = x_0 \in \mathcal{S}$ with $\mathcal{S} = \{x \in \mathbb{R}^n : h(x) = 0\}$ [67]; (ii) determining missing dynamics and eliminating redundant ones by means of the Pantelides algorithm [90].

For a parallel robotic manipulator consisting of n serial arms, this task requires taking into account the algebraic restrictions, deriving them with respect to time as much as to recover the dynamics in the original equation (second order for Euler-Lagrange configurations, first-order for state-space representations), and combining them with the original one. This usually leads to simplification because the dynamics of each joint are mutually dependent.

Simulation of the motoBOTTE as a set of DAEs

The DAE Toolbox of MATLAB [91] allows simulating a set of DAEs once the symbolic dynamics, restrictions, and variables are captured, provided they are consistent and the number of variables is equal to the number of restrictions (both dynamical and algebraic) [92]. Alternatively, ODE routines can be employed if the steps above are followed, i.e., if the first-order time derivative of the algebraic restrictions in (2.7)

$$\begin{bmatrix} 1 & l_2\cos\Theta_1 + l_3\sin\Theta_1 & l_4\cos\Theta_2 \\ 0 & -l_2\sin\Theta_1 + l_3\cos\Theta_1 & -l_4\sin\Theta_2 \end{bmatrix} \begin{bmatrix} \dot{d} \\ \dot{\Theta}_1 \\ \dot{\Theta}_2 \end{bmatrix} = 0,$$

and the second-order ones

$$\begin{bmatrix} 1 & l_2\cos\Theta_1 + l_3\sin\Theta_1 & l_4\cos\Theta_2 \\ 0 & -l_2\sin\Theta_1 + l_3\cos\Theta_1 & -l_4\sin\Theta_2 \end{bmatrix} \begin{bmatrix} \ddot{d} \\ \ddot{\Theta}_1 \\ \ddot{\Theta}_2 \end{bmatrix} + \begin{bmatrix} -l_2\sin\Theta_1 + l_3\cos\Theta_1 & -l_4\sin\Theta_2 \\ -l_2\cos\Theta_1 - l_3\sin\Theta_1 & -l_4\cos\Theta_2 \end{bmatrix} \begin{bmatrix} \dot{\Theta}_1^2 \\ \dot{\Theta}_2^2 \end{bmatrix} = 0, \tag{2.10}$$

are considered.

Due to the fact that the motoBOTTE has only 1 actuated input corresponding to the prismatic joint, $\ddot{d}$ can be solved from the open-loop kinematic equation (2.4) with $M(q)$, $C(q,\dot{q})$, and $G(q)$ defined in the previous section; then, $\ddot{d}$ can be substituted in (2.10)

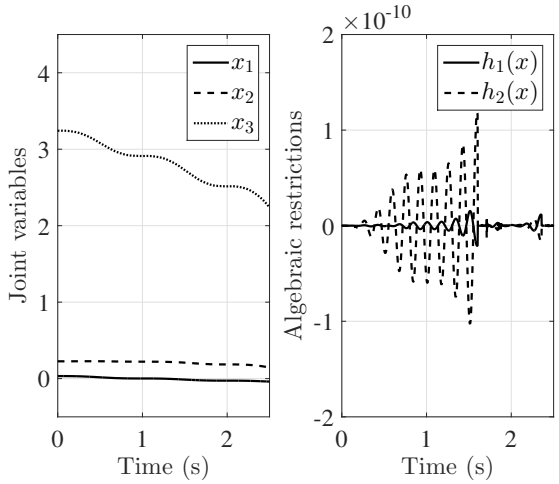

FIGURE 2.11: Time evolution of the joint variables (left) and algebraic restrictions (right).

so that $\ddot{\Theta}_1$ and $\ddot{\Theta}_2$ can be solved. It is obvious from this procedure that the prismatic joint determines the behaviour of the others. These steps leave us with 3 2nd-order dynamic equations which are omitted for brevity. From them, of course, a 6-state-space representation can be obtained. Any of these representations can now be simulated as ODEs without any concern of leaving the manifold corresponding to the algebraic constraints; yet, it requires an initial condition to be consistent, i.e., within the manifold in order to avoid impulsive behavior [67].

Another issue is that the motoBOTTE behavior should be such that it remains at rest if the actuator input is zero, i.e., if $\tau_1 = 0$. This is equivalent to the system not being affected by gravity, i.e., compensating the effects of gravitation in each joint. Thus, the following modification in the generalised vector must be done: the first actuator preserves its input by replacing it by $\tau_1 + g(m_1 + m_2 + m_3 + m_4)$ while the second and the third only compensate the gravitational terms as they are passive $\tau_2 = (l_2 \cos\Theta_1 + l_3 \sin\Theta_1)(m_2 + m_3 + m_4)g$ and $\tau_3 = l_4 \cos\Theta_2(m_3 + m_4)g$. With the previous considerations if the only input τ_1 is equal to zero the system will not move.

Fig. 2.11 corresponds to the time evolution of the joint variables $d = x_1$, $\Theta_1 = x_2$, and $\Theta_2 = x_3$ under an arbitrary sinusoidal input $\tau_1(t) = -0.4\sin(2\pi t) + 0.2\cos(12\pi t)$ and the value of the algebraic restrictions in (2.7); initial conditions are $x_0 = \begin{bmatrix} 0.0331 & 0.2263 & 3.2416 & 0 & 0 & 0 \end{bmatrix}^T$. The parameter values are $l_1 = 0.303267$, $l_2 = 0.097688$, $l_3 = 0.476157$, $l_4 = 0.098445$, $l_5 = 0.155532$, $m_1 = 1$, $m_2 = 1$, $m_3 = 1$, and $m_4 = 1$.

2.2.3 Grey box modelling

Parallel robots dynamics can be described using differential algebraic equations (DAEs), also known as singular systems, semi-state representations, implicit differential equations, among other names, which arise in several areas, not only in robotics [93]. Controller design for DAEs is a challenging task for many reasons: the state-space representation is not an ordinary one, but a descriptor [89]; algebraic restrictions oblige to consistent initialization and holding [90]; numerical simulation cannot be directly performed via ordinary differential equations (ODEs) [91].

The motoBOTTE, shown schematically in Fig. 2.12, is actuated by a linear piston whose variable length is denoted by d with an operation range $\Omega = d \in [0, 0.103]$ in meters, the ankle angle ϕ is measured via the voltage of a potentiometer in the piston [63, 68]. The dynamic of the ideal noise-free piston is described by

$$\dot{d} = b_1 u, \tag{2.11}$$

where u is the control signal, b_1 is a constant term that will be estimated later and there is an input saturator such that $u \in [-10\text{ V}, 10\text{ V}]$. Previously, a model for the motoBOTTE was identified using a black box model approach, but it does not provide information about how forces interact in the system [63]. The following procedure will take into account these forces; a preliminary work on this direction can be found in [94].

The steps for modelling a non-redundant parallel robot can be summarized as :

1. Open the kinematic chain and follow the Euler-Lagrange methodology to obtain the actuated or open-loop dynamics of the system.
2. The dynamics for the passive joints can be obtained by substituting the actuated dynamics into the second-time derivative of the algebraic constraints.

This procedure is illustrated below.

Open-Loop Kinematics

Consider the system in Fig. 2.12 with punctual masses m_1, m_2, m_3, the length of the links l_1, l_2, l_3, l_4, l_5, the angles between the links and the horizontal plane Θ_1, Θ_2, γ_1,

and the fixed inner angle γ_2. The total kinetic energy is given by $K = K_1 + K_2 + K_3$ with

$$K_1 = \frac{1}{2} m_1 \dot{d}^2,\; K_2 = \frac{1}{2} m_2 \left(\left(\dot{d} + z_1 \dot{\Theta}_1 \right)^2 + z_3^2 \dot{\Theta}_1^2 \right),$$
$$K_3 = \frac{1}{2} m_3 \left(\left(\dot{d} + z_1 \dot{\Theta}_1 + z_2 \dot{\Theta}_2 \right)^2 + \left(z_3 \dot{\Theta}_1 + z_4 \dot{\Theta}_2 \right)^2 \right),$$

as the kinetic energies of individual joints. The potential energy is $P = P_1 + P_2 + P_3$ with

$$P_1 = (l_1 + d + z_5)\, m_1 g, \quad P_2 = (l_1 + d - z_3 + z_5)\, m_2 g, \quad P_3 = (l_1 + d - z_3 + z_5 - z_4)\, m_3 g,$$

as individual potential energies with $z_1 = l_2 \cos\Theta_1 + l_3 \sin\Theta_1$, $z_2 = l_4 \cos\Theta_2$, $z_3 = l_3 \cos\Theta_1 - l_2 \sin\Theta_1$, $z_4 = -l_4 \sin\Theta_2$, $z_5 = l_5 \sin\gamma_1$, and $g = 9.806$.

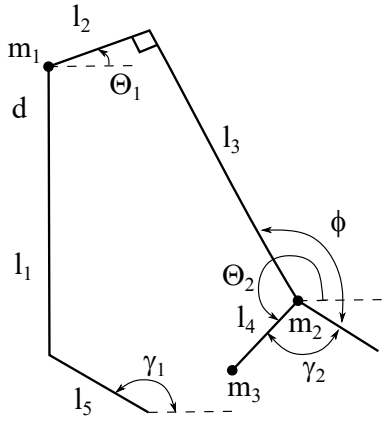

FIGURE 2.12: Scheme of the motoBOTTE.

Since the Lagrange equation for a conservative system [65] is $L = K - P$, the dynamical equations for the open-loop kinematics are $\frac{d}{dt}\left(\frac{\partial L}{\partial \dot{q}}\right) - \frac{\partial L}{\partial q} = \tau$, where q is a $n-$vector of generalized coordinates composed by the prismatic joint d and two revolute joint angles Θ_1 and Θ_2 in radians; this yields $q = \begin{bmatrix} d & \Theta_1 & \Theta_2 \end{bmatrix}^T$ with τ as a vector of generalized external forces. The Euler-Lagrange equations can be written in the matrix form:

$$M(q)\ddot{q} + C(q, \dot{q}) + G(q) + F(\dot{q}) = \tau, \tag{2.12}$$

TABLE 2.2: Measured parameters of the system.

Parameter	Value
l_1	0.35 m
l_2	0.125 m
l_3	0.445 m
l_4	0.1014 m
l_5	0.15 m
m_1	6.15 kg
m_2	2.13 kg
m_3	2.86 kg
γ_1	2.4086 rad
γ_2	2.0952 rad

whose matrices are defined as:

$$C\left(\dot{q},q\right)=\begin{bmatrix}\left(m_2+m_3\right)z_3\dot{\Theta}_1^2+m_3z_4\dot{\Theta}_2^2\\ m_3\left(z_1z_4-z_2z_3\right)\dot{\Theta}_2^2\\ m_3\left(z_2z_3-z_1z_4\right)\dot{\Theta}_1^2\end{bmatrix},\ \tau=\begin{bmatrix}b_0\dot{u}\\0\\0\end{bmatrix},$$

$$M(q)=\begin{bmatrix}m_1+m_2+m_3 & \left(m_2+m_3\right)z_1 & m_3l_4z_2\\ \left(m_2+m_3\right)z_1 & \left(m_2+m_3\right)\left(l_2^2+l_3^2\right) & M_{23}\\ m_3l_4z_2 & M_{23} & m_3l_4^2\end{bmatrix},$$

with $M_{23}=m_3l_4\left(z_1z_2+z_3z_4\right)$, b_0 is an unknown parameter that will be estimated later and $\dot{u}$ corresponds to the time-derivative of the control signal. Gravity does not affect the system due to the piston mechanical structure [68] and the configuration of the motor driver [69], therefore, it will be considered as $G(q)=0$ and be omitted in developments thereafter. The measurable parameters of the system are presented in Table 2.2.

Assuming that friction is a local effect [65] with unknown dynamics that can be described by a continuously differentiable function within a region of interest Ω (as in the viscous friction case), there exists, by Taylor-series, a polynomial that can approximate it [80] as

$$F\left(\dot{q}\right)=\begin{bmatrix}v_{11}\dot{d}^2+v_{12}\dot{d}\\ v_{21}\dot{\Theta}_1^2+v_{22}\dot{\Theta}_1\\ v_{31}\dot{\Theta}_2^2+v_{32}\dot{\Theta}_2\end{bmatrix},$$

where the polynomial coefficients v_{11}, v_{12}, v_{21}, v_{22}, v_{31} and v_{32} are unknown and will be estimated later.

Dynamical Equations of the Passive Joints

Once the open-loop kinematics are closed to yield the motoBOTTE structure, the vector of generalized coordinates q must satisfy the following set of algebraic constraints inherited from its geometric structure [66]:

$$\begin{aligned} d + l_1 + l_2 \sin\Theta_1 - l_3 \cos\Theta_1 + l_4 \sin\Theta_2 + l_5 \sin\gamma_1 = 0, \\ l_2 \cos\Theta_1 + l_3 \sin\Theta_1 + l_4 \cos\Theta_2 + l_5 \cos\gamma_1 = 0, \\ \phi = \Theta_1 - \Theta_2 + \pi/2 - \gamma_2, \end{aligned} \tag{2.13}$$

where the first two restrictions arise from $x-$ and $y-$axis oriented requirements for closure and the third one is a constraint for the ankle angle. These restrictions can be combined to determine the vector of generalized coordinates q using the measured variable ϕ, which yields

$$\begin{aligned} d &= -l_1 + z_3 + z_4 + z_5, \\ \Theta_1 &= \phi + \gamma_2 - \pi + \Theta_2, \\ \Theta_2 &= \arcsin\left(\frac{-l_2\cos\gamma_1}{\sqrt{\alpha_1^2+\alpha_2^2}}\right) - \arctan\left(\frac{\alpha_1}{-\alpha_2}\right), \end{aligned} \tag{2.14}$$

with $\alpha_1 = l_2\cos\left(\phi+\gamma_2-\frac{\pi}{2}\right) + l_3\cos\left(\phi+\gamma_2-\pi\right) + l_4$ and $\alpha_2 = l_2\sin\left(\phi+\gamma_2-\frac{\pi}{2}\right) + l_3\sin\left(\phi+\gamma_2-\pi\right)$. The constraints (2.13) also impose others in the trajectory derivatives $\dot{q}$ and $\ddot{q}$; for the first-order derivative case these are

$$\begin{aligned} \dot{d} + z_1\dot{\Theta}_1 + z_2\dot{\Theta}_2 = 0, \\ z_3\dot{\Theta}_1 + z_4\dot{\Theta}_2 = 0, \end{aligned} \tag{2.15}$$

while for the 2nd-order derivative the constraints obtained are

$$\begin{aligned} \ddot{d} + z_1\ddot{\Theta}_1 + z_2\ddot{\Theta}_2 + z_3\dot{\Theta}_1^2 + z_4\dot{\Theta}_2^2 = 0, \\ z_3\ddot{\Theta}_1 + z_4\ddot{\Theta}_2 - z_1\dot{\Theta}_1^2 - z_2\dot{\Theta}_2^2 = 0. \end{aligned} \tag{2.16}$$

Now we have expressions for describing the dynamics of the passive joints.

Remark 2.2. The dynamics of the motoBOTTE are obtained by selecting the actuated dynamics $\ddot{d}$ in (2.12) and substituting it in (2.16), which concludes this two-step modelling method. Notice that this is a single model for the parallel robot, the model itself is a combination of two sets of equations, the first equations (2.12) provide a description

TABLE 2.3: Estimated parameters using the simplex algorithm of the Parameter Estimation Toolbox in Matlab.

Parameter	**Value**	**Parameter**	**Value**
v_{11}	56.3869	v_{12}	-2.8211
v_{21}	-9.3843	v_{22}	-0.6755
v_{31}	-0.0841	v_{32}	0.0440
b_0	0.0627	b_1	0.00745

for the behavior of the actuator and the equations in (2.16) describe the dynamics that the passive joints must have to satisfy the algebraic constraints inherit to the system. Therefore, our model is a set of differential-algebraic-equations (DAEs).

The procedure above, i.e., obtaining explicit expressions for 'missing' or 'implicit' dynamics for a set of DAEs is known as the Pantelides algorithm [90], which has been already implemented in the Symbolic Math Toolbox in MATLAB [95, 96]. When this procedure is combined with the Euler-Lagrange approach as in this work, it resembles the Lagrange-D'Alembert formulation [87, 97].

Parameter Estimation

So far, the input parameters b_0, b_1 as well as the friction coefficients v_{11}, v_{12}, v_{21}, v_{22} v_{31} and v_{32} have been considered as unknown. These parameters can be estimated with 2-dimensional input-1-dimensional output pairs $((u, \dot{u}), (\phi))$ taken from real-time tests and fed into the simplex algorithm [98], which is already implemented in the Parameter Estimation Toolbox in MATLAB. The algorithm minimizes a sum-of-squared error cost function $c_f = \sum(\phi - \hat{\phi})^2$ to match the real-time output data ϕ with our estimated output $\hat{\phi}$ computed with our mathematical model (2.12) and (2.16).

The signals used in the estimation process are shown in Fig. 2.13(a); they show 8 trajectories from real-time data and estimation. Rich signals are expected for estimation (not necessarily rehabilitation routines); therefore, the pair $(u, \dot{u})$ has been chosen as to produce sinusoidals of varying frequency and amplitude on ϕ. As a result, the estimated parameters in Table 2.3 were obtained, which completes our modelling task. As customary, a different set of data was used for model validation; these trajectories are shown in Fig. 2.13(b) and illustrate the fact that the estimated parameters are acceptable.

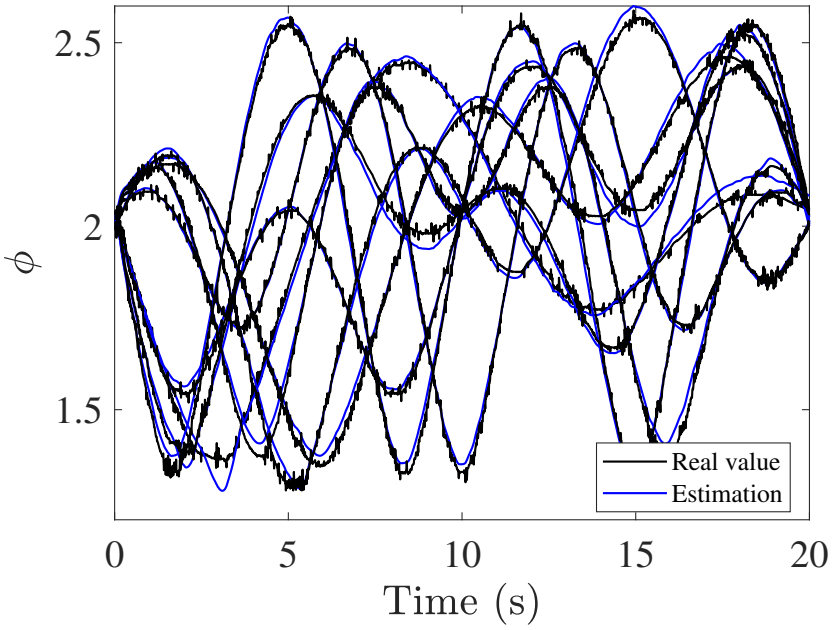

(a) Trajectories estimation.

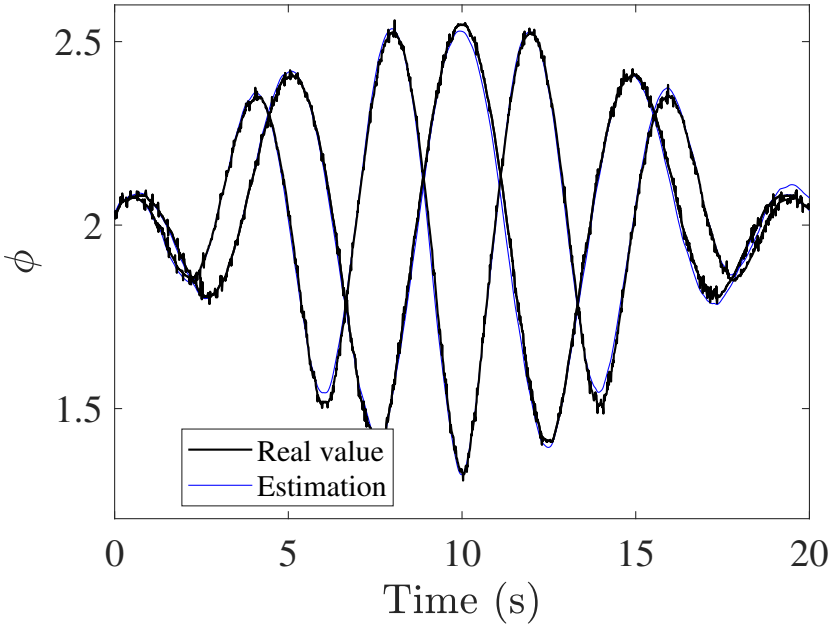

(b) Validation trajectories.

FIGURE 2.13: Estimation and validation processes.

2.3 Chronological order of the models

The different models presented in this chapter for the motoBOTTE were obtained in the chronological order shown in Fig. 2.14, the publications associated with each model

are indicated below them.

The first model obtained was obtained employing the black-box methodology, it is a modified version of an auto-regressive system with exogenous input, a non linear term in the input was considered, this non linear term is assumed to be continuously differentiable and it was approximated via first order polynomial of the ankle position. The model has been calibrated using data from real-time experiments. This data are the input (control voltage) and output (ankle position) signals of the robot. One of the main disadvantages of employing this methodology is that it does not provide an internal description of the system, which means that we are capable of predicting the future values of the ankle position, but, there is no information about the forces involved to produce this movement, and the main advantage is that the resulting model as we will see in further sections was easy to be employed for control design.

The second model was obtained via a white-box approach and modification of the classical Euler-Lagrange methodology, which is commonly employed for serial robots; but, since we are dealing with a parallel manipulator it has to be modified to incorporate the algebraic constraints inherit to these systems. For this model it was assumed that we knew the value of all the parameters, which means that there was no calibration and the resulting model was not realistic, that is, the trajectories of the model in simulation did not match the ones obtained in real-time and the advantage is that it offers an internal description of the forces involved inside the system.

The third model was deduced from a grey-box methodology, which is a combination of the previous two (black- and white-box), most of the system expressions were deduced from physical laws, algebraic constraints related to position, speed and acceleration were incorporated into the system description. The effect of gravity was neglected due to the configuration of the motor driver card and uncertain terms related to friction had to be incorporated in order to obtain a realistic description of the system while having an internal description of the system.

The final model employed in this manuscript is a simplification of the model obtained via the grey-box approach, it is possible to describe its behavior via first order differential equations and a set of algebraic constraints.

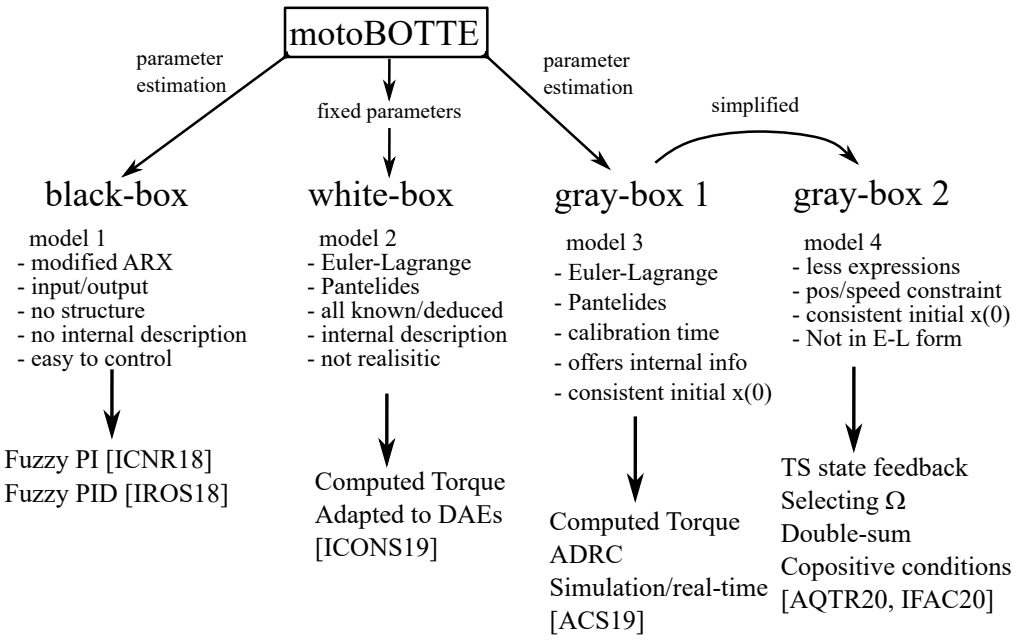

FIGURE 2.14: Relation between models and publications presented in this manuscript.

2.4 Conclusion

In this chapter the motoBOTTE as well as the devices involved in the functioning of this parallel robot were introduced, after that, different mathematical models were obtained for describing the behavior of this system, the models presented were based on black box, white box and grey box modelling approaches, respectively.

The first model presented is quite simple, but efficient, since the output error seems to be reasonable small, and more important, it can be used for controlling design purposes as it will be shown in further chapters. The second and third models obtained are a variation of the Euler-Lagrange methodology known as the Lagrange-D'Alemberg formulation, one of the advantages from using this approach is that it does not require Lagrange multipliers to incorporate the algebraic constraints; therefore, we do not need to compute the value of these multipliers. It is important to recall that as mentioned in the previous chapter, these algebraic constraints are important and must be taken into account when the initial conditions of the system are computed for proper simulation and also in the models used for trajectory generation for the robot.

The parameters for grey box and black box approaches were obtained by solving a non-linear optimization problem, which is minimizing a sum-of-squared error cost function,

the error is computed by taking the difference between the real-time measured output of the system and the estimated output with our candidate mathematical model.

Please recall that the gravity does not affect the behavior of the system in real-time, this is due to the configuration of the ESCON motor driver card in Fig. 2.4(a). Thus, a different configuration of this card will produce a different behavior of the system and therefore, different models for the system would be required to be identified again if the configuration is modified.

Finally, during some of the experiments with the robot we found that the motor driver card that was located below the foot platform (that is made of metal) seemed to affect the behavior of the electromyography sensors. This device was producing an electrical noise that was amplified by the amplifiers of the sensor; therefore, we decided to put this motor driver card away in order to avoid it being in direct contact with the platform, and it reduced the electrical noise in the sensors.

Chapter 3

Control of Parallel Robots

The goal for robot-based rehabilitation exercises is to promote motor recovery of the affected limbs by performing repetitive tasks [99]. To attain this goal, the robot is usually a wearable device, which thus become a sort of exoskeleton; see, for instance, [100, 101] for lower-limb examples as those considered in this work. In [102], an exoskeleton device has been successfully employed for an active ankle support, where the patient is supposed to be able to walk; this is not the case in most of stroke-hit patients for which robot assistants are usually voluminous and expensive [61]. Moreover, constructing a device for assisted rehabilitation requires controller design in order to reproduce clinically validated routines; this task has been tackled with a variety of control techniques for trajectory tracking of joint positions and velocities, for instance: proportional [103], feed-forward [104, 105], and torque control [106]. Importantly, the latter technique is only adequate if the device is an open kinematic chain.

This chapter deals with different control strategies adapted to parallel robots for tracking predefined trajectories. The first one introduced in section 3.1 is an extension of the computed torque control to parallel robots described as a set of DAEs. The second strategy is a model-free approach that is based on active disturbance rejection, it has been adapted for tracking trajectories with parallel robots. Section 3.2 presents simulations and real-time results for both strategies on the MotoBOTTE device.

The organization of this chapter is the following computed-torque control for DAEs in a state-space representation is shown in subsection 3.1.1, it is illustrated by applying this technique to the white box model of the motoBOTTE, within this subsection the

importance of taking into account the algebraic constraints inherit to the system into the trajectory generation model is remarked. The algebraic constraints are needed to translate a desired trajectory from the end effector of the robot (which in the case of the motoBOTTE is the ankle angle ϕ) to the variables of the state-space representation or generalised coordinates. Subsection 3.1.2 presents some adaptations needed for applying this control in generalized coordinates such as using the algebraic constraints of the system in order to obtain the variables that were unmeasured. As a comparison, a model-free approach that is based on active disturbance rejection control is developed as well. Simulations and real-time implementation of the proposals are shown by tracking the ankle trajectory during gait and an isokinetic/isometric exercise taken from the literature.

3.1 Computed-Torque Control for Parallel Robots

From the point of view of robotics, a device for motor reeducation usually belongs to the class of rigid body systems; when they consist in serial arms, potential and kinetic energies are employed to obtain their dynamics via the Euler-Lagrange equations [88]. With the model at hand and based on feedback linearisation [107], the so-called computed-torque control successfully drives the manipulator to a desired trajectory [108], provided appropriate issues of path generation [109], memory [110], and possibly discretisation [111] are considered.

Nevertheless, if the employed device is a parallel robot, i.e., a closed kinematic chain mechanism whose end effector is linked to the base [64], Euler-Lagrange methodologies cannot longer be directly applied [86]. Up to our knowledge, most of the solutions available [87, 112] ignore the fact that the resulting dynamics can be seen as differential algebraic equations (DAEs), i.e., system dynamics (serial arms) subject to algebraic restrictions (parallel characteristics) [89]. As expected, both physically and mathematically, DAEs require proper initialisation as the dynamics are restricted to a subset of the free ones [67]; moreover, the Pantelides algorithm is required to find such conditions as well as recover the missing dynamics for simulation purposes [90].

This section is organized as follows : subsection 3.1.1 is about computed torque control design for singular systems in a state-space representation, the methodology is illustrated

via the white box model presented in subsection 2.2.2, simulation results are presented for this case. Subsection 3.1.2 deals with computed torque control design for parallel robots in generalized coordinates, this strategy is illustrated via the grey box model that was presented in subsection 2.2.3, simulation and real-time results are presented.

3.1.1 Computed-Torque in State-Space Representation

The previous discussions are relevant as the sought generalisation of computed-torque techniques for parallel robots is supposed to take into account only actuated joints while the ordinary approach assumes the whole generalised torque is available. The solution to this problem in [87] is based on solving the actuated dynamics and substituting them in the algebraic restrictions for obtaining the passive dynamics. Nevertheless, the DAE nature of the result is not considered in this reference as neither the desired trajectory nor the initialisation takes into account the manifold to which the system is restricted. The solution hereby proposed does not require any solving but ensures the system dynamics are restricted to the resulting manifold once algebraic restrictions and torque availability is taken into account.

Ordinary computed-torque control is usually split in two parts: path generation and inverse control. For the first part, the fact that we are dealing with a parallel robot whose model is a DAE obliges us to provide a consistent trajectory, a task that can be performed by a cascade-like process. Consider a DAE model $\dot{x}(t) = f(x) + g(x)u(t)$ with $f(\cdot)$ and $g(\cdot)$ sufficiently smooth fields, subject to the algebraic restrictions $h(x) = 0$, whose output is given by $y(t) = o(x)$. A consistent desired trajectory $y_d(t)$ is a sufficiently smooth signal such that $y(t) \to y_d(t)$ as $t \to \infty$, inducing a state trajectory $x_d(t)$ such that $h(x_d) = 0$. Thus, $x_d(t)$ should be algebraically solvable from $y_d(t) = o(x_d)$; otherwise claim the approach fails. While some issues related to path generation remain in parallel robots, such as memory storage and approximation with via points [93], some others might be simplified, for example the non-uniqueness of the inverse kinematics [113].

For the second part, i.e., the control itself, the error signal $e(t) = x_d(t) - x(t)$ with $x_d = \begin{bmatrix} q_d^T & \dot{q}_d^T \end{bmatrix}^T$ as the desired state trajectory in joint coordinates (deduced from $y_d(t)$), is considered along with the state-space representation ((2.5) in general or (2.8)

for the white box model of the motoBOTTE) to write the error dynamics as follows:

$$\dot{e}(t) = \dot{x}_d(t) - \dot{x}(t) = \begin{bmatrix} \dot{q}_d \\ \ddot{q} \end{bmatrix} - \begin{bmatrix} \dot{q} \\ u \end{bmatrix} = \begin{bmatrix} 0 & I \\ 0 & 0 \end{bmatrix} e(t) + \begin{bmatrix} 0 \\ I \end{bmatrix} v(t), \tag{3.1}$$

with $v(t) = \ddot{q}_d + M^{-1}(q)\left(C(q,\dot{q}) + G(q) - \tau\right)$. Any control law in $v(t)$ stabilising the previous system would be enough for determining a τ achieving trajectory tracking for an ordinary robotic manipulator. The usual approach is a linear state feedback $v(t) = -Ke(t)$ with possibly integral terms of the form $K_i\epsilon$ with $\epsilon = \int(q_d(t) - q(t))dt$, guaranteeing the closed loop to be stable, a task that can be performed via pole placement [114] or linear matrix inequalities [115]. The final control law has the form

$$\tau = M(q)(\ddot{q}_d - v(t)) + C(q,\dot{q}) + G(q). \tag{3.2}$$

Nevertheless, a parallel robot requires using only actuated torques which, due to redundancy, are usually less than for the open-loop kinematics. Our proposal consists in using the DAE procedure in the previous section for using the actuated inputs in τ resulting from a stabilising $v(t)$ of (3.1); such actuator directly influences the dynamics of the states associated to the actuated joint. The rest of the actuators (the passive ones) are fixed to zero (or, their equivalent values for "rest" position). Simulation of the controlled plant can thus be performed via the DAE Toolbox. Should an ODE be used instead, the known dynamics should be substituted in the algebraic restrictions yielding the missing ones associated to passive joints; the latter is equivalent to what is done in [87].

Simulation Results

The output $y(t)$ of the motoBOTTE is the ankle angle $\phi(t)$. It relates with the joint coordinates by $\phi(t) = \Theta_1 - \Theta_2 - 13°$, which can be equivalently written in terms of the states as $y(t) = o(x) = x_2 - x_3 - 13°$. Consider a sufficiently smooth trajectory reference $y_d(t) = \phi_d(t)$. In order to find $x_d(t)$ (i.e., the state trajectory corresponding to $\phi_d(t)$) as well as the computed-torque control law, the following algebraic relationships come at hand; they describe the relationship between ϕ, $\dot{\phi}$, and $\ddot{\phi}$ with the states variables x

and their time derivatives $\dot{x}$:

$$\begin{aligned} -x_2 + x_3 &= -13^\circ - \phi, \\ -x_5 + x_6 &= -\dot{\phi}, \\ -\dot{x}_5 + \dot{x}_6 &= -\ddot{\phi}. \end{aligned} \tag{3.3}$$

If $\phi = \phi_d$ in the expressions above and (2.9), the expressions for x_{1d}, x_{2d}, and x_{3d} can be solved:

$$\begin{aligned} x_{1d} &= -l_1 - l_2 \sin x_{2d} + l_3 \cos x_{2d} - l_4 \sin x_{3d} - l_5 \sin \gamma_1, \\ x_{2d} &= \phi_d + 13^\circ + x_{3d}, \\ x_{3d} &= \arcsin\left(-l_5 \frac{\cos \gamma_1}{\sqrt{\alpha_1^2 + \alpha_2^2}} \right) - \psi, \end{aligned}$$

with $\alpha_1 = l_2 \cos(\phi_d + 13^\circ) + l_3 \cos(\phi_d - 77^\circ) + l_4$, $\alpha_2 = l_2 \sin(\phi_d + 13^\circ) + l_3 \sin(\phi_d - 77^\circ)$, $\psi = \arctan(\alpha_1, -\alpha_2)$. Based on the desired position states just found, expressions for the corresponding velocities x_{4d}, x_{5d}, and x_{6d} can be calculated; again, (2.9) and (3.3) with $\dot{\phi} = \dot{\phi}_d$ are required:

$$\begin{bmatrix} x_{4d} \\ x_{5d} \\ x_{6d} \end{bmatrix} = \underbrace{\begin{bmatrix} 1 & l_2 \cos x_{2d} + l_3 \sin x_{2d} & l_4 \cos x_{3d} \\ 0 & -l_2 \sin x_{2d} + l_3 \cos x_{2d} & -l_4 \sin x_{3d} \\ 0 & -1 & 1 \end{bmatrix}^{-1}}_{\mathcal{A}} \begin{bmatrix} 0 \\ 0 \\ -\dot{\phi}_d \end{bmatrix},$$

Finally, expressions for $\dot{x}_{4d}$, $\dot{x}_{5d}$, and $\dot{x}_{6d}$, corresponding to $\ddot{q}_d$ and required in the computed-torque control law, can be calculated using the relationships above:

$$\begin{bmatrix} \dot{x}_{4d} \\ \dot{x}_{5d} \\ \dot{x}_{6d} \end{bmatrix} = \mathcal{A} \begin{bmatrix} (-l_2 \sin x_{2d} + l_3 \cos x_{2d}) x_{5d}^2 - l_4 \sin x_{3d} x_{6d}^2 \\ (-l_2 \cos x_{2d} - l_3 \sin x_{2d}) x_{5d}^2 - l_4 \cos x_{3d} x_{6d}^2 \\ -\ddot{\phi}_d \end{bmatrix}.$$

Only the first of the three entries in τ is required once the computed torque is calculated, due both to the fact that it is the only actuator and that the parallel characteristics of the system make any other action redundant. The result of applying the corresponding torque with gains $k_i = -9000$, $k_p = -1350$ and $k_v = -65$, for a PID-like $v(t) = k_p (d_d - d) + k_i \int (d_d - d) dt + k_v \left(\dot{d}_d - \dot{d} \right)$ appears in Fig. 3.1 from initial condition

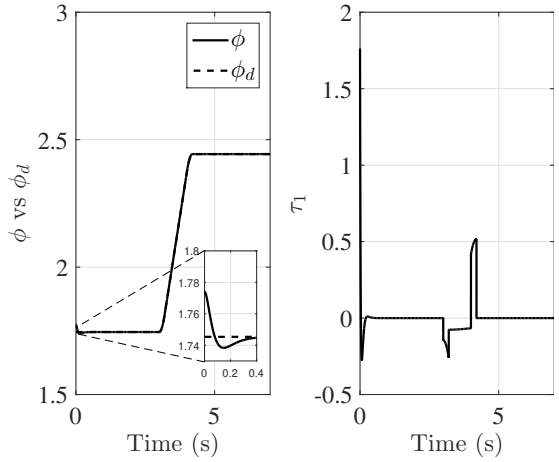

FIGURE 3.1: Output tracking ϕ vs ϕ_d (left) and the corresponding torque τ_1 (right).

$x_0 = \begin{bmatrix} 0.14 & 0.08433 & 4.3665 & 0 & 0 & 0 \end{bmatrix}^T$. The poles of the resulting closed-loop linear system are at $s_1 = -15$, $s_2 = -20$ and $s_3 = -30$. Clearly, $\phi(t)$ tracks the desired $\phi_d(t)$ corresponding to an ankle reeducation routine at a speed of $40°/s$ [63].

3.1.2 Computed-Torque in Generalized Coordinates

The traditional form of the computed torque control is

$$\tau = M(q)\left(\ddot{q}_d - v(t)\right) + C(q,\dot{q}) + F(\dot{q}), \tag{3.4}$$

where $\ddot{q}_d$ corresponds to the second-time derivative of the desired trajectory q_d, and $M(q)$, $C(q,\dot{q})$ and $F(\dot{q})$ are the same as (2.12). Hence, as $\ddot{d}$ is the only actuated dynamic in (2.12) via $\dot{u}$. we must design the corresponding entry in (3.4), i.e.,

$$\dot{u} = b_0^{-1} M_{11}\left(\ddot{d}_d - v(t)\right) + C_1(q,\dot{q}) + F_1(\dot{q}), \tag{3.5}$$

with $M_{11} = m_1 + m_2 + m_3$, $C_1(q,\dot{q}) = (m_2 + m_3) z_3 \dot{\Theta}_1^2 + m_3 z_4 \dot{\Theta}_2^2$ and $F_1(\dot{q}) = v_{11}\dot{d}^2 + v_{12}\dot{d}$.

Remark 3.1. Within this section we are not using approximations of the model for design, these should be considered with the measured and estimated parameters values given in Table 2.2 and Table 2.3, respectively.

After applying the control law (3.5) to the actuated dynamics in (2.12) a linear system for the tracking error is obtained

$$\begin{bmatrix} \dot{\epsilon}(t) \\ \dot{e}(t) \\ \ddot{e}(t) \end{bmatrix} = \begin{bmatrix} 0 & 1 & 0 \\ 0 & 0 & 1 \\ 0 & 0 & 0 \end{bmatrix} \begin{bmatrix} \epsilon(t) \\ e(t) \\ \dot{e}(t) \end{bmatrix} + \begin{bmatrix} 0 \\ 0 \\ 1 \end{bmatrix} v(t), \tag{3.6}$$

where the tracking error is $e(t) = d_d(t) - d(t)$ and $v(t) = k_p e(t) + k_i \epsilon(t) + k_v \dot{e}(t)$ is a PID-like control signal that can be designed via any of the methodologies for linear control with $\epsilon(t) = \int_0^t (d_d(t) - d(t))\, dt$ and $\dot{e}(t) = \dot{d}_d(t) - \dot{d}(t)$.

Notice that the first time-derivative of the vector of generalized coordinates $\dot{q}$ is required for implementing the control law (3.5); yet, only ϕ can be measured directly, which combined with (2.14) only gives the position vector q to be computed. Nevertheless, taking into account the actuator dynamics (2.11) and the two algebraic constraints involving $\dot{q}$ in (2.15), it is possible to obtain

$$\dot{d} = b_1 u, \quad \dot{\Theta}_1 = \frac{-z_4 b_1 u}{z_1 z_4 - z_2 z_3}, \quad \dot{\Theta}_2 = \frac{z_3 b_1 u}{z_1 z_4 - z_2 z_3}, \tag{3.7}$$

from which it is clear that $\dot{q}$ can be computed if the control signal u is known. Importantly, this procedure avoids using observers which might compromise the control task.

Simulation Results To illustrate the proposed model-based control scheme with a challenging trajectory, consider the signal specified by

$$\begin{aligned} d_d(t) &= 0.05 + 0.025 \sin(0.45\pi t) - 0.025 \sin(0.55\pi t), \\ \dot{d}_d(t) &= 0.01125\pi \cos(0.45\pi t) - 0.01375\pi \cos(0.55\pi t), \\ \ddot{d}_d(t) &= 0.0075625\pi^2 \sin(0.55\pi t) - 0.0050625\pi^2 \sin(0.45\pi t), \end{aligned} \tag{3.8}$$

which does not correspond to a rehabilitation path but to a complex dynamic to follow. Poles of the linear error system (3.6) can be assigned to $s_1 = -5$, $s_2 = -6$ and $s_3 = -7$, since it was verified by simulation that these poles avoid input saturation and oscillation; using pole placement gains $k_p = -210$, $k_i = -107$, and $k_v = -18$, have been found for $v(t)$. Simulations are run from the initial conditions $q(0) = \begin{bmatrix} 0.0906 & 0.0369 & -1.9944 \end{bmatrix}^T$ and $\dot{q}(0) = \begin{bmatrix} 0 & 0 & 0 \end{bmatrix}^T$, which are consistent with the algebraic constraints in (2.13) and

(2.15), respectively. Results in Fig. 3.2 are obtained, which clearly indicate the control technique is able to track the desired trajectory despite its complexity.

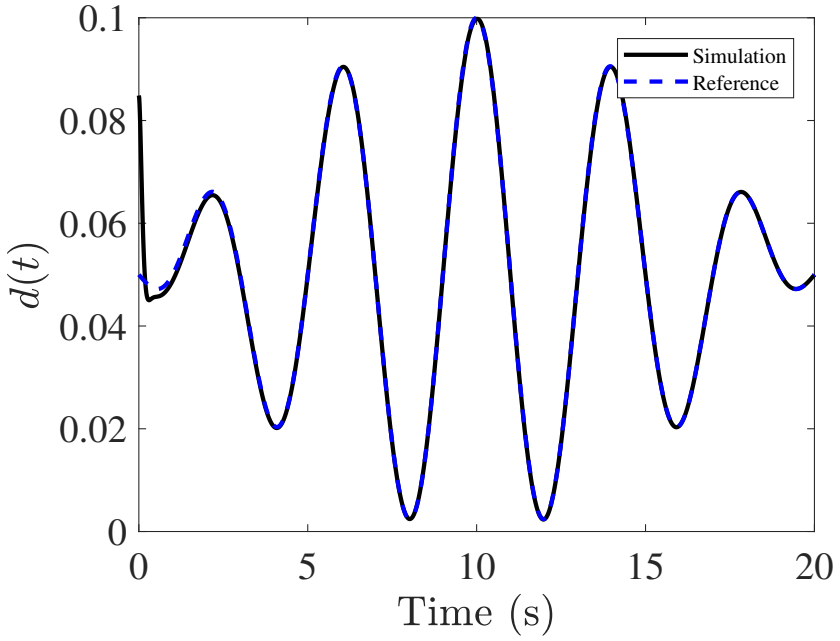

FIGURE 3.2: Time evolution for the piston and its trajectory.

3.2 Active Disturbance Rejection Control for DAEs

If first principles or identification routines cannot be accurately performed in the motoBOTTE, model-free approaches can still be developed, as proven in this section which is concerned with an adaptation of a recently developed technique. This, of course, comes at a price: complexity of using identification and first principles in the model-based approach of the previous sections translates into the difficulty of tuning controller parameters in model-free approaches.

PID controllers are the most popular model-free technique in industrial environments, including rehabilitation engineering [116], but other approaches such as fuzzy [117] or model predictive control [118] can be found in such applications. Active disturbance rejection control (ADRC), a novel technique appeared in [119], widely acknowledged as a plausible successor of the PID as it overcomes the limitations of the latter while achieving remarkable robustness to unmodelled dynamics and disturbances, has gained a remarkable popularity in recent years. We adapt this approach to single-input parallel robots such as the motoBOTTE.

ADRC consists on the parts shown in the block diagram of Fig. 3.3: a transient profile generator which helps avoiding set-point jumps (therefore, not really needed in the context of rehabilitation trajectories which change continuously), an extended state observer which estimates disturbances and nonlinearities in the spirit of finite-time approaches such as sliding modes [120], and a nonlinear weighted sum which employs both the transient profile and the estimations of the observer to cancel out undesired effects as to guarantee the tracking error is going to zero.

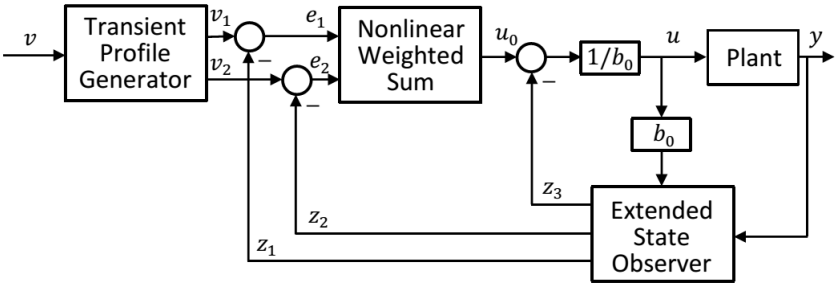

FIGURE 3.3: ADRC topology.

Since the model is not used in this section, some design parameters are named after [119] in the sequel. A desired transient profile is obtained by solving the differential equations

$$\begin{aligned}\dot{v}_1 &= v_2,\\ \dot{v}_2 &= fhan(v_1 - v, v_2, r),\end{aligned}$$

where v_1 is the desired trajectory, v_2 is its derivative and the function $fhan = -r\text{sign}\left(v_1 - v + \frac{v_2|v_2|}{2r}\right)$. The parameter r allows to change the dynamic of the transient profile guided by the physical limitations of the plant.

The nonlinear weighted sum effectively provides feedback by nonlinearly combining PID-like laws on an interval, let say $fal(e,\alpha,\delta) = \frac{e}{\delta^{1-\alpha}}$ if $|e| \leq \delta$ with discontinuous-like ones such as $fal(e,\alpha,\delta) = |e|^{\alpha}\text{sign}(e)$, $|e| \geq \delta$, where $\alpha, \delta > 0$ are design parameters and $e = z_1 - y$ is an error signal.

For SISO plants total disturbance estimation and rejection is achieved by implementing $\dot{x}_1 = x_2$, $\dot{x}_2 = f(x_1, x_2, w(t), t) + bu$, with $y = x_1$ as the measurable output to be controlled, u being the input, and $f(\cdot)$ being a multivariable function of both the states and external disturbances. Treating $F(t) = f(x_1, x_2, w(t), t)$ as an additional state variable, $x_3 = F(t)$ and letting $\dot{F}(t) = G(t)$ with $G(t)$ unknown, the original plant is

now described as $\dot{x}_1 = x_2$, $\dot{x}_2 = x_3 + bu$, $\dot{x}_3 = G(t)$, $y = x_1$, which is always observable, thus allowing the extended state observer (ESO) with equations $\dot{z}_1 = z_2 - \beta_{01}e$, $\dot{z}_2 = z_3 + bu - \beta_{02}fe$, $\dot{z}_3 = -\beta_{03}fe_1$, to be constructed, where $fe = fal(e, 0.5, \delta)$ and $fe_1 = fal(e, 0.25, \delta)$. The observer gains β_{01}, β_{02}, and β_{03} are usually chosen as $\beta_{01} = 1$, $\beta_{02} = \frac{1}{3h}$, $\beta_{03} = \frac{2}{5^2 h^{1.2}}$.

Combining the transient profile generation, the nonlinear feedback combination, and the total disturbance rejection, the ADRC control law is $u = -\frac{fhan(e_1, ce_2, r) + z_3}{b_0}$, where $e_1 = v_1 - z_1$ and $e_2 = v_2 - z_2$, leaving only three parameters to tune: r as the amplification coefficient that corresponds to the limit of acceleration, c as a damping coefficient to be adjusted in the neighborhood of unity, and b_0 as a rough approximation of the coefficient b in the plant within a $\pm 50\%$ range.

3.3 Real-Time Implementation

3.3.1 Rehabilitation Routines

A specific and repetitive task used for rehabilitation is gait training, it can increase the strength at patient's foot and ankle [121]. Human gait is a complex movement that requires coordination of the neuro-musculo-skeletal system and it is splitted into stance and swing phases for its analysis [122, 123]. Among these phases, there are some important events where the ankle (ϕ) is involved such as : the initial contact with the floor (IC), toe landing (TL), maximum dorsiflexion (MD) and heel off (HO) [102], these events are illustrated in Fig. 3.4, the ankle and time values for these events considering a step speed of 4 seconds per step are given in Table 3.1, see [102] for more details. This will be denoted as the desired trajectory (ϕ_d) and can be approximated by an 11th order polynomial $\phi_d = 0.0049t^{11} - 0.1227t^{10} + 1.3103t^9 - 7.8109t^8 + 28.5069t^7 - 65.7025t^6 + 95.2514t^5 - 83.9365t^4 + 41.7027t^3 - 9.8969t^2 + 0.7538t + 1.6123$ when the inversion of a Vandermonde matrix for the indicated points is computed [124], the ankle trajectory during gait is shown in Fig. 3.4 with a black line.

A second trajectory is an isokinetic/isometric exercise found in [31], the reference signal has been adequated to be used with the motoBOTTE while achieving an ankle speed of 40 degrees per second [125, 126], this trajectory is shown in Fig. 3.4 with a blue line

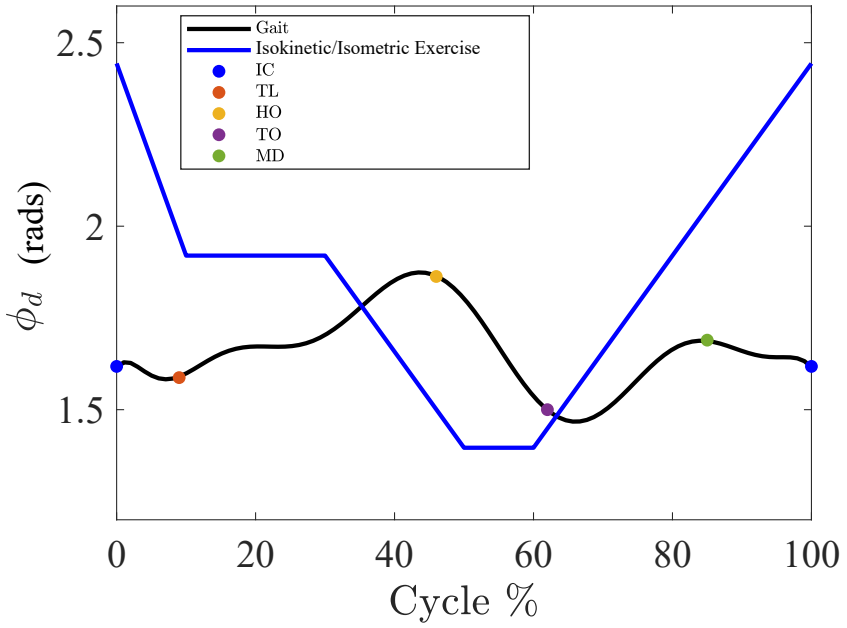

FIGURE 3.4: Ankle trajectory during gait and isokinetic/isometric exercise.

and it is defined as :

$$\phi_d = \begin{cases} \frac{\pi(7-2t)}{9} & t < 0.75 \\ 1.9199 & 0.75 \leq t < 2.25 \\ \frac{\pi(31-4t)}{36} & 2.25 \leq t < 3.75 \\ 1.3963 & 3.75 \leq t < 4.5 \\ \frac{\pi(2t-1)}{18} & 4.5 \leq t \leq 7.5. \end{cases} \tag{3.9}$$

3.3.2 Discrete adaptations

In order to implement the rehabilitation routines just described, the control schemes developed in subsection 3.1.2 and section 3.2 should be translated into control signals for the motoBOTTE real-time setup. This goal requires translating continuous signals into discrete-time ones as the control laws are programmed in C language into an embedded myRIO 1900 digital device from National Instruments [70] (see Fig. 3.5).

TABLE 3.1: Events in the gait cycle.

Event	IC	TL	HO	TO	MD
ϕ value	1.6179	1.5874	1.863	1.45	1.6895
Cycle %	0	9	49	62	89

Recall that only one entry of the control law (3.4) is available and it corresponds to $\dot{u}$; this signal in turn depends on designing $v(t)$ in (3.5). By Euler's approximation [127], we have:

$$u(k+1) = u(k) + T_s \dot{u}(k), \tag{3.10}$$

with $u(0) = 0$. In this way, $u(k)$ can be sent as a discrete signal into the servo controller, where $T_s = 0.01$ second is the sampling time for the embedded device.

Let us first consider the model-based computed-torque implementation. For the discrete signal $v(k)$ in subsection 3.1.2, consisting on three parts, Euler's approximation is used for the integral of the error

$$\epsilon(k+1) = \epsilon(k) + T_s \left(d_d(k) - d(k) \right), \tag{3.11}$$

with $\epsilon(0) = 0$, while $e(k)$ and $\dot{e}(k)$ are directly available. The linear error system (3.6) is discretized using Tustin approximation [128], which yields

$$\begin{bmatrix} \epsilon(k+1) \\ e(k+1) \\ \dot{e}(k+1) \end{bmatrix} = \begin{bmatrix} 1 & 0.01 & 5\times10^{-5} \\ 0 & 1 & 0.01 \\ 0 & 0 & 1 \end{bmatrix} \begin{bmatrix} \epsilon(k) \\ e(k) \\ \dot{e}(k) \end{bmatrix} + \begin{bmatrix} 2.5\times10^{-7} \\ 5\times10^{-5} \\ 0.01 \end{bmatrix} v(k),$$

where the signal $v(k) = k_p e(k) + k_i \epsilon(k) + k_v \dot{e}(k)$ is designed using pole placement.

The specification of the poles is usually given in continuous time; it is well-known their location is related to a variety of performance measures of the controller. The poles in continuous time have been chosen as $s_1 = -5$, $s_2 = -6$, and $s_3 = -7$, which is ensured with gains $k_p = -192.0135$, $k_i = -98.8243$, and $k_v = -16.9623$; it was verified by simulation that these poles avoid input saturation while achieving the trajectory tracking goals

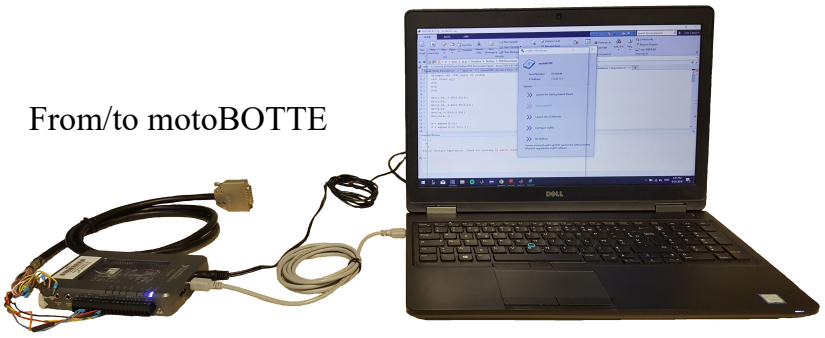

FIGURE 3.5: DSP interface.

without oscillation. For discrete implementation, poles were translated into discrete frequency domain as $z_i = e^{s_i T_s}$ and $i \in \{1, 2, 3\}$, yielding $z_1 = 0.9512$, $z_2 = 0.9418$ and $z_3 = 0.9324$.

A first experiment intends to follow the rehabilitation routine for gait given in Fig. 3.4 but transformed from ankle angle $\phi(t)$ to the piston actuator coordinates $d(t)$ via (2.14) and (2.15); this trajectory is defined by real-time results obtained when tracking this reference using the discrete version of (3.5) with the gains above are shown in Fig. 3.6(a), the control signal is shown in Fig. 3.6(b); the initial conditions in simulation were $q(0) = \begin{bmatrix} 0.0841 & 0.0543 & -2.0822 \end{bmatrix}$ and $\dot{q}(0) = \begin{bmatrix} 0 & 0 & 0 \end{bmatrix}^T$; these initial conditions must satisfy the algebraic constraints in (2.13) and (2.15) to be considered as consistent.

A second experiment tracking the trajectory for isokinetic/isometric exercise (3.9) the trajectory is shown in Fig. 3.7(a). The control signals applied are in Fig. 3.7(b). The gains for the controller are the same as in the previous case. The consistent initial conditions for simulation were $q(0) = \begin{bmatrix} 0.0107 & 0.1574 & -2.8105 \end{bmatrix}^T$ and $\dot{q}(0) = \begin{bmatrix} 0 & 0 & 0 \end{bmatrix}^T$.

Let us now consider the model-free ADRC implementation. The gains for the controller and the extended state observer with the input parameter were obtained using the Parameter Estimation Toolbox with the simplex algorithm [98], then, the input parameter b_2 was manually adjusted by minimizing a sum of absolute error cost function in real-time $c_{f2} = \sum |d(k) - d_d(k)|$ via bisection. The values obtained were $\beta_{01} = 0.97777$, $\beta_{02} = 2.3586$, $\beta_{03} = 0.0044$ $r_0 = 0.38843$, $c_0 = 7.5321$, $h_0 = 0.0058355$, $b_2 = 0.1088$.

The time evolution of the system when applying the active disturbance rejection control scheme with the ankle trajectory for gait is shown in Fig. 3.8(a) and its respective control signal is presented in Fig. 3.8(b). The time evolution of the system when applying the active disturbance rejection control scheme for the isokinetic/isometric exercise is shown in Fig. 3.9(a) and its respective control signal is presented in Fig. 3.9(b).

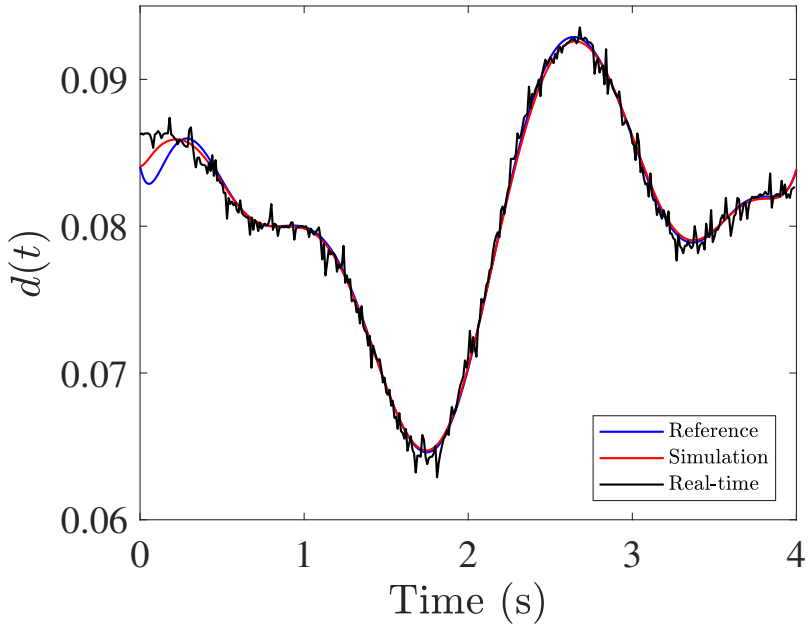

(a) Time evolution of the piston position in simulation and real-time.

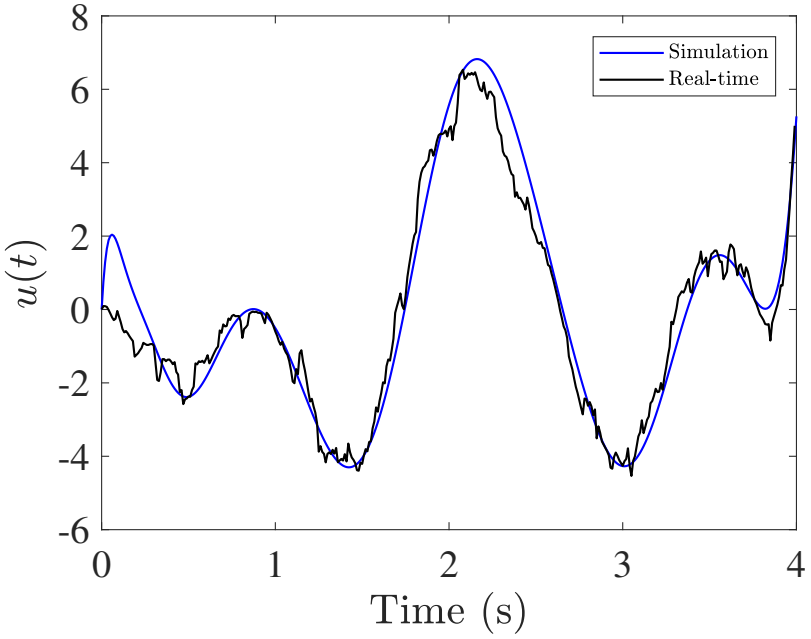

(b) Time evolution of the control signal in simulation and real-time.

FIGURE 3.6: Gait trajectory under computed-torque control.

3.3.3 Discussion

From Figs. 3.6(a) and 3.8(a) it is clear that trajectory tracking for the gait rehabilitation routine is almost identical in both schemes, though the model-free ADRC proposal is slightly better, possibly due to the sliding-like characteristics of both the extended

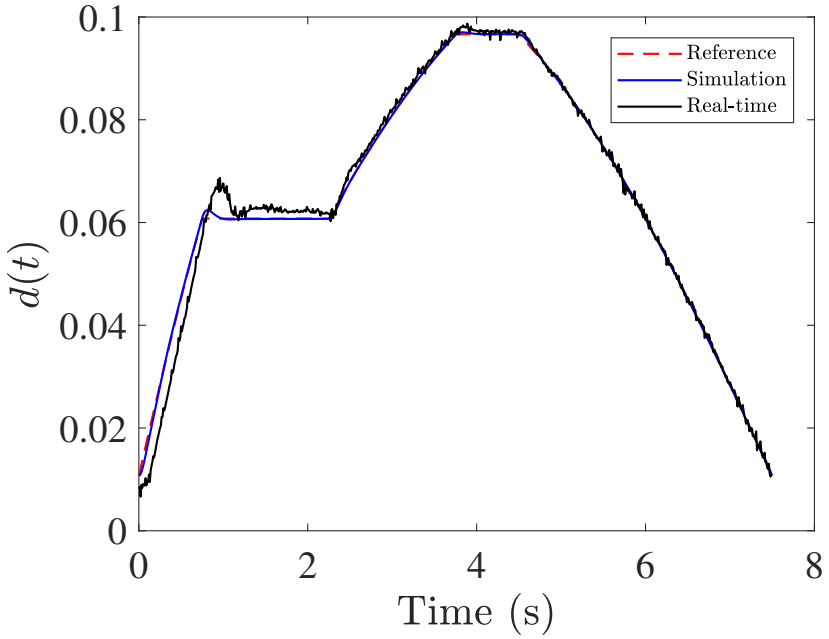

(a) Time evolution of the piston position in simulation and real-time.

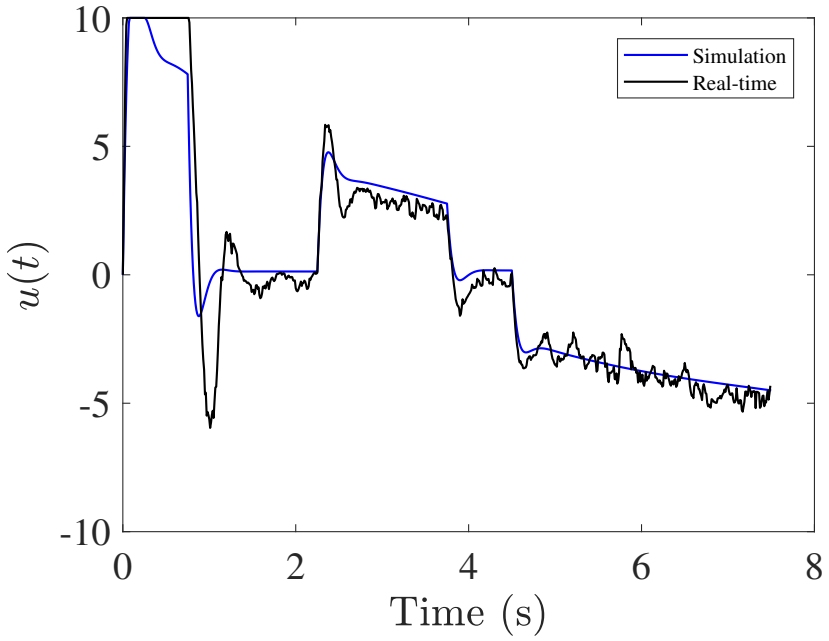

(b) Time evolution of the control signal in simulation and real-time.

FIGURE 3.7: Isokinetic/Isometric exercise under computed-torque control.

observer and the control law. A more remarkable difference emerges when control signals in Figs. 3.6(b) and 3.8(b) are compared: that of the ADRC in real-time implementation is clearly more noisy than the computed-torque control law, which is a very well-known disadvantage (or price to pay, if otherwise considered) of variable structure control [120].

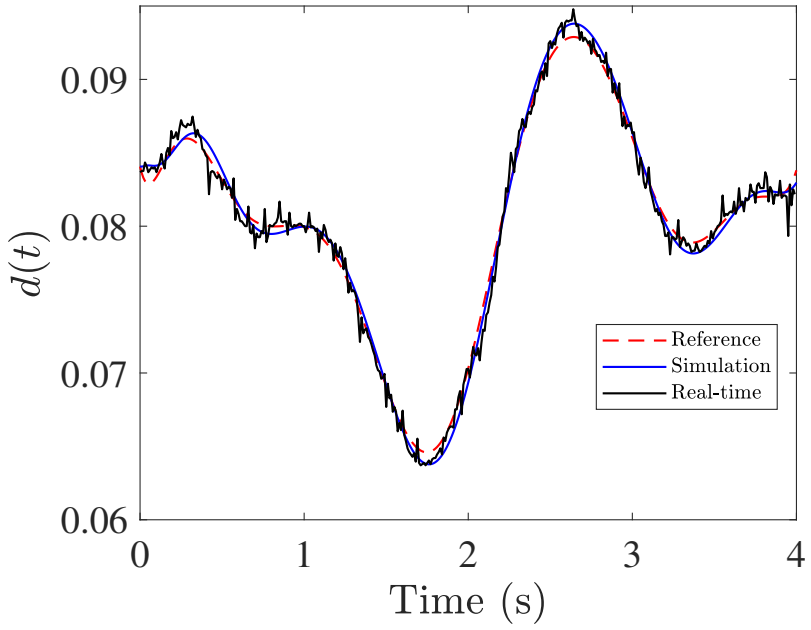

(a) Time evolution of the piston position in simulation and real-time.

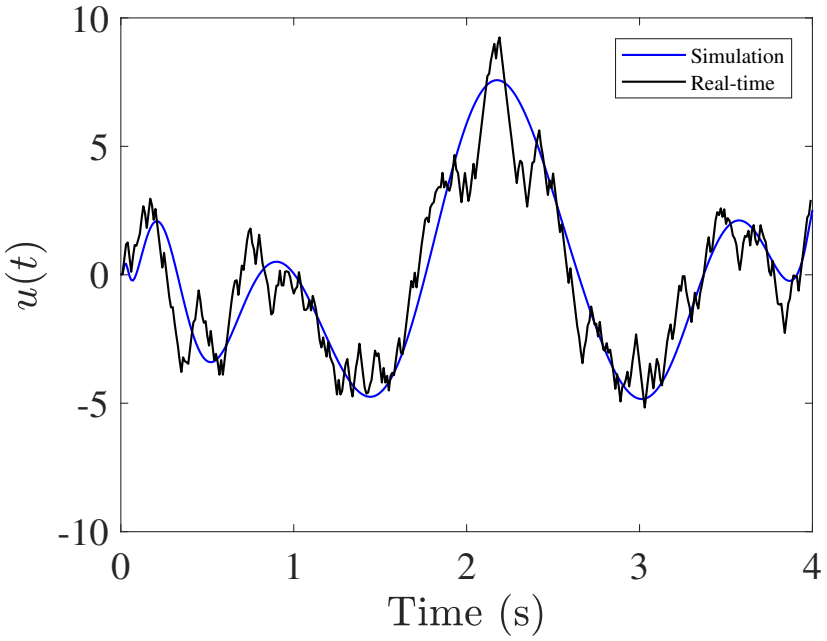

(b) Time evolution of the control signal in simulation and real-time.

FIGURE 3.8: Gait trajectory under ADRC.

In this case, chattering of the control signal does not pose any threat to the motoBOTTE piston as the actuator stands well the training cycle; yet, for a long-term use model-based computed-torque control or a smoother version of the ADRC might be advisable.

Figs. 3.7(a) and 3.9(a) prevent us from jumping to hasty conclusions about advantages

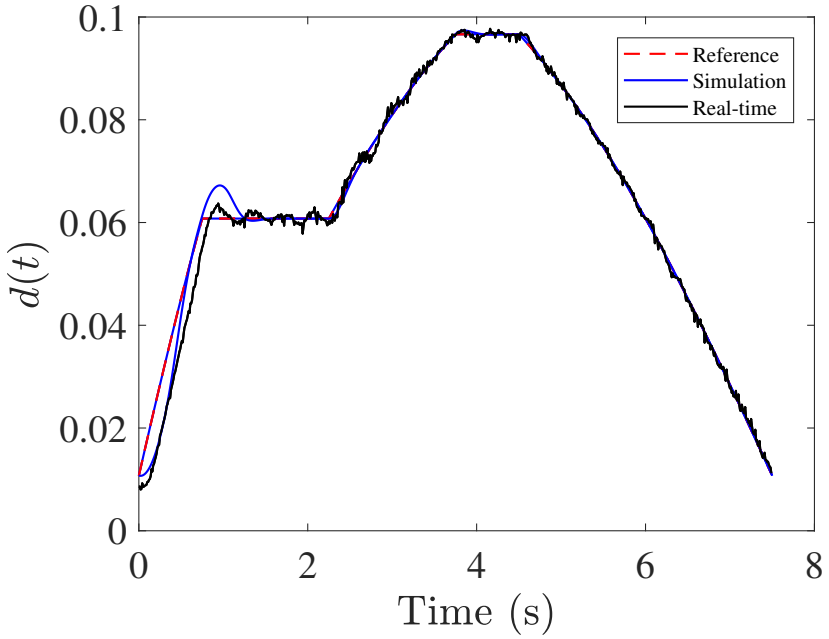

(a) Time evolution of the piston position in simulation and real-time.

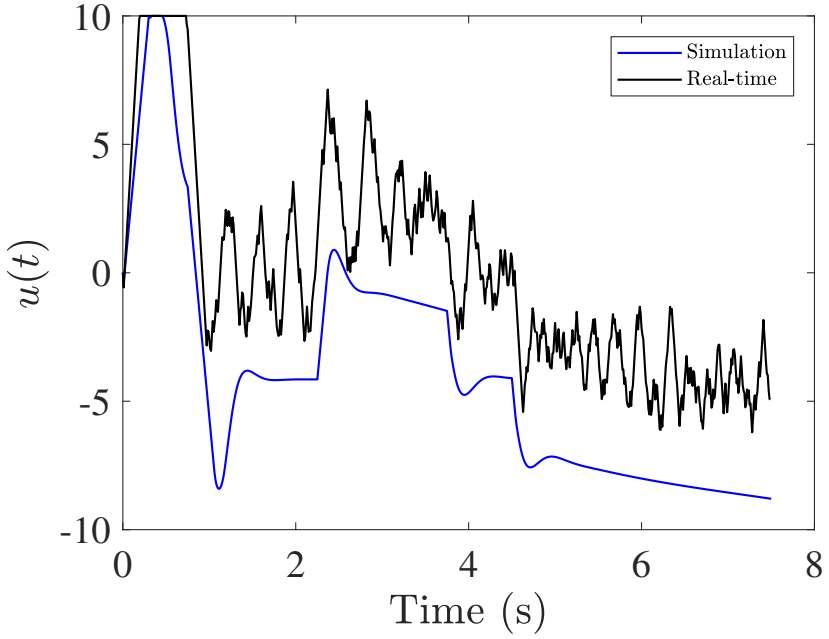

(b) Time evolution of the control signal in simulation and real-time.

FIGURE 3.9: Isokinetic/Isometric exercise under ADRC.

and disadvantages of computed-torque and ADRC approaches: it is clear that the first one tracks the isokinetic/isometric routine better than the ADRC controller. A possible explanation lies on the less differentiability of the reference signal (it presents sudden jumps): it causes overshooting in the computed-torque trajectory tracking (see around

$t = 1$ in Fig. 3.7(a)) and chattering (high-frequency signals) in Fig. 3.9(a). This chattering is more remarkable in the control signal of the ADRC controller of Fig. 3.9(b), which despite its wild variations realizes the tracking task; nevertheless, this is damaging for the DC motor of the piston and is not advised for practical use. On the other hand, computed-torque signal in Fig. 3.7(b), although being more noisy than the one used for the gait routine, presents less variations than the ADRC control signal in Fig. 3.9(b).

Based on the results just described, the control technique should be chosen according to the ankle rehabilitation routine that is going to be implemented: it is not advisable to decide it beforehand. The model-free and model-based techniques employed in this work, namely ADRC and computed-torque adaptations, respectively, have well-known properties that have been confirmed in this implementation: model-free requires tuning against fixed design, computed-torque control signals are smoother than ADRC ones, etc. However, these characteristics may differ from the general criterium when they are applied to a particular plant (a parallel robot such as the motoBOTTE) subject to particular tasks (such as the gait and isokinetic/isometric routines).

3.4 Conclusion

Within this chapter, model-based and model-free control strategies have been adapted to be applied for tracking trajectories with parallel robots that are described by a set of differential-algebraic-equations. The algebraic constraints inherit to the singular system have been incorporated into the trajectory generation model x_d, such that all the variables of the trajectory generation model lie within the manifold of these constraints.

The control strategy based on computed-torque for a system written in a state-space representation has been illustrated in simulation by applying it to the white box model of the motoBOTTE that was presented in the previous chapter, and the computed-torque control technique adapted to parallel robots written in general coordinates and a model-free approach based on active disturbance rejection control were illustrated using the model from the grey box approach in the previous chapter, these latter strategies were simulated and implemented in real-time.

Details about the real-time implementation, simulation and trajectories selected were provided, these details include discretization of the control signal, dealing with unmeasured variables, the consistent initial conditions for simulation were provided and reference for the trajectories selected. The control signal was verified to be within the operation range ($u \in [-10, 10]$ Volts) in simulation, before performing the designs in real-time implementation.

Finally, there was no notorious difference in term of performances between the computed-torque control and ADRC design during the real-time implementations except that the latter is a little bit more sensitive to noise due to it structure.

Chapter 4

Convex Control for DAEs

Singular systems also known as differential-algebraic-equation systems (DAEs) [67], singular descriptors, semi-state representations, implicit systems, among other names, appear when differential equations are required to be combined with algebraic expressions for describing the behavior of systems, some examples include electrical circuits [129], chemical processes [130], parallel robots [131], mechanical systems [90, 132], and more.

DAEs do not have solution for all the values of x due to their algebraic constraints; this allow us to consider a candidate Lyapunov function $V(x)$ that does not require to be valid for all x (i.e., $V(x) > 0$ and $\dot{V}(x) < 0$), but only for those values of x that satisfy the algebraic constraints in the DAEs. As indicated in previous results for stability [89, 133] i.e., such as LaSalle's theorem, the definition of asymptotic stability is different to the one given by Lyapunov.

Even for the linear case, attempts to find conditions for stability analysis [134] have yield to misleading conclusions that were proved to be wrong [135]. A notorious contribution for the linear case can be found in [136], in which Finsler's lemma is combined with Lyapunov's direct method.

This chapter deals with nonlinear control design based on convex structures obtained via applying the nonlinear sector methodology, most of the conditions presented on this chapter are given in terms of linear matrix inequalities (LMIs).

The chapter is organized as follows : section 4.1 presents a brief synthesis of the well known nonlinear sector methodology that can be used to obtain an exact convex representation of nonlinear systems and finish with a remark of the issues found when methodologies of this kind are employed for control and observer design, then, subsection presents classic conditions for nonlinear controller and observer design based on a parallel distributed compensation 4.1.1, these conditions for nonlinear synthesis yield to the problem of Positivstellensatz that is formally introduced in subsection 4.1.2, new conditions based on copositive matrices are established in subsection 4.1.3. Afterwards, in subsections 4.1.4 and 4.1.5 the black box model of the motoBOTTE combined with an exact convex representation of the tracking error is employed to design a PI and PID controllers for tracking trajectories, simulation and real-time results for these approaches are presented. The last section 4.2 provides some insight about how the algebraic constraints must be taken into account when selecting the modeling region Ω for a singular system, this idea is illustrated by examining the determinant of the matrix $E(x)$ when the dynamical equations of the singular system are expressed in a descriptor form, finally, new conditions for control design of nonlinear singular systems are established in subsection 4.3.

4.1 Convex Structures via Nonlinear Sector Method

Consider a continuous time nonlinear system

$$\dot{x}(t) = f\left(x(t)\right) + g\left(x(t)\right)u(t), \quad y(t) = z\left(x(t)\right), \tag{4.1}$$

these systems can be rewritten for all x within a compact of interest Ω by means of the nonlinear sector methodology from [137]; thus, obtaining an exact convex representation for

$$\dot{x} = A(x)x + B(x)u, \quad y = C(x)x.$$

The method consists on rewriting each of the ρ non constant terms (denoted by z_i, with $i \in \{1, 2, \cdots, \rho\}$) in the matrices $A(x)$, $B(x)$ and $C(x)$ in (4.3) for all $x \in \Omega$, via the interpolation or membership functions defined as $h_i = w_{i_1}^1 w_{i_2}^2 \cdots w_{i_r}^r$, where $[i_1, i_2, \cdots, i_r]$ is a $\rho-$digit binary representation of $(i-1)$ with $i \in \{1, 2, \cdots, r\}$ and $r = 2^\rho$ is the number of membership or interpolation functions necessary to obtain this exact convex

representation, the weight functions w_0^i and w_1^i that compose the membership functions are defined as

$$w_0^i = \frac{z_i^1 - z_i}{z_i^1 - z_i^0}, \quad w_1^i = \frac{z_i - z_i^0}{z_i^1 - z_i^0},$$

where z_i^1 and z_i^0 stands for the maximum and minimum values of each non constant term z_i within Ω, respectively. Each non constant term is expressed as the convex sum of its constant extreme values $z_i = w_0^i\left(z_i^0\right) + w_1^i\left(z_i^1\right)$, the constant matrices can be obtained by evaluating

$$A_i = A(x)|_{h_i=1},\ B_i = B(x)|_{h_i=1},\ C_i = C(x)|_{h_i=1}, \tag{4.2}$$

it yields to the following *exact convex representation*

$$\dot{x}(t) = \sum_{i=1}^{r} h_i \left(A_i x(t) + B_i u(t)\right), \quad y(t) = \sum_{i=1}^{r} h_i C_i x(t). \tag{4.3}$$

The membership functions (denoted by h_i) belong to the standard simplex (i.e., they hold the convex sum properties)

$$0 \leq h_i \leq 1, \quad \sum_{i=1}^{r} h_i = 1. \tag{4.4}$$

Most of the developments thereafter assume that the mathematical model of the system has been rewritten as a convex structure, and also that the origin of the system $x = 0$ is contained in the modeling region Ω. These systems are known as Takagi-Sugeno (T-S) due to its historical background in the area of Fuzzy Systems or polytopic systems in the area of linear parameter varying systems (LPV). It is important to recall that this is not the only way to obtain an exact convex representation, there are some widely known alternatives such as polynomial fuzzy models [80] or tensor product models [138]; therefore, the models after this modelling process obtained are not unique and the selected approach might have an impact on the conservativeness of the solution found for the controller design problem [139].

4.1.1 Classic conditions for synthesis of nonlinear systems

Stability conditions for nonlinear control design

First, consider a nonlinear system (4.1) written as an exact convex representation (4.3), assuming that the state vector x can be fully measured and applying a parallel distributed compensation control law (denoted as PDC) has the form

$$u = F(x)x = \sum_{j=1}^{r} h_j F_j x, \tag{4.5}$$

where h_j are the same membership functions as the original system, then, our closed-loop system is

$$\dot{x} = (A(x) + B(x)F(x))\, x = \sum_{i=1}^{r}\sum_{j=1}^{r} h_i h_j \left(A_i + B_i F_j\right) x. \tag{4.6}$$

Consider a quadratic candidate Lyapunov function of the form $V(x) = x^T P x$, it is positive definite if $P > 0$, its time derivative is $\dot{V}(x) = x^T P \dot{x} + \dot{x}^T P x$, substituting (4.6) gives

$$\dot{V} = x^T \left[\sum_{i=1}^{r}\sum_{j=1}^{r} h_i h_j \left(P\left(A_i + B_i F_j\right) + \left(F_j^T B_i^T + A_i^T\right) P\right)\right] x,$$

it will be negative $\forall x$ if the following holds

$$\sum_{i=1}^{r}\sum_{j=1}^{r} h_i h_j \left(P\left(A_i + B_i F_j\right) + \left(F_j^T B_i^T + A_i^T\right) P\right) < 0,$$

since $h_i \geq 0$ and $h_j \geq 0$ in Ω they can be just removed

$$P\left(A_i + B_i F_j\right) + \left(F_j^T B_i^T + A_i^T\right) P < 0,$$

applying congruence with $X = P^{-1}$, yields to

$$-A_i X - B_i F_j X - X F_j^T B_i^T - X A_i^T > 0,$$

applying substitution with $M_j = F_j X$, then, $\dot{V}$ is negative definite if $\sum_{i,j=1}^{r} h_i h_j Q_{ij} > 0$, with $Q_{ij} = -A_i X - B_i M_j - M_j^T B_i^T - X A_i^T$.

Stability Conditions for Nonlinear Observer Design

If the membership functions depend only on measured variables then a nonlinear observer for the system (4.3) can be defined as

$$\hat{x}=\sum_{i=1}^{r}\sum_{j=1}^{r} h_i h_j \left(A_i\hat{x}+B_i u+L_j\left(y-\hat{y}\right)\right), \qquad \hat{y}=\sum_{i=1}^{r} h_i C_i\hat{x}, \tag{4.7}$$

the observation error is $e=x-\hat{x}$ and its time derivative is

$$\dot{e}=\dot{x}-\dot{\hat{x}}=\sum_{i=1}^{r}\sum_{j=1}^{r} h_i h_j \left(A_i-L_jC_i\right)e. \tag{4.8}$$

Consider a quadratic candidate Lyapunov function for the error $V=e^TPe$, is positive definite if $P>0$, its time derivative is $\dot{V}=e^TP\dot{e}+\dot{e}^TPe$ and substituting (4.8) gives

$$\dot{V}=e^T\left[\sum_{i=1}^{r}\sum_{j=1}^{r} h_i h_j \left(PA_i-PL_jC_i-C_i^TL_j^TP+A_i^TP\right)\right]e,$$

it is negative $\forall e$ if the following holds

$$\sum_{i=1}^{r}\sum_{j=1}^{r} h_i h_j \left(-PA_i+PL_jC_i+C_i^TL_j^TP-A_i^TP\right)>0,$$

since $h_i\geq 0$ and $h_j\geq 0$ in Ω they can be just removed

$$-PA_i+PL_jC_i+C_i^TL_j^TP-A_i^TP>0,$$

substituting $N_j=PL_j$, then $\dot{V}$ is negative definite if $\sum_{i,j=1}^{r} h_i h_j Q_{ij}>0$, with $Q_{ij}=-PA_i+N_jC_i+C_i^TN_j^T-A_i^TP$.

4.1.2 The Problem of Positivstellensatz

Both cases controller and observer design have been transformed into a problem of Positivstellensatz, which is basically proving that a constrained polynomial is positive [140]. Notice that Q_{hh} is a quadratic function of h and increasing the number of membership functions involved will increase the degree of this polynomial function as in results based on Polya's theorem such as [80, 141, 142]. The stability conditions obtained for both

cases are of the form

$$Q_{hh} > 0, \tag{4.9}$$

with $Q_{hh} = \sum_{i,j=1}^{r} h_i h_j Q_{ij}$, where Q_{ij} are matrices with constant terms and some of them are decision variables (terms to be found). A trivial solution for (4.9) would be $Q_{ij} > 0 \ \forall i, j$, but this is a conservative solution, it does not take into account the interaction between subsystems nor the positiveness in the h functions. There are many shape-independent relaxations available to satisfy the positiveness of (4.9) such as :

Lemma 4.1 ([143]). *A sufficient condition for the expression* (4.9) *to be positive is*

$$\begin{aligned} Q_{ii} &> 0, \\ Q_{ij} + Q_{ji} &\geq 0, \quad \forall j < i, \end{aligned} \tag{4.10}$$

holds for $i, j \in \{1, 2, \cdots, r\}$.

Lemma 4.2 ([144]). *The equation* (4.9) *is positive for* $h_i \geq 0$ *if*

$$\begin{bmatrix} \frac{1}{r-1} Q_{ii} & \frac{1}{2}\left(Q_{ij} + Q_{ji}\right) \\ \frac{1}{2}\left(Q_{ij} + Q_{ji}\right) & \frac{1}{r-1} Q_{jj} \end{bmatrix} > 0, \quad \forall j < i. \tag{4.11}$$

holds for $i, j \in \{1, 2, \cdots, r\}$.

Lemma 4.3 ([145]). *The expression* (4.9) *holds if we guarantee that*

$$\begin{aligned} Q_{ii} - Z_{ii} &\geq 0, \\ Q_{ij} + Q_{ji} - 2Z_{ij} &\geq 0, \quad \forall j < i, \\ \begin{bmatrix} Z_{11} & Z_{21} & \cdots & Z_{r1} \\ Z_{21} & Z_{22} & \cdots & Z_{r2} \\ \vdots & \vdots & \ddots & \vdots \\ Z_{r1} & Z_{r2} & \cdots & Z_{rr} \end{bmatrix} &> 0. \end{aligned} \tag{4.12}$$

Lemma 4.4 ([146]). *The inequality in (4.9) holds if there are matrices such that*

$$\begin{aligned} Q_{ii} - Z_{ii} &\geq 0, \\ Q_{ij} + Q_{ji} - Z_{ij} - Z_{ij}^T &\geq 0, \quad \forall j < i, \\ \begin{bmatrix} Z_{11} & Z_{21}^T & \cdots & Z_{r1}^T \\ Z_{21} & Z_{22} & \cdots & Z_{r2}^T \\ \vdots & \vdots & \ddots & \vdots \\ Z_{r1} & Z_{r2} & \cdots & Z_{rr} \end{bmatrix} &> 0. \end{aligned} \tag{4.13}$$

All the previous lemmas consider the h functions as positive scalars subject to an algebraic and inequality constraint (i.e., $h \geq 0$ and $\sum h = 1$); is easy to check that the condition $h \leq 1$ is *also guaranteed*, since you can only satisfy $\sum h = 1$ with positive scalars smaller or equal to 1.

Verifying that a matrix Q is not copositive is a well known NP-complete problem [147], it can not be verified by checking its eigenvalues, all the positive definite matrices are copositive, but the converse is false.

Lemma 4.5 ([148]). *A sufficient condition for a matrix Q to be copositive is that it can be written as the sum of a positive semidefinite matrix P_d and a nonnegative matrix Λ with entries λ_{ij} :*

$$Q = P_d + \Lambda \tag{4.14}$$

with $P_d \geq 0$ and $\lambda_{ij} \geq 0$; there are copositive matrices that can not be expressed in this form [149].

Lemma 4.6 (Finsler's). *[136] Let $x \in \mathbb{R}^n$, $\mathcal{Q} \in \mathbb{S}^n$ and $\mathcal{B} \in \mathbb{R}^{m \times n}$ such that rank $(\mathcal{B}) < n$. The following statements are equivalent :*

1. $x^T Q x < 0$, $\mathcal{B}x = 0$, $x \neq 0$.
2. $\exists \mathcal{X} \in \mathbb{R}^{n \times m} : \mathcal{Q} + \mathcal{X}\mathcal{B} + \mathcal{B}^T \mathcal{X}^T < 0$.

Definition 4.7 (Positive [150]). Let a matrix $Q \in \mathbb{R}^{n \times n}$, be called positive definite if $x^T Q x > 0$ holds for $x \neq 0$ and $x \in \mathbb{R}^n$. A matrix Q is positive definite if and only if its symmetric part is positive definite $\frac{1}{2}\left(Q + Q^T\right) > 0$.

Definition 4.8 (Copositive [148]). Let a matrix Q be called strictly copositive if $h^T Q h > 0$ holds for $h \geq 0$, with $Q \in \mathbb{R}^{r \times r}$ and $h \in \mathbb{R}^r$.

4.1.3 New Conditions for Nonlinear Controller and Observer Design

In this section positiveness of the membership functions is considered into the Lyapunov analysis for nonlinear control and observer design, the new theorems obtained are based on the concept of copositive matrix.

Theorem 4.9. *The origin of the system (4.3) is asymptotically stable under a control of the form (4.5) if there are proper size matrices* $X = X^T > 0$, M_j, $\lambda_{ij} = \lambda_{ij}^T \geq 0$, *for all* $j < i$ *such that :*

$$\begin{bmatrix} Q_{11} - \lambda_{11} & Q_{21}^T - \lambda_{21}^T & \cdots & Q_{r1}^T - \lambda_{r1}^T \\ Q_{21} - \lambda_{21} & Q_{22} - \lambda_{22} & \cdots & Q_{r2}^T - \lambda_{r2}^T \\ \vdots & \vdots & \ddots & \vdots \\ Q_{r1} - \lambda_{r1} & Q_{r2} - \lambda_{r2} & \cdots & Q_{rr} - \lambda_{rr} \end{bmatrix} > 0, \tag{4.15}$$

is strictly positive definite with the matrices defined as $Q_{ii} = -A_iX - B_iM_i - XA_i^T - M_i^T B_i^T$, $Q_{ij} = \frac{1}{2}\left(-A_iX - B_iM_j - XA_i^T - M_j^T B_i^T\right) + \frac{1}{2}\left(-A_jX - B_jM_i - XA_j^T - M_i^T B_j^T\right)$ *for all* $j < i$ *and* $i, j \in \{1, 2, \cdots, r\}$. *The gains for the controller are* $F_j = M_jX^{-1}$.

Proof. The closed-loop system (4.6) can be written as

$$\dot{x}(t) = \sum_{i=1}^{r} h_i^2 G_{ii} x(t) + 2 \sum_{i<j\leq r} h_i h_j \left(\frac{G_{ij} + G_{ji}}{2}\right) x(t),$$

with $G_{ij} = A_i + B_iF_j$ and consider a quadratic candidate Lyapunov function $V = x^T Px$, with $P > 0$, its time-derivative is $\dot{V} = x^T P\dot{x} + \dot{x}^T Px = -x^T Q_{hh} x$, where Q_{hh} is equal to

$$Q_{hh} = \sum_{i=1}^{r} \sum_{j=1}^{r} h_i h_j \left(\Delta_{ij}^T P + P\Delta_{ij}\right), \tag{4.16}$$

this can be rewritten as

$$\bar{h}^T \begin{bmatrix} P\Delta_{11} + \Delta_{11}^T P & P\Delta_{21} + \Delta_{21}^T P & \cdots & P\Delta_{r1} + \Delta_{r1}^T P \\ P\Delta_{21} + \Delta_{21}^T P & P\Delta_{22} + \Delta_{22}^T P & \cdots & P\Delta_{r2} + \Delta_{r2}^T P \\ \vdots & \vdots & \ddots & \vdots \\ P\Delta_{r1} + \Delta_{r1}^T P & P\Delta_{r2} + \Delta_{r2}^T P & \cdots & P\Delta_{rr} + \Delta_{rr}^T P \end{bmatrix} \bar{h}, \tag{4.17}$$

with $\bar{h} = \begin{bmatrix} h_1 I & h_2 I & \cdots & h_r I \end{bmatrix}^T$ and $\Delta_{ij} = \frac{1}{2}(G_{ij} + G_{ji})$. Now, consider a copositive matrix $\Gamma_{ij} \in \mathbb{R}^{rn \times rn}$, which means that the quadratic form

$$\Gamma_{hh} = \begin{bmatrix} h_1 I \\ h_2 I \\ \vdots \\ h_r I \end{bmatrix}^T \underbrace{\begin{bmatrix} \gamma_{11} & \gamma_{21}^T & \cdots & \gamma_{r1}^T \\ \gamma_{21} & \gamma_{22} & \cdots & \gamma_{r2}^T \\ \vdots & \vdots & \ddots & \vdots \\ \gamma_{r1} & \gamma_{r2}^T & \cdots & \gamma_{rr} \end{bmatrix}}_{\Gamma_{ij}} \begin{bmatrix} h_1 I \\ h_2 I \\ \vdots \\ h_r I \end{bmatrix},$$

is positive for $h_i, h_j \geq 0$, with $\gamma_{ij} \in \mathbb{R}^{n \times n}$ for all $1 \leq j < i \leq r$, a sufficient condition for Γ_{ij} to be copositive is that it is composed by blocks of positive semidefinite matrices, therefore, $\gamma_{ij} \geq 0$. According to Lemma 4.5, if Γ_{ij} is a copositive matrix, then, (4.17) is also copositive if (4.18) holds.

$$\begin{bmatrix} P\Delta_{11}+\Delta_{11}^T P-\gamma_{11} & P\Delta_{21}+\Delta_{21}^T P-\gamma_{21} & \cdots & P\Delta_{r1}+\Delta_{r1}^T P-\gamma_{r1} \\ P\Delta_{21}+\Delta_{21}^T P-\gamma_{21} & P\Delta_{22}+\Delta_{22}^T P-\gamma_{22} & \cdots & P\Delta_{r2}+\Delta_{r2}^T P-\gamma_{r2}^T \\ \vdots & \vdots & \ddots & \vdots \\ P\Delta_{r1}+\Delta_{r1}^T P-\gamma_{r1} & P\Delta_{r2}+\Delta_{r2}^T P-\gamma_{r2} & \cdots & P\Delta_{rr}+\Delta_{rr}^T P-\gamma_{rr} \end{bmatrix} > 0. \quad (4.18)$$

Then, pre- and post- multiplying it by a proper size diagonal matrix of X, with $X = P^{-1}$ yields to

$$\begin{bmatrix} \Delta_{11}X+X\Delta_{11}^T-X\gamma_{11}X & \Delta_{21}X+X\Delta_{21}^T-X\gamma_{21}X & \cdots & \Delta_{r1}X+X\Delta_{r1}^T-X\gamma_{r1}X \\ \Delta_{21}X+X\Delta_{21}^T-X\gamma_{21}X & \Delta_{22}X+X\Delta_{22}^T-X\gamma_{22}X & \cdots & \Delta_{r2}X+X\Delta_{r2}^T-X\gamma_{r2}^T X \\ \vdots & \vdots & \ddots & \vdots \\ \Delta_{r1}X+X\Delta_{r1}^T-X\gamma_{r1}X & \Delta_{r2}X+X\Delta_{r2}^T-X\gamma_{r2}X & \cdots & \Delta_{rr}X+X\Delta_{rr}^T-X\gamma_{rr}X \end{bmatrix} > 0, \quad (4.19)$$

substituting $M_j = F_j X$ and $\lambda_{ij} = X\gamma_{ij}X$, with $\lambda_{ij} \geq 0$, yields to conditions in Theorem 4.9, which is equivalent to find $P_d > 0$ for $P_d = Q - \Lambda$ in Lemma 4.5, this concludes the proof.

Theorem 4.10. *The origin of the system (4.3) is asymptotically stable under a control of the form (4.5) if there are proper size matrices $X = X^T > 0$, M_j, $\lambda_{ii} = \lambda_{ii}^T \geq 0$,*

$\frac{1}{2}\left(\lambda_{ij}-\lambda_{ij}^T\right)>0$ *for all* $j<i$, *such that :*

$$\begin{bmatrix} Q_{11}-\lambda_{11} & Q_{21}^T-\lambda_{21}^T & \cdots & Q_{r1}^T-\lambda_{r1}^T \\ Q_{21}-\lambda_{21} & Q_{22}-\lambda_{22} & \cdots & Q_{r2}^T-\lambda_{r2}^T \\ \vdots & \vdots & \ddots & \vdots \\ Q_{r1}-\lambda_{r1} & Q_{r2}-\lambda_{r2} & \cdots & Q_{rr}-\lambda_{rr} \end{bmatrix} > 0. \tag{4.20}$$

is strictly positive definite with the matrices defined as $Q_{ii}=-A_iX-B_iM_i-XA_i^T-M_i^TB_i^T$, $Q_{ij}=\frac{1}{2}\left(-A_iX-B_iM_j-XA_i^T-M_j^TB_i^T\right)+\frac{1}{2}\left(-A_jX-B_jM_i-XA_j^T-M_i^TB_j^T\right)$ *for all* $j<i$ *and* $i,j\in\{1,2,\cdots,r\}$. *The gains for the controller are* $F_j=M_jX^{-1}$.

Proof. It follows directly from previous developments, consider that the elements λ_{ij} with $j<i$ are full matrices and they hold the positive condition $\frac{1}{2}\left(\lambda_{ij}+\lambda_{ij}^T\right)>0$.

Theorem 4.11. *The origin of the error system* (4.8) *with the observer* (4.7) *is asymptotically stable if there are proper size matrices* $P=P^T>0$, N_j, $\gamma_{ij}\geq 0$, *for all* $j<i$ *such that*

$$\begin{bmatrix} Q_{11}-\gamma_{11} & Q_{21}^T-\gamma_{21}^T & \cdots & Q_{r1}^T-\gamma_{r1}^T \\ Q_{21}-\gamma_{21} & Q_{22}-\gamma_{22} & \cdots & Q_{r2}^T-\gamma_{r2}^T \\ \vdots & \vdots & \ddots & \vdots \\ Q_{r1}-\gamma_{r1} & Q_{r2}-\gamma_{r2} & \cdots & Q_{rr}-\gamma_{rr} \end{bmatrix} > 0. \tag{4.21}$$

is elementwise strictly positive definite with $Q_{ij}=-PA_i+N_jC_i+C_i^TN_j^T-A_i^TP$ *and* $i,j\in\{1,2,\cdots,r\}$, *where the gains for the observer are computed as* $L_j=P^{-1}N_j$.

Proof. It follows directly from previous developments.

Theorem 4.12. *The origin of the error system* (4.8) *with the observer* (4.7) *is asymptotically stable if there are proper size matrices* $P=P^T>0$, N_j, $\frac{1}{2}\left(\gamma_{ij}-\gamma_{ij}^T\right)\geq 0$, *for all* $j<i$, *such that*

$$\begin{bmatrix} Q_{11}-\gamma_{11} & Q_{21}^T-\gamma_{21}^T & \cdots & Q_{r1}^T-\gamma_{r1}^T \\ Q_{21}-\gamma_{21} & Q_{22}-\gamma_{22} & \cdots & Q_{r2}^T-\gamma_{r2}^T \\ \vdots & \vdots & \ddots & \vdots \\ Q_{r1}-\gamma_{r1} & Q_{r2}-\gamma_{r2} & \cdots & Q_{rr}-\gamma_{rr} \end{bmatrix} > 0. \tag{4.22}$$

is elementwise strictly positive definite with $Q_{ij}=-PA_i+N_jC_i+C_i^TN_j^T-A_i^TP$ *and* $i,j\in\{1,2,\cdots,r\}$, *where the gains for the observer are computed as* $L_j=P^{-1}N_j$.

Proof. It follows directly from previous developments, just consider $\frac{1}{2}\left(\gamma_{ij}+\gamma_{ij}^{T}\right)>0$.

The conditions for control design in Theorems 4.9 and 4.10 should be at least as good as Lemma 4.3 and 4.4, respectively, there is an equivalence given by Lemma 4.5.

The concept of copositive matrices can be applied to previous results where the Positivstellensatz problem appears, not only to controller and observer design for continuous systems as it was the case for this report. It is neither constrained to be applied only for systems with double-sums, it can be adapted for analyzing higher-order polynomials as shown in [148].

It is important to remark that only the property of positiveness in the membership functions was taken into account $h_i \geq 0$ in the previous developments, therefore, an appropriate method for including the information of the algebraic constraint $\sum_{i=1}^{r} h_i = 1$ in the stability analysis should reduce the existing gap. To illustrate this fact consider the easier case, which is a nonlinear system with two membership functions h_1 and h_2, the inequalities in Theorem 4.9 and 4.10 are sufficient to satisfy stability conditions in the grey region that represents $h_i \geq 0$ in Fig. 4.1, the region corresponding to the algebraic constraint $h_1+h_2=1$ is indicated with a black-dashed line and we must satisfy stability conditions only for the intersection of both, which is indicated with a red-line.

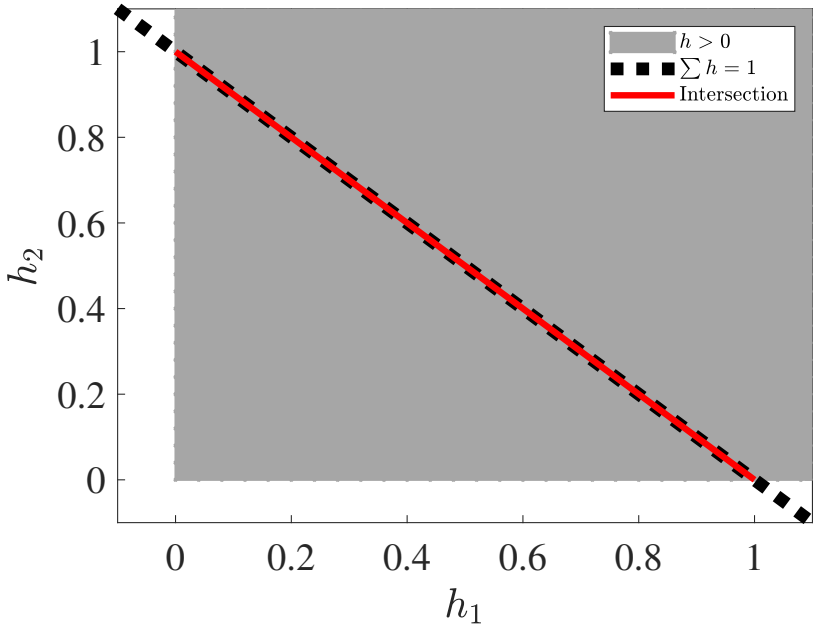

FIGURE 4.1: Illustration of the algebraic condition.

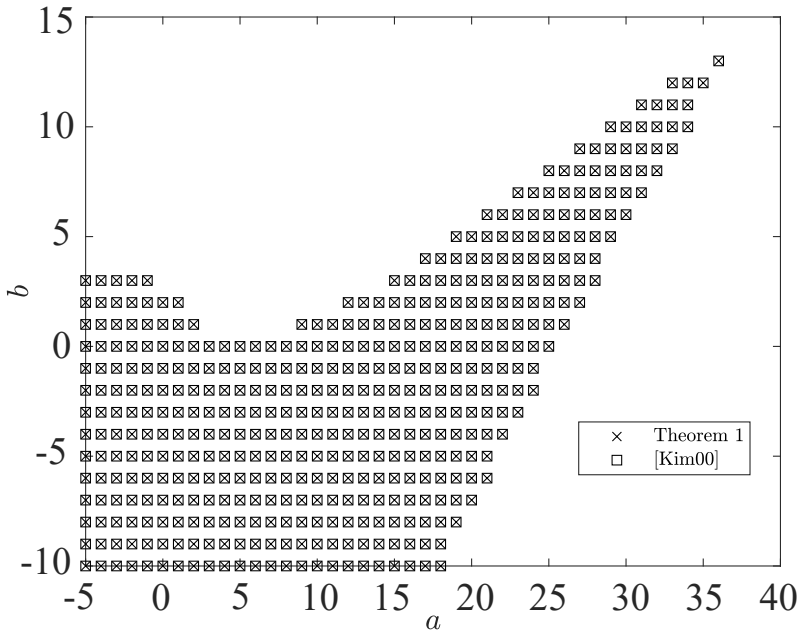

FIGURE 4.2: Comparison between Theorem 4.9 and Lemma 4.3.

Example 4.1. *Consider the matrices for a nonlinear system given in [141, 142] written in a convex representation (4.3) are* $A_1 = \begin{bmatrix} 1.59 & -7.29 \\ 0.01 & 0 \end{bmatrix}$, $B_1 = \begin{bmatrix} 1 \\ 0 \end{bmatrix}$, $A_2 = \begin{bmatrix} 0.02 & -4.64 \\ 0.35 & 0.21 \end{bmatrix}$, $B_2 = \begin{bmatrix} 8 \\ 0 \end{bmatrix}$, $A_3 = \begin{bmatrix} -a & -4.33 \\ 0 & 0.05 \end{bmatrix}$ *and* $B_3 = \begin{bmatrix} -b+6 \\ -1 \end{bmatrix}$, *the parameters* (a, b) *vary within the range* $a \in [-10, 40]$ *and* $b \in [-10, 17]$ *and a control law of the form (4.5) is designed. The feasible points for Theorem 4.9 and Lemma 4.3 are indicated with are indicated with* $\times$ *and* $\square$, *respectively in Fig. 4.2. The feasible points for Theorem 4.10 and Lemma 4.4 are indicated with are indicated with* $\times$ *and* $\square$, *respectively in Fig. 4.3. These points were obtained via the LMI solvers available in the Robust Control Toolbox in MATLAB R2019b, see [151].*

The solution for the point $(a, b) = (38, 15)$ *found using Theorem 4.10, the matrices found are*

$$F_1 = \begin{bmatrix} -1.7053 & 5.1795 \end{bmatrix}, F_2 = \begin{bmatrix} -0.8528 & -11.9668 \end{bmatrix}, F_3 = \begin{bmatrix} -1.8248 & 49.1549 \end{bmatrix},$$

the matrix associated to the Lyapunov function is

$$P = \begin{bmatrix} 0.0568 & 0.2863 \\ 0.2863 & 6.8039 \end{bmatrix},$$

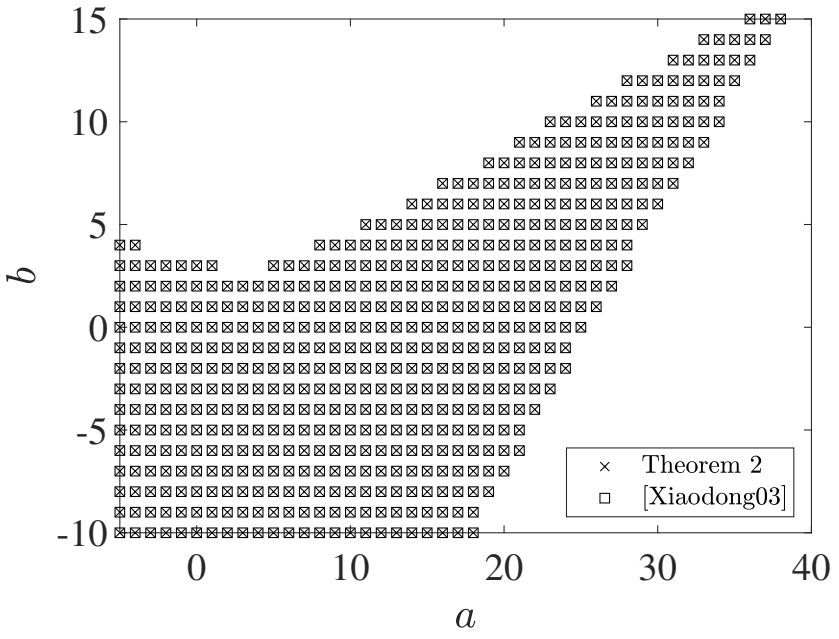

FIGURE 4.3: Comparison between Theorem 4.10 and Lemma 4.4.

the solution obtained was simulated with initial conditions $x(0)^T = \begin{bmatrix} -10 & 20 \end{bmatrix}$ *and the membership functions are*

$$h_1 = \frac{\cos(10x_1) + 1}{4}, \; h_2 = \frac{\sin(10x_1) + 1}{4}, \; h_3 = -\frac{\sin(10x_1) + \cos(10x_1)}{4} + \frac{1}{2},$$

these functions has been taken from [152] and the time evolution of the system with the Lyapunov function obtained is shown in Fig. 4.4(a) and Fig. 4.4(b), respectively.

4.1.4 Convex Proportional-Integral Control Design

We want to use the nonlinear time-discrete model obtained in (2.2) for tracking a reference signal $r(t)$ and to do so first we can filter the reference as

$$x_r(t+1) = A_r x_r(t) + (1 - A_r) r(t) \tag{4.23}$$

where $A_r = 0.05$ is an asymptotically stable matrix and $x_r(t)$ the reference signal filtered. Let us define the tracking error $e(t)$ using this filtered reference signal and the integral

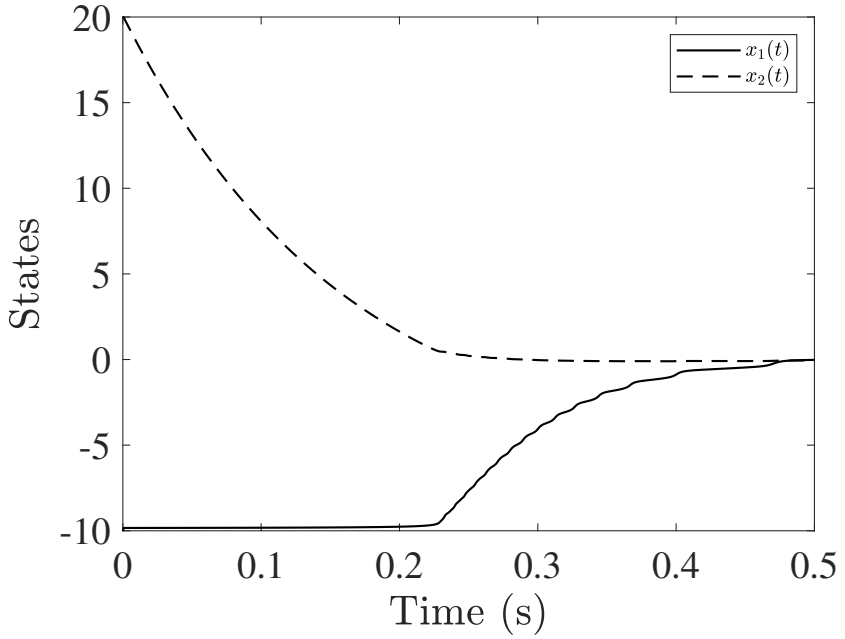

(a) States of the system.

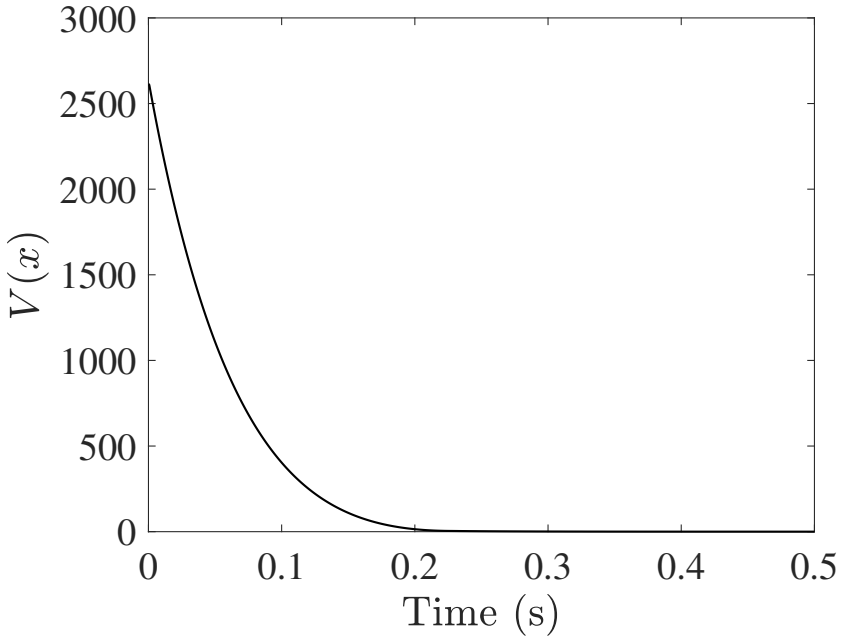

(b) Time evolution of the Lyapunov function.

FIGURE 4.4: Time evolution of the system in closed-loop.

of the tracking error $e_i(t)$ as

$$e(t+1) = \phi(t+1) - x_r(t+1), \tag{4.24}$$

$$e_i(t+1) = e_i(t) + T_s\left(\phi(t) - x_r(t)\right), \tag{4.25}$$

where $T_s = 0.01$ is the sampling time of 10 milliseconds; using the relations $\Delta_1 = \frac{r(t)}{x_r(t)}$ and $\Delta_2 = \frac{x_r(t)}{\phi(t)}$ the latter expressions along with (2.2) and (4.23) can be gathered in a matrix representation of the error which gives

$$\begin{bmatrix} e(t+1) \\ e_i(t+1) \end{bmatrix} = \begin{bmatrix} \Delta_1 & 0 \\ T_s & 1 \end{bmatrix} \begin{bmatrix} e(t) \\ e_i(t) \end{bmatrix} + \begin{bmatrix} b_0 + b_1\phi(t) \\ 0 \end{bmatrix} u(t) + \begin{bmatrix} (1-\Delta_1)(1-A_r\Delta_2)\phi(t) \\ 0 \end{bmatrix},$$

$$x(t+1) = A(\Delta_1)x(t) + B(\phi)u(t) + \xi(\phi, \Delta_1, \Delta_2),$$

with $x(t) = \begin{bmatrix} e(t) & e_i(t) \end{bmatrix}^T$, where $\xi(\phi, \Delta_1, \Delta_2)$ can be seen as a disturbance, notice that if $\Delta_1 = \frac{r(t)}{x_r(t)} = 1$ then it banishes (i.e., $\xi(\phi, \Delta_1, \Delta_2) = 0$), we will focus on designing a controller only for this case, it leads to the error system

$$x(t+1) = Ax(t) + B(\phi)u(t). \tag{4.26}$$

Notice that the error system contain a non-constant term but, it can be *exactly* rewritten as the convex sum of constant terms within our compact of interest defined as $\Omega = (\phi \in \{1.27, 2.52\})$ by means of the nonlinear sector methodology [137].

Convex modeling of the error system

The nonlinear sector methodology indicates the following 3 steps for obtaining a convex model from systems like the one presented in (4.8) :

1. Identify and indicate the p non-constant terms in the system and gather them in $z_i(x)$ with $i \in \{1, 2, \cdots, p\}$. Their maximum and minimum value within the compact of interest Ω will be denoted as z_i^1 and z_i^0, respectively. Therefore, the non-constant term in our system (4.8) is $z_1(\phi) = \phi(t) \in [\phi_{\min}, \phi_{\max}]$.

2. Using this values we can define the interpolation functions, also named membership functions as

$$h_1(\phi) = \frac{\phi_{\max} - \phi}{\phi_{\max} - \phi_{\min}}, \quad h_2(\phi) = 1 - h_1(\phi).$$

   Notice that these membership functions hold the convex sum property, this means that $0 \leq h_i \leq 1$ with $i \in \{1, 2\}$ for $x \in \Omega$ and also $h_1 + h_2 = 1$ for all x. Therefore,

each non-constant term can be expressed as the convex sum of two constant values $z(x) = h_1 z^0 + h_2 z^1$.

3. The algebraically equivalent convex representation of the system (4.8) is

$$\begin{aligned} x(t+1) &= \sum_{i=1}^{r} h_i \left(Ax(t) + B_i u(t) \right), \\ &= Ax(t) + B_h u(t), \end{aligned} \tag{4.27}$$

where the constant terms are $B_i = B(\phi)|_{h_i=1}$ with $i \in \{1, 2, \cdots, r\}$ and $r = 2^p = 2$. It is important to recall that this is not an approximation, but the convex property holds only within the compact Ω.

The constant matrices obtained from applying the nonlinear sector to the error system (4.26) are $A = \begin{bmatrix} 1 & 0 \\ 0.01 & 1 \end{bmatrix}$, $B_1 = \begin{bmatrix} -0.0013 \\ 0 \end{bmatrix}$ and $B_2 = 10^{-3} \times \begin{bmatrix} -0.6651 \\ 0 \end{bmatrix}$.

Developments thereafter will be based on the exact convex representation (4.27).

Conditions for Parallel Distributed Compensation with Decay Rate

First, notice that we have written the system to control it in terms of the error (4.24) and the candidate Lyapunov function proposed will be for this error system; recall that if there is a Lyapunov function associated to a system $V(x(t))$ then $x \to 0$ as $t \to \infty$; this is important because, using the same principle we want the $e(t) \to 0$ and $e_i(t) \to 0$ as $t \to \infty$ when tracking our reference $r(t)$.

Consider a parallel compensated distribution (PDC) control law with an integral action of the following form

$$u(t) = \sum_{j=1}^{r} h_j F_j \begin{bmatrix} e(t) & e_i(t) \end{bmatrix}^T = F_h x(t), \tag{4.28}$$

substituting the latter expression in (4.26) yields to

$$\begin{aligned} x(t+1) &= \sum_{i=1}^{r} \sum_{j=1}^{r} h_i h_j \left((A + B_i F_j) x(t) \right), \\ &= (A + B_h F_h) x(t). \end{aligned} \tag{4.29}$$

The controller will be designed by using Lyapunov's direct method, it consists on providing a Lyapunov function that proves stability for the closed-loop system and we can find this function by solving a set of LMI, the conditions that a function needs to satisfy such as $V(x(t)) > 0$ and $\Delta V(x(t)) < 0$ to be a valid Lyapunov function will be expressed in terms of linear matrix inequalities. This begins with proposing a candidate quadratic Lyapunov function of the form

$$V(x(t)) = x^T(t)Px(t),$$

it is positive definite if $P > 0$ and we can impose a decay rate α on its time derivative by considering

$$\Delta V(x(t)) = x^T(t+1)Px(t+1) - \alpha^2 x^T(t)Px(t),$$

substituting the expression for the closed-loop system in (4.29) gives

$$x(t)^T(A+B_hF_h)^TP(A+B_hF_h)x(t) - \alpha^2 x(t)^TPx(t),$$

this time derivative is negative definite if

$$(A+B_hF_h)^TP(A+B_hF_h) - \alpha^2 P < 0,$$

defining the new variable $X = P^{-1}$ and then pre- and post-multiplying the expression by X we can rewrite it as

$$X(A+B_hF_h)^TX^{-1}(A+B_hF_h)X - \alpha^2 X < 0,$$

substituting $M_h = F_hX$ as a new variable in the latter expression and dividing it by α^2 gives

$$X - (AX+B_hM_h)^T\frac{X^{-1}}{\alpha^2}(AX+B_hM_h) > 0,$$

applying Schur's complement it is possible to transform this nonlinear inequality to a linear one

$$\Upsilon_{hh} = \begin{bmatrix} X & XA^T + M_h^TB_h^T \\ AX + B_hM_h & \alpha^2 X \end{bmatrix} > 0,$$

then, by taking into account the convex sum property (i.e., $0 \leq h_i \leq 1$) in the membership functions we can remove them from the expression without changing the sign of the

inequality. Using Tuan's relaxation [144] which takes advantage of the double convex sum (i.e., $h_i = h_j$ for $i = j$) , then the expression $\Upsilon_{hh} > 0$ holds if we can can satisfy

$$\frac{2}{r-1}\Upsilon_{ii} + \Upsilon_{ij} + \Upsilon_{ji} > 0.$$

Finally, the error system (4.26) can be driven asymptotically to zero via a PDC control law of the form (4.28) with decay rate α^2 if there exists matrices $X > 0$, M_j for all $(i, j) \in \{1, 2, \cdots, r\}$ such that $\frac{2}{r-1}\Upsilon_{ii} + \Upsilon_{ij} + \Upsilon_{ji} > 0$ holds with

$$\Upsilon_{ij} = \begin{bmatrix} X & XA^T + M_j^T B_i^T \\ AX + B_i M_j & \alpha^2 X \end{bmatrix}, \tag{4.30}$$

where the gains of the nonlinear controller can be computed as $F_j = M_j X^{-1}$; this concludes the controller design process. Recall that more performance parameters can be included in the design by including more proper LMI conditions.

Simulation and Real-Time Results

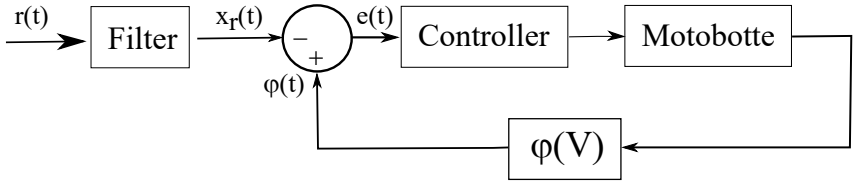

FIGURE 4.5: Scheme used for simulation and real-time implementation.

The scheme of the closed-loop system that will be used for simulation and real-time implementation purposes is shown in Fig. 4.5, every block shown has been explained in the previous sections. Now, we are interested in following a piece-wise reference $r(t)$ defined as

$$r(t) = \begin{cases} 1.4 & t < 1, \\ 1.4 + \frac{(2.4-1.4)}{(2.4323-1)}(t-1) & 1 \leq t \leq 2.4323, \\ 2.4 & t \geq 2.4323. \end{cases}$$

For the LMI conditions in (4.30) and constant matrices in 4.1.4 a solution was found with

$$F_1 = \begin{bmatrix} 124.7902 & 471.4880 \end{bmatrix}, F_2 = \begin{bmatrix} 133.7383 & 504.7693 \end{bmatrix}$$
$$X = \begin{bmatrix} 1.7519 & -0.2794 \\ -0.2794 & 0.0711 \end{bmatrix}$$

with a decay rate $\alpha^2 = 0.93657$.

Simulation results are exhibited in Fig. 4.6, the behavior of the output and reference is shown in Fig. 4.6(a) and Fig. 4.6(b) shows the time evolution of the input signal obtained with the control law designed. The real-time implementation results of this control scheme are shown in Fig. 4.7.

4.1.5 Convex Proportional-Integral-Derivative Control Design

Now, let us define the filtered reference signal as

$$r_f(t+1) = Ar_f(t) + (1-A)r(t),$$

with $|A| < 1$, $r(t)$ is the reference, the error between the output of the system and the filtered reference signal is defined as

$$e(t+1) = \phi(t+1) - r_f(t+1),$$

where the integral and first time derivative of this signal are

$$e_i(t+1) = e_i(t) + T_s e(t),$$
$$e_d(t+1) = \frac{e(t+1)}{T_s} - \frac{e(t)}{T_s},$$

defining the variables $\Delta_1 = \frac{r}{r_f}$ and $\Delta_2 = \frac{r_f}{\phi}$ it is possible to gather those expressions as

$$Ex(t+1) = A(\Delta_1)x(t) + B(\phi)u(t) + \xi(\Delta_1, \Delta_2, \phi),$$

selecting the state vector as $x(t) = \begin{bmatrix} e(t) & e_i(t) & e_d(t) \end{bmatrix}^T$. Let us recall that if $r_f = r$, then $\Delta_1 = 1$ and $\xi(\cdot) = 0$, we will design a controller for this. As there exists E^{-1}, our

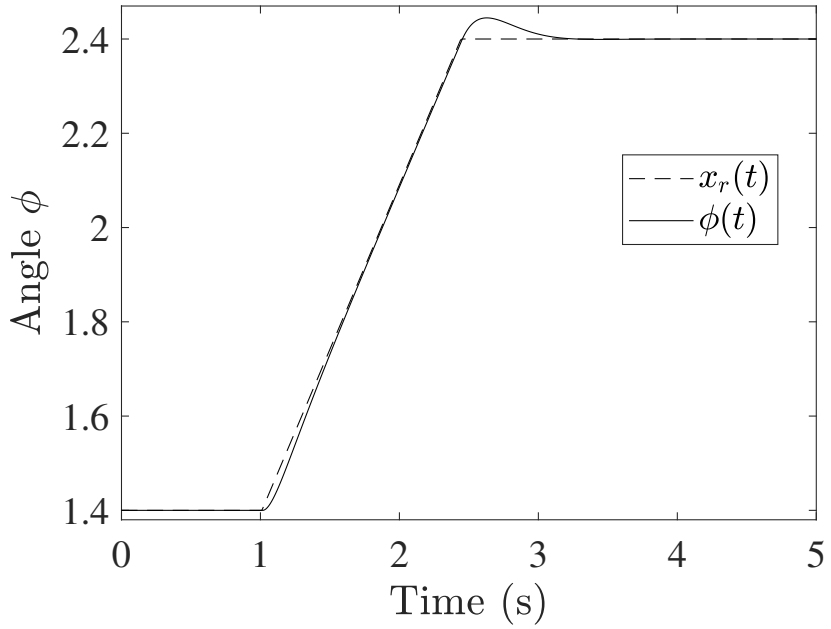

(a) Filtered reference $x_r(t)$ and output angle $\phi(t)$.

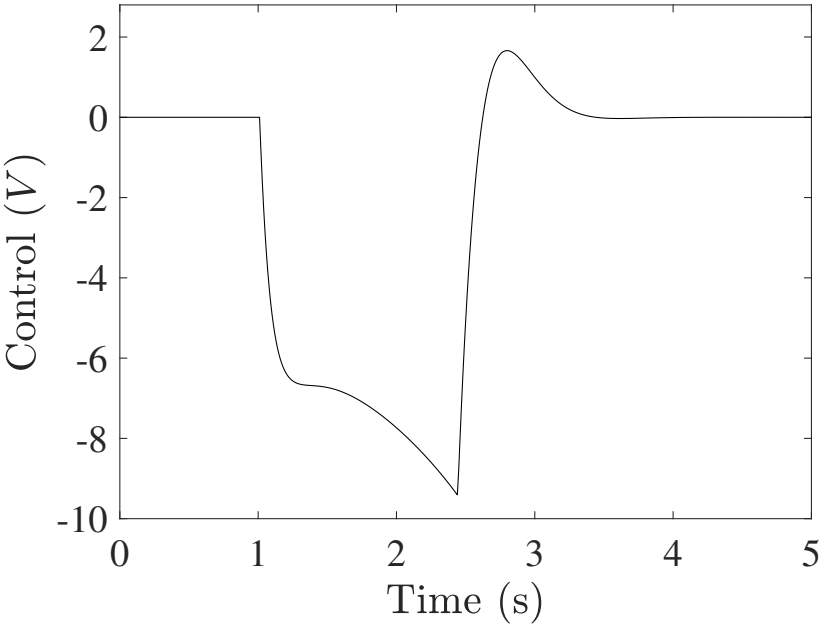

(b) Control signal $u(t) = F_h x(t)$.

FIGURE 4.6: Time evolution of the system in simulation.

error system can be expressed as

$$x\left(t+1\right) = \bar{A}x\left(t\right) + \bar{B}\left(\phi\right)u\left(t\right),$$

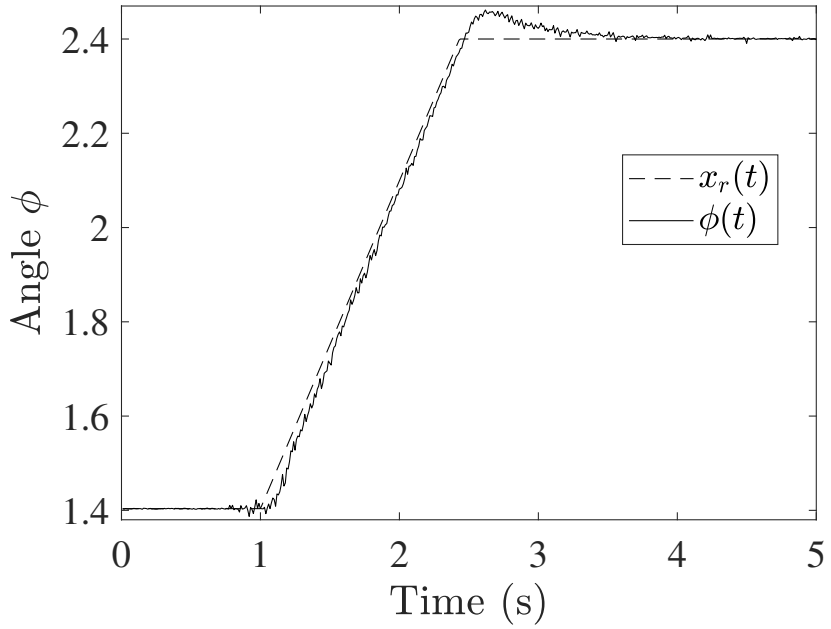

(a) Filtered reference $x_r(t)$ and output angle $\phi(t)$.

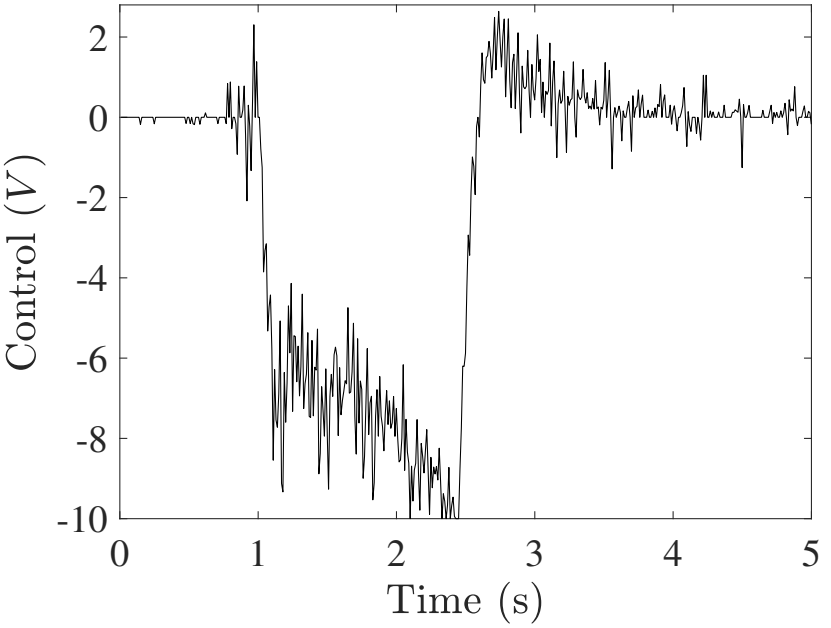

(b) Time evolution of the control signal $u(t) = F_h x(t)$.

FIGURE 4.7: Evolution of the system in real-time.

with $E = \begin{bmatrix} 1 & 0 & 0 \\ 0 & 1 & 0 \\ -1 & 0 & T_s \end{bmatrix}$, $A = \begin{bmatrix} 1 & 0 & 0 \\ T_s & 1 & 0 \\ -1 & 0 & 0 \end{bmatrix}$, and a non constant matrix $B = \begin{bmatrix} b_0 + b_1\phi(t) \\ 0 \\ 0 \end{bmatrix}$, $\bar{A} = E^{-1}A$ and $\bar{B}(\phi) = E^{-1}B$. The nonconstant term $\phi(t)$ can be rewritten by means

of the nonlinear sector approach [137], it is bounded by $\phi \in [1.273, 2.5212]$. Define the interpolation functions as $h_1 = \frac{\phi_{\max}-\phi(t)}{\phi_{\max}-\phi_{\min}}$ and $h_2 = \frac{\phi(t)-\phi_{\min}}{\phi_{\max}-\phi_{\min}}$, the convex system obtained from this modeling process is

$$x(t+1) = \sum_{i=1}^{2} h_i \left(\bar{A}x(t) + \bar{B}_i u(t)\right),$$

with $\bar{B}_i = \bar{B}(\phi)|_{h_i=1}$ constant terms $\bar{B}_1 = \begin{bmatrix} -0.0013 \\ 0 \\ -0.1340 \end{bmatrix}$ and $\bar{B}_2 = \begin{bmatrix} -0.0007 \\ 0 \\ -0.0665 \end{bmatrix}$.

Lemma 4.13 (Output disturbance attenuation [153])**.** *For control design with disturbance attenuation consider a disturbance $w(t)$ measured in the output $y(t) = Cx(t) + Dw(t)$. The origin of the system is asymptotically stable with a PDC control law $u(t) = \sum_{j=1}^{2} F_j x(t) = F_h x(t)$, decay rate α^2 and γ is minimized subject to $\|\frac{y(t)}{w(t)}\| \leq \gamma$ if there are matrices $X > 0$, $\gamma > 0$, M_j for $(i,j) \in \{1,2\}$, where $F_i = M_i X^{-1}$ and $2\Upsilon_{ii} + \Upsilon_{ij} + \Upsilon_{ji} < 0$ [144] holds with :*

$$\Upsilon_{ij} = \begin{bmatrix} -\alpha^2 X & XC^T D & XA_i^T + M_j^T B_i^T & XC^T \\ D^T CX & D^T D - \gamma^2 I & 0 & 0 \\ A_i X + B_i M_j & 0 & -X & 0 \\ CX & 0 & 0 & -I \end{bmatrix}. \tag{4.31}$$

Simulation and Real-Time Results The output and disturbance matrices are $C = I_3$ and $D = 0.1 \times \begin{bmatrix} 1 & 0.01 & 100 \end{bmatrix}^T$, we want a decay rate of $\alpha^2 = 0.935$. A solution was found for the LMIs in lemma 4.13 with $\gamma = 10.0241$, $F_1 = \begin{bmatrix} 146.7459 & 578.6829 & 0.1757 \end{bmatrix}$ and $F_2 = \begin{bmatrix} 285.8307 & 1127.1404 & 0.3419 \end{bmatrix}$. The closed-loop response is shown in Fig. 4.8(a), where the dashed line is the filtered reference, the solid black line is the output angle in simulation, the blue line is the real-time output angle and the red line is the real-time output angle where the disturbance is a leg pushing in an opposite direction to r_f. The control signal used for each case is illustrated in Fig. 4.8(b).

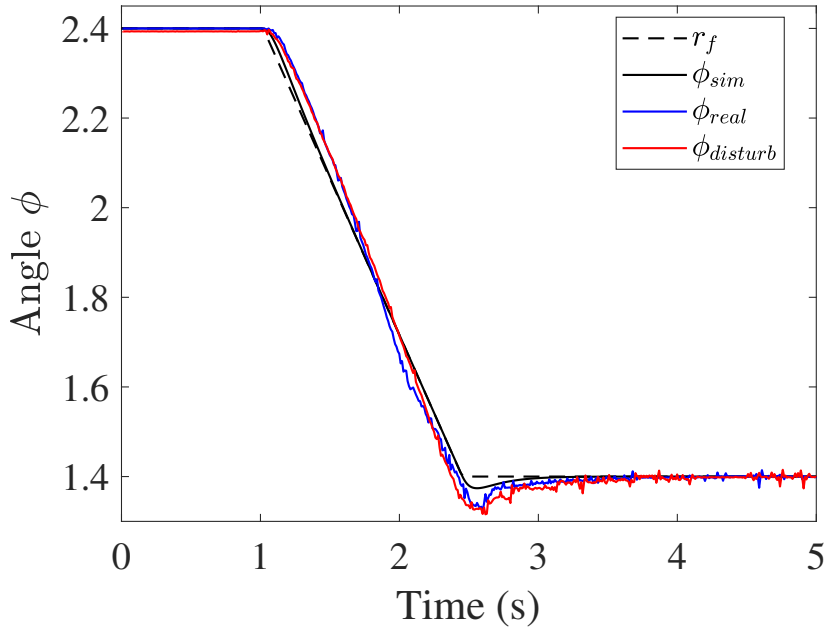

(a) Simulation and real-time response.

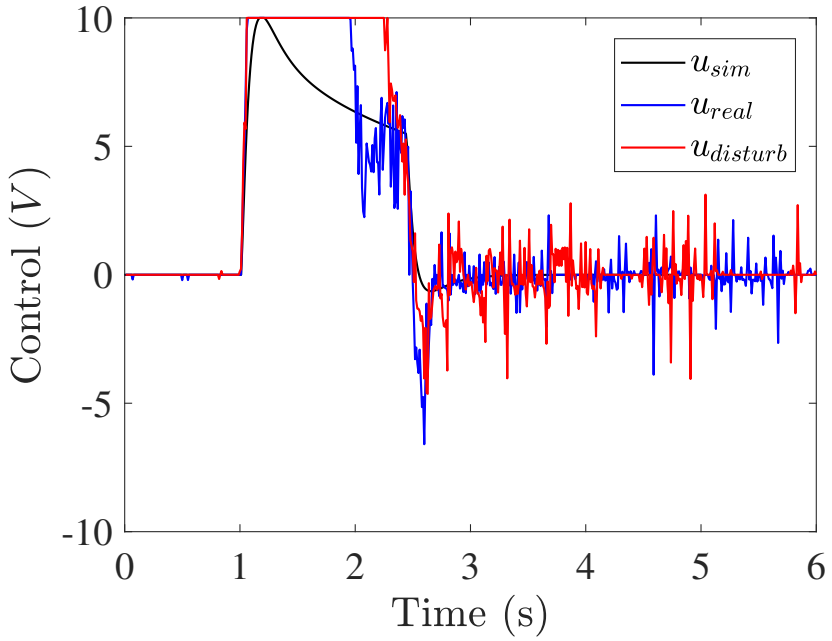

(b) Simulation and real-time control.

FIGURE 4.8: Control and time-evolution of the system.

4.2 Exact Convex Representations for Singular Systems

A common way to express singular systems is the singular descriptor form, in order to illustrate some phenomena that occurs in the modeling of these systems consider a

nonlinear singular system of the form

$$E(x)\dot{x} = A(x)x + B(x)u, \tag{4.32}$$

where $x \in \mathbb{R}^n$ is the state vector, $u \in \mathbb{R}^m$ is the input signal and $\text{rank}(E(x)) < n$. First, the system (4.32) can be expressed in the algebraically equivalent descriptor redundancy form by using the extended state vector $\bar{x} = \begin{bmatrix} x & \dot{x} \end{bmatrix}^T$:

$$\bar{E}\dot{\bar{x}} = \bar{A}(x)\bar{x} + \bar{B}(x)u, \tag{4.33}$$

with $\bar{E} = \begin{bmatrix} I & 0 \\ 0 & 0 \end{bmatrix}$, $\bar{A}(x) = \begin{bmatrix} 0 & I \\ A(x) & -E(x) \end{bmatrix}$ and $\bar{B}_h = \begin{bmatrix} 0 \\ B(x) \end{bmatrix}$.

Following the well-known nonlinear sector methodology [137] we can rewrite (4.33) as an exact convex representation. This methodology consists on rewriting each of the ρ non constant terms in $E(x)$, $A(x)$ and $B(x)$ inside an operating region denoted as Ω. The rewriting process is done by using interpolation or membership functions (MFs). The MFs are composed by permutations of weight functions (w_i^0, w_i^1), each of the ρ non constant terms (z_i) can be expressed as the convex sum of its extreme values :

$$z_i = \underbrace{\left(\frac{z_i^1 - z_i}{z_i^1 - z_i^0}\right)}_{w_i^0} z_i^0 + \underbrace{\left(\frac{z_i - z_i^0}{z_i^1 - z_i^0}\right)}_{w_i^1} z_i^1, \tag{4.34}$$

the maximum and minimum are denoted z_i^1 and z_i^0, respectively. These weight functions hold the convex sum properties

$$0 \leq w_i^j \leq 1, \quad w_i^0 + w_i^1 = 1,$$

with $i \in \{1, 2, \cdots, \rho\}$ and $j \in \{0, 1\}$, the MFs are defined with permutations of the weight functions $h_i = w_1^{j_1} w_2^{j_2} \cdots w_\rho^{j_\rho}$, here $[j_1, j_2, \cdots, j_\rho]$ is a binary count for $(i-1)$ where $i \in \{1, 2, \cdots, r\}$, $r = 2^\rho$. The convex representation for our system written in the descriptor redundancy form is

$$\bar{E}\dot{\bar{x}} = \bar{A}_h\bar{x} + \bar{B}_h u, \quad \bar{A}_h = \sum_{i=1}^{r} h_i \bar{A}_i, \quad \bar{B}_h = \sum_{i=1}^{r} h_i \bar{B}_i, \tag{4.35}$$

where $\bar{A}_i = \begin{bmatrix} 0 & I \\ A_i & -E_i \end{bmatrix}$, $\bar{B}_i = \begin{bmatrix} 0 \\ B_i \end{bmatrix}$, E_i, A_i and B_i are constant terms that can be obtained by evaluating the membership functions

$$A_i = A(x)|_{h_i=1}, E_i = E(x)|_{h_i=1}, \quad B_i = B(x)|_{h_i=1}.$$

Developments thereafter will be based on a singular system expressed in a descriptor redundancy form and rewritten in an exact convex representation as (4.35).

Lemma 4.14 (Classical descriptor)**.** *[154] The nonlinear descriptor system (4.32) is asymptotically stable with a control law of the form* $u = \sum_{j=1}^{r} h_j F_j x$*, if there are matrices* $X_{11} > 0$*,* X_1*,* X_3*,* X_4 *and* M_j*, such that*

$$Q_{ii} < 0,$$
$$\frac{2}{r-1} Q_{ii} + Q_{ij} + Q_{ji} < 0,$$

holds with

$$Q_{ij} = \begin{bmatrix} X_3 + X_3^T & (*) \\ A_i X_1 + B_i M_j - E_i X_3 + X_4^T & -E_i X_4 - X_4^T E_i^T \end{bmatrix},$$

where $F_j = M_j X_1^{-1}$ *with* $i, j \in \{1, 2, \ldots, r\}$.

Now, let us recall that the motoBOTTE in Fig. 2.1 is a five-bars closed-loop mechanism actuated by a linear piston, the variable distance of this piston is denoted by $d \in [0, 0.103]$ in meters, the fixed length of the bars is denoted by l_1, l_2, l_3, l_4 and l_5; γ_1 and γ_2 are fixed inner angles of the robot, the masses of the links are denoted by m_1, m_2 and m_3. The dynamics of the actuator d can be described by

$$\dot{d} = b_1 u, \tag{4.36}$$

with respect to the control input, there is an input constraint at $u \in [-10V, 10V]$, the angle variables Θ_1 and Θ_2 are passive. Due to the closed-loop nature of the system it has constraints on its position, this produce loss in the degrees-of-freedom. The constraints

in the position variables (d, Θ_1 and Θ_2) are :

$$\begin{aligned} d+l_1+l_2\sin\Theta_1 - l_3\cos\Theta_1+l_4\sin\Theta_2+l_5\sin\Theta_3=0,\\ l_2\cos\Theta_1 + l_3\sin\Theta_1 + l_4\cos\Theta_2 + l_5\cos\Theta_3 = 0,\\ \Theta_1 - \Theta_2 + \pi/2 - \gamma = \phi, \end{aligned} \tag{4.37}$$

where the first two expressions can be obtained as displacements over $x-$ and $y-$axis, respectively [66]. The value for each parameter in the motoBOTTE are given in Table 4.1.

The algebraic constraints in the position (4.37) also impose constraints on the speed of the variables, these constraints can be explicitly obtained by computing the corresponding time derivatives :

$$\begin{aligned} \dot{d} + (l_2\cos\Theta_1 + l_3\sin\Theta_1)\,\dot{\Theta}_1 + l_4\cos\Theta_2\dot{\Theta}_2 = 0,\\ (l_3\cos\Theta_1 - l_2\sin\Theta_1)\,\dot{\Theta}_1 - l_4\sin\Theta_2\dot{\Theta}_2 = 0,\\ \dot{\Theta}_1 - \dot{\Theta}_2 = \dot{\phi}. \end{aligned} \tag{4.38}$$

Selecting the state vector as $x = \begin{bmatrix} d & \Theta_1 & \Theta_2 \end{bmatrix}^T$ yields to the following descriptor form

$$\underbrace{\begin{bmatrix} 1 & 0 & 0 \\ 1 & z_1 & z_2 \\ 0 & z_3 & z_4 \end{bmatrix}}_{E(x)} \begin{bmatrix} \dot{x}_1 \\ \dot{x}_2 \\ \dot{x}_3 \end{bmatrix} = \underbrace{\begin{bmatrix} 0 & 0 & 0 \\ 0 & 0 & 0 \\ 0 & 0 & 0 \end{bmatrix}}_{A} \begin{bmatrix} x_1 \\ x_2 \\ x_3 \end{bmatrix} + \underbrace{\begin{bmatrix} b_1 \\ 0 \\ 0 \end{bmatrix}}_{B} u, \tag{4.39}$$

where the non constant terms are $z_1 = l_2\cos x_2 + l_3\sin x_2$, $z_2 = l_4\cos x_3$, $z_3 = l_3\cos x_2 - l_2\sin x_2$ and $z_4 = -l_4\sin x_3$.

TABLE 4.1: Parameters considered in this model.

Parameter	**Value**
l_1	0.35 m
l_2	0.125 m
l_3	0.445 m
l_4	0.1014 m
l_5	0.15 m
b_1	0.00745
Θ_3	2.4086 rad
γ	2.0952 rad

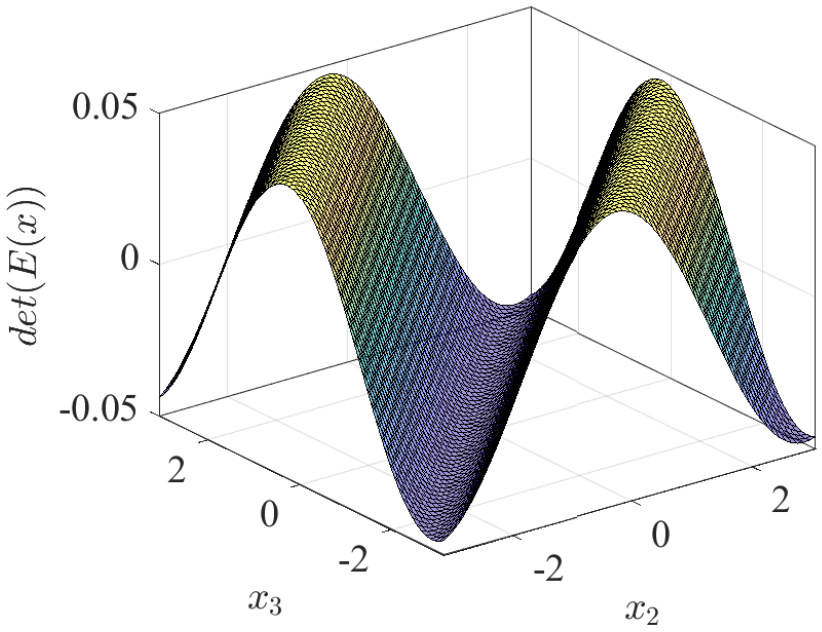

(a) Determinant of $E(x)$ in the region Ω_1.

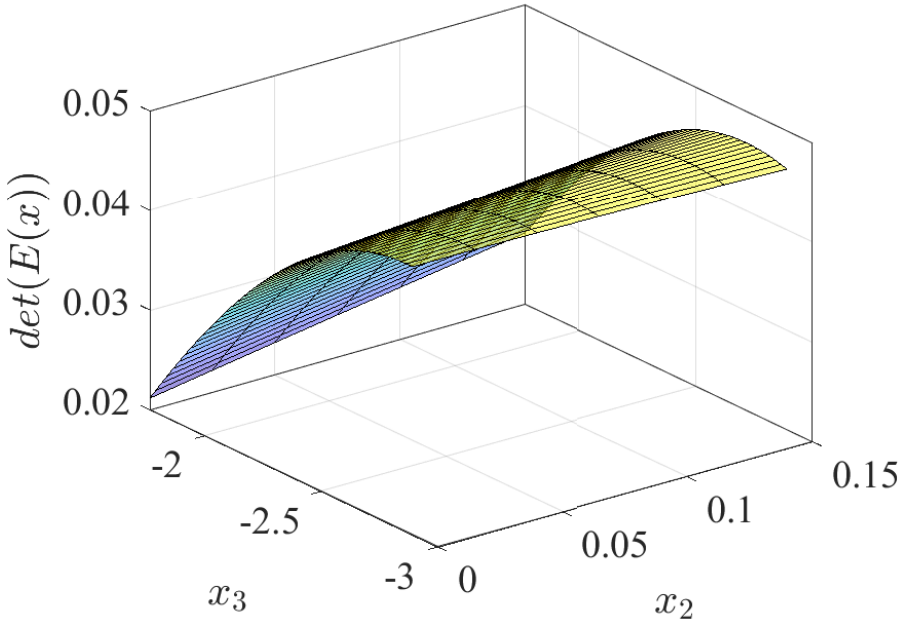

(b) Determinant of $E(x)$ in the region Ω_2.

FIGURE 4.9: Graphical comparison of both regions.

If we consider our region as $\Omega_1 = \{x_2, x_3 \in [-\pi, \pi]\}$ for convex modeling (i.e., ignoring the algebraic constraints), then, as it is illustrated in Fig. 4.9(a) that $\nexists E^{-1}(x)$ for some values of x in Ω_1 since $\det(E(x)) = 0$.

The constraints (4.37) have unique solution for the ankle angle values $\phi \in [1.273, 2.5212]$

TABLE 4.2: Maximum and minimum values for z_i in Ω_2.

Parameter	z_i^1	z_i^0
z_1	0.20015	0.12500
z_2	−0.01953	−0.09822
z_3	0.44499	0.41664
z_4	0.09950	0.02520

as indicated in [63], which corresponds to $\Omega_2 = \{x_2 \in [0, 0.174]\,, x_3 \in [-2.8904, -1.76465]\}$, the determinant of $E(x)$ inside the region Ω_2 is illustrated in Fig. 4.9(b), notice that the determinant is not crossing zero as before and therefore $\exists E^{-1}(x)\ \forall x \in \Omega_2$, this region Ω_2 will be used for convex modeling. The maximum and minimum values obtained for the non constant terms in the region Ω_2 are given in Table 4.2, when the nonlinear sector methodology is applied yields to the form $\sum_{i=1}^{16} h_i E_i \dot{x} = Ax + Bu$.

4.3 LMI-Based Conditions for Control of DAEs

Consider a set of DAEs whose index has been reduced by applying the Pantelides algorithm, then, modeled via the nonlinear sector methodology as (4.35) under a parallel distributed compensation control law as

$$u = \sum_{j=1}^{r} h_j F_j x = \sum_{j=1}^{r} h_j \underbrace{\begin{bmatrix} F_j & 0 \end{bmatrix}}_{\bar{F}_j} \begin{bmatrix} x \\ \dot{x} \end{bmatrix} = \bar{F}_h \bar{x}, \tag{4.40}$$

where h_j are the membership functions of the system obtained during the convex rewriting process, this yields to a closed-loop system with a double-sum in the MFs

$$\bar{E}\dot{\bar{x}} = \tilde{A}_{hh}\bar{x} = \sum_{i=1}^{r}\sum_{j=1}^{r} h_i h_j \left(\bar{A}_i + \bar{B}_i \bar{F}_j\right) \bar{x}, \tag{4.41}$$

where $\bar{E} = \begin{bmatrix} I & 0 \\ 0 & 0 \end{bmatrix}$, $\bar{A}_i = \begin{bmatrix} 0 & I \\ A_i & -E_i \end{bmatrix}$ and $\bar{B}_i = \begin{bmatrix} 0 \\ B_i \end{bmatrix}$,

Theorem 4.15. *The origin $x = 0$ of the descriptor system (4.32), is asymptotically stable under a PDC control law of the form (4.40), with given gains F_j where $j =$*

$\{1, 2, \ldots, r\}$, *if the LMIs :*

$$\bar{E}^T P = P^T E \geq 0,$$
$$Q_{ii} \leq 0,$$
$$\frac{2}{r-1} Q_{ii} + Q_{ij} + Q_{ji} \leq 0,$$

hold with $Q_{ij} = P^T \bar{A}_{ij} + \bar{A}_{ij}^T P$ *and nontrivial* P, $rank(\bar{E}^T P) = n$ *and* $i, j \in \{1, 2, \cdots, r\}$, *when* E *is not singular the LMIs involving* Q_{ij} *are strict.*

Proof. Consider a generalized candidate Lyapunov function

$$V(x) = \bar{x}^T \bar{E}^T P \bar{x} : \bar{E}^T P = P^T \bar{E} \geq 0, \tag{4.42}$$

where $P = \begin{bmatrix} P_{11} & 0 \\ P_{21} & P_{21} \end{bmatrix}$, due to symmetry, then, taking into account that $V(x)$ reduces to $V(x) = x^T P_{11} x$, it will be positive definite if $P_{11} > 0$, its time derivative is equal to

$$\dot{V}(x) = \bar{x}^T \bar{E}^T P \dot{\bar{x}} + \dot{\bar{x}}^T \bar{E}^T P \bar{x},$$

applying the symmetric property (4.42) and substituting (4.41)

$$\dot{V}(x) = \bar{x}^T P^T \bar{E} \dot{\bar{x}} + \dot{\bar{x}}^T \bar{E}^T P \bar{x} = \bar{x}^T \left(P^T \bar{A}_{hh} + \bar{A}_{hh}^T P \right) \bar{x},$$

is negative if Lemma 4.2 holds with $Q_{ij} = P^T \bar{A}_{ij} + \bar{A}_{ij}^T P$, which concludes the proof. □

Theorem 4.16. *The origin* $x = 0$ *of the descriptor system* (4.32) *is assymptotically stable under a PDC control law of the form* (4.40), *with given gains* F_j *where* $j = \{1, 2, \ldots, r\}$, *if there exists* $P = P^T$, Z_{1i}, Z_{2i}, $\epsilon_i \geq 0$, *with* $i = 1, 2$ *such that the following LMIs hold*

$$Q_{ii}^1 > 0, \quad Q_{ii}^2 < 0,$$
$$\frac{2}{r-1} Q_{ii}^1 + Q_{ij}^1 + Q_{ji}^1 > 0,$$
$$\frac{2}{r-1} Q_{ii}^2 + Q_{ij}^2 + Q_{ji}^2 < 0,$$

with

$$Q_{ij}^1 = \begin{bmatrix} Z_{11}A_i + Z_{11}B_iF_j + (*) + P - \epsilon_1 I & (*) \\ Z_{12}A_i + Z_{12}B_iF_j - E_i^T Z_{11}^T & -Z_{12}E_i + (*) \end{bmatrix},$$
$$Q_{ij}^2 = \begin{bmatrix} Z_{21}A_i + Z_{21}B_iF_j + (*) + \epsilon_2 I & (*) \\ P - E_i^T Z_{21}^T + Z_{22}A_i + Z_{22}B_iF_j & -Z_{22}E_i + (*) \end{bmatrix}.$$

Proof. Consider the following candidate Lyapunov function

$$V(x) = \begin{bmatrix} x \\ \dot{x} \end{bmatrix}^T \begin{bmatrix} P - \epsilon_1 I & 0 \\ 0 & 0 \end{bmatrix} \begin{bmatrix} x \\ \dot{x} \end{bmatrix} \geq 0,$$

subject to the algebraic constraint

$$\begin{bmatrix} A_h + B_hF_h & -E_h \end{bmatrix} \begin{bmatrix} x \\ \dot{x} \end{bmatrix} = 0, \tag{4.43}$$

by Lemma 4.6 (Finsler's) it will be positive definite if there exists matrices such that

$$\begin{bmatrix} P - \epsilon_1 I & 0 \\ 0 & 0 \end{bmatrix} + \begin{bmatrix} Z_{11} \\ Z_{12} \end{bmatrix} \begin{bmatrix} A_h + B_hF_h & -E_h \end{bmatrix} + (*) > 0,$$

selecting Q_{ij}^1 as indicated in Theorem 4.16 and combined with Lemma 4.6, this concludes the demonstration for $V(x) = x^T Px > \epsilon_1 x^T x$ for all $x \neq 0$ subject to (4.43). Now, the time derivative of the candidate function is

$$\dot{V}(x) = \begin{bmatrix} x \\ \dot{x} \end{bmatrix}^T \begin{bmatrix} \epsilon_2 I & P \\ P & 0 \end{bmatrix} \begin{bmatrix} x \\ \dot{x} \end{bmatrix} \leq 0,$$

by Lemma 4.6 (Finsler's) it is negative $\forall \begin{bmatrix} x^T & \dot{x}^T \end{bmatrix}^T \neq 0$ such that (4.43) holds if

$$\begin{bmatrix} \epsilon_2 I & P \\ P & 0 \end{bmatrix} + \begin{bmatrix} Z_{21} \\ Z_{22} \end{bmatrix} \begin{bmatrix} A_h + B_hF_h & -E_h \end{bmatrix} + (*) < 0,$$

it is satisfied by applying Lemma 4.2 with Q_{ij}^2 selected as indicated by the Theorem; this conduces to $\dot{V}(x) \leq -\epsilon_2 x^T x < 0$, for all $\begin{bmatrix} x^T & \dot{x}^T \end{bmatrix}^T \neq 0$ subject to (4.43). □

Example 4.2. *Consider the exact convex representation of the motoBOTTE and employ Theorem 4.16 to design a controller for stabilizing the system in a desired set point, which is assumed to be consistent and will be denoted as x_d. Now, consider an error feedback of the form $u = -Ke$, with gain $K = \begin{bmatrix} 20 & 30 & 40 \end{bmatrix}$, the error signal is defined as $e = x - x_d$, using the LMI conditions in Theorem 4.16 with the LMI Toolbox we are able to find the following solution, for $\epsilon_1 = \epsilon_2 = 0$:*

$$P = \begin{bmatrix} 0.3448 & 0.4984 & 0.2939 \\ 0.4984 & 0.6736 & 0.4261 \\ 0.2939 & 0.4261 & 0.1741 \end{bmatrix},$$

$$Z_{11} = \begin{bmatrix} 2.3701 & -2.2865 & 0.7625 \\ 3.2047 & -3.0827 & 1.0232 \\ 2.2091 & -2.1574 & 0.7335 \end{bmatrix},$$

$$Z_{12} = \begin{bmatrix} -1.1042 & 0.5952 & -0.1985 \\ 0.6810 & -0.6942 & -0.9057 \\ -3.4018 & 3.4679 & -1.3964 \end{bmatrix},$$

$$Z_{21} = \begin{bmatrix} -0.1053 & 0.4069 & 1.0251 \\ -0.1719 & 0.6056 & 1.3677 \\ -0.0155 & 0.2870 & 0.8913 \end{bmatrix},$$

$$Z_{22} = \begin{bmatrix} 0.6171 & -0.1087 & -0.2624 \\ -0.2549 & 0.3881 & 1.0225 \\ 3.9496 & -3.9503 & 1.4949 \end{bmatrix}.$$

Recall that for Theorem 4.16 P is not required to be positive definite, only symmetric, in this case the eigenvalues of P are $\sigma(P) = \{-0.0707, -0.0136, 1.2769\}$. Also for the same reason, since P is not definite positive this solution is out of the scope of Lemma 4.14, in which $P = X_1^{-1} > 0$.

A simulation was carried out considering the following consistent initial condition $x(0) = \begin{bmatrix} 0.0842 & 0.0614 & -2.0630 \end{bmatrix}$, which is equivalent to an ankle angle $\phi(0) = 1.6$ rad, with the desired set point $x_d = \begin{bmatrix} 0.0620 & 0.1076 & -2.3168 \end{bmatrix}$, that corresponds to $\phi_d = 1.9$, the trajectories for the states are shown in Fig. 4.10(a), the ankle trajectory is in Fig. 4.11(a), the corresponding control signal is in Fig. 4.10(b) and the evolution of the Lyapunov function $V(e) = e^T P e$ is given in Fig. 4.11(b).

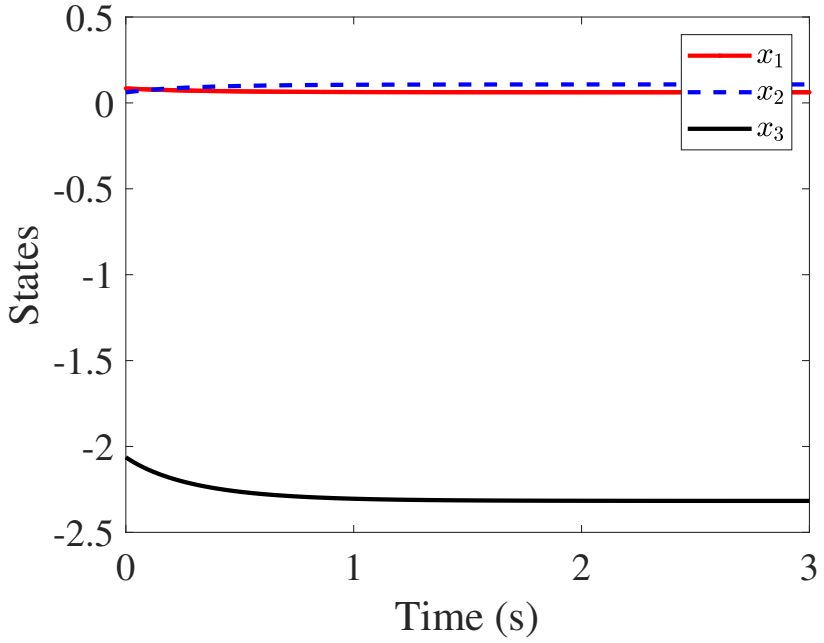

(a) Time evolution of the states.

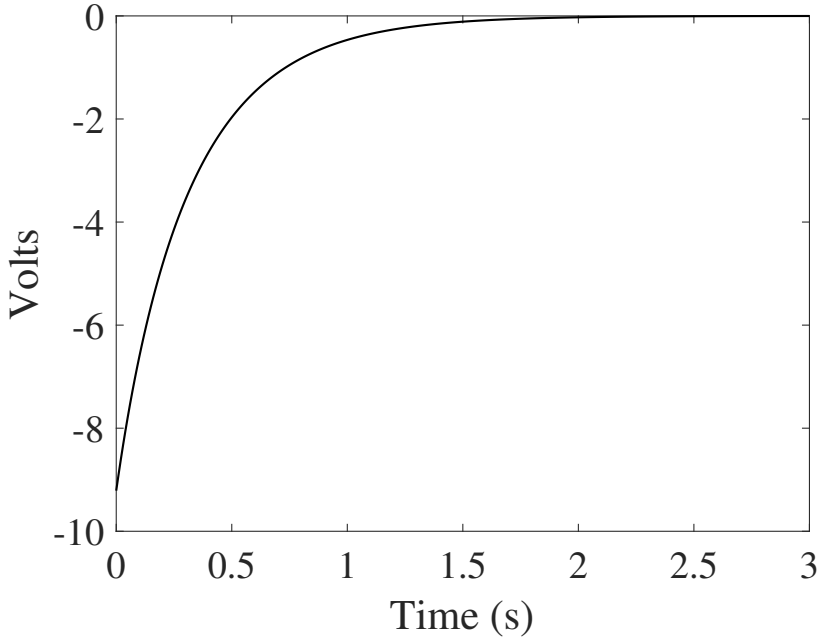

(b) Control signal obtained with $u = -Ke$.

FIGURE 4.10: System states and control signal.

4.4 Conclusion

In this chapter the nonlinear sector methodology was employed to obtain an exact convex representation of a nonlinear system, after that, issues related to conservative solutions

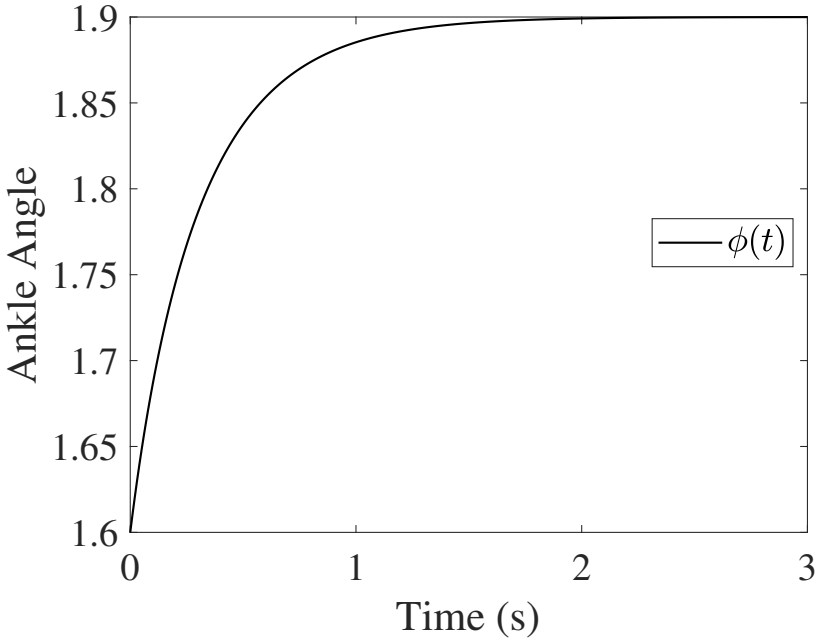

(a) Time evolution of the ankle angle ϕ.

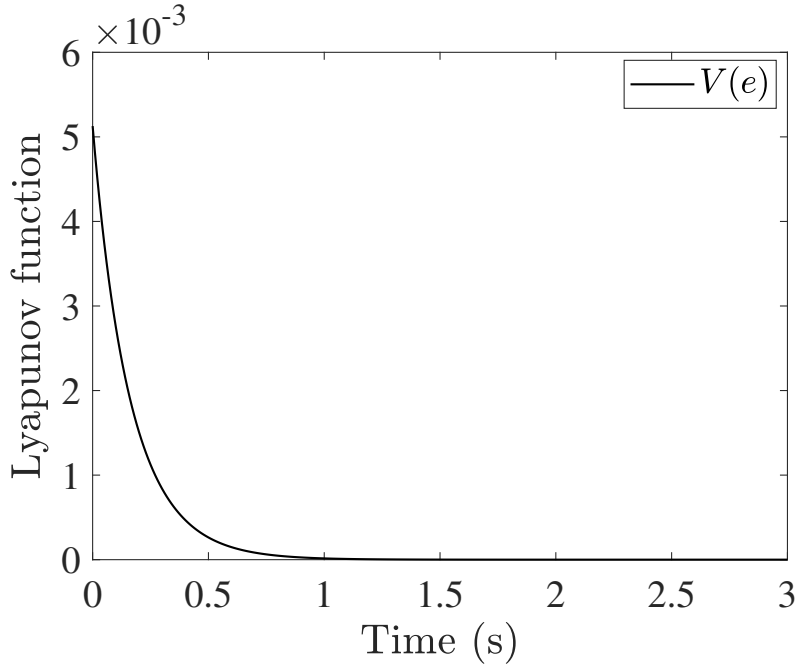

(b) Time evolution of the Lyapunov function.

FIGURE 4.11: Ankle angle and Lyapunov function.

in nonlinear control and observer design were addressed, specifically, those related to considering the positiveness of the membership functions and it was addressed via a known property for copositive matrices, but, even after considering this property we found that it seems to be only equivalent to existent conditions; therefore, a more relaxed

condition for copositive matrices than the one from Parrilo's employed in subsection 4.1.3 would provide a more relaxed solution.

The only condition employed for obtaining the results in subsection 4.1.3 was positiveness of the membership functions, the new conditions obtained are shape-independent. When the second property of convex models is taken into account (i.e., $\sum_{i=1}^{r} h_i = 1$), it allows to increase the order of the polynomial function in the Positivstellensatz problem as much as needed [141], since $\sum_{i=1}^{r} h_i = (\sum_{i=1}^{r} h_i)^2 = 1 = \cdots = (\sum_{i=1}^{r} h_i)^n = 1$, this approach has led to asymptotically necessary and sufficient conditions [139, 142], and by Polya's theorem, if there is a feasible solution it will be eventually found; but, maybe there could be another way to include this algebraic condition into the LMIs of the problem to solve it without having an exponentially increase in the number of inequality constraints. Attempts to include this algebraic constraint were made by increasing the $\bar{h}$ vector as $\bar{h} = \begin{bmatrix} h_1 I & h_2 I & \dots & h_n I & I \end{bmatrix}$ and arranging the values of Q_{ij} in (4.16), then, tried to include the information of the algebraic constraint via Finsler's Lemma, but no improvements were found by doing this. Since the double-sum condition generally appears in the time-derivative of the Lyapunov function, the idea would be that we only need to satisfy the negative condition on it (i.e., $\dot{V} < 0$) for values of the membership functions that are not only positive, but also for the ones that satisfy the algebraic constraint ($\sum_{i=1}^{r} h_i = 1$), this has been illustrated in Fig. 4.1 for a system with only two membership functions.

After that, two different controllers were designed with the parallel distributed compensation technique for a tracking desired ankle trajectory ϕ_d with the motoBOTTE; the purpose of the controller designs was to accomplish asymptotic stability in a tracking error system (i.e, $e(t) \to 0$ when $t \to \infty$), this tracking error system is defined using the black box model that was identified in the previous chapter, an exact convex representation of the error system was obtained and the gains of the controller was obtained by solving a LMI problem, the designs obtained were implemented in simulation and real-time, the efficiency of these controllers was illustrated in their respective figures.

Finally, the convex modeling process of nonlinear singular systems was reviewed, indicating that the algebraic constraints must be taken into account for selecting an appropriate modeling region Ω, the importance of selecting it properly is illustrated by examination of the determinant of the matrix $E(x)$ when the system is written in a nonlinear descriptor form. New conditions for convex control design for nonlinear systems described

by a set of DAEs were obtained in terms of linear matrix inequalities, the proposal of the convex modeling and the efficiency of the control design technique was illustrated by applying it to the model of the motoBOTTE.

This chapter is the last one that deals with nonlinear control design for the motoBOTTE, the next chapters will focus on integrating or considering the human interacting with the robot.

Chapter 5

EMG-Force Estimation Models

5.1 Ankle Torque Estimation

Torque production of the impaired limb of stroke patients can be directly measured using a force sensor or estimated using surface EMG sensors combined with a mathematical model [155–157]. Although force sensors are accurate and simple to use they present some clear disadvantages : 1) these devices are expensive, 2) must be calibrated from time to time due to the stress effect in the extensiometric gauges, such task can only be done by the manufacturer, 3) might be damaged due to electrical failures and 4) can be affected by the gravity and acceleration forces when placed over a moving surface, among other disadvantages.

Muscle force estimation models have been widely used in gait analysis [156] as well as during isometric contractions [158] of healthy subjects and impaired ones [157]. The use of an accurate mathematical model in real-time force estimation would allow to reduce the production cost of rehabilitation robots (avoiding the requirement of a force sensor) and making it more accessible for everyone, while providing a tool for monitoring the development of the patient at the same time. The main disadvantage of this approach is that each human body is different and the parameters in the models vary as well; but, an advantage is that the mathematical structure seems to be common for healthy subjects and impaired ones [157].

The relation between EMG and muscle force is not so straightforward and some misleads have been done in this procedure. There are different commercial softwares available

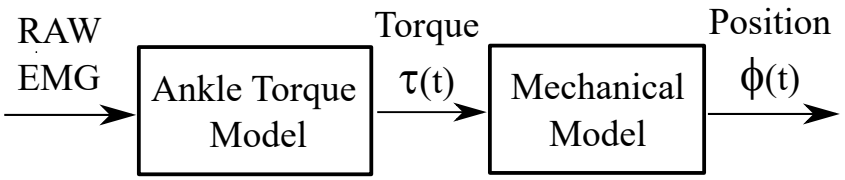

FIGURE 5.1: Torque estimation and reference generation scheme.

for analysis of musculoskeletal systems such as the Anybody Modeling System [159] and open source solutions as OpenSim [160]. The analysis and calibration of these models is mainly done offline [161] and some efforts have been made to extend these results to real-time applications [162, 163]

In this chapter we are interested in identifying and validating mathematical models to : 1) estimate ankle force production by the ankle muscles in real-time; specifically forces produced by Tibialis Anterior (TA) and Soleus (SOL) muscles, 2) generate a dynamic ankle trajectory that can be followed by the rehabilitation device, the general scheme used for controlling the robot position is presented in Fig. 5.1. Note that Tibialis Anterior is the main dorsiflexors. However, Soleus is not the most powerful of the plantarflexors and other muscles act for plantarflexion (Gastrocnemii, Tibialis Posterior, Peroneus Longus and Peroneus Brevis, Flexor Digitorum Longus, Flexor Hallucis Longus, Plantaris); but, the muscle fiber length, moment arm and tendon length of some of those muscles depend on the knee position and that is a variable that we can not directly measure when performing experiments with the motoBOTTE.

Some models have been taken from the available literature, where different techniques and approaches were used for offline muscle force estimation. The approaches presented vary on several different aspects such as the signal processing procedure to transform EMG into smooth rectified electromyogram (SRE), the procedure to model SRE into neural activation, the model of neural activation into muscle activation and the muscle model itself, and so on. Therefore, a brief comparison of the performance between some of these models is carried out later.

This section is organized as follows : subsection 5.1.1 gives some background information about the state-of-the art in signal processing that must be carried out before introducing the EMG signals into any mathematical model, then, subsection 5.1.2 deals with the modeling of neural activation dynamics, subsection 5.1.3 approaches for muscle activation are presented, in subsection 5.1.4 formulas of a Hill-type muscle model are

explicitly given; in subsection 5.1.5 polynomials for estimating the muscle fiber length, tendon length, moment arm, maximum force produced and pennation angle in Tibialis Anterior and Soleus from ankle position are presented, the data for computing these polynomials has been taken from an anatomical state-of-the-art model developed by experts in the field and widely used for analysis [164], in subsection 5.1.6 the hardware set up employed in the experiments and the signal processing used are described, then, the parameters for the models are estimated and validated, the range for these parameters are given; in subsection 5.2 a new reference generation model for the ankle is presented, parameters are estimated and validated as well.

Some of the contributions found within this chapter are summarized as follows : the space for searching a solution for the recursive filter model is reduced based on signal characteristics, the complexity in the estimation process for activation dynamics model is reduced by employing polynomials instead of using an iterative process, the precision of these polynomials can be further improved as needed, the introduction of a real-time muscle model that can be adjusted for each individual and considers anatomical parameters taken from state-of-the-art literature; as well as polynomials for approximating muscle fiber-lengths, moment arms and tendon-lengths are explicitly given.

5.1.1 EMG signal processing

Before applying the electromyogram as an input to any mathematical model for force estimation the signal must be processed. According to [155, 157, 165–170] the procedure for processing the signal is

1. Remove the offset of the signal.
2. Apply a full wave rectification of the signal and normalize it using the peak values of maximum voluntary contraction (MVC).
3. Use a low-pass filter on it.

In this predefined order, after that we obtain a smooth rectified electromyogram signal (SRE), that will be denoted $e(t)$. Applying a full wave rectification, which consists on computing the absolute value of the signal and the normalization procedure will vary for each subject; but, the cutoff frequency for the low-pass filters is not something trivial,

these can be given via a designer or obtained by an algorithm [171]. After a small review of the literature is carried out to find how these filters are designed. The articles with their cutoff frequencies f_c values high-pass and low-pass filter, the type and order for filters found in the literature are shown in Table 5.2. Please notice that there are propositions for these cutoff frequencies that does not make any sense as in the cases of [157] or [165, 166, 169, 170]; specially [157] since the low-pass filter is almost one decade below the high-pass filter, that would eliminate the useful information.

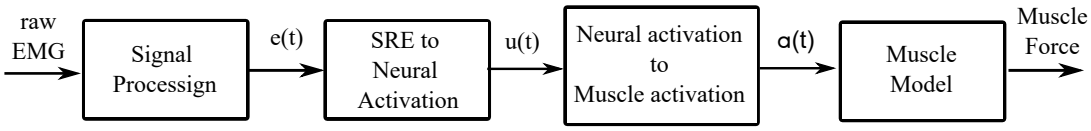

FIGURE 5.2: Muscle force estimation scheme.

TABLE 5.1: Information of the muscles considered.

Muscle	**Twitch time**	F_o^m	l_s^t	$\mathcal{L}_o^m$	Θ_o
TA	58.0 milliseconds	905 N	0.223 m	0.098 m	5°
SO	74.0 milliseconds	3549 N	0.250 m	0.050 m	25°

TABLE 5.2: Filter found in the literature with wrong values.

Reference	**High-pass frequency**	**Low-pass frequency**
[157]	50 Hz	4 Hz
[165, 166]	30 Hz	6 Hz
[169, 170]	20 Hz	10 Hz

Some references assume that the muscle force dynamics can be approximated with a critically damped second order system $F(t) = F_0 \frac{t}{T} e^{-\frac{t}{T}}$, where the T is the twitch time or time required to reach the maximum force value, it varies for each muscle, the operation ranges for the ankle muscles of interest are shown in Table 5.1, these values were taken from an anatomical model that has been previously validated [164], the parameters shown in the table are the twitch time of the muscles, the maximum force produced by the muscle F_o^m, optimal tendon length l_s^t, optimal fiber length $\mathcal{L}_o^m$ and optimal pennation angle Θ_o, this information will be useful later in this chapter. The cutoff frequency f_c in a critically damped second order low-pass filter is related to the twitch time of the muscle as $f_c = \frac{1}{2\pi T}$ and to the muscle force, therefore, we should take it into account for filtering, by considering this we can avoid reported issues such as crosstalk [172, 173], since the surface EMG signals can be recorded far from the origin and this electrical activity might be misunderstood if not properly filtered.

After the processing the SRE signal can be introduced in an activation dynamics model to obtain the neural activation signals $u(t)$, these neural activation signals go through a model of muscle activation and this muscle activation $a(t)$ is the input of a muscle model, the output of this muscle model is the muscle force computed, and then, after that we can compute the ankle torque. The whole procedure is illustrated in Fig. 5.2.

5.1.2 Activation dynamics

There is an electromechanical delay inherent to the muscle activation patterns [174, 175], similar to muscle twitch time, this activation delay varies for each muscle [122]. The models used to estimate neural activation $u(t)$ from SRE $e(t)$ aim to take this electromechanical delay into account, this process is commonly referred as *activation dynamics*. The following models are attempts to describe the release, diffusion and uptake of calcium by the sarcoplasmic reticulum in muscle cells [158, 176].

5.1.2.1 First order differential equation

A first approach presented in [177] for modeling activation dynamics as an unidirectional process via a first order differential equation [176] is

$$\dot{u}\left(t\right)=\frac{1}{\tau_{act}}e\left(t\right)-\left[\beta+\left(1-\beta\right)e\left(t\right)\right]\left(\frac{1}{\tau_{act}}\right)u\left(t\right), \tag{5.1}$$

where β is a constant such that $0<\beta<1$ and τ_{act} is the muscle twitch time during isometric contraction[155]. Notice that when the muscle is activated, i.e. $e(t)=1$, the time constant is τ_{act} and when the muscle is deactivated, i.e. $e(t)=0$, the time constant is τ_{act}/β.

5.1.2.2 Recursive filter

According to [122, 155] neural activation dynamics can also be approximated by a critically damped second order system, whose discrete transfer function is

$$\frac{u(z)}{e(z)}=\frac{\alpha_1}{1+\beta_1 z^{-1}+\beta_2 z^{-2}}=\frac{\alpha}{(1+\gamma_1 z^{-1})(1+\gamma_2 z^{-1})}, \tag{5.2}$$

its poles are located at $z = -\gamma_1$ and $z = -\gamma_2$. The values for the parameters β_1 and β_2 are

$$\beta_1 = \gamma_1 + \gamma_2, \quad \beta_2 = \gamma_1 \times \gamma_2, \tag{5.3}$$

and its discrete-time solution is

$$u(k) = \alpha_1 e(k-d) - \beta_1 u(k-1) - \beta_2 u(k-2), \tag{5.4}$$

where d is the electromechanical delay of the neural activation, previous reports indicate that the time solution of this recursive filter should be positive, stable and have a unitary gain. Stability of the solution can be guaranteed with $|\gamma_1| < 1$ and $|\gamma_2| < 1$, then, if we know that the smooth rectified EMG signal is positive, i.e., $e(t) > 0$, the only way $u(t)$ can be negative is if $\beta_1 > 0$, $\beta_2 > 0$ or $\alpha < 0$. Therefore, we can guarantee $\beta_1 < 0$ and $\beta_2 < 0$ with $-1 < \gamma_1 \leq 0 \leq \gamma_2 < 1$, and $|\gamma_1| \geq |\gamma_2|$, which reduces the previous region for searching a solution for γ_1 and γ_2 [155]. A unitary gain can be guaranteed by setting $\alpha_1 = 1 + \beta_1 + \beta_2$, and verifying that $\alpha_1 > 0$.

5.1.3 Muscle activation

There are different approaches for modeling the transformation between neural activation $u(t)$ into muscle activation $a(t)$, the later signal can be used as an input for a Hill-type model. The main purpose of these models is to consider a nonlinear relationship EMG-force in the modeling at low levels of force [178] and the main advantage of the models listed below is that they only require a single parameter to be estimated for each muscle.

5.1.3.1 Exponential model

A simple approach for modeling muscle activation taken from [155, 179] is the exponential model

$$a(t) = \frac{e^{Au(t)} - 1}{e^A - 1}, \tag{5.5}$$

where the parameter $A \in [-3, 0]$ is a nonlinear shape factor to be found.

5.1.3.2 Single parameter model

A second model presented in [178]. The equations for this model can be obtained by defining the coordinates of a node point (u_0, a_0) as $u_0 = 0.3085 - A\cos(45°)$ and $a_0 = 0.3085 + A\sin(45°)$; then, the plane $a(t) - u(t)$, with $a(t) \in [0,1]$ and $u(t) \in [0,1]$ is partitioned in two, where for the first half the relation $a(t) - u(t)$ is a nonlinear curve and for the second half the relation is linear, this is defined via a piece-wise function

$$\begin{aligned} a(t) &= \alpha_2 ln\left(\beta_3 u(t) + 1\right), \quad 0 \leq u(t) \leq u_0, \\ a(t) &= mu(t) + c, \qquad\qquad\quad u_0 \leq u(t) < 1, \end{aligned} \tag{5.6}$$

the parameters m, c and β_3 can be easily computed as

$$m = \frac{1 - a_0}{1 - u_0}, \qquad c = m - 1, \qquad \beta_3 = \frac{e^{a_0/\alpha} - 1}{u_0}, \tag{5.7}$$

but, there was no closed-form solution for α_2, instead an iterative solution based on Newton-Raphson method was proposed [178], in which a new value called $\alpha_2(k+1)$ can be found from the following expressions

$$\alpha_2(k+1) = \alpha_2(k) - \frac{f\left(\alpha_2(k)\right)}{\dot{f}\left(\alpha_2(k)\right)}, \tag{5.8}$$

with $f(\alpha_2) = m - \frac{\alpha_2\beta_3}{\beta_3 u_0 + 1}$ and $\dot{f}(\alpha_2) = \frac{1}{u_0}\left[-1 + \left(1 - \frac{a_0}{\alpha_2}\right)e^{-a_0/\alpha_2}\right]$; this iterative process must be carried out until the absolute value of the difference $\Delta\alpha_2 = |\alpha_2(k+1) - \alpha_2(k)|$ is below a certain tolerance value, i.e. $\Delta\alpha_2 < \epsilon_1$, with $\epsilon_1 > 0$. According to [178] the A-parameter is in $0 < A \leq 0.12$, we can use second order polynomials of the form $\alpha_2 = \gamma_2 A^2 + \gamma_1 A + \gamma_0$ to approximate these solutions within a desired region, this reduces the complexity in the parameter estimation problem. The iterative solution in equation (5.8) and the piece-wise polynomial approximation for the parameter α_2 are shown in Fig. 5.3. The value of the coefficients obtained and the regions for the approximation are in Table 5.3. These approximations can be improved as needed by selecting smaller regions or increasing the order of the polynomials employed. The curves $u(t) - a(t)$ generated with this approach for some values of A are illustrated in Fig. 5.4.

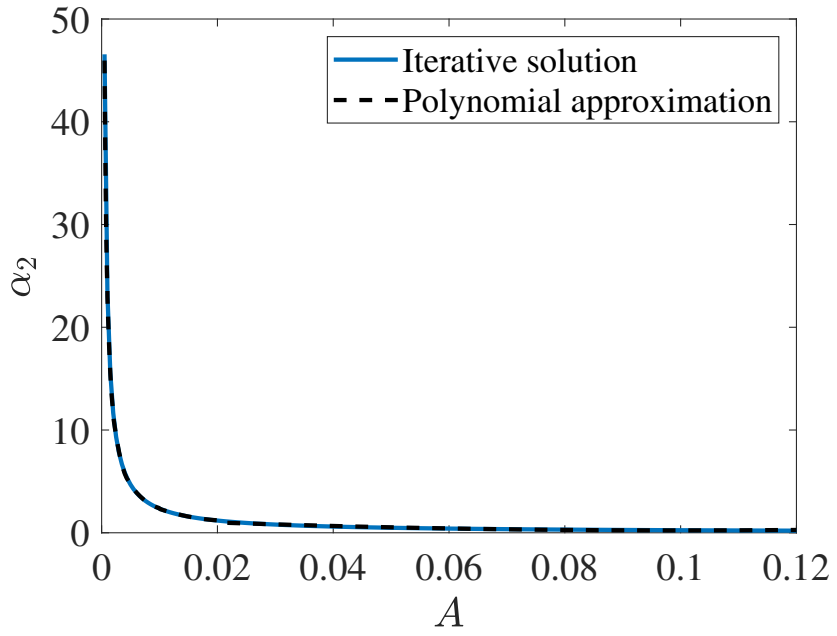

FIGURE 5.3: Relation between parameters A and α_2.

TABLE 5.3: Coefficient values for the piece-wise polynomials.

Region	γ_2	γ_1	γ_0
$0.0005 \leq A < 0.001$	61190838.85	-136277.86	98.79
$0.001 \leq A < 0.002$	7633638.27	-34007.87	49.35
$0.002 \leq A < 0.005$	644423.84	-6653.77	22.04
$0.005 \leq A < 0.01$	60968.69	-1358.40	9.88
$0.01 \leq A < 0.02$	7619.35	-339.62	4.95
$0.02 \leq A$	119.8063	-24.01557	1.4294

5.1.4 Muscle-tendon model

There are different muscle models available in the literature where most of them are attempts to describe muscle based on the external behavior of the system. The Hill-type model is a widely used approach to estimate the force produced by a muscle fiber connected in series with a tendon. The muscle fiber force is approximated with a contractile element in parallel with a passive element, the scheme is shown in Fig. 5.5. Where F^T is the tendon force, F^M is the muscle fiber force, F_A is the active force produced by a contractile element, F_P is the passive force produced by the parallel elastic component, θ is the pennation angle, ℓ^t is the tendon length, ℓ^m is the muscle fiber length and ℓ^{mt} is the muscle-tendon fiber length.

The human muscles produce their maximum force when the sarcomeres length within a

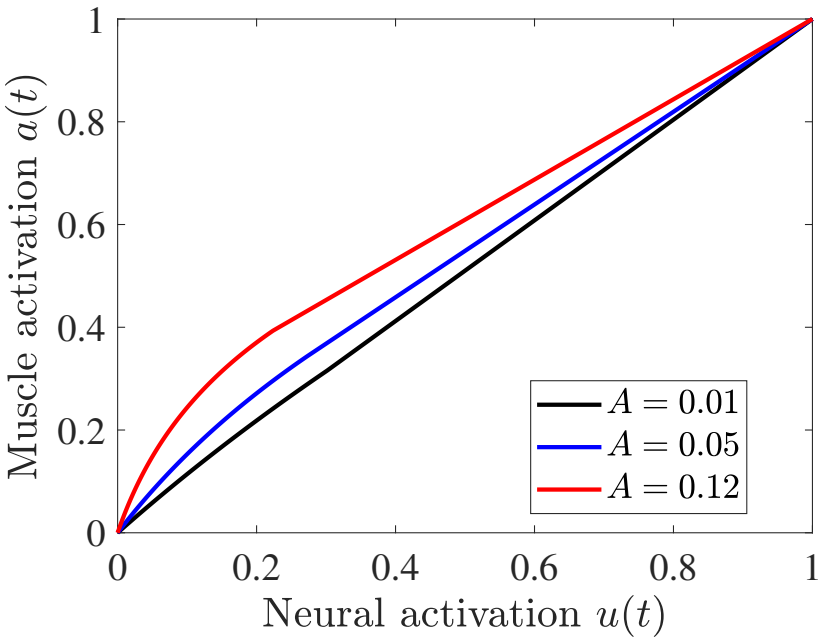

FIGURE 5.4: Transformation from neural to muscle activation.

muscle are at $2.8\mu m$, this is also named as optimal fiber length ℓ_o^m [155], these optimal fiber lengths increase when the muscle activation decrease [165], this relation between neural activation and optimal fiber-length is equivalent to consider :

$$\ell_o^m(t) = \ell_o^m\left(\lambda_1\left(1 - a(t)\right) + 1\right), \tag{5.9}$$

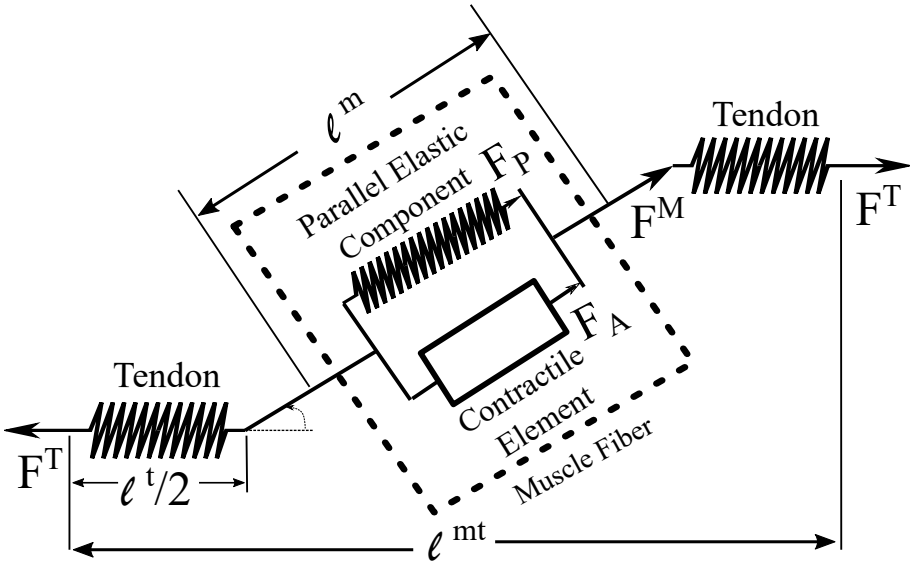

FIGURE 5.5: Muscle model diagram.

pennation angle varies with instantaneous optimal fiber as

$$\theta(t) = \sin^{-1}\left(\frac{\ell_o^m \sin\theta_o}{\ell_o^m(t)}\right). \tag{5.10}$$

The tendon-muscle force can be described by [155, 158, 165]

$$\begin{aligned} F^{MT}(\phi,t) = F^T = F^M &= F_A + F_P, \\ &= \left[f_A\left(\tilde{\ell}\right) f(v)\, a(t) + f_P\left(\tilde{\ell}\right)\right] F_o^M \cos\left(\theta(t)\right). \end{aligned}$$

Continuing with description of the diagram in Fig. 5.5, the force produced by the active contractile element in the muscle fiber is $F_A = f_A\left(\tilde{\ell}\right) f(v)\, a(t)\, F_o^m\left(\cos\theta(t)\right)$ and the force produced by the parallel passive elastic component is $F_P = f_P\left(\tilde{\ell}\right) F_o^M \cos\left(\theta(t)\right)$, where $f_A(\tilde{\ell})$ is the normalized active force-length, $f(v)$ is the normalized force-velocity function and $f_P(\tilde{\ell})$ is the normalized passive force-length, F_o^m is the maximum isometric muscle force and $a(t)$ is the muscle activation. The normalized muscle fiber length is defined as $\tilde{\ell} = \frac{\ell^m(t)}{\ell_o^m}$.

The force produced by the tendon element [155] can be computed as

$$F^T = \tilde{F}^T F_o^m, \tag{5.11}$$

where $\tilde{F}^T$ is the normalized tendon force (normalized with respect to the maximum muscle force produced, indicated by F_o^m, the same is considered for the following normalized functions) and it can be defined using the tendon strain $\epsilon = \frac{\ell^T - \ell_s^T}{\ell_s^T}$ as

$$\begin{aligned} \tilde{F}^t &= 0 && \epsilon \le 0, \\ \tilde{F}^t &= 1480.3\epsilon^2 && 0 < \epsilon < 0.0127, \\ \tilde{F}^t &= 37.5\epsilon - 0.2375 && \epsilon \ge 0.0127. \end{aligned} \tag{5.12}$$

The relation between active force and normalized fiber length can be described using a Gaussian function [158, 180]

$$f_A\left(\tilde{\ell}\right) = e^{\frac{-(\tilde{\ell}-1)^2}{\sigma}}, \tag{5.13}$$

where $\sigma = 0.45$ is a nonlinear shape factor[158], the function that describes the passive force in terms of normalized fiber length is

$$\begin{aligned} f_P\left(\tilde{\ell}\right) &= e^{\epsilon_1\left(\tilde{\ell}-\epsilon_2\right)} - \epsilon_3, \quad \tilde{\ell} \geq 1, \\ f_P\left(\tilde{\ell}\right) &= 0, \qquad\qquad\quad \tilde{\ell} \leq 1. \end{aligned} \tag{5.14}$$

with $\epsilon_1 = 6.6667$, $\epsilon_2 = 1.5972$ and $\epsilon_3 = 0.018657$, these values were obtained after fitting the function with the model [164] using OpenSim [160] using the Parameter Estimation Toolbox available in MATLAB with the Trust-Region algorithm [181].

Finally, the last term corresponding to the normalized force-velocity $f\left(v\right)$ can be estimated by considering the muscle activation equals one (i.e., $a(t) = 1$) and compute

$$f\left(v\right) = \frac{F^T - f_P\left(\tilde{\ell}\right) F_o^M \cos\left(\theta(t)\right)}{f_A\left(\tilde{\ell}\right) F_o^M \cos\left(\theta\left(t\right)\right)}. \tag{5.15}$$

5.1.5 Musculoskeletal parameters

Usually, the software used to integrate muscle-tendon models with musculoskeletal geometry available in gait analysis are OpenSim [160] or Anybody Modeling System [159], in our case we are interested in obtaining a solution that can be implemented in real-time for two main purposes 1) monitoring the individual muscle force generation of the subject and 2) generate a reference for the rehabilitation device to follow. The OpenSim software [160] allows to plot and extract data from previous validated anatomical models; in our case we are extracting this anatomical information for the muscles Tibialis Anterior and Soleus from the model in [164]. The extracted data from this model was optimal fiber lengths ℓ_o^m, optimal pennation angles Θ_o, maximum isometric forces F_o^m, and tendon slack ℓ_s^t, as well as to calibrate the functions for active force f_A and passive force f_P; this data was used to compute muscle-fiber length $\ell^m\left(\phi\right)$, tendon length $\ell^t\left(\phi\right)$ and moment arm $r\left(\phi\right)$ from a given position of the ankle angle ϕ.

The fiber-length, tendon length and moment arm data from the model [164] was approximated within our region of interest $\phi \in [1.27, 2.52]$ in radians [63] via polynomials of the form $\ell = \gamma_n\phi^n(t) + \gamma_{n-1}\phi^{n-1}(t) + \cdots + \gamma_0$, the coefficient values for fiber-length $\ell^m\left(\phi\right)$, tendon-length $\ell^t\left(\phi\right)$ and moment arm polynomials are given in Table 5.4. The

Fig. 5.6 illustrates a comparison between the data obtained via Opensim from [164] and our polynomial approximation.

TABLE 5.4: Coefficients for fiber-length $\ell^m(\phi)$, tendon-length $\ell^t(\phi)$ and moment arm $r(\phi)$ polynomials.

Polynomial function	γ_4	γ_3	γ_2	γ_1	γ_0
$\ell^m_{TA}(\phi)$	0	0.008294	-0.043684	0.035151	0.094895
$\ell^m_{SOL}(\phi)$	0	-0.009777	0.049179	-0.046497	0.029774
$\ell^t_{TA}(\phi)$	0.000337	-0.001642	0.001634	0.000256	0.229737
$\ell^t_{SOL}(\phi)$	0.00238	-0.015861	0.035313	-0.027316	0.259927
$r_{TA}(\phi)$	0	-0.022564	0.097821	-0.129152	0.090772
$r_{SOL}(\phi)$	0	0	0.014618	-0.030328	-0.033501

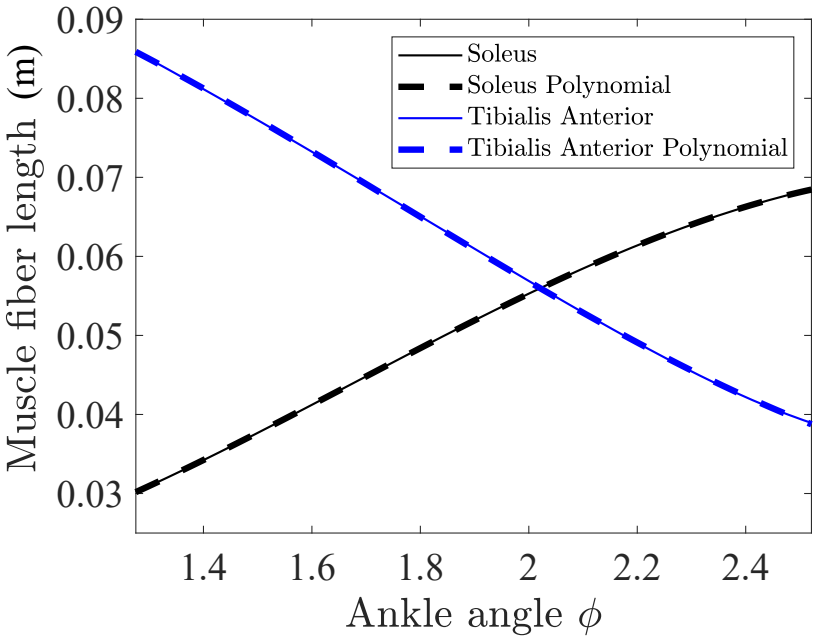

FIGURE 5.6: Fiber lengths and the approximation.

5.1.6 Signal acquisition and processing

Electrodes for measuring Tibialis Anterior and Soleus muscles were positioned following the recommendations from SENIAM [182] using EMG Cometa wireless sensors. The EMG signals were initially sampled with a frequency of 1000 Hz, these signals were rectified, low-pass filtered using a zero-lag Butterworth filter with a cutoff frequency of 5 Hz and finally re-sampled at 10 milliseconds to homogenize the EMG sampling with the other devices. The Vicon Motion Capture System [183] and the motoBOTTE system were set up to operate at 10 milliseconds.

The cutoff frequency was selected by analyzing the signals spectrum, applying a fast Fourier transform to the rectified EMG signals for both Tibialis Anterior and Soleus of the experiments and selecting a frequency that includes the signal components with higher magnitude, we assume that the information would be contained on those components, these are shown in Fig. 5.7 for one of the experiments, in our case 5 Hz seemed to be a reasonable cutoff frequency.

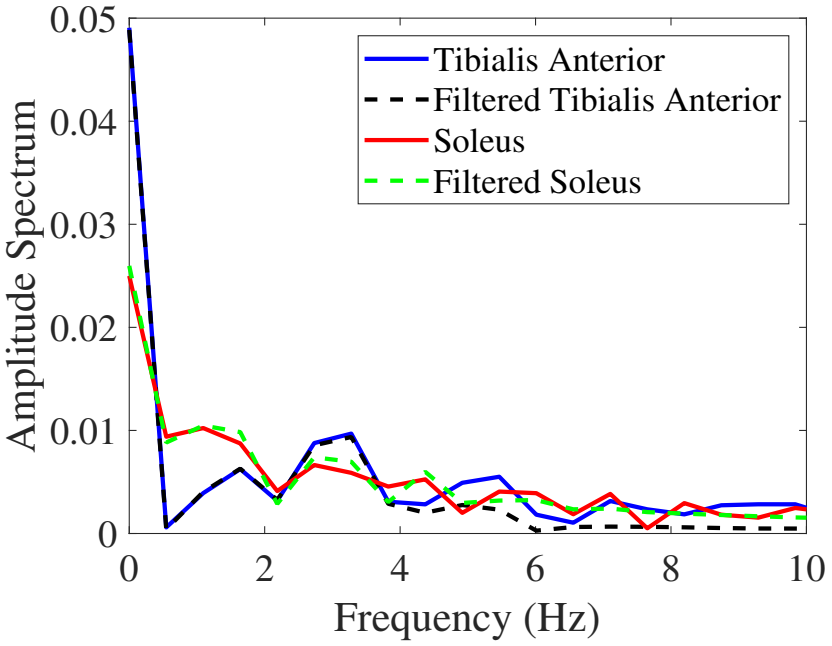

FIGURE 5.7: Amplitude spectrum of the rectified EMG signals.

During these experiments the subjects walked over a force plate sensor with position markers on both legs while wearing wireless EMG sensors on the muscles of interest (Tibialis Anterior and Soleus). The signals obtained through the motion capture system were coupled to a force plate. The ankle torque production was estimated via inverse dynamics [184, 185], this biomechanical analysis has been limited only to two-dimensions and we are assuming that most of the dynamics occur over the sagittal plane [156], the proceeding for tuning the model consists on minimizing the error signal illustrated in Fig. 5.8, where each muscle force has been estimated as it is indicated in the previous sections.

The parameters involved in the transformation between smooth rectified EMG and neural activation are $\tau_{act} \in [0, 1]$ and $\beta \in [0, 1]$ for the model in subsection 5.1.2.1 and the parameters $d \in [0, 0.12]$, $\gamma_1 \in (-1, 0)$ and $\gamma_2 \in (0, 1)$ for the model in subsection 5.1.2.2. For neural activation models the parameter A must be found according to the model

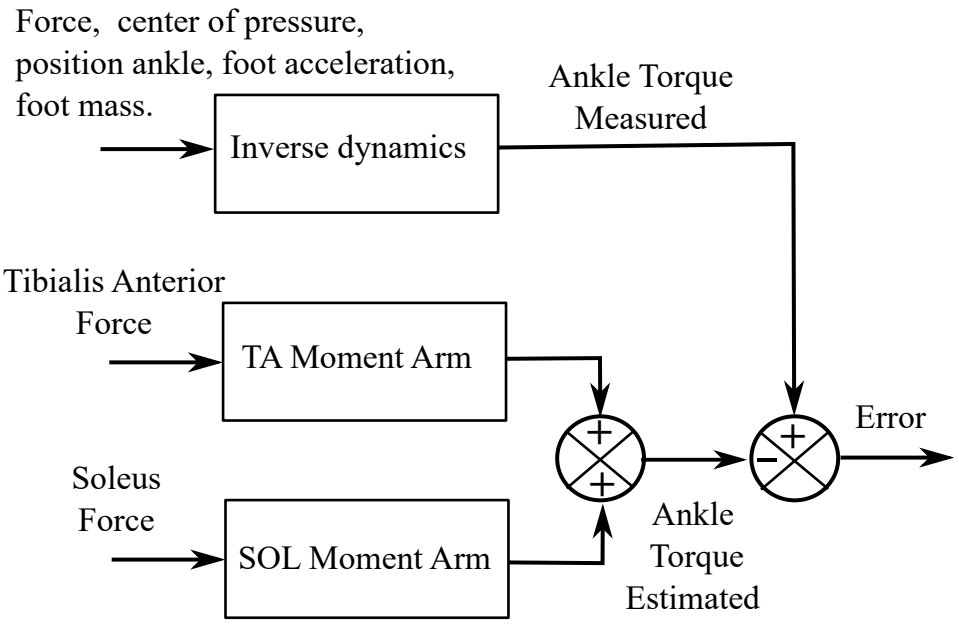

FIGURE 5.8: Torque error computation scheme.

it can vary from $A_a \in [-3, 0]$ or $A_b \in [0.005, 0.12]$, where the sub-index denotes the subsection of the corresponding model in Section 5.1.3.

The combination of different models for activation dynamics, muscle activation with the Hill-type muscle model and the musculoskeletal model yields to different models for ankle force estimation. For the sake of comparison of the different approaches presented all the model combinations are assumed to have the same musculoskeletal parameters varying only on activation dynamics and muscle activation model. The optimal anatomical parameters have been scaled for a better model fitting considering $\mathcal{L}_o^m = \lambda_3 \tilde{\mathcal{L}}_o^m$, $l_s^t = \lambda_3 \tilde{l}_s^t$ and $\Theta_o = \lambda_4 \tilde{\Theta}_o$; the percentage of muscle fiber-length variation in relation with the muscle activation in (5.9) was assumed to be $0 - 30\%$, i.e., $\lambda_1 \in [0, 0.3]$, the maximum force produced by each muscle was scaled as $F_o^m = \lambda_2 \tilde{F}_o^m$, we considered λ_2 equals for both muscles, where $\tilde{\mathcal{L}}_o^m$, $\tilde{\Theta}_o$, $\tilde{l}_s^t$ and $\tilde{F}_o^m$ denotes the optimal values from the model [164] in Table 5.1, $\mathcal{L}_o^m$, Θ_o and $\tilde{l}_s^t$ are the parameters used in the model equations with $\lambda_2 \in [0.5, 2.5]$ as in [157], the tendon and muscle fiber lengths were equally scaled via the parameter λ_3, here we are considering a $\pm 5\%$ variation, which yields to $\lambda_3 \in [0.95, 1.05]$, and the variation of the optimal pennation angle was $\pm 50\%$, therefore $\lambda_4 \in [0.5, 1.5]$. All these variations are considered with respect to the optimal values found in a validated model [164].

Usually, the models in OpenSim are scaled [160] to match the anthropometry of a specific

subject with respect to the position of the given markers, this would be related to the height of the subject, but in our case we are scaling all of them when minimizing the sum-of-squared errors of the experiments using trust region algorithm available in the Parameter Estimation Toolbox in MATLAB [186, 187].

First, the experimental data of four subjects, denoted as S_1, S_2, S_3 and S_4 were used for trying to estimate a common model that could fit better in comparison with a different combination, i.e., the model resulting from the combination of the formulas found in section 2 subsection a and section 3 subsection a would be denoted as model $2a3a$, and so on; but, it seems that there are no significant differences in the performance of the different models. It is worth noticing that the models $2a3a$ and $2a3b$ have 6 parameters and the models $2b3a$ and $2b3b$ have 10 parameters, something that affects the computational time required during the estimation process. The data of the subjects such as gender, age, height, body mass and body mass index (BIM) are provided in Table 5.5. The signals used in the estimation process are shown in Fig. 5.9(a). One of the ankle torque signals used to validate the model is shown in Fig. 5.9(b), where dorsiflexion corresponds to positive values and plantarflexion to the negative ones.

TABLE 5.5: Subjects information.

Subject	**Gender**	**Age**	**Height**	**Body mass**	**BIM**
S_1	Male	20	1.78 m	67 kg	21.15
S_2	Male	27	1.73 m	75 kg	25.06
S_3	Female	24	1.7 m	59 kg	20.42
S_4	Female	37	1.74 m	58 kg	19.16

Since there was no big difference among the different models and the combination $2a3a$ has less parameters we will continue thereafter with that model. The parameter values obtained during the previous estimation process for this model are given in Table 5.6, where $u(0)$ denotes the initial condition of the neural activation $u(t)$.

Remark 5.1. The methodology presented in this chapter is an adaptation of a model-based approach for computing the ankle torque in terms of the ankle position and electromiography, the information of Vicon and the force plate was used to calibrate these models, the adaptation consists in making the necessary modifications to use the models in real-time. There are excellent tools for computing muscle forces offline such as OpenSim, but it can not be programmed in an embedded system and therefore, it can not be employed in a real-time scenario, this is one of the motivations behind this proposal.

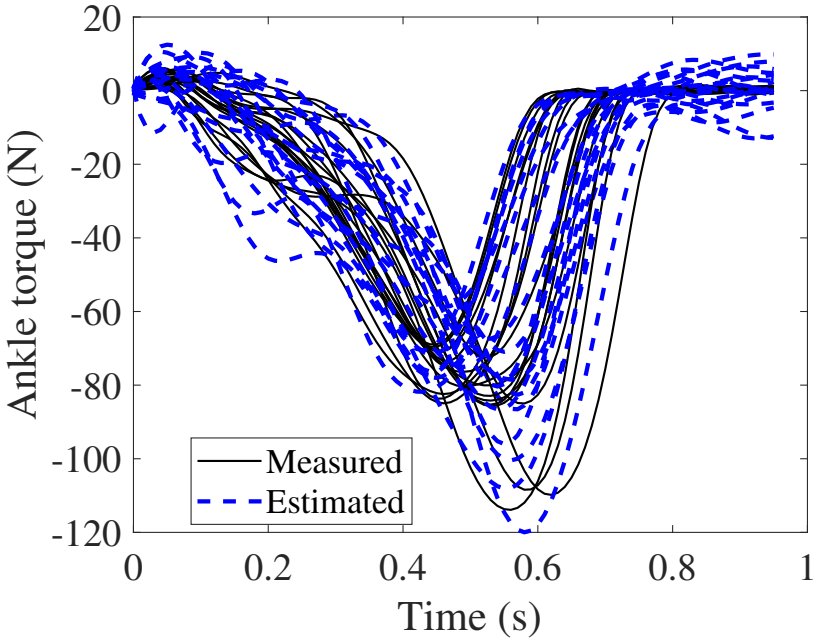

(a) Performance comparison of the different models.

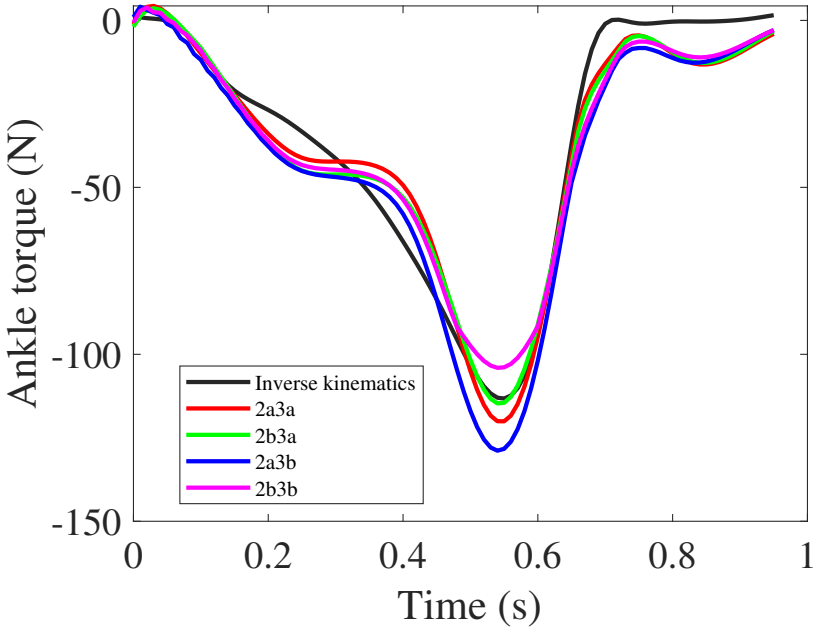

(b) Performance comparison of the different models estimated.

FIGURE 5.9: Estimation and validation process.

5.2 Position reference generation

We assume that the dynamics of the human ankle $\phi(t)$ during swing-phase of the gait cycle can be approximated via a nonlinear second order system, whose input is the ankle

TABLE 5.6: Parameters for the estimated model 2a3a.

Musculoskeletal Parameters	λ_1	λ_2	λ_3	λ_4
Tibialis Anterior	0	0.5	0.9514	0.5
Soleus	0.3	0.5	0.9514	1.5
Activation Parameters	τ_{act}	β	$u(0)$	A_a
Tibialis Anterior	0.060613	1	0.024611	-1.4904
Soleus	0.022776	0.55594	0.0010001	-0.83896

torque τ. The structure proposed is :

$$\begin{bmatrix} \dot{x}_1 \\ \dot{x}_2 \end{bmatrix} = \begin{bmatrix} 0 & 1 \\ \mu_1 + \mu_2 x_1 & \mu_3 + \mu_4 x_2 \end{bmatrix} \begin{bmatrix} x_1 \\ x_2 \end{bmatrix} + \begin{bmatrix} 0 \\ \mu_5 + \mu_6 x_1 \end{bmatrix} \tau,$$

where $x_1 = \phi$ and $x_2 = \dot{\phi}$; the parameters to find are μ_i, with $i \in \{1, 2, \cdots, 6\}$; these parameters can be estimated via Parameter Estimation Toolbox. By considering Euler's approximation $\dot{x} = (x_{k+1} - x_k)/T_s$, with $T_s = 0.01$ as the sampling time of 10 milliseconds we can obtain the following discrete expressions

$$\begin{aligned} x_{1k+1} &= x_{1k} + T_s x_{2k}, \\ x_{2k+1} &= x_{2k} + T_s \left(\mu_1 x_1 + \mu_2 x_1^2 + \mu_3 x_2 + \mu_4 x_2^2 + \mu_5 \tau + \mu_6 x_1 \tau\right), \end{aligned}$$

the signals obtained during the previous steps from the inverse dynamics procedure corresponds to the input τ for our proposed reference generation model, but, only during the swing-phase, since we consider that it is during this phase where the ankle position is not affected by ground reaction forces. The parameters estimated for different subjects are shown in Table 5.7. The signals produced during the validation process for some of the subjects model are shown in Fig. 5.10.

TABLE 5.7: Model parameters for each subject.

Subject	μ_1	μ_2	μ_3	μ_4	μ_5	μ_6
S_1	-88.30	158.26	-22.77	-0.71	-202.12	123.71
S_2	-91.45	153.88	-21.21	6.17	-201.27	138.30
S_3	-79.33	134.88	-18.90	0.85	-267.91	165.43
S_4	-75.17	124.39	-8.03	3.40	-30.04	38.33
S_5	-171.05	315.65	-5.00	24.32	700.66	-378.04
S_6	-140.87	244.38	-22.62	-2.61	50.68	-30.91

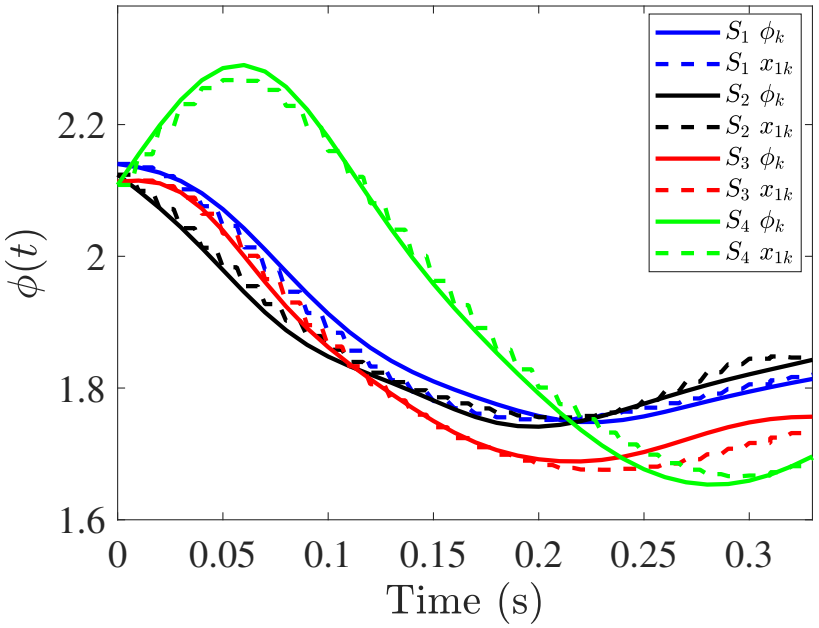

FIGURE 5.10: Validation trajectories of the position model.

5.3 Conclusion

Within this chapter new models that have been adapted from state-of-the-art were presented, these can be used in real-time to estimate the force produced by the Tibialis Antrior (TA) and Soleus (SOL) muscles, the parameters of the models have been estimated and validated by estimating the ankle force during gait in simulation for every individual, recall that the models presented must be calibrated before applying them in real-time, the structure of the mathematical models might be the same for healthy subjects or impaired ones, as it was pointed out by [157], but the value of the parameters in the model must be estimated as shown in subsection 5.1.6, after the calibration process they can be employed for monitoring the subject as an alternative of employing a force sensor, since the commercially available electromyography sensors are generally cheaper compared with the force sensors.

One of the disadvantages that has been observed in these models is that there is an oversimplification in some of the blocks; for example, muscle and neural activation are the result of a chemical process occurring at a cellular level and those dynamics are modeled or approximated only by a first order differential equations. Although, other different models are available for those blocks in the literature, they were left out of the scope in this study.

We know that neural activation and muscle activation usually are not directly available to be measured and the range for those signals is between $[0, 1]$; maybe, instead of using the actual fully model-based approach from the literature a better idea would be using a sort of hybrid model approach, we can substitute the neural activation and muscle activation dynamics for a recurrent neural network and take advantage of the properties demonstrated in that kind of systems (universal approximation capabilities and the naturally bounded output of the synapses), while preserving the other blocks that contain important knowledge of the human modeling, such as the moment arm, fiber-length, tendon-length, and so on.

Something to consider from the gait experiments is that we also had available the EMG measurements from Gastrocnemius Lateralis and Gastrocnemius Medialis muscles; but, since the muscle fiber length, tendon length and moment arm from those muscles depend also on the knee position and we cannot directly measure that position with the motoBOTTE, therefore, those muscles were left out of this analysis. Thus, a better model for ankle force estimation would consider also the knee position and more muscles.

The analysis presented in this chapter has been delimited to be applied only to ankle force estimation, but, is important noticing that the methodology presented is quite general and it should be possible to apply it to different joints, not only to the ankle joint. For the case of muscles that depends on multiple variables a good idea would be using the data from the anatomical models from the state-of-the-art literature again and define some polynomial functions that interpolate depending on the knee and ankle moment in order to compute the value of the muscle fiber lengths, tendon lengths and moment arms.

In the next chapter the human interaction with the system will be considered though a brain computer interface, and the effects of using the motoBOTTE and a new wrist exoskeleton as rehabilitation devices will be evaluated.

Chapter 6

Assisted Rehabilitation via Brain Computer Interfaces

This chapter deals with the results obtained when the motoBOTTE and a new wrist exoskeleton were coupled to a brain computer interface (BCI). The movement of both devices was triggered by detecting the intention of movement of the patient, but, the experiments in both sections are different. The first study in section 6.1 is an investigation for comparing which type of afferent feedback would be better for inducing neural plasticity in ankle rehabilitation, three different afferent feedbacks are compared in this case : electrical stimulation, passive movements and a combination of both. The feedbacks are triggered when there is a detection of the intention of movement. The detection of the intention of movement is carried out by employing a brain computer interface for measuring the brain activity of the subject. The report presented in section 6.2 introduces a new low-cost wrist exoskeleton, that was designed, 3D printed and built specifically for this study. The experiment in this case consists on the following procedure : first, transcranial magnetic stimulation (TMS) is performed on the subject, such that it induces a wrist extension, the motor evoked potential resulting from this action is measured using an EMG sensor; then, the subject performs a motor imaginary exercise where he imagines a wrist extension, the signals from this imaginary exercise are recorded via a low-cost BCI, the Motor Imaginary BCI package from OpenVibe is employed with these signals to detect the motor intention of the subject. After proper training the software is capable of detecting this motor intention. Once the software calibration has been finished, the subject performs a training session of motor imaginary

where the exoskeleton device is used to provide a feedback to the subject. Right after this training session TMS is performed on the subject, finally, after waiting 30 minutes, TMS is performed again on the subject. The motor evoked potentials are measured for each case of the TMS and a statistical analysis is carried out on the measured motor evoked potential to evaluate the performance of combining this exoskeleton with a BCI for wrist rehabilitation.

6.1 Optimal afferent feedback for inducing plasticity

Brain–computer interfaces (BCIs) have over the past years been proposed also as a tool for motor rehabilitation after neural injuries, such as spinal cord injury or stroke [188–193]. It is well-established that BCIs can be used for inducing neural plasticity [125, 126, 194–196], which is believed to be the underlying mechanism of motor learning/recovery [197]. These neuroplastic changes are induced in the brain by pairing the movement-related activity of the brain with the inflow of congruent somatosensory feedback from, e.g., electrical stimulation [194], rehabilitation robots, or exoskeletons [125]. Movement-related cortical potentials [198] or event-related desynchronization [199, 200] have typically been extracted from single-trial EEG recordings and used as the control signals for triggering the external device that is going to elicit the somatosensory feedback. Patients are asked to imagine or attempt to perform a movement which is then detected through EEG recordings and translated into a device command that provides feedback to the patient; this can, e.g., be somatosensory afferent or visual feedback. Especially the somatosensory afferent feedback may be important for rehabilitation since it is a motor learning task [201, 202].

As mentioned in Chapter 1, the underlying physiological mechanism for motor learning is neural plasticity [197], and it has been shown in several studies that the neural plasticity can be induced by BCI training [125, 194, 203]. In these studies, it has been suggested that Hebbian-associative plasticity is induced by pairing motor cortical activity with relevant somatosensory afferent feedback in the same way as has been done in paired associative stimulation protocols [204]. The difference between BCI and paired associative stimulation is that the motor cortex is activated through imagined movements rather than by stimulation so that brain activation corresponds to the natural activity [205]. The imagined movement must be detected on a single-trial level immediately during the

execution to obtain the strict temporal association between motor cortical activity and somatosensory afferent feedback which is needed to induce plasticity [203], as validated in several previous studies [125, 206–209]. It has previously been shown that proprioceptive/somatosensory afferent feedback induces more cortical changes than visual feedback when combined with a BCI [210]. It has been suggested that improved BCI performance could increase the induction of plasticity [194]. Thus, different approaches have been investigated to optimize the BCI performance, such as using different signal processing techniques [56, 198, 211–216], combining two different control signals [200], training the user [126], and facilitate motor imagination [217]. In addition to the technical optimization of the BCI, it is likely that the induction of plasticity can be improved by identifying the optimal type of afferent feedback. Motor-driven orthotic devices and exoskeletons have been used in BCI-related studies and electrical stimulation has been applied with different parameters in terms of stimulation frequency, intensity and location (nerve or muscle stimulation) [125, 188, 203, 218–224]. These afferent feedback modalities have all been shown to induce plasticity when they were paired with motor cortical activity from imagined or executed movements. Different electrical stimulation frequencies, parameters and locations as well as passive movements have been compared, but due to a large number of combinations it is not feasible to include every combination in a single study. The aim of the current study is to investigate the induction of plasticity when imagined movements are detected in a self-paced BCI system and paired with: (1) single-pulse electrical nerve stimulation, (2) passive movement through a motorized orthotic device, and (3) the combination of electrical nerve stimulation and passive movement. The plasticity induction of the BCI training is evaluated through motor evoked potentials (MEPs) elicited with transcranial magnetic stimulation (TMS). We hypothesize that it is possible to induce plasticity in all three scenarios, but that there is an additive effect by combining electrical stimulation with passive movements

6.1.1 Materials and Methods

6.1.1.1 Participants

Twelve healthy participants were included in the study (four women: 25 ± 4 years). All participants gave their written informed consent prior to the experiment, and they filled in a TMS questionnaire for eligibility based on the recommendations in [225]. All

procedures were approved by the Northern B Health and Disability ethical committee (17/NTB/261) New Zealand. All the procedures were carried out according to the Helsinki Declaration.

6.1.1.2 Experimental Setup

The experiment was divided into three experimental sessions that all followed the same structure where the only difference was the type of afferent feedback: (1) BCI-triggered electrical nerve stimulation, (2) BCI-triggered passive movements, and (3) BCI-triggered electrical nerve stimulation and passive movement. The order of the experimental sessions was randomized, and experimental sessions were separated by at least 24 h. Initially, the participant was seated in a comfortable chair and asked to do 50 self-paced movements, while continuous EEG and EMG was recorded. These movements were used to calibrate the BCI system. After the calibration of the BCI system, the stimulation sites and parameters for the TMS and electrical stimulation were determined. Before the BCI intervention, 15 MEPs were recorded; this was repeated immediately after and 30 min after the BCI intervention. The BCI system was calibrated in each of the three experimental sessions. The BCI intervention lasted until 50 correct pairings of imagined movements and afferent feedback were obtained.

6.1.1.3 Recordings

EEG Ten channels of continuous EEG were recorded from FP1, F3, Fz, F4, C3, Cz, C4, P3, Pz, and P4 with a sampling frequency of 2048 Hz (Refa amplifiers, TMSi, TMS International, Zuidplas, The Netherlands). FP1 was used to monitor eye movements and eye blinks. The location of these channels over the EEG cap is indicated in Fig. 6.1. The channels were referenced to the right earlobe. During the experiment all channels were below $5k\Omega$. The participants were instructed to sit as still as possible and to minimize blinking.

Surface EMG MEPs were recorded with surface EMG electrodes. Two electrodes (20 mm Blue Sensor Ag-AgCl, AMBU A/S, Ballerup, Denmark) were placed on the belly of the right tibialis anterior muscle in a bipolar configuration with the ground electrode

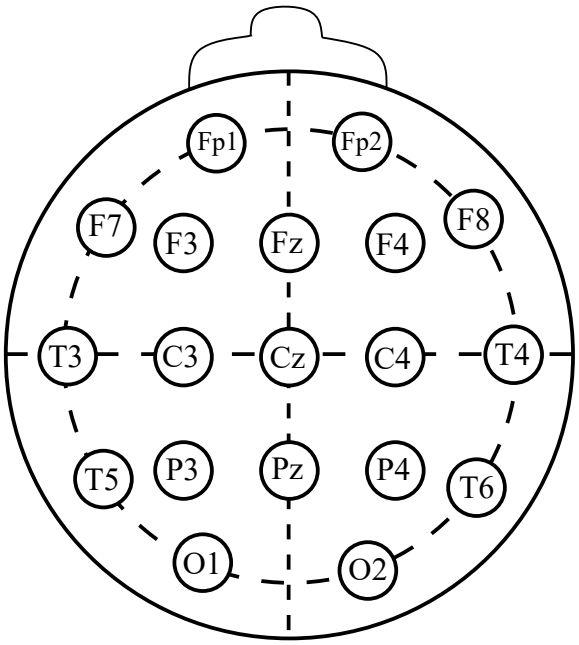

FIGURE 6.1: Channel location on the EEG cap.

placed on the tibia. The signals were amplified with a custom-made amplifier with a gain of 1000 and a sampling frequency of 4000 Hz. The signals were band-pass filtered from 20–1000 Hz.

6.1.1.4 Stimulation and Motorized Orthotic Device

Transcranial Magnetic Stimulation Single pulse TMS was used to elicit MEPs in the tibialis anterior with a Magstim 200 (Magstim Company, Dyfed, UK) using a figure-of-eight double-cone coil with a posterior-anterior current direction. Before recordings, the optimal stimulation site was determined as the site where the largest peak-to-peak amplitude of the MEP in tibialis anterior was elicited compared to the adjacent areas. This area was marked to make sure the coil was placed in the same position for the pre-, post-, and post-30 min intervention measurements. The resting threshold was then determined as the lowest stimulator output where five out of 10 peak-to-peak amplitude MEPs were greater than $50\mu V$. In the pre-, post-, and post-30 min intervention measurements, 15 stimuli were given at 120% of the resting threshold. Each stimulus was separated by 5–7 s.

Electrical Stimulation Peripheral nerve stimulation was delivered to the deep branch of the common peroneal nerve supplying the tibialis anterior. The electrical stimulation was delivered through two stimulation electrodes (32 mm, PALS, Platinum, Patented Conductive Neurostimulation Electrodes, Axelgaard Manufacturing Co., Ltd., Fallbrook, CA, USA) that were placed on the skin overlying the nerve with the cathode placed proximal and the anode placed distal. The optimal stimulation site was determined by searching for the location that determined activity in the tibialis anterior without any activity in synergistic or antagonistic muscles (as determined by palpation of the muscles). The motor threshold was then determined as the lowest intensity required to elicit a palpable response in the tibialis anterior muscle. In the two interventions involving electrical stimulation, a single 1-ms wide pulse was delivered with an intensity corresponding to 110% of the motor threshold.

Passive Movements Through the Motorized Orthotic Device The passive dorsiflexion ankle movement was delivered through a custom-made motorized orthotic device based on the design of an ergometer [226] coupled with a CAHB–21 linear actuator (SKF, Goteborg, Sweden) arranged together to rotate the ankle joint [63, 227]. The foot and leg were fixed to the orthosis with straps. The initial position of the orthotic device corresponded to 110° of plantar flexion. The orthosis performed a 15° dorsiflexion rotation around the ankle joint at a constant angular speed of $40°s^{-1}$.

6.1.1.5 Brain-Computer Interface

The BCI system used in this study has been previously described [194]. Briefly, the system was trained from 50 self-paced movements. From these movements, an EEG signal template of the initial negative phase of the movement-related cortical potentials was extracted from the onset of the movement (determined from the EMG). For this purpose, the EEG was band-pass filtered from 0.05–10 Hz with a 2nd-order zero-phase shift Butterworth filtered, down sampled (at 32 Hz) and filtered with an optimised spatial filter [206] with Cz as the centre electrode. Template matching was used to calibrate the BCI detector as explained in [194, 206]. The threshold for detecting the movements was obtained through a receiver operating characteristics curve to achieve a trade-off between the true positive and false positive detections/10 min (length of the

training data set) as shown in Figure 6.2. When the output from the template matching exceeded the threshold, the BCI system registered it as a movement. During the BCI intervention, the BCI system was disabled for five seconds after an event was detected and in this interval the participant indicated if it was a true positive detection or a false positive detection. The participants also indicated the presence of false negatives. Moreover, the detector was disabled if the activity in FP1 exceeded a $125\mu V$ threshold. The BCI system performance was evaluated through the true positive rate (TPR) and number of false positive detections per minute (FPm).

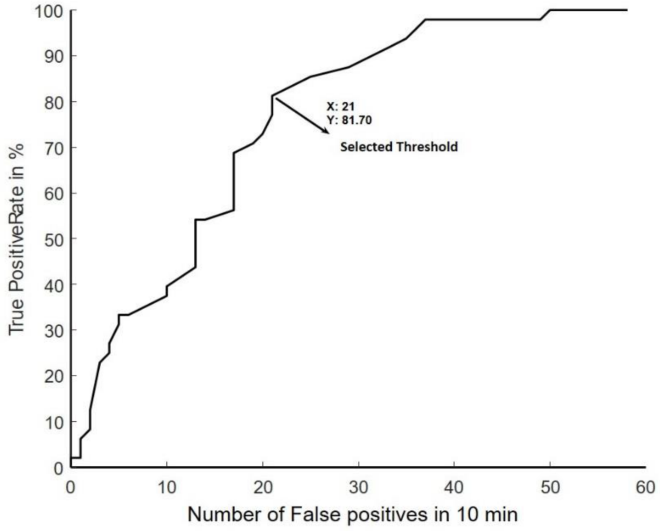

FIGURE 6.2: ROC curve from a training set.

Statistical Analysis In the statistical analysis, we were concerned with three questions: (a) Did the BCI performance have an effect on the MEP amplitude? (b) did the pre- to post- and post-30 treatment effect of electrical stimulation (ES), passive movements (PM), and electrical stimulation combined with passive movements (Comb) induced plasticity? (c) What was the difference in these effects across the three paradigms? We evaluated (a) in terms of absolute units (mV) using blinded covariate analysis [228], and (b), (c) in terms of both absolute units and relative units (% change). For absolute units, we computed the peak-peak amplitudes of the MEPs and averaged them across the 15 trials. For the relative units, we computed subject wise % changes from the averaged peak-peak amplitudes of the MEPs as (post- − pre-)/pre-× 100. To answer these questions, we setup linear mixed regression models. In all the models, time, session, and subject were codified as categorical variables. All the remaining variables were codified as continuous. The statistical analysis was performed in R (R Foundation for Statistical

Computing) version 3.5.0. lme4 package version 1.1-17 was used for fitting all the models [229]. For question (a), four performance metrics were considered as covariates: (i) true positive rate (TPR), (ii) false positives per minutes (FPm), (iii) time taken to complete the task (T_t), and (iv) total number of movement repetitions executed (M_r). Following linear mixed model, presented in R formula syntax, was used for this purpose:

$$\text{MEP}_{abs} \backsim 1 + \text{MEP}_{pre} + \text{Time} + \text{TPR} + \text{FP}_m + T_t + M_r + (1|\text{Subject}) \tag{6.1}$$

This model estimates MEP amplitudes at two time points (post- and post-30) while also considering the effect of pre- MEP amplitudes (MEPpre), TPR, FP_m, T_t, and M_r. The random intercept term for subjects (1|Subject) entered into the model, estimates the variance across the subjects. This model was fitted to data from the three sessions. However, the Session variable was not added to the model to keep the analysis blinded as suggested by [228]. This procedure has two benefits. First, it allows for an unbiased selection of covariates as the selection is done before obtaining the final results. Second, it leaves out unnecessary covariates which can potentially act as noise in the final model, thus, improving the statistical power. It was planned a priori that a covariate which explained greater than or equal to 5% of the variance in the data will be considered as potentially having a significant effect on the MEP amplitudes. Furthermore, it will be added to models used for answering questions (b) and (c) in order to statistically control for its effect. Semi-partial R^2 statistic was obtained using the Kenward-Roger method as a measure of explained variance. The r2glmm package version 0.1.2 was used for this purpose [230]. For questions (b) and (c), following model, expressed as an R formula, was used for absolute units:

$$\text{MEP}_{abs} \backsim 1 + \text{Session} \times \text{Time} + \text{MEP}_{pre} + T_t + (1|\text{Subject:Session})\,, \tag{6.2}$$

This model estimates MEP amplitude across the three sessions (ES, PM, Comb) at both time points (post-, post-30) while adjusting for the pre- MEP amplitudes. This model also controls for total time taken to complete the task as it explained more than 5% of the variance in MEP amplitudes. This model is similar to model 1 suggested by [231] with two important improvements. First, as the subjects across the sessions were same and it is reasonable to assume that the subjects respond differently to the three paradigms,

thus, we used a subject and session wise random intercept (1|Subject : Session) to estimate the between subject variance. This model also suits to the repeated measures design of this study. Second, as the MEP amplitudes are always positive and are not normally distributed, we used Gamma distribution to model the data. The choice of the link function (identity or log) was evaluated using Akaike information criterion corrected for small samples (AICc). The AICc penalises both under fitting and over fitting. We used the log link. For relative units, we setup the same model with the exception that we used Gaussian distribution and identity link. The residuals of the model were normally distributed. The model, expressed as an R formula, is given below:

$$\text{MEP}_{\%} \backsim 1 + \text{Session} \times \text{Time} + \text{MEP}_{pre} + T_t + (1|\text{Subject:Session})\,, \tag{6.3}$$

Significance level was set at 0.05. Effects estimated by the model were reported with their standard errors. Pair-wise contrasts were performed with Tukey's HSD method.

6.1.2 Results

6.1.2.1 BCI Performance

The performance metrics and the corresponding variance explained statistics are given in Table 6.1. Time taken to complete the task explained 6% of the variance in MEP amplitudes and, therefore, was included as a covariate to statistically control its effect in the subsequent models used to estimate MEP_{abs} and $\text{MEP}_{\%}$.

TABLE 6.1: BCI performance metrics and percentages of variance explained in MEP amplitudes by each metric.

Performance Metric	**Mean[min,max]**	**Variance Explained** $R^2(\%)$
TPR	78.13[58.82,96.15]%	1.5
FP_m	1.21[0.22,4.62]	0.8
T_t	13.42[7,23]min	6.0
M_r	64.36[52,85]	0.3

TABLE 6.2: The linear trends between T_t and MEP_{abs} and $\text{MEP}_{\%}$ estimated by the statistical models.

Trend for T_t	**Estimate**	**Std. Error**	$\rho, H_0 : \mu = 0$
With MEP_{abs} (mV/min)	0.01	0.02	$z = 0.65, \rho = 0.51$
With $\text{MEP}_{\%}$(%/min)	1.32	2.79	$t[31] = 0.47, \rho = 0.63$

The linear trends between T_t and MEP_{abs} and $\text{MEP}_{\%}$ estimated by the statistical models are given in Table 6.2. These results suggest that the time taken to complete the task did not have a statistically significant effect on the MEP amplitudes. As the remaining performance metrics did not explain considerable ($R^2_{\text{partial}} < 5\%$) variance in the data, they were not added to the statistical models and, thus, their trends were not estimated. To further elaborate on the differences in true positive rate (TPR) and false positive detections per minute (FP_m) across all subjects and sessions, their means and standard errors are given in Figure 6.3, where ES, PM and Comb denote electrical stimulation, passive movement, and combined electrical stimulation and passive movement, respectively. One-way ANOVAs suggested that there was no difference between the sessions in terms of both the true positive rate ($F(2, 22) = 0.001; \rho = 1.0$) or number of false positive detections per minute ($F(2, 22) = 0.59; \rho = 0.57$). These results together with the explained variance statistic suggest that none of the BCI performance metrics had any significant effect on the MEP amplitudes.

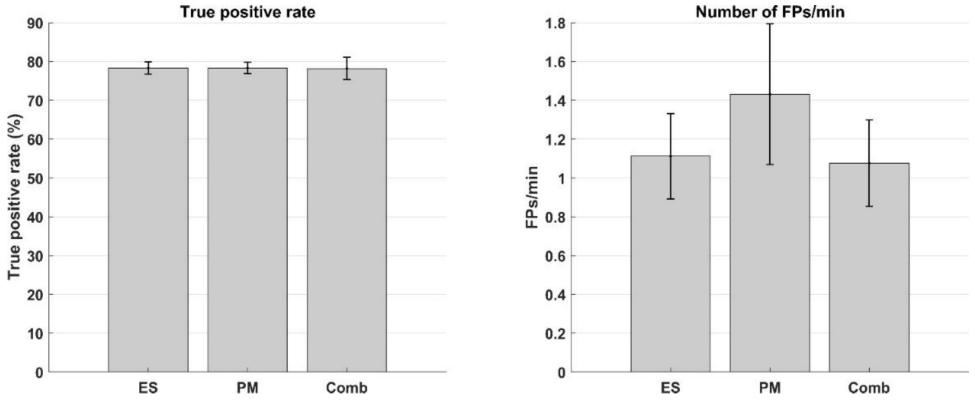

FIGURE 6.3: TPR and FP_m detections (mean ± standard errors) across all subjects.

6.1.2.2 MEP Size

The peak-peak MEP raw amplitude values in pre- to post- and post-30 times for all the subjects are plotted in Figure 6.4. The individual trends suggest that there was a larger increase in pre- to post-MEP amplitude in case of ES and Comb compared to PM. The pre- to post-effect sizes estimated from the statistical models are given in Table 6.3. These effects were computed with T_t set to its mean value (13.42 min). Similarly, pair-wise contrasts across the sessions at the two time points are given in Table 6.3. The pair-wise contrasts across sessions and time are given in Tables 6.4 and 6.5, respectively.

As a log link was used in modeling the MEP amplitudes in absolute units, thus the contrasts performed on the log scale are presented as ratios on the response scale.

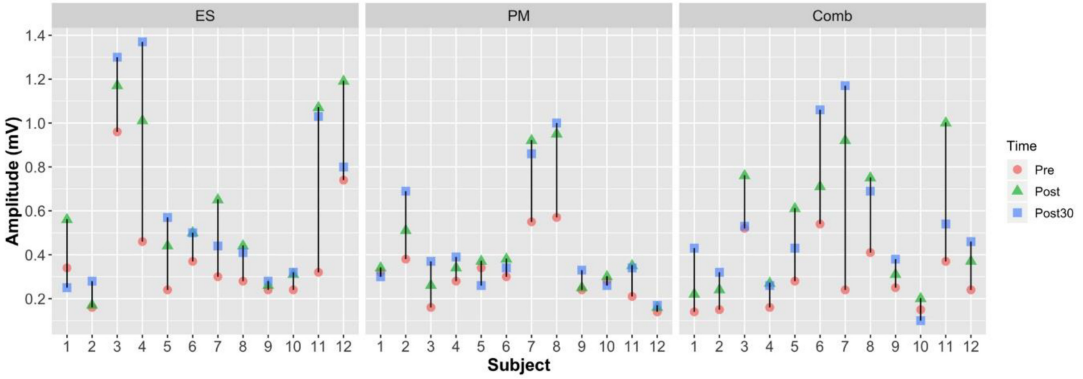

FIGURE 6.4: Peak-peak MEP amplitudes for all the subjects.

These results suggest that the three paradigms increased ($\rho < 0.05$) the MEP amplitudes from pre- to post- and post-30 in terms of the absolute units. The effect sizes of Comb paradigm were larger than ES and PM, although, these differences were not statistically significant ($\rho > 0.05$).

TABLE 6.3: Pre- to post- and post 30-effect sizes along with the standard errors estimated from the statistical models.

Session	**Time**	MEP_{abs} **(mV)**	**Std. Error (mV)**	$z, \rho, H_0 : \mu = 0$
ES		0.21	0.05	$z = -6.97, \rho < 0.001$
PM	post-	0.17	0.03	$z = -8.83, \rho < 0.001$
Comb.		0.22	0.04	$z = -7.98, \rho < 0.001$
ES		0.20	0.05	$z = -7.13, \rho < 0.001$
PM	post-30	0.19	0.04	$z = -8.40, \rho < 0.001$
Comb.		0.22	0.04	$z = -8.00, \rho < 0.001$
Session	**Time**	$MEP_{\%}$ (%)	**Std. Error** (%)	$z, \rho, H_0 : \mu = 0$
ES		81.26	32.86	$t[35.29] = 2.47, \rho = 0.02$
PM	post-	41.16	29.59	$t[36.37] = 1.39, \rho = 0.17$
Comb.		94.90	27.99	$t[37.05] = 3.39, \rho < 0.01$
ES		80.44	32.86	$t[32.29] = 2.47, \rho = 0.02$
PM	post-30	56.37	29.59	$t[36.37] = 1.91, \rho = 0.06$
Comb.		104.69	27.99	$t[37.05] = 3.74, \rho < 0.001$

Discussion

The study confirmed that neural plasticity can be induced by BCI-triggered electrical stimulation or passive movements. However, the three afferent feedback modalities did not differ in their effects on plasticity. The contrasts suggested that electrical stimulation

TABLE 6.4: Contrasts across sessions and their standard errors estimated from the statistical models.

Contrast	**Time**	**Ratio**	**Std. Error (Ratio)**	$z, \rho, H_0 : \mu = 1$
ES/PM	post-	1.23	0.25	$z = 0.99, \rho = 0.57$
ES/Comb.		0.94	0.19	$z = -0.32, \rho = 0.95$
PM/Comb.		0.77	0.15	$z = -1.32, \rho = 0.39$
ES/PM	post-30	1.08	0.22	$z = 0.39, \rho = 0.92$
ES/Comb.		0.91	0.18	$z = -0.46, \rho = 0.89$
PM/Comb.		0.84	0.17	$z = -0.85, \rho = 0.67$
Contrast	**Time**	**Difference (%)**	**Std. Error (%)**	$z, \rho, H_0 : \mu = 0$
ES	post-	40.10	29.90	$t[42.22] = 1.34, \rho = 0.38$
PM		-13.64	301.16	$t[42.00] = -0.45, \rho = 0.89$
Comb.		-53.74	29.77	$t[42.33] = -1.81, \rho = 0.18$
ES	post-30	24.06	29.90	$t[42.22] = 0.81, \rho = 0.70$
PM		-24.25	30.16	$t[42.00] = -0.80, \rho = 0.70$
Comb.		-48.31	29.77	$t[42.33] = -1.62, \rho = 0.25$

TABLE 6.5: Contrasts across time and their standard errors estimated from the statistical models.

Contrast	**Session**	**Ratio**	**Std. Error (Ratio)**	$z, \rho, H_0 : \mu = 1$
post-/post-30	ES	1.03	0.08	$z = 0.42, \rho = 0.67$
	PM	0.94	0.07	$z = -1.13, \rho = 0.26$
	ES + PM	1.00	0.08	$z = 0.05, \rho = 0.96$
Contrast	**Session**	**Difference (%)**	**Std. Error (%)**	$t[df], \rho, H_0 : \mu = 0$
pos- – post-30	ES	0.82	16.74	$t[33] = 0.05, \rho = 0.96$
	PM	-15.22	16.74	$t[33] = -0.91, \rho = 0.37$
	ES + PM	-9.79	16.74	$t[33] = -0.59, \rho = 0.56$

consistently resulted in slightly higher mean MEP amplitudes than passive movement and the combination of passive movement with electrical stimulation consistently resulted in slightly higher mean MEP amplitudes than electrical stimulation alone.

Effect of BCI-Triggered Afferent Feedback

All three types of afferent feedback induced neural plasticity when combined with the BCI, but there was no statistically significant difference between the types of afferent feedback although larger percentage changes from pre-to post- and pre-to post-30 were obtained when electrical stimulation was involved. However, there was a large variability between participants, presumably due to factors such as attention and time of the day

[232]. It is also likely that there might be a difference in the amount and type of sensory feedback that is sent to the brain, which depends on the activation of afferents and the type of receptors that are active during the electrical stimulation (no movement of the foot) and the passive movement. For the electrical stimulation, only the nerve innervating the tibialis anterior was stimulated, thus only low-threshold afferents were recruited [233]. Conversely, during the passive movements, cutaneous and high threshold afferents would be activated because of joint movement. Moreover, other non-muscle afferents should also be active via a transcortical loop resulting in an activation which was close to a voluntary dorsiflexion [233, 234]. However, different types of sensory feedback may have different effects on the cortical motor networks when applied as part of an intervention [235]. The latency of the different types of afferent feedback to reach cortex was presumably similar [236, 237]. Moreover, another advantage of having the electrical stimulation over peripheral nerve trunk is that it generates contraction facilitated via central pathways by maximizing the afferent (sensory) volley to spinal cord where sensorimotor integration occurs, resulting in optimal recruitment of the spinal motor neuron [216]. It is known in the literature that if the central contribution is maximized it can lead to reduced muscle atrophy which in turn can be used to restore movement in persons with movement disorders [238]. The observation of no difference between electrical stimulation and passive movements supports previous findings by [220]. This means that the choice of the type of afferent feedback modality may not be crucial, and it should rather be selected based on the available equipment in the rehabilitation centers or by the comfort of the patient. However, contrary to the previous study by [220], in the current study the BCI operated in a self-paced way. The pros of the electrical stimulation are that it is low-cost, and it has been used by many, but the cons are that electrical stimulation can lead to muscle fatigue (especially when using functional electrical stimulation) and it may be painful for some patients (depending on the stimulation parameters). The pros of the motor-driven orthotic device are that there is no muscle fatigue and the movement can be executed with great precision, so it mimics a natural movement. The cons of the motor-driven orthotic device are that it is more expensive than the electrical stimulation and it is less portable. To overcome this latter disadvantage, we developed and used a transportable motorized ergometer [220, 221]. It remains to optimize the passive-movement feedback so that it is as close as possible to the dynamic of a real movement.

Neural Mechanisms

It has been suggested in several BCI studies [125, 194, 203, 239] that the neural mechanisms for the changes observed in BCI intervention studies are similar to that of paired associated stimulation [204], which rely on long-term potentiation properties such as rapid onset, persistence on cessation of stimulation and associativity but with likely differences in the origins of those effects [240]. The increase in cortical excitability was retained at least for 30 min following the intervention [241]. It has previously been shown that this type of BCI intervention is specific [203, 239], which is another indication of that it is long-term potentiation-like plasticity that is induced. Furthermore, the origin of the neural plastic changes was not assessed, but it has been suggested that it is likely to be changes in the cortical plasticity [125, 194, 203, 220].

Limitations

In the current study, we did not detect a statistically significant difference for the alternative hypothesis that ES and PM combined (Comb) have a larger effect in terms of inducing cortical excitability. As the estimated effect sizes supported this hypothesis, the potential reason for not achieving statistical significance seems to be the small sample size ($n = 12$). Sample size for this study was based on the previous studies [125, 194, 203, 220, 241] in which it ranged between 8 and 12. Future studies can plan a higher sample size by using the estimated effects and their standard errors reported in the current study. Another limitation is the effect of the BCI intervention without sensory feedback was not tested as well as afferent feedback without the BCI intervention. However, it has previously been shown that 50 electrical stimuli or passive movements alone do not change the size of the MEPs [125, 203]. The same has been found for the BCI intervention without any afferent feedback [125, 203]. All findings in the current study are based on healthy volunteers which limits the generalization/transfer of the results to stroke rehabilitation. However, similar work has been done for the upper limb where stroke patients have received upper limb BCI training using functional electrical stimulation [192] and rehabilitation robots where functional improvements have been shown [190, 191, 218]. It is likely that similar beneficial effects may be observed for the lower limbs as well [239].

6.2 Induction of neural plasticity via a low-cost open source BCI and a 3D printed exoskeleton

6.2.1 Introduction

The concept of inducing plasticity using a BCI has been shown in several studies; however, this technology is rarely used in rehabilitation clinics and patient's home. This is due to several reasons, one of them being that it is still a fairly new technology, while some of the translational issues include the complexity of the systems in terms of setting up (e.g., mounting the EEG cap and calibrating the system), ensuring a good and stable signal quality, which may require a skilled operator, the mental fatigue of the user, user compliance, the price of the technology, and access to the detection algorithms [20, 242]. In recent years, several low-cost commercial EEG systems have become available [243]. Some of these systems may not be useful for applications where neural plasticity is induced in the motor system, since they do not record electrical activity from the relevant brain areas [242]. However, it is possible to record the electrical activity of the motor cortex with some low-cost EEG systems. Moreover, several research groups have made their detection algorithms publicly available (see, e.g., the OpenViBE project [244]). The feasibility of using such low-cost systems for detecting movement-related brain activity has been outlined recently [245–247], thus making the BCI technology available to a wider audience than BCI researchers. To use the BCI for inducing neural plasticity, besides for neurofeedback applications [248], an external device is needed to provide congruent somatosensory feedback. This could be a stimulator that could stimulate the relevant nerves and muscles electrically, or it could be an exoskeleton. With the current advances made within the design and manufacturing of exoskeletons through 3D printing [249, 250], it has become cheap to create simple exoskeletons for controlling certain joints such as the wrist or ankle. It is possible to create a simple exoskeleton that can perform wrist extensions or the dorsiflexion of the ankle joint with a single actuator [126]. Both of these movement types are important to train during stroke rehabilitation. It has been shown previously that neural plasticity, when quantified with TMS, can be induced using BCI-triggered electrical stimulation and passive movements from rehabilitation robots/exoskeletons for the cortical projections of the lower limb muscles [125, 126, 194–196], but this has not been shown for the cortical projections of the upper

limb muscles, although functional improvements in stroke patients have been reported for the upper limbs (see, e.g., Refs. [191, 192, 251, 252]). Therefore, the aim of this study is to investigate if a BCI-triggered exoskeleton can induce neural plasticity in the cortical projections of the forearm muscles that control wrist extension. Moreover, it will be tested if this is possible using a low-cost EEG amplifier and open source BCI software. Lastly, a cheap 3D-printed exoskeleton will be developed to replicate wrist extension. The BCI-triggered exoskeleton will be evaluated in terms of BCI system performance and the ability to induce neural plasticity.

6.2.2 Materials and Methods

6.2.2.1 Subjects

Eleven healthy subjects participated (four females, age: 28 ± 3 years). Prior to participation, the subjects provided their written informed consent and filled in a questionnaire for their eligibility for TMS based on the recommendations in [225]. All procedures were approved by the local ethical committee (N-20130081), and were in accordance with the Helsinki Declaration.

6.2.2.2 Experimental Setup

Initially, the subjects were seated in a comfortable chair, where the procedures were explained, and they were familiarized with TMS. See Figure 6.5 for a timeline of the experiment. Afterwards, they were instructed and trained on how to perform motor imagination, and they spent 5 min training this. After the motor imagination training, the subjects imagined 30 wrist extensions of the right wrist while continuous EEG was recorded. A visual cue was generated by the "Motor Imagery BCI" in OpenViBE; the visual cue was modified such that 30 idle/rest trials ("REST" was displayed on the screen) and 30 motor imagination trials (a red arrow pointing to the right was displayed on the screen) were performed. The imaginary movement was maintained for four seconds. These trials were used to calibrate the asynchronous BCI for controlling the wrist exoskeleton. During the actual BCI training, the wrist exoskeleton was mounted on the subject on the right forearm and hand. The forearm and hand rested on the armrest of the chair during the training. The subjects were asked to trigger the exoskeleton by

imagining an extension of the right wrist; the training was complete when 50 correct pairings of motor imagination and the movement of the exoskeleton were obtained. The subjects had to keep imagining the movement while the exoskeleton performed the movement. Before, immediately after, and 30 min after the BCI training, TMS measurements were performed, whereby 30 motor-evoked potentials (MEPs) were obtained.

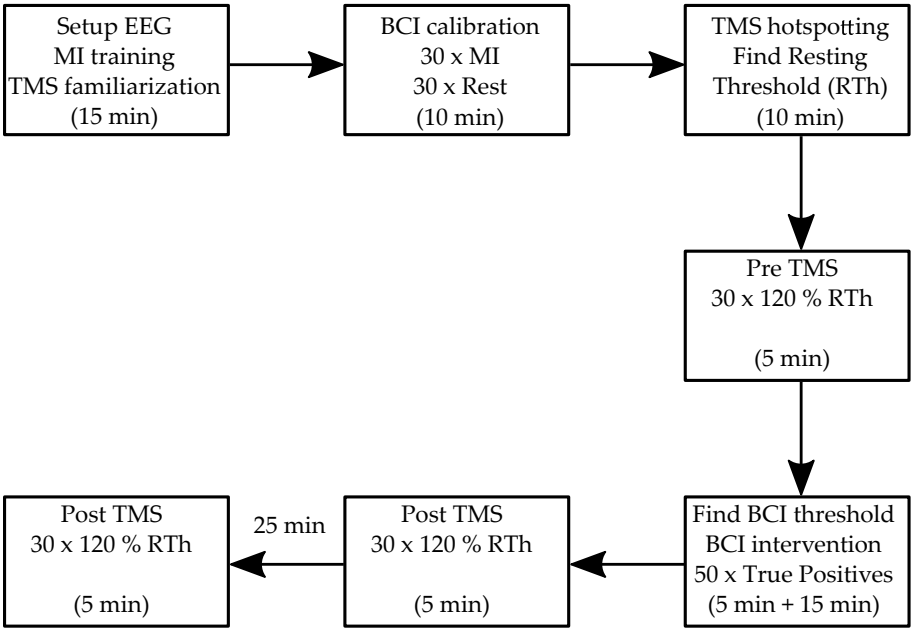

FIGURE 6.5: Timeline of the experiment.

6.2.2.3 Recordings

EEG

Seven channels of continuous EEG were recorded (Cyton Biosensing Board, OpenBCI, Brooklyn, New York, USA) from F1, F2, C3, Cz, C4, P1, and P2 with respect to the International 10-20 System using sintered ring electrodes placed in an EASYCAP EEG cap (EASYCAP GmbH, Herrsching, Germany). The location of these channels are indicated in Fig. 6.1. The signals were sampled at 250 Hz. The ground electrode was placed at AFz, and the reference electrode was placed on the mastoid bone behind the right ear. The subjects were asked to sit still and avoid the contraction of facial muscles and blinking.

EMG

MEPs were recorded using surface EMG electrodes (Neuroline 720, Ambu A/S, Denmark) placed on the extensor digitorum muscle in a bipolar derivation. Two electrodes were placed on the belly of the muscle, which was identified through palpation, and a ground electrode was placed on the distal head of the Humerus bone. The signals were amplified with a gain of 5000 using a customized amplifier (Jan Stavnshøj, Aalborg University), and the signals were sampled at 4000 Hz using the Mr. Kick software (Knud Larsen, Aalborg University).

6.2.2.4 Transcranial Magnetic Stimulation

Motor evoked potentials (illustrated in Figure 6.6) were elicited with a single-pulse TMS (Magstim 200, Magstim Company, Dyfed, UK) using a figure-of-eight coil with a posterior–anterior current direction. First, the optimal stimulation site was determined. This was defined as the location where the largest MEP peak-peak amplitudes were obtained. Next, the resting threshold was determined. It was defined as the lowest stimulation intensity that would elicit an MEP of at least $50\mu V$ peak–peak amplitude in five out of ten simulations. In the measurements before, immediately after and 30 min after the intervention, 30 stimuli were given at 120% of the resting threshold. A random break of $5-7$ s separated two consecutive stimuli.

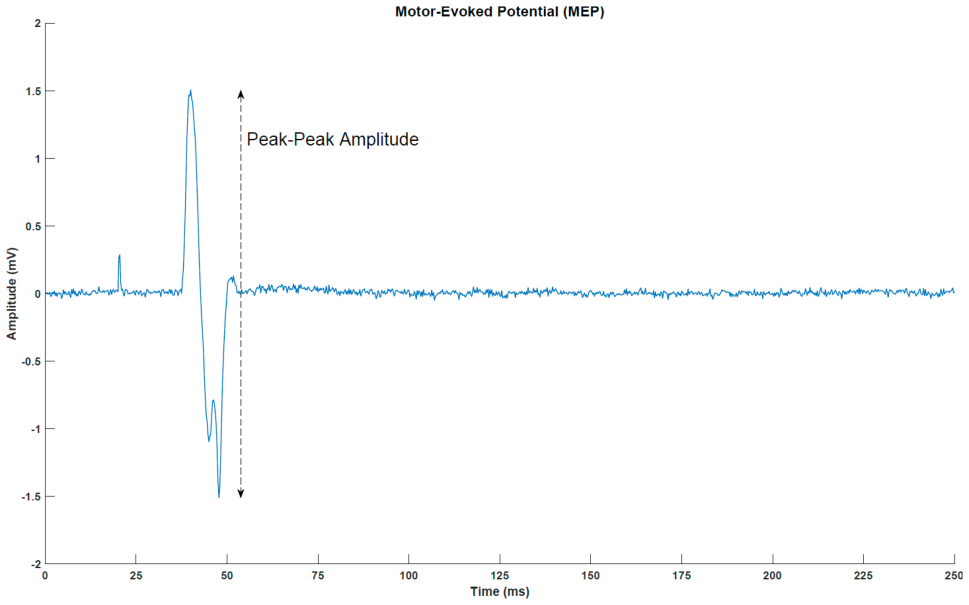

FIGURE 6.6: Motor-evoked potential (MEP) from a representative subject.

6.2.2.5 Brain Computer Interface

The "Motor Imagery BCI" from OpenViBE was used for the detection of the imaginary wrist extensions. The data were bandpass filtered from 8 to 30 Hz using a 5th order Butterworth filter, and a common spatial pattern spatial filter was calculated from the calibration data, which maximized the differences in spectral power between the idle and motor imagery classes. The trials were divided into 1 s windows with a shift of 1/16 s, and the logarithmic band powers were calculated from each window and used as features. Based on the features extracted from the training data, a linear discriminant analysis classifier was trained using 5-fold cross-validation. In the online test, the classification of the imagined movement was altered compared to the original OpenViBE scenario. An imagined movement was detected when eight consecutive windows (8/16 s = 0.5 s) exceeded a threshold that was determined for each subject individually. The determination of the threshold took less than five minutes (see Figure 6.5), and it was done to obtain a trade-off between true positive and false-positive detections. When the BCI detected an imagined movement, a trigger was sent through a transmission control protocol to an Arduino MKR1000 that activated the wrist exoskeleton (see Figure 6.7). The performance metrics of the BCI were the true positive rate, the number of false negatives per minute, and the number of false positive detections per minute. The subjects indicated verbally if the trial was correct (true positive) or incorrect (false positive or false negative).

6.2.2.6 Exoskeleton

The exoskeleton was 3D-printed and developed specifically for this study (see Figure 6.8). The purpose of the exoskeleton was to control the wrist angle position (denoted by Ψ) to replicate an extension of the wrist (see Figure 6.7). The exoskeleton was 3D-printed using the material PLAMAX, and it was actuated by a model L16-P linear piston (Actuonix, Motion Devices Inc ®, Victoria, BC, Canada) which was connected to the X2 input of a linear actuator control (LAC) board (Actuonix, Motion Devices Inc ®, Victoria, BC, Canada) with default settings. A $12V$ power supply was connected to the piston and LAC board in the ($\pm$) X6 inputs. The analog output (A0) and ground reference of the Arduino MKR1000 were connected to the (VC) and (-) X6 inputs of the LAC board, respectively; the Arduino board was programmed and powered via a USB

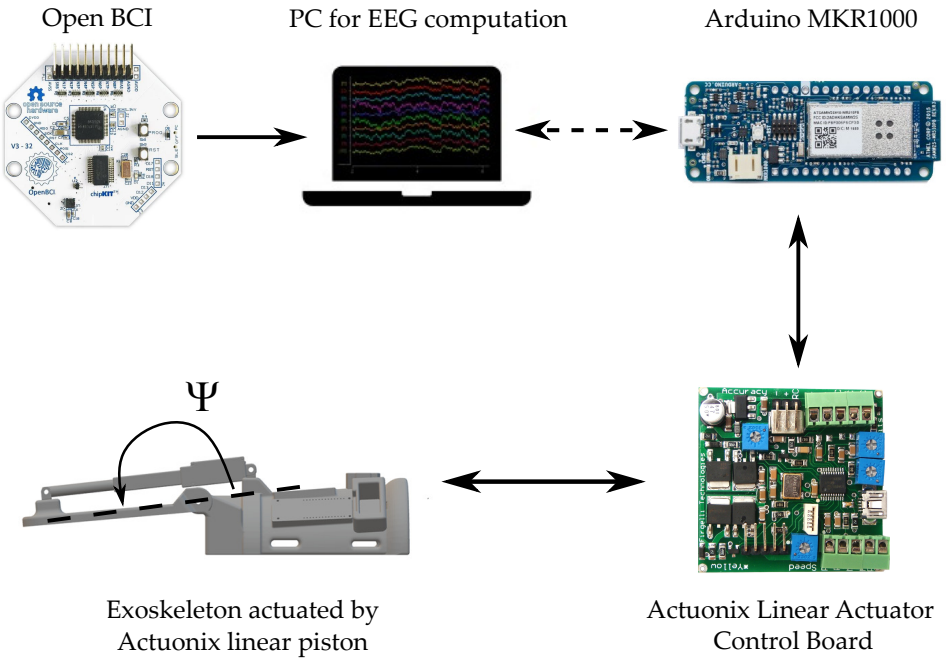

FIGURE 6.7: Overview of the hardware setup.

connection ($5V$ power supply). Finally, the design includes a LED bar that indicates the wrist angle position, which was connected to the ($\pm$) X3 inputs and (P) X4 input of the LAC board. The exoskeleton received an activation signal from the BCI through serial communication to the Arduino board with a baud rate of 9600 (bits per second). The Arduino sends a reference position signal for the linear piston and the LAC board for compensating for the position error signal of the position in order to follow the desired trajectory. The predefined trajectory $\Psi_d(t)$ begins at the initial position $\Psi_d(0) = 180°$, then the wrist is extended in 1.8 s to $\Psi_d(1.8) = 112.36°$ and stays in this position for 0.5 s before returning to the initial position, which also takes 1.8 s. The average movement speed while moving is 37.58°/second. The 3D printed wrist exoskeleton is shown in Figure 6.9.

6.2.2.7 Statistics

A one-way repeated measure analysis of variance (ANOVA) with time as a factor (3 levels: pre-, post-, and post-30 intervention) was performed on the median MEP peak–peak amplitudes to investigate if there was a difference between the MEP amplitudes at the three different time points. A significant statistic test was followed up with a posthoc analysis using Bonferroni correction to avoid multiple comparisons. Moreover, Spearman correlation was calculated between the BCI performance metrics (true positive rate,

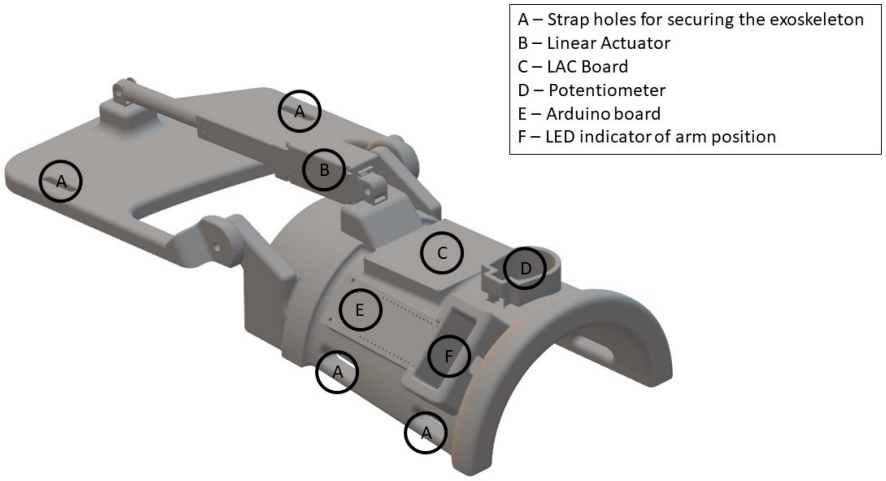

FIGURE 6.8: Isometric view of the 3D-printed exoskeleton.

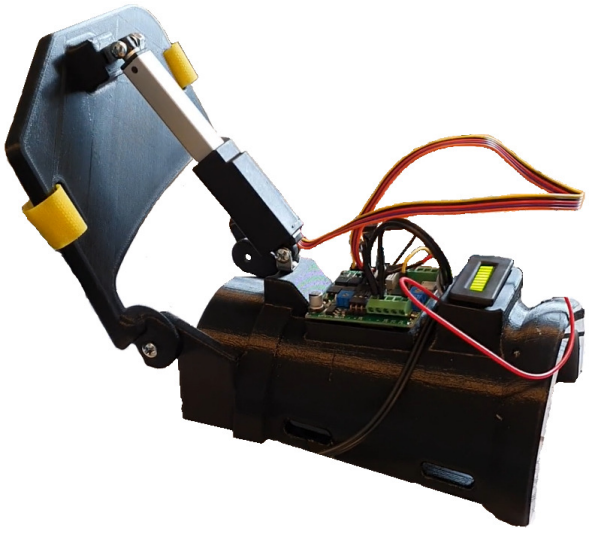

FIGURE 6.9: Isometric view of the wrist exoskeleton.

the number of false negatives per minute, and the number of false positive detections per minute) including the duration of the training and the changes in MEP amplitude. Additionally, the correlation between the MEP changes and BCI performance metrics was calculated with respect to age (Spearman correlation) and gender (Point Biserial correlation). A significant test was assumed when $\rho < 0.05$.

6.2.3 Results

The results are summarized in Table 6.6 and Figure 6.10. The presented ρ-values for the posthoc test have been Bonferroni corrected. On average, $86 \pm 12\%$ of the imaginary wrist extensions were correctly detected by the asynchronous BCI, while there were

1.20 ± 0.57 false positive detection per minute and 0.63 ± 0.58 false negative per minute (see Table 6.6). It should be noted that there is a large standard deviation, especially for the true positive rate, and especially subject 2 had difficulties in activating the exoskeleton through the BCI. The true positive rate was nearly average for subjects 5 and 6, but they had a large number of false positive detections per minute.

TABLE 6.6: Brain computer interface performance.

Subject	**True Positive Rate (%)**	**False Negatives per Minute**	**False Positive Detections per Minute**	**Duration of Training (minutes)**
1	93	0.36	0.55	11
2	56	2.11	0.78	18
3	98	0.1	1.00	11
4	79	1.08	0.5	12
5	81	1.09	2.10	11
6	83	0.67	1.93	15
7	100	0	1.81	16
8	94	0.23	1.77	13
9	86	0.53	1.10	15
10	89	0.43	0.57	14
11	94	0.33	1.11	9
Mean $\pm$sd	86 ± 12	0.63 ± 0.58	1.20 ± 0.57	13 ± 3

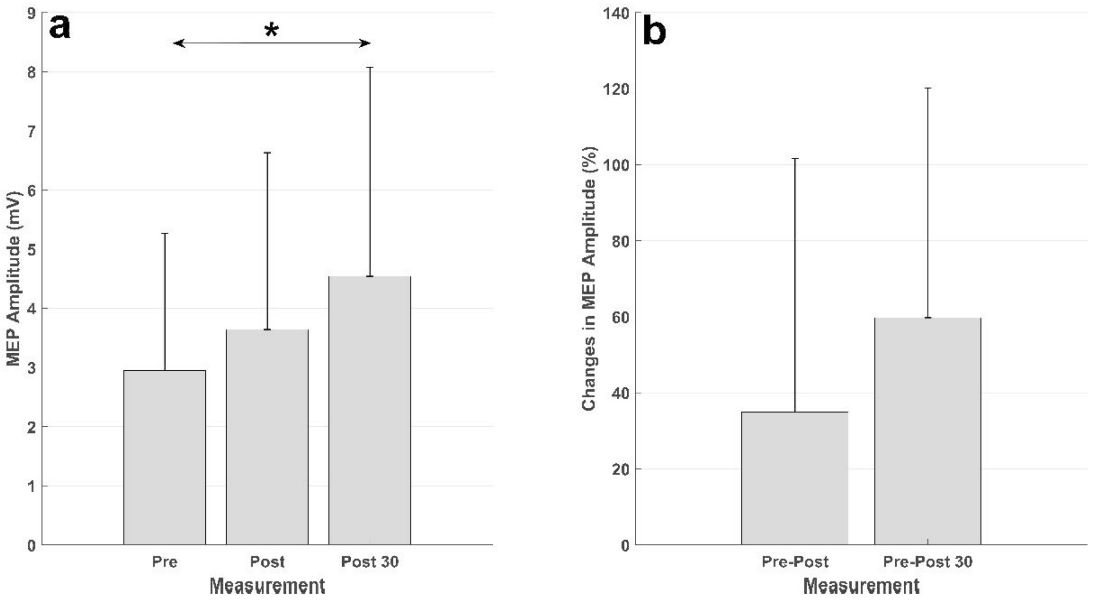

FIGURE 6.10: Summary of the MEP results.

The results of the intervention are presented in Figure 6.10. There was an increase in the MEP from before intervention to immediately after, and 30 min after, the intervention in both absolute units (mV) and relative units (percentage). The statistical analysis

showed a significant effect of time ($F(2, 20) = 4.63$; $\rho = 0.022$). The posthoc analysis revealed a significant increase in the MEP amplitude from the measurement before the intervention to the measurement 30 min after the intervention ($\rho = 0.028$). There was no difference between the MEP from the measurement before the intervention and that immediately after ($\rho = 0.73$), or the MEPs in the measurements after the intervention ($\rho = 0.34$).

There was no correlation between the true positive rate (correlation coefficient: 0.36; $\rho = 0.28$), the number of false positive detections per minute (correlation coefficient: -0.35; $\rho = 0.30$), the number of false negatives per minute (correlation coefficient: -0.39; $\rho = 0.24$), or duration (correlation coefficient: 0.31; $\rho = 0.36$), and the changes in MEP amplitude from before to 30 min after the intervention. Age and gender did not correlate with any of the other measures.

6.2.4 Discussion

It was possible to detect imaginary wrist movements with a low-cost BCI with a true positive rate of $86 \pm 12\%$, with 1.20 ± 0.57 false detection and 0.63 ± 0.58 false negative per minute. The BCI training with the exoskeleton led to increased MEPs after the training with respect to the pre-intervention measurement. There was a non-significant increase from pre- to post-intervention measurements of $35 \pm 60\%$, and a significant increase from pre- to post-30 min intervention measurements of $67 \pm 60\%$.

6.2.4.1 Induction of Plasticity

The BCI-triggered exoskeleton movements increased the excitability of the cortical projections to the forearm extensor muscles. The increase in MEP size was similar to what has been reported previously for the electrical stimulation of the radial nerve based on an associative BCI, which was approximately 50% compared to baseline MEPs [253]. In addition, the changes in excitability are in a similar range of what has been reported previously for BCI-triggered electrical stimulation of the common peroneal nerve and exoskeleton movement of the ankle joint. The BCI intervention in these studies has consistently reported increases in corticospinal excitability in the range of $40 - 100\%$

[125, 126, 194–196, 253]. In this study, the increase from pre- to post-intervention measurement was not significant, however, it could be attributed to the large standard deviation of approximately 60%, or to the fact that the effect of the intervention takes some time to consolidate. Large variability has commonly been reported in neuromodulation studies where the effect of the intervention was quantified using MEPs elicited through TMS [125, 126, 194–196, 220]. The variability in the MEP size is affected by multiple factors, such as attention and time of day (reviewed in [232, 254]), but it may also be due to the variable response of neuromodulation interventions [255–258]. It should also be noted that there exist other types of techniques that have been used for the induction of neural plasticity and proposed for stroke rehabilitation, and that activate the cortical brain areas [28]. One of these techniques is repetitive TMS, whereby the cortical excitability of specific brain areas can be upregulated, which has led to increased amplitudes of motor-evoked potentials [259]. TMS has also been paired with afferent inflow from the electrical stimulation of a peripheral nerve (paired associative stimulation). This protocol has been used to consistently induce neural plasticity when the correct interstimulus interval between the magnetic and electrical stimulation has been selected [254]. However, the use of TMS may not be tolerated well by some stroke patients [260], and there would be safety precautions to consider [225]. Another way to activate the motor cortex is by the use of transcranial direct current stimulation, which has been used to increase the excitability in the motor cortex [261–263]. Moreover, this technique has been used for priming before BCI training, but there is no clear indication of an additive effect [218, 264]. However, it has been shown that transcranial direct current stimulation can improve the BCI performance [218], possible through the modulation of the mu event-related desynchronization [265].

The induction of plasticity in this study is expected to be due to the combination of motor imagery and afferent feedback that was temporally correlated. Two control experiments could have been performed to investigate the effect of motor imagery alone on the MEP and the effect of passive movement alone on the MEP amplitude. However, the control experiment for motor imagery has been conducted three times, wherein 50 imaginary movements have been performed, and no change in MEP amplitudes has been reported [125, 194, 219]. For the afferent feedback alone (i.e., passive movement in this study), it has been reported that 50 passive movements do not change the MEP amplitudes [125], and when delivering afferent feedback through electrical stimulation alone (50

stimuli), no change in MEP amplitudes has been reported [194, 266]. The changes in plasticity in this study are expected to be mediated through long-term potentiation (LTP)-like changes, as has been suggested in several previous studies using a similar methodology [125, 195, 219]. The criteria of LTP-like plasticity include associativity (pairing between motor imagery and afferent feedback from the passive movement), rapid onset (indicated by the post-intervention measurement), and lasting effects (at least 30 min, as indicated by the post-30 min intervention measurement) [241]. There was only a measurement 30 min after the intervention, but the changes associated with this intervention have been reported to last at least 60 min [218]. It is possible that the effects last longer, but probably not longer than 24 h. It has been reported that there was no difference in MEP amplitude between two pre-intervention measurements before two similar plasticity-inducing protocols, when separated by 24 h [266]. Another criterion for LTP-like plasticity is specificity, which was not tested in this study, but it has been reported that this type of intervention is specific [203]. The changes in the neural plasticity that were observed could happen throughout the nervous system, but it has been suggested in several studies using the stretch reflex that the changes are supraspinal [125, 194, 219, 220].

6.2.4.2 BCI system performance

The BCI system that was used in this study performed well in terms of the true positive rate and number of false positive detections per minute. The performance is comparable with other asynchronous BCI studies that have been used for inducing plasticity, which have reported true positive rates in the range of $67 - 85\%$ and a number of false positive detections per minute in the range of $0.5 - 2.8$ [125, 126, 192, 194–196, 253]. The approaches to movement intention detection in those studies have primarily relied on movement-related cortical potentials, but the results of the current study show that a BCI based on sensorimotor rhythms is just as effective in terms of movement intention detection, and it has also been used successfully for BCI training in stroke patients [191, 192, 218, 267]. The BCI performance of the participants in this study was variable, but there was only a single participant that experienced low control (true positive rate of 56%). It would be possible to reduce the detection threshold to allow a higher true positive rate, but that also increases the number of false-positive detections per minute. However, the number of false-positive detections could potentially be controlled

using a paradigm whereby the BCI only accepts inputs in predefined periods, instead of always being active, as in the asynchronous paradigm, or if the number of windows is increased when the detection is exceeded; the latter approach would increase the detection latency. It has been shown previously that the afferent feedback should coincide with the movement intention (i.e., short detection latency) [203], but recent findings have suggested that plasticity can be induced with less strict detection latencies [195]. This may allow the use of residual EMG, from which it is possible to decode multiple movement types [242], which could introduce some task variability in the training [201], and it may be easier for the stroke patients to control the exoskeleton. The correlation analysis showed that there was no correlation between the induction of plasticity in terms of peak–peak amplitudes in the MEP and the performance metrics of the BCI system. This may suggest that the current level of BCI system performance is sufficient for inducing plasticity, and that it may not be needed to optimize the system further from the movement detection point of view, although it should be pointed out that correlation analyses were performed on a limited sample wherein all subjects (except one) had good performance. It has been reported previously that the true positive rate, number of false positive detections and total time of the intervention explain little of the variance in the peak–peak amplitude of the MEP, with the duration explaining more than the other two measures [126, 195]. However, in a similar BCI study, Niazi et al. reported a statistically significant correlation of 0.8 between the BCI system's performance and changes in MEP amplitude in eight healthy subjects [194]. The BCI system performance in that study was calculated as the ratio between the true positive rate and false positive detections; when performing the same calculation in the current study, a similar significant correlation is observed (correlation coefficient: 0.64; $\rho = 0.034$). This indicates that there is an incentive to improve the BCI performance.

6.2.4.3 Limitations and Future Perspectives

In this study, it was shown that young healthy participants could control the BCI, and it could be used for inducing neural plasticity. These findings should be validated in future studies with the intended end-users, which are stroke survivors with motor impairment who often are more than 65 years old. The motor cortex excitability decreases with age [232], but it has been shown that the MEP amplitudes can increase 100% in stroke patients using an associative BCI protocol [239]. It is likely that the reported BCI

system's performance will be slightly lower for stroke patients [198, 268, 269], and if the same experimental protocol is used, it must be considered that some of the stroke patients may not be able to communicate due to, e.g., aphasia, and hence will not be able to indicate what they intended to do (i.e., true positive, false positive or false negative). An alternative approach to verbal feedback to the experimenter could be to use error-related potentials as a check to indicate if the trial was a true positive or false positive; however, this approach will also be prone to the uncertainty related to the decoding algorithm used for these potentials [270]. The lower BCI system performance for stroke patients may cause frustration, and the performance can be affected by fatigue and inattention. To avoid this, it could be a possibility to implement the BCI training in a game to make the training more engaging. Using game mechanics, it would be possible to bias the classifier to improve the performance and conceal it for the user. The proposed system may be used for motor training in this patient group, but it is important to note that an increase in MEP size does not equal improvement in motor function, although increases in MEP size have been reported alongside skill acquisition in healthy participants [197] and motor recovery in stroke patients [239, 271]. The BCI training may be used as a training intervention in itself, but it could also be possible to utilize the lasting increase in the MEP size (more than 30 min) in a rehabilitation scenario where the BCI training is used to prime the nervous system before other types of training, such as physiotherapy or occupational therapy. For the BCI to be used in rehabilitation clinics or home of the patient, the usability should be improved in terms of various aspects, such as the hardware setup, which should be simplified, and the safety of BCI use in acute patients should be assessed [272]. The BCI system should be coded on the Arduino to reduce the amount of hardware, eliminate potential communication problems and delays, which could allow a faster response of the exoskeleton, and the calibration time should be reduced or removed using, e.g., a subject-independent movement intention detector [273, 274]. As regards to communication problems, the robustness of the EEG recordings and usability testing is where the expensive systems potentially differ most from the current cheaper alternatives (this is just a speculation); these are important factors to consider for the technology to be adopted in a clinical setting. It should be investigated if the cost of the BCI (i.e., the EEG amplifier) and exoskeleton can be reduced further. In total, the price for the BCI system (including EEG amplifier, cap, electrodes and cables) and the exoskeleton (all parts including motor, control board and Arduino) was less than USD 1000. Additionally, the design of the exoskeleton should be improved so

it will be easier to put on and take off by the users, and the comfort should be increased as well. This could be done by adapting the exoskeleton to the individual, which would be possible when the components are 3D-printed. Another option could be to use soft exoskeletons, such as a glove or sleeve, that can perform the intended movements [275]. In this study, the exoskeleton was used to execute the intended movement and provide afferent feedback, but it would be possible to use electrical stimulation as well to provide the afferent feedback. In two recent studies, it has been shown that there is no difference between the afferent feedback from electrical stimulation and passive movements from an exoskeleton/robot in terms of the induction of plasticity [126, 220]. This gives the patient and therapist freedom to choose the modality that works best for the patient. Some patients may not be able to tolerate electrical stimulation well, or may have problems in placing the stimulation electrodes correctly, so the usability of the exoskeleton may be better compared to electrical stimulation; however, this has not been tested, and it should be validated in future studies with the end-users. To summarize, for this technology to be used in a home setting the BCI and exoskeleton have to fulfill some requirements, as follows: (1) it must be easy to take on and off the exoskeleton; (2) the software must be easy to use, since the user may not be used to working with technology and may suffer from cognitive impairments to some degree; (3) the system calibration should be done automatically; (4) the hardware setup of the BCI must be simple, and (5) the patient should be able to place EEG electrodes over the motor cortex. The latter may be difficult for patients with severe motor impairments; in a recent study it was shown that half of the stroke participants were able to mount EEG headsets that covered the motor cortex while the other half was unable to mount the EEG headsets [242]. Those that could mount the headset spent roughly 10 min. On the contrary, relatives to the patients and therapists could quickly mount the EEG headset with little prior instruction (5 min). The setup times for them were between 3 and 5 min. Thus, it would be important to have a headset that is easy to mount with one hand for the most affected patients, unless they have someone to help them with the setup.

6.3 Conclusion

In this chapter two different experiments of exoskeletons in rehabilitation were presented. In the first case of study three different types of feedbacks for ankle rehabilitation were

evaluated to determine which strategy provides the best afferent feedback for inducing neural plasticity, these are : electrical stimulation (ES), a passive movement (PM) or a combination of both (Comb).

In order to generate the passive movement, the motoBOTTE was coupled to a brain computer interface (BCI) that after proper training was capable of detecting the intention of movement of the subject, this detection of the intention of movement triggered the tracking of a predefined ankle trajectory in the robot. The same BCI was coupled to the electrical stimulation device and the electrical stimulation signal was provided when the motor intention was detected. The performance of both strategies as well as its combination were evaluated using the amplitude of motor evoked potentials of the Tibialis Anterior muscle, these were obtained via applying transcranial magnetic stimulation.

For the second experiment, a new wrist exoskeleton was designed, 3D printed and built specially for this study, the aim of this investigation was evaluating the performance of low-cost devices for inducing neural plasticity. In this case the experiment consisted on five steps : 1) calibrate a low-cost BCI (OpenBCI) to detect the intention of movement of the subject with the signals from a motor imaginary training session, 2) perform transcranial magnetic stimulation (TMS) to the subject, 3) the subject does a training session of motor imaginary using the exoskeleton to provide a passive feedback to the subject, 4) perform a post-TMS, and finally, 5) perform a post-30 TMS. The efficiency of this strategy with these devices was evaluated again via the motor evoked potentials obtained via TMS.

In both studies the human interaction with the robots has been considered via a BCI, these BCIs were employed only for triggering the tracking of predefined trajectories, which translates into a passive movement feedback for the subject. Therefore, from the perspective of the reference it is operating in open-loop, there is no feedback from the user to the reference signal, besides initializing the tracking of the reference, it would be interesting to consider if a dynamic reference could be generated with the BCI or a combination of EMG with BCI, in this case the system will be operating in closed-loop; but, one of the difficulties found in that direction is that the devices employed must be able to operate in real-time.

Chapter 7

Conclusion and Future Work

This chapter provides a general conclusion of the project and finishes by establishing perspectives about the possible future of this work.

During this project some steps have been made towards the development of a hybrid brain computer interface for post-stroke rehabilitation. The main device employed was the motoBOTTE, an ankle exoskeleton that was designed and built at the LAMIH (UMR CNRS 8201) with the purpose of providing assisted rehabilitation. The different devices that interact with this robot have been described, then, different modeling methodologies were illustrated by employing the motoBOTTE (which is a parallel robot) as example.

The computer-torque and active disturbance rejection control methodologies were adapted to be implemented in parallel robots that are described by a set of differential-algebraic equations. These new methodologies were illustrated using the identified mathematical models for nonlinear controller design. The designs obtained have been implemented in simulation and real-time. Graphics of these implementations were provided.

Considerations for extending the nonlinear sector methodology to the case of nonlinear singular systems were pointed out in the respective chapter, exact convex representations of differential algebraic equations were obtained and illustrated using the mathematical models of the motoBOTTE. A new relaxation that can be used when a double-sum appears in controller and observer design based in parallel distributed compensation (which is a problem of Positivstellensatz) have been obtained, it is based on copositive matrices. Later, controllers based on parallel distributed compensation were designed,

simulated and implemented in real-time for tracking trajectories with the robot and new conditions for controller design for nonlinear singular system were established as well.

Models for estimating ankle force production via EMG were adapted from the existing literature to be used in real-time applications. The efficiency of these models was illustrated by analyzing the data from different subjects walking over a force platform. Inverse kinematics techniques were employed to estimate the ankle force produced by each subject and were compared to the ankle force produced by the mathematical model presented. The value of different anatomical parameters have been taken from state-of-the-art literature, the methodology presented is purely model-based, but modifications have been suggested to improve this force estimation.

Finally, in the last part, a brain computer interface was coupled to the motoBOTTE to investigate which type of feedback (passive movement, electrical stimulation or a combination of both) would be optimal for inducing neural plasticity. In addition to this, a new wrist exoskeleton was designed, 3D printed and build for wrist rehabilitation. This robot was coupled to a brain computer as well. In both cases, the BCI was used to detect the intention of movement of the subject, and this detection triggered a passive movement in the respective robot. Motor evoked potentials were measured pre-, post- and post-30 minutes of the experiments to evaluate the efficiency of employing these kind of systems for rehabilitation.

These following perspectives will be classified in three categories defined as follows : short-term (< 1 year), mid-term ($1 - 3$ years) and long-term (> 3 years).

- ***Short-term*:**

  1. The first next step will be to validate the EMG driven models presented in chapter 5 for estimating the ankle force in real-time using the force sensor from SENSIX shown in Fig 2.6.
  2. A statistical analysis can be performed on the mathematical models obtained in Chapter 2 to evaluate the performance of the models in terms of accuracy when predicting the system's position, i.e., find which model is more accurate.
  3. A statistical analysis can be performed on the controllers designed in Chapter 3 to evaluate which controller is more accurate for tracking predefined trajectories.

4. Once the force estimation models have been validated with the sensor, we can continue by modifying these models, in order to explore if there are other structures capable of achieving a smaller error or may fit for a wider range of subjects; ideally, we would be able to keep or preserve some of the parameters values (anatomical parameters taken from validated models found in the literature) and structure of the model, i.e., equations for passive, active and tendon forces, and we would only need to substitute the first two blocks in Fig. 5.2 by a neural network, for example, to keep some data from anatomical models that have been already validated and take advantage of the universal estimator capabilities of neural networks for blocks that are oversimplified.
5. All the techniques employed for parameter estimation within this manuscript were offline, once we have a fixed structure, it would be interesting if an online parameter estimation can be employed, maybe based on the classical extended Kalman filter. I think that something interesting would be trying to combine convex structures with the Kalman filter to avoid the linearization step of the methodology.

- ***Mid-term*** **:**

1. Once an accurate model for the force production in terms of electromiography signals have been obtained and a force plate is available for performing experiments, it would be interesting to explore the possibility of using an unknown input observer or an interval observer to compute which EMG signals produce that ankle torque.
2. A possible scenario would be trying to improve the reference generation models for controlling the position of the motoBOTTE. This might involve the use of a motion capture system as in chapter 5 to obtain accurate signals from subjects performing dorsiflexion and plantarflexion movements in a sort of swing phase (without being in contact with the ground), but, with a wider time-window. Then applying inverse kinematics to this data in order to determine the ankle force applied by the subject, we could determine and construct some models that can fit to a wide panel of users.
3. Couple a brain computer interface with the myRIO card permanently, in the experiments the EEG signal has been only used to trigger the control and it

would be interesting to capture the signals of the subject while performing exercises with the motoBOTTE and consider them in real-time. Most of the analog inputs and outputs of the myRIO card have been used, but an option to couple the BCI is connecting it to the digital I/O, whether using a low-cost BCI as in Chapter 6 (Open BCI) or building a BCI from scratch, something that would require more time but can be more economic in terms of material.

- ***Long-term* :**

  1. Develop a graphic user interface (GUI) that connected the myRIO card to a computer. This GUI can be used for many purposes such as : verify all the robot (force sensor, piston position and control signal) and subject (EEG and EMG) signals before performing experiments, capture and save these signals after the experiments to create a database.
  2. The database in the previous point, might be able to include useful information from the subjects such as height, age, body mass, gender, ethnicity, personal habits (smoking, alcohol consumption, physical activity, stress level perception), and so on, as well as signals from the experiments performed; in summary, this should include information about stroke risk factors and real-time experiments. The information contained in this database might be shared with other research groups, such that more models for real-time applications and maybe diagnosis can be developed taking advantage of the benefits of combining all these devices at once.
  3. Perform statistical analysis on the parameters of the models developed in this work and try to adapt them to different categories of subjects. This can be done in order to investigate if there is a relation between the physical characteristics (or physical disease) of the subject and the parameters in the model obtained. These relations (if found) can be used to 1) estimate parameters of the models related to specific group of subjects, 2) provide a good initial condition for this parameter values to reduce the time employed for calibration of the models, or 3) classify the users detecting if the signal patterns of the subject and physical parameters correspond to a determined illness.
  4. Develop new tools and indexes that can be used for evaluating the efficiency of assisted rehabilitation therapy in post-stroke patients. Recall that Katz

Index and Bartel Index mentioned in Chapter 1 do not take into account all the possible information that could be acquired with this new hybrid brain computer interface when finished (EEG, EMG, Ankle Force). Those tools have been widely used; but, they were developed more than 4 decades ago, and maybe these should be updated to fit better within the context of robot assisted rehabilitation via brain computer interfaces.

Bibliography

[1] P. Kirchhof, A. Adamou, E. Knight, G. Y.H. Lip, B. Norrving, G. de Pouvourville, and T. Ulmer. How can we avoid a stroke crisis? *Working group report: stroke prevention in patients with atrial fribrillation*, 2009.

[2] G. Gillen. *Stroke rehabilitation: a function-based approach*. Elsevier Health Sciences, 2015.

[3] R. L. Harvey, R. F. Macko, J. Stein, C. J. Winstein, R. D. Zorowitz, et al. *Stroke recovery and rehabilitation*. Demos Medical Publishing, 2008.

[4] E. Vogiatzaki and A. Krukowski. *Modern stroke rehabilitation through e-health-based entertainment*. Springer, 2016.

[5] K. Chevreul, I. Durand-Zaleski, A. Gouépo, E. Fery-Lemonnier, M. Hommel, and F. Woimant. Cost of stroke in france. *European journal of neurology*, 20(7):1094–1100, 2013.

[6] A. Carolei, C. Marini, M. Di Napoli, G. Di Gianfilippo, P. Santalucia, M. Baldassarre, G. De Matteis, and F. Di Orio. High stroke incidence in the prospective community-based l'aquila registry (1994–1998) first year's results. *Stroke*, 28(12): 2500–2506, 1997.

[7] R. J. Farris, H. A. Quintero, S. A. Murray, K. H. Ha, C. Hartigan, and M. Goldfarb. A preliminary assessment of legged mobility provided by a lower limb exoskeleton for persons with paraplegia. *IEEE Transactions on neural systems and rehabilitation engineering*, 22(3):482–490, 2013.

[8] P. Langhorne, J. Bernhardt, and G. Kwakkel. Stroke rehabilitation. *The Lancet*, 377(9778):1693–1702, 2011.

[9] Shanthi Mendis, Pekka Puska, Bo Norrving, World Health Organization, et al. *Global atlas on cardiovascular disease prevention and control*. World Health Organization, 2011.

[10] W. Johnson, O. Onuma, M. Owolabi, and S. Sachdev. Stroke: a global response is needed. *Bulletin of the World Health Organization*, 94(9):634, 2016.

[11] S. Kaptoge, L. Pennells, D. De Bacquer, M. T. Cooney, M. Kavousi, G. Stevens, L. M. Riley, S. Savin, T. Khan, S. Altay, et al. World health organization cardiovascular disease risk charts: revised models to estimate risk in 21 global regions. *The Lancet Global Health*, 7(10):e1332–e1345, 2019.

[12] M. P. Lindsay, B. Norrving, R. L. Sacco, M. Brainin, W. Hacke, S. Martins, J. Pandian, and V. Feigin. World stroke organization (wso): global stroke fact sheet 2019, 2019.

[13] S. Paolucci, G. Antonucci, E. Troisi, M. Bragoni, P. Coiro, D. De Angelis, L. Pratesi, V. Venturiero, and M. G. Grasso. Aging and stroke rehabilitation. *Cerebrovascular Diseases*, 15(1-2):98–105, 2003.

[14] K. Reynolds, B. Lewis, J. D. L. Nolen, G. L. Kinney, B. Sathya, and J. He. Alcohol consumption and risk of stroke: a meta-analysis. *Jama*, 289(5):579–588, 2003.

[15] R. Bonita, J. Duncan, T. Truelsen, R. T. Jackson, and R. Beaglehole. Passive smoking as well as active smoking increases the risk of acute stroke. *Tobacco control*, 8(2):156–160, 1999.

[16] A. C. Fonseca and J. M. Ferro. Drug abuse and stroke. *Current neurology and neuroscience reports*, 13(2):1–9, 2013.

[17] I. Idris, G.A. Thomson, and J.C. Sharma. Diabetes mellitus and stroke. *International journal of clinical practice*, 60(1):48–56, 2006.

[18] P. Harmsen, A. Rosengren, A. Tsipogianni, and L. Wilhelmsen. Risk factors for stroke in middle-aged men in goteborg, sweden. *Stroke*, 21(2):223–229, 1990.

[19] K. Jood, P. Redfors, A. Rosengren, C. Blomstrand, and C. Jern. Self-perceived psychological stress and ischemic stroke: a case-control study. *BMC medicine*, 7 (1):53, 2009.

[20] I.M. Lee, C. H. Hennekens, K. Berger, J. E. Buring, and J. E. Manson. Exercise and risk of stroke in male physicians. *Stroke*, 30(1):1–6, 1999.

[21] P. Belani, J. Schefflein, S. Kihira, B. Rigney, B.N. Delman, K. Mahmoudi, J. Mocco, S. Majidi, J. Yeckley, A. Aggarwal, et al. Covid-19 is an independent risk factor for acute ischemic stroke. *American Journal of Neuroradiology*, 41 (8):1361–1364, 2020.

[22] H. S. Markus and M. Brainin. Covid-19 and stroke—a global world stroke organization perspective. *International journal of stroke*, 15(4):361–364, 2020.

[23] S. Zayet, T. Klopfenstein, R. Kovacs, S. Stancescu, and B. Hagenkotter. Acute cerebral stroke with multiple infarctions and covid-19, france, 2020. *Emerging infectious diseases*, 26(9):2258–2260, 2020.

[24] R. L. Sacco. Risk factors and outcomes for ischemic stroke. *Neurology*, 45(2 Suppl 1):S10, 1995.

[25] J. Hippisley-Cox, C. Coupland, and P. Brindle. Development and validation of qrisk3 risk prediction algorithms to estimate future risk of cardiovascular disease: prospective cohort study. *bmj*, 357:j2099, 2017.

[26] R. Pylypchuk, S. Wells, A. Kerr, K. Poppe, T. Riddell, M. Harwood, D. Exeter, S. Mehta, C. Grey, B. P. Wu, et al. Cardiovascular disease risk prediction equations in 400 000 primary care patients in new zealand: a derivation and validation study. *The Lancet*, 391(10133):1897–1907, 2018.

[27] B. H. Dobkin. Strategies for stroke rehabilitation. *The Lancet Neurology*, 3(9): 528–536, 2004.

[28] A. Zimmermann-Schlatter, C. Schuster, M. A. Puhan, E. Siekierka, and J. Steurer. Efficacy of motor imagery in post-stroke rehabilitation: a systematic review. *Journal of neuroengineering and rehabilitation*, 5(1):8, 2008.

[29] T. J. Quinn, P. Langhorne, and D. J. Stott. Barthel index for stroke trials: development, properties, and application. *Stroke*, 42(4):1146–1151, 2011.

[30] R. W. Bohannon. Muscle strength and muscle training after stroke. *Journal of rehabilitation Medicine*, 39(1):14–20, 2007.

[31] J. Yoon, J. Ryu, and K.-B. Lim. Reconfigurable ankle rehabilitation robot for various exercises. *Journal of Robotic Systems*, 22(S1):S15–S33, 2006.

[32] G. Kwakkel, J. M. Veerbeek, E. E. H. van Wegen, and S. L. Wolf. Constraint-induced movement therapy after stroke. *The Lancet Neurology*, 14(2):224–234, 2015.

[33] T. J. Kimberley, S. M. Lewis, E. J. Auerbach, L. L. Dorsey, J. M. Lojovich, and J. R. Carey. Electrical stimulation driving functional improvements and cortical changes in subjects with stroke. *Experimental Brain Research*, 154(4):450–460, 2004.

[34] M. Hallett. Transcranial magnetic stimulation and the human brain. *Nature*, 406 (6792):147–150, 2000.

[35] M. Kobayashi and A. Pascual-Leone. Transcranial magnetic stimulation in neurology. *The Lancet Neurology*, 2(3):145–156, 2003.

[36] S. Masiero, A. Celia, G. Rosati, and M. Armani. Robotic-assisted rehabilitation of the upper limb after acute stroke. *Archives of physical medicine and rehabilitation*, 88(2):142–149, 2007.

[37] C. E. Skilbeck, D. T. Wade, R. L. Hewer, and V. A. Wood. Recovery after stroke. *Journal of Neurology, Neurosurgery & Psychiatry*, 46(1):5–8, 1983.

[38] B. Hobbs and P. Artemiadis. A review of robot-assisted lower-limb stroke therapy: Unexplored paths and future directions in gait rehabilitation. *Frontiers in Neurorobotics*, 14, 2020.

[39] S. C. Cramer, M. Sur, B. H. Dobkin, C. O'brien, T. D. Sanger, J. Q. Trojanowski, J. M. Rumsey, R. Hicks, J. Cameron, D. Chen, et al. Harnessing neuroplasticity for clinical applications. *Brain*, 134(6):1591–1609, 2011.

[40] S. Balasubramanian, J. Klein, and E. Burdet. Robot-assisted rehabilitation of hand function. *Current opinion in neurology*, 23(6):661–670, 2010.

[41] W. Meng, Q. Liu, Z. Zhou, Q. Ai, B. Sheng, and S. S. Xie. Recent development of mechanisms and control strategies for robot-assisted lower limb rehabilitation. *Mechatronics*, 31:132–145, 2015.

[42] F. Zhang, P. Li, Z.-G. Hou, Z. Lu, Y. Chen, Q. Li, and M. Tan. semg-based continuous estimation of joint angles of human legs by using bp neural network. *Neurocomputing*, 78(1):139–148, 2012.

[43] H. J. Asl, T. Narikiyo, and M. Kawanishi. An assist-as-needed control scheme for robot-assisted rehabilitation. In *2017 American control conference (acc)*, pages 198–203. IEEE, 2017.

[44] G. Aguirre-Ollinger, J. E. Colgate, M. A. Peshkin, and A. Goswami. Design of an active one-degree-of-freedom lower-limb exoskeleton with inertia compensation. *The International Journal of Robotics Research*, 30(4):486–499, 2011.

[45] P. Beyl, M. Van Damme, R. Van Ham, B. Vanderborght, and D. Lefeber. Design and control of a lower limb exoskeleton for robot-assisted gait training. *Applied Bionics and Biomechanics*, 6(2):229–243, 2009.

[46] R. J. Farris, H. A. Quintero, and M. Goldfarb. Performance evaluation of a lower limb exoskeleton for stair ascent and descent with paraplegia. In *2012 Annual international conference of the IEEE engineering in medicine and biology society*, pages 1908–1911. IEEE, 2012.

[47] N.-S. Kwak, K.-R. Müller, and S.-W. Lee. A lower limb exoskeleton control system based on steady state visual evoked potentials. *Journal of neural engineering*, 12 (5):056009, 2015.

[48] T. Lenzi, S. M. M. De Rossi, N. Vitiello, and M. C. Carrozza. Intention-based emg control for powered exoskeletons. *IEEE transactions on biomedical engineering*, 59(8):2180–2190, 2012.

[49] J. Li, T. Wu, Z. Xu, and X. Gu. A pilot study of post-total knee replacement gait rehabilitation using lower limbs robot-assisted training system. *European Journal of Orthopaedic Surgery & Traumatology*, 24(2):203–208, 2014.

[50] S. A. Murray, K. H Ha, C. Hartigan, and M. Goldfarb. An assistive control approach for a lower-limb exoskeleton to facilitate recovery of walking following stroke. *IEEE Transactions on Neural Systems and Rehabilitation Engineering*, 23 (3):441–449, 2014.

[51] D. Sanz-Merodio, Manuel Cestari, Juan Carlos Arevalo, and Elena Garcia. A lower-limb exoskeleton for gait assistance in quadriplegia. In *2012 IEEE International Conference on Robotics and Biomimetics (ROBIO)*, pages 122–127. IEEE, 2012.

[52] L. Wang, S. Wang, E. H. F. van Asseldonk, and H. van der Kooij. Actively controlled lateral gait assistance in a lower limb exoskeleton. In *2013 IEEE/RSJ International Conference on Intelligent Robots and Systems*, pages 965–970. IEEE, 2013.

[53] Y. Huang, W. P. Lai, Q. Qian, X. Hu, E. W. C. Tam, and Y. Zheng. Translation of robot-assisted rehabilitation to clinical service: a comparison of the rehabilitation effectiveness of emg-driven robot hand assisted upper limb training in practical clinical service and in clinical trial with laboratory configuration for chronic stroke. *Biomedical engineering online*, 17(1):91, 2018.

[54] J.-F. Zhang, Y.-M. Dong, C.-J. Yang, Y. Geng, Y. Chen, and Y. Yang. 5-link model based gait trajectory adaption control strategies of the gait rehabilitation exoskeleton for post-stroke patients. *Mechatronics*, 20(3):368–376, 2010.

[55] H. I. Krebs, J. J. Palazzolo, L. Dipietro, M. Ferraro, J. Krol, K. Rannekleiv, B. T. Volpe, and N. Hogan. Rehabilitation robotics: Performance-based progressive robot-assisted therapy. *Autonomous robots*, 15(1):7–20, 2003.

[56] X. Zhang, Z. Yue, and J. Wang. Robotics in lower-limb rehabilitation after stroke. *Behavioural neurology*, 2017, 2017.

[57] H. Suryotrisongko and F. Samopa. Evaluating openbci spiderclaw v1 headwear's electrodes placements for brain-computer interface (bci) motor imagery application. *Procedia Computer Science*, 72:398–405, 2015.

[58] S. Hesse, J. Mehrholz, and C. Werner. Robot-assisted upper and lower limb rehabilitation after stroke: walking and arm/hand function. *Deutsches Ärzteblatt International*, 105(18):330, 2008.

[59] D. Shakti, L. Mathew, N. Kumar, and C. Kataria. Effectiveness of robo-assisted lower limb rehabilitation for spastic patients: A systematic review. *Biosensors and Bioelectronics*, 117:403–415, 2018.

[60] K. Lo, M. Stephenson, and C. Lockwood. Effectiveness of robotic assisted rehabilitation for mobility and functional ability in adult stroke patients: a systematic review. *JBI database of systematic reviews and implementation reports*, 15(12): 3049–3091, 2017.

[61] S. Jezernik, G. Colombo, T. Keller, H. Frueh, and M. Morari. Robotic orthosis lokomat: A rehabilitation and research tool. *Neuromodulation: Technology at the neural interface*, 6(2):108–115, 2003.

[62] E. Simoneau-Buessinger, C. Gillet, S. Leteneur, J.-F. Debril, and N. Decoufour. Ankle ergometer, November 17 2020. US Patent 10,835,173.

[63] J. C. Arceo, J. Lauber, L. Robinault, S. Paganelli, M. Jochumsen, I. K. Niazi, E. Simoneau, and S. Cremoux. Modeling and control of rehabilitation robotic device: motobotte. In *International Conference on NeuroRehabilitation*, pages 546–550. Springer, 2018.

[64] J.P. Merlet. *Parallel robots*, volume 128. Springer Science & Business Media, 2006.

[65] D. M. Dawson, C. T. Abdallah, and F. L. Lewis. *Robot manipulator control: theory and practice*. CRC Press, 2003.

[66] O. Vinogradov. *Fundamentals of kinematics and dynamics of machines and mechanisms*. CRC press, 2000.

[67] P. J. Rabier and W. C. Rheinboldt. *Theoretical and numerical analysis of differential-algebraic equations*. Elsevier, 2002.

[68] SKF. *CAHB-21: Linear Actuator. Installation, operation and maintenance manual*. SKF Taiwan Co., Ltd, No. 3, Lane 11, Tzu-Chiang St., Tu-Cheng Industrial District, Taipei, Taiwan, August 2010.

[69] Maxon Motor. *ESCON 50/5 DC Servo Controller Hardware Reference*. Maxon Motor, Bränigstrasse 220 P.O.Box 263 CH-6072 Sachseln, rel7125 edition, November 2018.

[70] National Instruments. *NI myRIO-1900 User Guide and Specifications*. National Instruments, 11500 North Mopac Expressway, Austin, Texas,78759-3504, 376047c-01 edition, May 2016.

[71] SENSIX. Force-torque sensor for biomechanics - cylindrical sensors, 2021. URL http://sensix.fr/cylindrical-sensors_std_23_uk.html.

[72] Emilie SIMONEAU-BUESSINGER, Christophe Gillet, Sebastien LETENEUR, Jean-Francois DEBRIL, and Nicolas DECOUFOUR. Ankle ergometer, Nov 2017.

[73] L. Ljung. Non-linear black box models in system identification. *IFAC Proceedings Volumes*, 30(9):1–12, 1997.

[74] L. Ljung. System identification. *Wiley encyclopedia of electrical and electronics engineering*, pages 1–19, 1999.

[75] O. Nelles. *Nonlinear system identification: from classical approaches to neural networks and fuzzy models*. Springer Science & Business Media, 2013.

[76] J. L. Melsa. *System identification*. Academic Press, 1971.

[77] K. J. Keesman. *System identification: an introduction*. Springer Science & Business Media, 2011.

[78] S. Haykin. *Neural networks: a comprehensive foundation*. Prentice-Hall, Inc., 2007.

[79] E. B. Kosmatopoulos, M. A. Christodoulou, and P. A. Ioannou. Dynamical neural networks that ensure exponential identification error convergence. *Neural Networks*, 10(2):299–314, 1997.

[80] A. Sala and C. Ariño. Polynomial fuzzy models for nonlinear control: A taylor series approach. *IEEE Transactions on Fuzzy Systems*, 17(6):1284–1295, 2009.

[81] F. Gustafsson. Determining the initial states in forward-backward filtering. *IEEE Transactions on Signal Processing*, 44(4):988–992, 1996.

[82] J. J. Moré. The levenberg-marquardt algorithm: implementation and theory. In *Numerical analysis*, pages 105–116. Springer, 1978.

[83] Y. Barlas. Formal aspects of model validity and validation in system dynamics. *System dynamics review*, 12(3):183–210, 1996.

[84] Y.-C. Chang and B.-S. Chen. Robust tracking designs for both holonomic and nonholonomic constrained mechanical systems: adaptive fuzzy approach. *IEEE Transactions on Fuzzy Systems*, 8(1):46–66, 2000.

[85] J. Sjöberg, Q. Zhang, L. Ljung, A. Benveniste, B. Delyon, P.-Y. Glorennec, H. Hjalmarsson, and A. Juditsky. Nonlinear black-box modeling in system identification: a unified overview. *Automatica*, 31(12):1691–1724, 1995.

[86] Alain Codourey. Dynamic modeling of parallel robots for computed-torque control implementation. *The International Journal of Robotics Research*, 17(12):1325–1336, 1998.

[87] H. Cheng, Y.-K. Yiu, and Z. Li. Dynamics and control of redundantly actuated parallel manipulators. *IEEE/ASME Transactions on mechatronics*, 8(4):483–491, 2003.

[88] F.L. Lewis, D.M. Dawson, and C.T. Abdallah. *Robot Manipulator Control: Theory and Practice*. CRC Press, 2003.

[89] J. C. Arceo, M. Sanchez, V. Estrada-Manzo, and M. Bernal. Convex stability analysis of nonlinear singular systems via linear matrix inequalities. *IEEE Transactions on Automatic Control*, 2018.

[90] C. C. Pantelides. The consistent initialization of differential-algebraic systems. *SIAM Journal on Scientific and Statistical Computing*, 9(2):213–231, 1988.

[91] N. S. Nedialkov, J. D. Pryce, and G. Tan. Algorithm 948: Daesa—a matlab tool for structural analysis of differential-algebraic equations: Software. *ACM Transactions on Mathematical Software (TOMS)*, 41(2):12, 2015.

[92] L. F. Shampine. Solving 0=f(t,y(t),y'(t)) in Matlab. *Journal of Numerical Mathematics*, 10(4):291–310, 2002.

[93] F. L. Lewis. A survey of linear singular systems. *Circuits, Systems and Signal Processing*, 5(1):3–36, 1986.

[94] J. Alvarez, J. C. Arceo, C. Armenta, J. Lauber, and M. Bernal. An extension of computed-torque control for parallel robots in ankle reeducation. *IFAC-PapersOnLine*, 52(11):1–6, 2019.

[95] P. Ghosh. *Numerical, Symbolic and Statistical Computing for Chemical Engineers using MATLAB*. PHI Learning Pvt. Ltd., 2018.

[96] L. F. Shampine, S. Thompson, J.A. Kierzenka, and G.D. Byrne. Non-negative solutions of odes. *Applied Mathematics and Computation*, 170(1):556–569, 2005.

[97] L. Peng, Z.-G. Hou, and W. Wang. Dynamic modeling and control of a parallel upper-limb rehabilitation robot. In *2015 IEEE International Conference on Rehabilitation Robotics (ICORR)*, pages 532–537, 2015.

[98] V. Klee and G. J. Minty. How good is the simplex algorithm. Technical report, Washington univ Seattle dept. of mathematics, 1970.

[99] I. Díaz, J. J. Gil, and E. Sánchez. Lower-limb robotic rehabilitation: literature review and challenges. *Journal of Robotics*, 2011, 2011.

[100] H. Herr. Exoskeletons and orthoses: classification, design challenges and future directions. *Journal of neuroengineering and rehabilitation*, 6(1):21, 2009.

[101] B. S. Rupal, S. Rafique, A. Singla, E. Singla, M. Isaksson, and G. S. Virk. Lower-limb exoskeletons: Research trends and regulatory guidelines in medical and non-medical applications. *International Journal of Advanced Robotic Systems*, 14(6): 1729881417743554, 2017.

[102] V. Arnez-Paniagua, H. Rifaï, Y. Amirat, M. Ghedira, J. M. Gracies, and S. Mohammed. Adaptive control of an actuated ankle foot orthosis for paretic patients. *Control Engineering Practice*, 90:207–220, 2019.

[103] J. C. Pérez-Ibarra and A. A. Siqueira. Comparison of kinematic and emg parameters between unassisted, fixed-and adaptive-stiffness robotic-assisted ankle movements in post-stroke subjects. In *2017 International Conference on Rehabilitation Robotics (ICORR)*, pages 461–466. IEEE, 2017.

[104] K Alex Shorter, Géza F Kogler, Eric Loth, William K Durfee, and Elizabeth T Hsiao-Wecksler. A portable powered ankle-foot orthosis for rehabilitation. *Journal of Rehabilitation Research & Development*, 48(4), 2011.

[105] H. Zhu, J. Doan, C. Stence, G. Lv, T. Elery, and R. Gregg. Design and validation of a torque dense, highly backdrivable powered knee-ankle orthosis. In *2017 IEEE International Conference on Robotics and Automation (ICRA)*, pages 504–510. IEEE, 2017.

[106] M. Noël, B. Cantin, S. Lambert, C. M. Gosselin, and L. J. Bouyer. An electro-hydraulic actuated ankle foot orthosis to generate force fields and to test proprioceptive reflexes during human walking. *IEEE Transactions on Neural Systems and Rehabilitation Engineering*, 16(4):390–399, 2008.

[107] A. Isidori. *Nonlinear Control Systems*. Springer, London, 3 edition, 1995.

[108] E.G. Gilbert and I.J. Ha. An approach to nonlinear feedback control with applications to robotics. *IEEE Transactions on Systems, Man, and Cybernetics*, SMC-14 (6):879–884, 1984.

[109] K. Shin and N. McKay. Minimum-time control of robotic manipulators with geometric path constraints. *IEEE Transactions on Automatic Control*, 30(6):531–541, 1985.

[110] F.L. Lewis and E.W. Kamen. Applied optimal control and estimation. *IEEE Transactions on Automatic Control*, 39(8):1773–1773, 1994.

[111] K.J. Åström and B. Wittenmark. *Computer-controlled systems: theory and design*. Courier Corporation, 2013.

[112] Weiwei Shang and Shuang Cong. Nonlinear computed torque control for a high-speed planar parallel manipulator. *Mechatronics*, 19(6):987–992, 2009.

[113] M.W. Spong and M. Vidyasagar. Dynamics and control of robot manipulators, 1989.

[114] C. T. Chen. *Linear System Theory and Design*. Saunders College Publishing, New York, USA, 1984.

[115] S. Boyd, L. E. Ghaoui, E. Feron, and V. Belakrishnan. *Linear Matrix Inequalities in System and Control Theory*, volume 15. SIAM: Studies In Applied Mathematics, Philadelphia, USA, 1994.

[116] M. Ferrarin, F. Palazzo, R. Riener, and J. Quintern. Model-based control of fes-induced single joint movements. *IEEE Transactions on Neural systems and rehabilitation engineering*, 9(3):245–257, 2001.

[117] N. Petroff, K. D. Reisinger, and P. A.C. Mason. Fuzzy-control of a hand orthosis for restoring tip pinch, lateral pinch, and cylindrical prehensions to patients with

elbow flexion intact. *IEEE Transactions on neural systems and rehabilitation engineering*, 9(2):225–231, 2001.

[118] N. Alibeji, N. Kirsch, S. Farrokhi, and N. Sharma. Further results on predictor-based control of neuromuscular electrical stimulation. *IEEE Transactions on Neural Systems and Rehabilitation Engineering*, 23(6):1095–1105, 2015.

[119] J. Han. From pid to active disturbance rejection control. *IEEE transactions on Industrial Electronics*, 56(3):900–906, 2009.

[120] Y. Shtessel, C. Edwards, L. Fridman, and A. Levant. *Sliding mode control and observation*. Springer, 2014.

[121] E. J. Rouse, L. J. Hargrove, E. J. Perreault, and T. A. Kuiken. Estimation of human ankle impedance during the stance phase of walking. *IEEE Transactions on Neural Systems and Rehabilitation Engineering*, 22(4):870–878, 2014.

[122] D. A. Winter. *Biomechanics and motor control of human movement*. John Wiley & Sons, 2009.

[123] G. C. Burdea, D. Cioi, A. Kale, W. E. Janes, S. A. Ross, and J. R. Engsberg. Robotics and gaming to improve ankle strength, motor control, and function in children with cerebral palsy—a case study series. *IEEE Transactions on Neural Systems and Rehabilitation Engineering*, 21(2):165–173, 2012.

[124] Å. Björck and V. Pereyra. Solution of vandermonde systems of equations. *Mathematics of computation*, 24(112):893–903, 1970.

[125] R. Xu, N. Jiang, N. Mrachacz-Kersting, C. Lin, G. A. Prieto, J. C. Moreno, J. L. Pons, K. Dremstrup, and D. Farina. A closed-loop brain–computer interface triggering an active ankle–foot orthosis for inducing cortical neural plasticity. *IEEE Transactions on Biomedical Engineering*, 61(7):2092–2101, 2014.

[126] M. Jochumsen, S. Cremoux, L. Robinault, J. Lauber, J. C. Arceo, M. Navid, R. Nedergaard, U. Rashid, H. Haavik, and I. Niazi. Investigation of optimal afferent feedback modality for inducing neural plasticity with a self-paced brain-computer interface. *Sensors*, 18(11):3761, 2018.

[127] A. Dontchev and W. Hager. The euler approximation in state constrained optimal control. *Mathematics of Computation*, 70(233):173–203, 2001.

[128] B. M. Vinagre, Y. Q. Chen, and I. Petráš. Two direct tustin discretization methods for fractional-order differentiator/integrator. *Journal of the franklin institute*, 340 (5):349–362, 2003.

[129] M. Günther and P. Rentrop. The differential-algebraic index concept in electric circuit simulation. *Zeitschrift für angewandte Mathematik und Mechanik*, 76:91–94, 1996.

[130] A. Kumar and P. Daoutidis. *Control of nonlinear differential algebraic equation systems with applications to chemical processes*, volume 397. CRC Press, 1999.

[131] M. Sielemann, F. Casella, M. Otter, C. Clauß, J. Eborn, S. E. Matsson, and H. Olsson. Robust initialization of differential-algebraic equations using homotopy. In *Proceedings of the 8th International Modelica Conference; March 20th-22nd; Technical Univeristy; Dresden; Germany*, pages 75–85. Linköping University Electronic Press, 2011.

[132] J. Sjöberg, K. Fujimoto, and T. Glad. Model reduction of nonlinear differential-algebraic equations. *IFAC Proceedings Volumes*, 40(12):176–181, 2007.

[133] H. K. Khalil. *Nonlinear control*. Pearson Higher Ed, 2014.

[134] K. Takaba, N. Morihira, and T. Katayama. A generalized lyapunov theorem for descriptor system. *Systems & Control Letters*, 24(1):49–51, 1995.

[135] J. Y. Ishihara and M. H. Terra. On the lyapunov theorem for singular systems. *IEEE transactions on Automatic Control*, 47(11):1926–1930, 2002.

[136] M. C. de Oliveira and R. E. Skelton. Stability tests for constrained linear systems. In *Perspectives in robust control*, pages 241–257. Springer, 2001.

[137] T. Taniguchi, K. Tanaka, H. Ohtake, and H. O. Wang. Model construction, rule reduction, and robust compensation for generalized form of takagi-sugeno fuzzy systems. *IEEE Transactions on Fuzzy Systems*, 9(4):525–538, 2001.

[138] P. Baranyi, Y. Yam, and P. Várlaki. *Tensor product model transformation in polytopic model-based control*. CRC press, 2018.

[139] A. Sala. On the conservativeness of fuzzy and fuzzy-polynomial control of nonlinear systems. *Annual Reviews in Control*, 33(1):48–58, 2009.

[140] G. Chesi. Lmi techniques for optimization over polynomials in control: a survey. *IEEE Transactions on Automatic Control*, 55(11):2500–2510, 2010.

[141] C.-H. Fang, Y.-S. Liu, S.-W. Kau, L. Hong, and C.-H. Lee. A new lmi-based approach to relaxed quadratic stabilization of ts fuzzy control systems. *IEEE Transactions on fuzzy systems*, 14(3):386–397, 2006.

[142] A. Kruszewski, A. Sala, T. M. Guerra, and C. Ariño. A triangulation approach to asymptotically exact conditions for fuzzy summations. *IEEE Transactions on Fuzzy Systems*, 17(5):985–994, 2009.

[143] K. Tanaka, T. Ikeda, and H. O. Wang. Fuzzy regulators and fuzzy observers: relaxed stability conditions and lmi-based designs. *IEEE Transactions on fuzzy systems*, 6(2):250–265, 1998.

[144] H. D. Tuan, P. Apkarian, T. Narikiyo, and Y. Yamamoto. Parameterized linear matrix inequality techniques in fuzzy control system design. *IEEE Transactions on fuzzy systems*, 9(2):324–332, 2001.

[145] E. Kim and H. Lee. New approaches to relaxed quadratic stability condition of fuzzy control systems. *IEEE Transactions on Fuzzy systems*, 8(5):523–534, 2000.

[146] L. Xiaodong and Z. Qingling. New approaches to h controller designs based on fuzzy observers for ts fuzzy systems via lmi. *Automatica*, 39(9):1571–1582, 2003.

[147] K. G. Murty and S. N. Kabadi. Some np-complete problems in quadratic and nonlinear programming. *Mathematical programming*, 39(2):117–129, 1987.

[148] P. A. Parrilo. *Structured semidefinite programs and semialgebraic geometry methods in robustness and optimization*. PhD thesis, California Institute of Technology, 2000.

[149] A. J. Quist, E. de Klerk, C. Roos, and T. Terlaky. Copositive realxation for genera quadratic programming. *Optimization methods and software*, 9(1-3):185–208, 1998.

[150] C.R. Johnson. Positive definite matrices. *The American Mathematical Monthly*, 77(3):259–264, 1970.

[151] P. Gahinet, A. Nemirovskii, A. J. Laub, and M. Chilali. The lmi control toolbox. In *Proceedings of 1994 33rd IEEE Conference on Decision and Control*, volume 3, pages 2038–2041. IEEE, 1994.

[152] V. F. Montagner, R. C.L.F. Oliveira, and P. L.D. Peres. Convergent lmi relaxations for quadratic stabilizability and h control of takagi–sugeno fuzzy systems. *IEEE Transactions on Fuzzy Systems*, 17(4):863–873, 2009.

[153] K. Tanaka and H.O. Wang. *Fuzzy Control Systems Design and Analysis: A linear matrix inequality approach*. John Wiley & Sons, New York, 2001.

[154] K. Tanaka and H. O. Wang. *Fuzzy control systems design and analysis: a linear matrix inequality approach*. John Wiley & Sons, 2004.

[155] T. S. Buchanan, D. G. Lloyd, K. Manal, and T. F. Besier. Neuromusculoskeletal modeling: estimation of muscle forces and joint moments and movements from measurements of neural command. *Journal of applied biomechanics*, 20(4):367–395, 2004.

[156] R.A. Bogey, J. Perry, and A.J. Gitter. An emg-to-force processing approach for determining ankle muscle forces during normal human gait. *IEEE Transactions on Neural Systems and Rehabilitation Engineering*, 13(3):302–310, 2005.

[157] Q. Shao, D. N. Bassett, K. Manal, and T. S. Buchanan. An emg-driven model to estimate muscle forces and joint moments in stroke patients. *Computers in biology and medicine*, 39(12):1083–1088, 2009.

[158] D. G. Thelen. Adjustment of muscle mechanics model parameters to simulate dynamic contractions in older adults. *J. Biomech. Eng.*, 125(1):70–77, 2003.

[159] M. Damsgaard, J. Rasmussen, S. T. Christensen, E. Surma, and M. De Zee. Analysis of musculoskeletal systems in the anybody modeling system. *Simulation Modelling Practice and Theory*, 14(8):1100–1111, 2006.

[160] S. L. Delp, F. C. Anderson, A. S. Arnold, P. Loan, A. Habib, C. T. John, E. Guendelman, and D. G. Thelen. Opensim: open-source software to create and analyze dynamic simulations of movement. *IEEE transactions on biomedical engineering*, 54(11):1940–1950, 2007.

[161] U. Trinler, H. Schwameder, R. Baker, and N. Alexander. Muscle force estimation in clinical gait analysis using anybody and opensim. *Journal of biomechanics*, 86: 55–63, 2019.

[162] H. M. Herr, K. Endo, P. Krishnaswamy, J. Markowitz, M. F. Eilenberg, and J. Wang. Neuromuscular model-based sensing and control paradigm for a robotic leg, May 22 2018. US Patent 9,975,249.

[163] J. Han, Q. Ding, A. Xiong, and X. Zhao. A state-space emg model for the estimation of continuous joint movements. *IEEE Transactions on Industrial Electronics*, 62(7):4267–4275, 2015.

[164] S. R. Hamner, A. Seth, and S. L. Delp. Muscle contributions to propulsion and support during running. *Journal of biomechanics*, 43(14):2709–2716, 2010.

[165] D. G. Lloyd and T. F. Besier. An emg-driven musculoskeletal model to estimate muscle forces and knee joint moments in vivo. *Journal of biomechanics*, 36(6): 765–776, 2003.

[166] K. Manal, K. Gravare-Silbernagel, and T. S. Buchanan. A real-time emg-driven musculoskeletal model of the ankle. *Multibody system dynamics*, 28(1-2):169–180, 2012.

[167] I.W. Hunter and R.E. Kearney. Dynamics of human ankle stiffness: variation with mean ankle torque. *Journal of biomechanics*, 15(10):747–752, 1982.

[168] I.W. Hunter and R.E. Kearney. Invariance of ankle dynamic stiffness during fatiguing muscle contractions. *Journal of Biomechanics*, 16(12):985–991, 1983.

[169] K. E. Gordon and D. P. Ferris. Learning to walk with a robotic ankle exoskeleton. *Journal of biomechanics*, 40(12):2636–2644, 2007.

[170] C. R. Kinnaird and D. P. Ferris. Medial gastrocnemius myoelectric control of a robotic ankle exoskeleton. *IEEE transactions on neural systems and rehabilitation engineering*, 17(1):31–37, 2008.

[171] D. Amarantini and L. Martin. A method to combine numerical optimization and emg data for the estimation of joint moments under dynamic conditions. *Journal of biomechanics*, 37(9):1393–1404, 2004.

[172] D.A. Winter, A. J. Fuglevand, and S.E. Archer. Crosstalk in surface electromyography: theoretical and practical estimates. *Journal of Electromyography and Kinesiology*, 4(1):15–26, 1994.

[173] D. Farina, R. Merletti, B. Indino, M. Nazzaro, and M. Pozzo. Surface emg crosstalk between knee extensor muscles: experimental and model results. *Muscle & Nerve: Official Journal of the American Association of Electrodiagnostic Medicine*, 26(5): 681–695, 2002.

[174] M. Blandeau, V. Estrada-Manzo, T.-M. Guerra, P. Pudlo, and F. Gabrielli. Fuzzy unknown input observer for understanding sitting control of persons living with spinal cord injury. *Engineering Applications of Artificial Intelligence*, 67:381–389, 2018.

[175] A.L. Hof. The relationship between electromyogram and muscle force. *Sportverletzung· Sportschaden*, 11(03):79–86, 1997.

[176] J. M. Winters. An improved muscle-reflex actuator for use in large-scale neuromusculoskeletal models. *Annals of biomedical engineering*, 23(4):359–374, 1995.

[177] F. E. Zajac. Muscle and tendon: properties, models, scaling, and application to biomechanics and motor control. *Critical reviews in biomedical engineering*, 17(4): 359–411, 1989.

[178] K. Manal and T. S. Buchanan. A one-parameter neural activation to muscle activation model: estimating isometric joint moments from electromyograms. *Journal of biomechanics*, 36(8):1197–1202, 2003.

[179] K. Manal, R. V. Gonzalez, D. G. Lloyd, and T. S. Buchanan. A real-time emg-driven virtual arm. *Computers in biology and medicine*, 32(1):25–36, 2002.

[180] J. M. Winters. Hill-based muscle models: a systems engineering perspective. In *Multiple muscle systems*, pages 69–93. Springer, 1990.

[181] T. F. Coleman and A. Verma. A preconditioned conjugate gradient approach to linear equality constrained minimization. *Computational Optimization and Applications*, 20(1):61–72, 2001.

[182] H. J. Hermens, B. Freriks, R. Merletti, D. Stegeman, J. Blok, G. Rau, C. Disselhorst-Klug, and G. Hagg. European recommendations for surface electromyography. *Roessingh research and development*, 8(2):13–54, 1999.

[183] Vicon Motion Systems Limited. *Vicon Nexus User Guide*. Nexus User GuideVicon Motion Systems Ltd., Vicon Oxford, 14 Minns Business Park, West Way, Oxford, OX2 0JB, UK, September 2016.

[184] L. Wang, Z. Lu, X. Liu, K. Liu, and D. Zhang. Adaptive control of a parallel robot via backstepping technique. *International Journal of Systems, Control and Communications*, 1(3):312–324, 2009.

[185] D. Gordon E. Robertson, G. E. Caldwell, J. Hamill, G. Kamen, and S. Whittlesey. *Research methods in biomechanics*. Human kinetics, 2013.

[186] T. F. Coleman and Y. Li. An interior trust region approach for nonlinear minimization subject to bounds. *SIAM Journal on optimization*, 6(2):418–445, 1996.

[187] J. E. Dennis Jr. Nonlinear least squares. *State of the art in numerical analysis*, pages 269–312, 1977.

[188] J. J. Daly, R. Cheng, J. Rogers, K. Litinas, K. Hrovat, and M. Dohring. Feasibility of a new application of noninvasive brain computer interface (bci): a case study of training for recovery of volitional motor control after stroke. *Journal of neurologic physical therapy*, 33(4):203–211, 2009.

[189] M. Grosse-Wentrup, D. Mattia, and K. Oweiss. Using brain–computer interfaces to induce neural plasticity and restore function. *Journal of neural engineering*, 8 (2):025004, 2011.

[190] A. Ramos-Murguialday, D. Broetz, M. Rea, L. Läer, Ö. Yilmaz, F. L. Brasil, G. Liberati, M. R. Curado, E. Garcia-Cossio, A. Vyziotis, et al. Brain–machine interface in chronic stroke rehabilitation: a controlled study. *Annals of neurology*, 74(1):100–108, 2013.

[191] A. A. Frolov, O. Mokienko, R. Lyukmanov, E. Biryukova, S. Kotov, L. Turbina, G. Nadareyshvily, and Y. Bushkova. Post-stroke rehabilitation training with a motor-imagery-based brain-computer interface (bci)-controlled hand exoskeleton: a randomized controlled multicenter trial. *Frontiers in neuroscience*, 11:400, 2017.

[192] A. Biasiucci, R. Leeb, I. Iturrate, S. Perdikis, A. Al-Khodairy, T. Corbet, A. Schnider, T. Schmidlin, H. Zhang, M. Bassolino, et al. Brain-actuated functional electrical stimulation elicits lasting arm motor recovery after stroke. *Nature communications*, 9(1):1–13, 2018.

[193] M. A. Cervera, S. R. Soekadar, J. Ushiba, J. del R. Millán, M. Liu, N. Birbaumer, and G. Garipelli. Brain-computer interfaces for post-stroke motor rehabilitation: a meta-analysis. *Annals of clinical and translational neurology*, 5(5):651–663, 2018.

[194] I. K. Niazi, N. Mrachacz-Kersting, N. Jiang, K. Dremstrup, and D. Farina. Peripheral electrical stimulation triggered by self-paced detection of motor intention enhances motor evoked potentials. *IEEE transactions on neural systems and rehabilitation engineering*, 20(4):595–604, 2012.

[195] M. Jochumsen, M. S. Navid, U. Rashid, H. Haavik, and I. K. Niazi. Emg-versus eeg-triggered electrical stimulation for inducing corticospinal plasticity. *IEEE Transactions on Neural Systems and Rehabilitation Engineering*, 27(9):1901–1908, 2019.

[196] M. Jochumsen, M. S. Navid, R. W. Nedergaard, N. Signal, U. Rashid, A. Hassan, H. Haavik, D. Taylor, and I. K. Niazi. Self-paced online vs. cue-based offline brain–computer interfaces for inducing neural plasticity. *Brain sciences*, 9(6):127, 2019.

[197] A. Pascual-Leone, D. Nguyet, L. G. Cohen, J. P. Brasil-Neto, A. Cammarota, and M. Hallett. Modulation of muscle responses evoked by transcranial magnetic stimulation during the acquisition of new fine motor skills. *Journal of neurophysiology*, 74(3):1037–1045, 1995.

[198] M. Jochumsen, I. K. Niazi, N. Mrachacz-Kersting, N. Jiang, D. Farina, and K. Dremstrup. Comparison of spatial filters and features for the detection and classification of movement-related cortical potentials in healthy individuals and stroke patients. *Journal of neural engineering*, 12(5):056003, 2015.

[199] G. R. Müller-Putz, V. Kaiser, T. Solis-Escalante, and G. Pfurtscheller. Fast set-up asynchronous brain-switch based on detection of foot motor imagery in 1-channel eeg. *Medical & biological engineering & computing*, 48(3):229–233, 2010.

[200] J. Ibáñez, J. I. Serrano, M. D. Del Castillo, E. Monge-Pereira, F. Molina-Rueda, I. Alguacil-Diego, and J. L. Pons. Detection of the onset of upper-limb movements based on the combined analysis of changes in the sensorimotor rhythms and slow cortical potentials. *Journal of neural engineering*, 11(5):056009, 2014.

[201] J. W. Krakauer. Motor learning: its relevance to stroke recovery and neurorehabilitation. *Current opinion in neurology*, 19(1):84–90, 2006.

[202] C. Pavlides, E. Miyashita, and H. Asanuma. Projection from the sensory to the motor cortex is important in learning motor skills in the monkey. *Journal of neurophysiology*, 70(2):733–741, 1993.

[203] N. Mrachacz-Kersting, S. R. Kristensen, I. K. Niazi, and D. Farina. Precise temporal association between cortical potentials evoked by motor imagination and afference induces cortical plasticity. *The Journal of physiology*, 590(7):1669–1682, 2012.

[204] K. Stefan, E. Kunesch, L. G. Cohen, R. Benecke, and J. Classen. Induction of plasticity in the human motor cortex by paired associative stimulation. *Brain*, 123 (3):572–584, 2000.

[205] S. De Vries and T. Mulder. Motor imagery and stroke rehabilitation: a critical discussion. *Journal of rehabilitation medicine*, 39(1):5–13, 2007.

[206] I. K. Niazi, N. Jiang, O. Tiberghien, J. F. Nielsen, K. Dremstrup, and D. Farina. Detection of movement intention from single-trial movement-related cortical potentials. *Journal of neural engineering*, 8(6):066009, 2011.

[207] M. Jochumsen, I. K. Niazi, N. Mrachacz-Kersting, D. Farina, and K. Dremstrup. Detection and classification of movement-related cortical potentials associated with task force and speed. *Journal of neural engineering*, 10(5):056015, 2013.

[208] E. Lew, R. Chavarriaga, S. Silvoni, and J. del R. Millán. Detection of self-paced reaching movement intention from eeg signals. *Frontiers in neuroengineering*, 5: 13, 2012.

[209] P. Ofner, A. Schwarz, J. Pereira, and G. R. Müller-Putz. Upper limb movements can be decoded from the time-domain of low-frequency eeg. *PloS one*, 12(8): e0182578, 2017.

[210] M. Vukelić and A. Gharabaghi. Oscillatory entrainment of the motor cortical network during motor imagery is modulated by the feedback modality. *Neuroimage*, 111:1–11, 2015.

[211] E. N. Kamavuako, M. Jochumsen, I. K. Niazi, and K. Dremstrup. Comparison of features for movement prediction from single-trial movement-related cortical potentials in healthy subjects and stroke patients. *Computational Intelligence and Neuroscience*, 2015, 2015.

[212] F. Karimi, J. Kofman, N. Mrachacz-Kersting, D. Farina, and N. Jiang. Detection of movement related cortical potentials from eeg using constrained ica for brain-computer interface applications. *Frontiers in neuroscience*, 11:356, 2017.

[213] Z. Jin, G. Zhou, D. Gao, and Y. Zhang. Eeg classification using sparse bayesian extreme learning machine for brain–computer interface. *Neural Computing and Applications*, 32(11):6601–6609, Jun 2018. ISSN 1433-3058. doi: 10.1007/s00521-018-3735-3. URL https://doi.org/10.1007/s00521-018-3735-3.

[214] J. Ma, Y. Zhang, A. Cichocki, and F. Matsuno. A novel eog/eeg hybrid human–machine interface adopting eye movements and erps: Application to robot control. *IEEE Transactions on Biomedical Engineering*, 62(3):876–889, 2014.

[215] Y. Zhang, G. Zhou, J. Jin, Q. Zhao, X. Wang, and A. Cichocki. Sparse bayesian classification of eeg for brain–computer interface. *IEEE transactions on neural networks and learning systems*, 27(11):2256–2267, 2015.

[216] A. J. Bergquist, J. M. Clair, and D. F. Collins. Motor unit recruitment when neuromuscular electrical stimulation is applied over a nerve trunk compared with a muscle belly: triceps surae. *Journal of Applied Physiology*, 110(3):627–637, 2011.

[217] T. Corbet, I. Iturrate, M. Pereira, S. Perdikis, and J. del R. Millán. Sensory threshold neuromuscular electrical stimulation fosters motor imagery performance. *Neuroimage*, 176:268–276, 2018.

[218] K. K. Ang, K. S. G. Chua, K. S. Phua, C. Wang, Z. Y. Chin, C. W. K. Kuah, W. Low, and C. Guan. A randomized controlled trial of eeg-based motor imagery brain-computer interface robotic rehabilitation for stroke. *Clinical EEG and neuroscience*, 46(4):310–320, 2015.

[219] M. Jochumsen, I. K. Niazi, N. Signal, R. W. Nedergaard, K. Holt, H. Haavik, and D. Taylor. Pairing voluntary movement and muscle-located electrical stimulation increases cortical excitability. *Frontiers in human neuroscience*, 10:482, 2016.

[220] N. Mrachacz-Kersting, M. Voigt, A. J. T. Stevenson, S. Aliakbaryhosseinabadi, N. Jiang, K. Dremstrup, and D. Farina. The effect of type of afferent feedback timed with motor imagery on the induction of cortical plasticity. *Brain research*, 1674:91–100, 2017.

[221] S. Khaslavskaia and T. Sinkjaer. Motor cortex excitability following repetitive electrical stimulation of the common peroneal nerve depends on the voluntary drive. *Experimental brain research*, 162(4):497–502, 2005.

[222] G. I. Barsi, D. B. Popovic, I. M. Tarkka, T. Sinkjær, and M. J. Grey. Cortical excitability changes following grasping exercise augmented with electrical stimulation. *Experimental brain research*, 191(1):57, 2008.

[223] L. Taylor, G. N. Lewis, and D. Taylor. Short-term effects of electrical stimulation and voluntary activity on corticomotor excitability in healthy individuals and people with stroke. *Journal of Clinical Neurophysiology*, 29(3):237–243, 2012.

[224] F. Kaneko, T. Hayami, T. Aoyama, and T. Kizuka. Motor imagery and electrical stimulation reproduce corticospinal excitability at levels similar to voluntary muscle contraction. *Journal of NeuroEngineering and Rehabilitation*, 11(1):94, 2014.

[225] S. Rossi, M. Hallett, P. M. Rossini, A. Pascual-Leone, Safety of TMS Consensus Group, et al. Safety, ethical considerations, and application guidelines for the use of transcranial magnetic stimulation in clinical practice and research. *Clinical neurophysiology*, 120(12):2008–2039, 2009.

[226] A. Toumi, S. Leteneur, C. Gillet, J.-F. Debril, N. Decoufour, F. Barbier, J. M. Jakobi, and E. Simoneau-Buessinger. Enhanced precision of ankle torque measure with an open-unit dynamometer mounted with a 3d force-torque sensor. *European journal of applied physiology*, 115(11):2303–2310, 2015.

[227] J. C. Arceo, J. Lauber, E. Simoneau, and S. Cremoux. Nonlinear convex control for robotic assistive therapy via lmis. In *Workshop on Assistance and Service Robotics*

in a Human Environment: From Personal Mobility Aids to Rehabilitation-Oriented Robotics in the International Conference on Intelligent Robots 2018 (IROS 2018), 2018.

[228] C. U. Kunz, N. Stallard, N. Parsons, S. Todd, and T. Friede. Blinded versus unblinded estimation of a correlation coefficient to inform interim design adaptations. *Biometrical Journal*, 59(2):344–357, 2017.

[229] D. Bates, M. Mächler, B. Bolker, and S. Walker. Fitting linear mixed-effects models using lme4. *arXiv preprint arXiv:1406.5823*, 2014.

[230] B. C. Jaeger. R2glmm: Computes r squared for mixed (multilevel models)(version r package version 0.1. 2), 2017.

[231] J. Twisk, L. Bosman, T. Hoekstra, J. Rijnhart, M. Welten, and M. Heymans. Different ways to estimate treatment effects in randomised controlled trials. *Contemporary clinical trials communications*, 10:80–85, 2018.

[232] M. C. Ridding and U. Ziemann. Determinants of the induction of cortical plasticity by non-invasive brain stimulation in healthy subjects. *The Journal of physiology*, 588(13):2291–2304, 2010.

[233] T. Sinkjær, J. B. Andersen, M. Ladouceur, L. O. D. Christensen, and J. B. Nielsen. Major role for sensory feedback in soleus emg activity in the stance phase of walking in man. *The Journal of physiology*, 523(Pt 3):817, 2000.

[234] J. B. Nielsen and T. Sinkjær. Afferent feedback in the control of human gait. *Journal of electromyography and kinesiology*, 12(3):213–217, 2002.

[235] K. Rosenkranz and J. C. Rothwell. Differences between the effects of three plasticity inducing protocols on the organization of the human motor cortex. *European Journal of Neuroscience*, 23(3):822–829, 2006.

[236] N. Mrachacz-Kersting, M. Fong, B. A. Murphy, and T. Sinkjær. Changes in excitability of the cortical projections to the human tibialis anterior after paired associative stimulation. *Journal of neurophysiology*, 97(3):1951–1958, 2007.

[237] N. Petersen, L. O. D. Christensen, H. Morita, T. Sinkjær, and J. Nielsen. Evidence that a transcortical pathway contributes to stretch reflexes in the tibialis anterior muscle in man. *The Journal of physiology*, 512(1):267–276, 1998.

[238] D. F. Collins. Central contributions to contractions evoked by tetanic neuromuscular electrical stimulation. *Exercise and sport sciences reviews*, 35(3):102–109, 2007.

[239] N. Mrachacz-Kersting, N. Jiang, A. J. T. Stevenson, I. K. Niazi, V. Kostic, A. Pavlovic, S. Radovanovic, M. Djuric-Jovicic, F. Agosta, K. Dremstrup, et al. Efficient neuroplasticity induction in chronic stroke patients by an associative brain-computer interface. *Journal of neurophysiology*, 115(3):1410–1421, 2016.

[240] A. Suppa, A. Quartarone, H. Siebner, R. Chen, V. Di Lazzaro, P. Del Giudice, W. Paulus, J. C. Rothwell, U. Ziemann, and J. Classen. The associative brain at work: evidence from paired associative stimulation studies in humans. *Clinical Neurophysiology*, 128(11):2140–2164, 2017.

[241] S. Olsen, N. Signal, I. K. Niazi, T. Christensen, M. Jochumsen, and D. Taylor. Paired associative stimulation delivered by pairing movement-related cortical potentials with peripheral electrical stimulation: An investigation of the duration of neuromodulatory effects. *Neuromodulation: Technology at the Neural Interface*, 21(4):362–367, 2018.

[242] M. Jochumsen, H. Knoche, P. Kidmose, T. W. Kjær, and B. I. Dinesen. Evaluation of eeg headset mounting for brain-computer interface-based stroke rehabilitation by patients, therapists, and relatives. *Frontiers in Human Neuroscience*, 14, 2020.

[243] W. D. Hairston, K. W. Whitaker, A. J Ries, J. M. Vettel, J. C. Bradford, S. E. Kerick, and K. McDowell. Usability of four commercially-oriented eeg systems. *Journal of neural engineering*, 11(4):046018, 2014.

[244] Y. Renard, F. Lotte, G. Gibert, M. Congedo, E. Maby, V. Delannoy, O. Bertrand, and A. Lécuyer. Openvibe: An open-source software platform to design, test, and use brain–computer interfaces in real and virtual environments. *Presence: teleoperators and virtual environments*, 19(1):35–53, 2010.

[245] C. M McCrimmon, Jonathan Lee Fu, Ming Wang, Lucas Silva Lopes, Po T Wang, Alireza Karimi-Bidhendi, Charles Y Liu, Payam Heydari, Zoran Nenadic, and An Hong Do. Performance assessment of a custom, portable, and low-cost brain–computer interface platform. *IEEE Transactions on Biomedical Engineering*, 64 (10):2313–2320, 2017.

[246] U. Rashid, I. K. Niazi, N. Signal, and D. Taylor. An eeg experimental study evaluating the performance of texas instruments ads1299. *Sensors*, 18(11):3721, 2018.

[247] V. Peterson, C. Galván, H. Hernández, and R. Spies. A feasibility study of a complete low-cost consumer-grade brain-computer interface system. *Heliyon*, 6 (3):e03425, 2020.

[248] F. Pichiorri, G. Morone, I. Pisotta, M. Petti, M. Molinari, L. Astolfi, F. Cincotti, and D. Mattia. Bci for stroke rehabilitation: a randomized controlled trial of efficacy. In *Proceedings of the Fifth International Brain-Computer Interface Meeting, Pacific Grove, CA, USA*, pages 3–7, 2013.

[249] D. R. Dudley, B. A. Knarr, K.-C. Siu, J. Peck, B. Ricks, and J. M. Zuniga. Testing of a 3d printed hand exoskeleton for an individual with stroke: a case study. *Disability and Rehabilitation: Assistive Technology*, pages 1–5, 2019.

[250] H.-J. Yoo, S. Lee, J. Kim, C. Park, and B. Lee. Development of 3d-printed myoelectric hand orthosis for patients with spinal cord injury. *Journal of NeuroEngineering and Rehabilitation*, 16(1):162, 2019.

[251] K. K. Ang, C. Guan, K. S. Phua, C. Wang, L. Zhou, K. Y. Tang, G. J. Ephraim Joseph, C. W. K. Kuah, and K. S. G. Chua. Brain-computer interface-based robotic end effector system for wrist and hand rehabilitation: results of a three-armed randomized controlled trial for chronic stroke. *Frontiers in neuroengineering*, 7:30, 2014.

[252] M. Sebastián-Romagosa, W. Cho, R. Ortner, N. Murovec, T. Von Oertzen, K. Kamada, B. Z. Allison, and C. Guger. Brain computer interface treatment for motor rehabilitation of upper extremity of stroke patients—a feasibility study. *Frontiers in Neuroscience*, 14, 2020.

[253] N. Mrachacz-Kersting and S. Aliakbaryhosseinabadi. Comparison of the efficacy of a real-time and offline associative brain-computer-interface. *Frontiers in neuroscience*, 12:455, 2018.

[254] G. Alder, N. Signal, S. Olsen, and D. Taylor. A systematic review of paired associative stimulation (pas) to modulate lower limb corticomotor excitability: Implications for stimulation parameter selection and experimental design. *Frontiers in neuroscience*, 13:895, 2019.

[255] S. Wiethoff, M. Hamada, and J. C. Rothwell. Variability in response to transcranial direct current stimulation of the motor cortex. *Brain stimulation*, 7(3):468–475, 2014.

[256] M. Hamada, N. Murase, A. Hasan, M. Balaratnam, and J. C. Rothwell. The role of interneuron networks in driving human motor cortical plasticity. *Cerebral cortex*, 23(7):1593–1605, 2013.

[257] J. Lahr, S. Paßmann, J. List, W. Vach, A. Flöel, and S. Klöppel. Effects of different analysis strategies on paired associative stimulation. a pooled data analysis from three research labs. *PLoS One*, 11(5):e0154880, 2016.

[258] V. López-Alonso, B. Cheeran, D. Río-Rodríguez, and M. Fernández-del Olmo. Inter-individual variability in response to non-invasive brain stimulation paradigms. *Brain stimulation*, 7(3):372–380, 2014.

[259] Y.-C. Tung, C.-H. Lai, C.-D. Liao, S.-W. Huang, T.-H. Liou, and H.-C. Chen. Repetitive transcranial magnetic stimulation of lower limb motor function in patients with stroke: a systematic review and meta-analysis of randomized controlled trials. *Clinical rehabilitation*, 33(7):1102–1112, 2019.

[260] A. Heald, D. Bates, N. E. F. Cartlidge, J. M. French, and S. Miller. Longitudinal study of central motor conduction time following stroke: 2. central motor conduction measured within 72 h after stroke as a predictor of functional outcome at 12 months. *Brain*, 116(6):1371–1385, 1993.

[261] F. Hummel, P. Celnik, P. Giraux, A. Floel, W.-H. Wu, C. Gerloff, and L. G. Cohen. Effects of non-invasive cortical stimulation on skilled motor function in chronic stroke. *Brain*, 128(3):490–499, 2005.

[262] A. Bastani and S. Jaberzadeh. Does anodal transcranial direct current stimulation enhance excitability of the motor cortex and motor function in healthy individuals and subjects with stroke: a systematic review and meta-analysis. *Clinical neurophysiology*, 123(4):644–657, 2012.

[263] D. J. Edwards, H. I. Krebs, A. Rykman, J. Zipse, G. W. Thickbroom, F. L. Mastaglia, A. Pascual-Leone, and B. T. Volpe. Raised corticomotor excitability of m1 forearm area following anodal tdcs is sustained during robotic wrist therapy in chronic stroke. *Restorative neurology and neuroscience*, 27(3):199–207, 2009.

[264] E. Chew, W.-P. Teo, N. Tang, K. K. Ang, Y. S. Ng, J. H. Zhou, I. Teh, K. S. Phua, L. Zhao, and C. Guan. Using transcranial direct current stimulation to augment the effect of motor imagery-assisted brain-computer interface training in chronic stroke patients—cortical reorganization considerations. *Frontiers in Neurology*, 11, 2020.

[265] Y. Kasashima, T. Fujiwara, Y. Matsushika, T. Tsuji, K. Hase, J. Ushiyama, J. Ushiba, and M. Liu. Modulation of event-related desynchronization during motor imagery with transcranial direct current stimulation (tdcs) in patients with chronic hemiparetic stroke. *Experimental brain research*, 221(3):263–268, 2012.

[266] M. A. Nitsche, A. Roth, M.-F. Kuo, A. K. Fischer, D. Liebetanz, N. Lang, F. Tergau, and W. Paulus. Timing-dependent modulation of associative plasticity by general network excitability in the human motor cortex. *Journal of Neuroscience*, 27(14):3807–3812, 2007.

[267] M. Kawakami, T. Fujiwara, J. Ushiba, A. Nishimoto, K. Abe, K. Honaga, A. Nishimura, K. Mizuno, M. Kodama, Y. Masakado, et al. A new therapeutic application of brain-machine interface (bmi) training followed by hybrid assistive neuromuscular dynamic stimulation (hands) therapy for patients with severe hemiparetic stroke: a proof of concept study. *Restorative neurology and neuroscience*, 34(5):789–797, 2016.

[268] M. Jochumsen, I. K. Niazi, M. S. Navid, M. N. Anwar, D. Farina, and K. Dremstrup. Online multi-class brain-computer interface for detection and classification of lower limb movement intentions and kinetics for stroke rehabilitation. *Brain-Computer Interfaces*, 2(4):202–210, 2015.

[269] M. Jochumsen, I. K. Niazi, D. Taylor, D. Farina, and K. Dremstrup. Detecting and classifying movement-related cortical potentials associated with hand movements in healthy subjects and stroke patients from single-electrode, single-trial eeg. *Journal of neural engineering*, 12(5):056013, 2015.

[270] N. Usama, K. K. Leerskov, I. K. Niazi, K. Dremstrup, and M. Jochumsen. Classification of error-related potentials from single-trial eeg in association with executed and imagined movements: a feature and classifier investigation. *Medical & Biological Engineering & Computing*, 58(11):2699–2710, 2020.

[271] N. Mrachacz-Kersting, A. J. T. Stevenson, H. R. M. Jørgensen, K. Eg. Severinsen, S. Aliakbaryhosseinabadi, N. Jiang, and D. Farina. Brain state–dependent stimulation boosts functional recovery following stroke. *Annals of neurology*, 85 (1):84–95, 2019.

[272] Y. Hashimoto, T. Kakui, J. Ushiba, M. Liu, K. Kamada, and T. Ota. Portable rehabilitation system with brain-computer interface for inpatients with acute and subacute stroke: A feasibility study. *Assistive Technology*, 2020.

[273] M. Jochumsen, I. K. Niazi, R. W. Nedergaard, M. S. Navid, and K. Dremstrup. Effect of subject training on a movement-related cortical potential-based brain-computer interface. *Biomedical Signal Processing and Control*, 41:63–68, 2018.

[274] I. K. Niazi, N. Jiang, M. Jochumsen, J. F. Nielsen, K. Dremstrup, and D. Farina. Detection of movement-related cortical potentials based on subject-independent training. *Medical & biological engineering & computing*, 51(5):507–512, 2013.

[275] N. Cheng, K. S. Phua, H. S. Lai, P. K. Tam, K. Y. Tang, K. K. Cheng, R. C.-H. Yeow, K. K. Ang, C. Guan, and J. H. Lim. Brain-computer interface-based soft robotic glove rehabilitation for stroke. *IEEE Transactions on Biomedical Engineering*, 2020.